A study investigating the blood-brain barrier penetration, distribution and elimination of retro-inverso peptides as candidate treatments for Alzheimer's disease

MARIA MICHAEL

A thesis submitted in fulfilment of the requirements

for the degree of Doctor of Philosophy

to

Lancaster University

November 2017

Declaration of Authorship

I, Maria Michael, declare that this thesis was composed by myself and that, unless otherwise stated in the text, the work presented therein is my own as a result of my original research, and has not been submitted in substantially the same form for the award of a higher degree elsewhere. I hereby declare that where contributions or published work of others are involved, are clearly attributed within the text and I have acknowledged all main sources of collaborative help. I can also confirm that this work was performed while in candidature for the degree of Doctor of Philosophy at Lancaster University.

Maria Michael

November 2017

Dedication

This thesis is dedicated to my father Nicos, my mother Despo and my sister Froso, who always picked me up and taught me that nothing is impossible.

“Not all those who wander are lost.”

J.R. R. Tolkien

From the poem “All that is gold does not glitter”, written for the “Lord of the Rings”.

Acknowledgements

Foremost, I would like to express my deepest gratitude to my supervisors, Prof. David Allsop and Prof. Christian Hölscher, for their full support, expert guidance and understanding throughout the course of my PhD at Lancaster University. Their knowledge and enthusiasm, along with their patience, effort, ideas and opportunities, motivated me to work harder for the accomplishment of this PhD thesis.

In addition, I owe a very important debt and appreciation to Dr. Mark Taylor for his continuous support, great assistance and encouragement throughout the laboratory research that was necessary to be performed for this work. I would also like to especially thank Dr. Kurimun Ismail for teaching me the Luminex technology, Dr. Simon Gengler for supporting me with the animal research and regulated procedures, and Dr. Jane Andre for her confocal imaging expertise.

Additionally, I would like to offer my special thanks and great appreciation to Prof. Massimo Masserini and Dr. Maria Gregori, Research Assistant at the University of Milano-Bicocca in Italy, for the advice and assistance provided on the development of one of our peptide inhibitors investigated in this thesis.

Furthermore, I would like to offer my special thanks to my fellow lab-mates and colleagues, in particular to Theodora Panagaki for her constant help and interest for the project, and her willingness to assist.

Last but not least, I would like to thank my family, particularly my mother Despo and my sister Froso, for supporting me throughout all my studies at Lancaster University. I will be grateful forever for their unconditional love. Special thanks also to my loved ones and close friends for keeping me strong through the entire process. I would not have been able to complete this project without their continuous love and encouragement.

Abstract

Title: A study investigating the blood-brain barrier penetration, distribution and elimination of retro-inverso peptides as candidate treatments for Alzheimer's disease.

Author: Maria Michael, November 2017.

Alzheimer's disease (AD) is an age-related neurodegenerative disease that mainly affects elderly individuals. The disease is characterised clinically by cognitive decline and neuropsychiatric symptoms, while its pathological features are the accumulation of senile plaques and neurofibrillary tangles in the brain. Aβ pathology is a central component of the disease. Early aggregated forms of Aβ known as "soluble oligomers" are believed to be a potent neurotoxic agent responsible for nerve cell damage and loss of synapses, so contributing to memory and learning deficits. Therefore, inhibiting the formation of these early aggregates could provide a novel approach to the treatment of AD.

A retro-inverso peptide, RI-OR2-TAT, has been developed previously in Lancaster, and this demonstrated good inhibition of early-stage Aβ aggregation, but only at high concentrations of inhibitor relative to Aβ. An improved peptide system was subsequently developed involving attachment of RI-OR2-TAT onto the surface of a lipid nanoparticle scaffold (nanoliposome). The resulting "Peptide inhibitor nanoparticles" (PINPs) demonstrated much more potent inhibition of aggregation, and could penetrate through an artificial BBB. In this project, RI-OR2-TAT, PINPs and a novel retro-inverso peptide, RI-OR2-NAG, were examined for their ability to cross the intact and functional blood-brain barrier (BBB) of WT mice. Their accumulation in the brain, distribution in peripheral tissues, and possible modes of excretion, were examined in WT mice, 1 h following peripheral administration.

In fluorescent imaging studies, fluorescein-labelled versions of RI-OR2-TAT, RI-OR2-NAG and PINPs all demonstrated effective penetration across an integral BBB and accumulation in the cortex, hippocampus, and dentate gyrus of the brain, where they were mainly co-localised with glial cells. Luminex technology was used to study the distribution of the first two peptides in the brain, heart, lungs, stomach, liver, spleen, kidneys and small intestine. The results of this study confirmed that these peptides accumulate in small amounts in the brain, but they are mainly found in the small intestine, suggesting a possible elimination route through bile secretions into the duodenum, followed by excretion through the faeces or reabsorption back into the general circulation, for possible excretion through the urine. Finally, as part of the project, the anti-aggregatory properties of the RI-OR2-NAG peptide were investigated, and this proved to be a more effective inhibitor of Aβ aggregation than RI-OR2-TAT.

In conclusion, the use of liposomes as an effective carrier nanosystem for targeted delivery could be extended to the RI-OR2-NAG peptide. The results of this PhD thesis project are encouraging and it is hoped that a version of these peptides can progress into clinical trials.

Table of Contents

List of Figures

List of Tables

List of Equations

Abbreviations

Aβ	Amyloid-β
AD	Alzheimer's disease
ADDLs	Amyloid β-derived diffusible ligands
AFM	Atomic force microscopy
AICD	Amyloid precursor protein intracellular domain
ANOVA	Analysis of variance
APOE	Apolipoprotein E
APP	Amyloid precursor protein
BBB	Blood-brain barrier
BCA	Bicinchoninic acid
BSA	Bovine serum albumin
B-CSFB	Blood-cerebrospinal fluid barrier
CA	Cornus ammonis
CL	PEGylated Control Liposomes
CNS	Central nervous system
CTF	C-terminal fragment
DG	Dentate gyrus
dH_2O	Deionised water
DMEM	Dulbecco's Modified Eagle's Medium
ECE1	Endothelin-converting enzyme 1
EDC	1-ethyl-3-(3-dimethylamino)propylcarbodiimide, hydrochloride
EDTA	Ethylenediaminetetraacetic acid
EEG	Electroencephalogram
ELISA	Enzyme-linked immunosorbent assay
FBS	Foetal Bovine Serum
FI	Fluorescent intensity
GFAP	Glial fibrillary acidic protein
GLUT	Glucose transporter
h	Hour / hours

HFIP	1,1,1,3,3,3-hexafluoro-2-propanol
HPLC	High performance liquid chromatography
Iba-1	Ionized calcium binding adapter molecule 1
IDE	Insulin-degrading enzyme
i.p.	Intraperitoneally
KH_2PO_4	Monopotassium phosphate bibasic acid
K_2HPO_4	Dipotassium phosphate monobasic acid
LDH	Lactate dehydrogenase
LDL	Low-density lipoprotein
LH	Left hemisphere (of brain)
MAL	Maleimide
MCI	Mild cognitive impairment
MES	2-(*N*-morpholino)ethanesulfonic acid
MFI	Median fluorescent intensity
min	Minute / minutes
MMSE	Mini-mental state examination
MS	Mass spectrometry
NaCl	Sodium Chloride
NAG	*N*-acetylglucosamine
NFTs	Neurofibrillary tangles
NeuN	Neuronal nuclei
NHS	*N*-hydroxysuccinimide
NMDA	N-methyl-D-aspartate
NSAID	Nonsteroidal anti-inflammatory drug
O/N	Overnight
PAGE	Polyacrylamide gel electrophoresis
PB	Phosphate buffer
PBS	Phosphate buffered saline
PBS-T	PBS with 0.05 % (v/v) Tween® 20
PB-2S	Phosphate buffered 2x saline
PE	R-phycoerythrin
PEG	Polyethylene glycol

PEN	Penicillin
PET	Positron Emission Tomography
PHFs	Paired helical filaments
PiB	Pittsburgh Compound-B
PINPs	Peptide inhibitor nanoparticles (Retro-inverted)
PSF	Point spread function
PS1	Presenilin 1 (gene)
PS2	Presenilin 2 (gene)
QWBA	Quantitative whole body analysis
RAGE	Receptor for advanced glycation endproducts
RCFmax	Relative centrifugal force
RH	Right hemisphere (of brain)
RI	Retro inverted
RIPA	Radioimmunoprecipitation assay
ROS	Reactive oxygen species
RPE	R-phycoerythrin
RPM	Revolutions per minute
RT	Room temperature
SDs	Standard deviations
SDS	Sodium dodecyl sulfate
Sec	Seconds
SEM	Standard error of mean
SLC	Solute carrier family of nucleotide sugar transporters
STREP	Streptavidin
S/N	Signal to noise ratio
TAT	Trans-activating transcriptional activator
TBS	Tris-buffered saline
TEM	Transmission Electron Microscopy
TFA	Trifluoroacetic acid
ThT	Thioflavin T
TREM	Triggering receptor expressed on myeloid cells
T2DM	Type 2 Diabetes Mellitus

v/v	Volume per volume
WT	Wild type
w/v	Weight per volume

Abbreviation key for amino acids used in inhibitors

C	Cysteine	(Cys)
F	Phenylalanine	(Phe)
G	Glycine	(Gly)
K	Lysine	(Lys)
L	Leucine	(Leu)
Q	Glutamine	(Gln)
R	Arginine	(Arg)
S	Serine	(Ser)
V	Valine	(Val)
Y	Tyrosine	(Tyr)

Chapter 1: Introduction

1.1. Alzheimer's disease

Alzheimer's disease (AD) is an age-related neurodegenerative disorder delineated mainly by cognitive impairment, and neuropsychiatric symptoms, as well as restriction in daily independence of living activities. AD is the leading and most common cause of dementia as it accounts for about two-thirds of all dementia cases (WWW, Alzheimer's Research UK), and affects mainly elderly individuals. Dementia is a general term used to describe a broad set of symptoms as a result of the damage present in the human brain caused by various degenerative diseases. Generally, dementia is a slow progressive condition, denoting that the symptoms will gradually become worse and more severe over time, resulting eventually in incapacitation. In particular, dementia symptoms comprise memory loss, confusion, mood changes, and difficulties with thinking, expression, language and problem-solving (WWW, Alzheimer's Society).

1.1.1. Alzheimer's first case

AD was first identified more than 100 years ago by a German psychiatrist and neuropathologist, Alois Alzheimer (1864 – 1915) (Alzheimer, 1907). In his first report published in 1907, Alzheimer described the symptoms of a 51-year-old female patient, Auguste Deter, who suffered from progressive memory impairment, reduced cognitive function, distorted and aggressive behaviour, language problems, hallucinations and disorientation (Alzheimer, 1907). Histological samples taken from the brain of the patient post-mortem showed widespread thinning of cerebrocortical grey matter, along with the presence of 'miliary bodies' between nerve cells and 'dense bundles of fibrils' inside nerve cells which today are known as the principal neuropathological and pathognomic hallmarks of AD (Blennow et al., 2006). These distinguishing focal lesions of the disease are respectively termed as senile or neuritic plaques which form as extracellular deposits of amyloid-β peptide (Aβ) in the grey matter of the brain, and neurofibrillary tangles (NFTs) that are

present intracellularly as aggregates of hyperphosphorylated tau protein (Figure 1.1.).

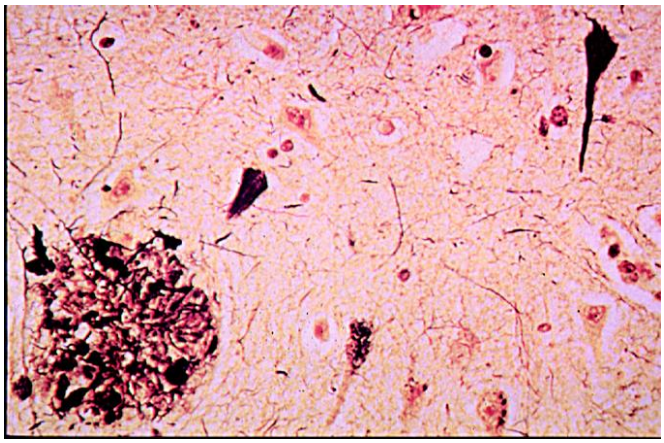

Figure 1.1. The neuropathological hallmarks of Alzheimer's disease.

Microscopic image of AD neuropathology showing a senile or neuritic plaque (lower left-hand corner) and a NFT (upper right-hand corner), which are known to be the pathognomic hallmarks of the disease (Bird, 2008).

1.1.2. Global prevalence and incidence rate

Currently, there are about 10 million people globally that suffer from neurodegenerative diseases each year, a figure that is expected to rise by 20% over the following decade due to the increased life expectancy of the population (OECD, 2010). What is more, neurodegenerative diseases are currently the fourth leading cause of death following the diseases of the heart, cancer and stroke (WWW, Organisation for Economic Co-operation and Development). With reference to AD, currently there are 46.8 million people worldwide who are believed to be living with the disease or related dementias; a number that is anticipated to increase to 74.7 million by 2030 and 131.5 million by 2050 (WWW, BrightFocus Foundation). Naturally due to the aging of the world population, AD is reaching an epidemic magnitude. It afflicts at least 6% of individuals over the age of 65, rising to 20% for those over the age of 80 (WWW, United Nations Population Division).

1.2. Pathological aspects and clinical features of Alzheimer's disease

AD is considered as one of the most debilitating conditions of the current century. Analogous to dementia, AD is considered as a progressive disorder with numerous pathological, structural and functional alterations ensuing and becoming gradually and irreversibly advanced over time.

1.2.1. Pathophysiological changes

The two main pathological hallmarks of the disease are the senile plaques composed of amyloid deposits and NFTs that are formed by intracellular deposits of hyperphosphorylated tau protein (Figure 1.1.). These characteristic lesions are predominantly found in the frontal and temporal lobes, including the hippocampus, and other cortical areas of the brain at autopsy (Morgan, 2011).

1.2.1.1. Senile plaques

The amyloid deposits are arranged in aggregated and accumulated forms of Aβ fibrils and are primarily found at the core of the senile plaques, in association with metals such as copper, iron and zinc (Selkoe, 2004; Zatta et al., 2009), and surrounded by activated microglia cells, reactive astrocytes and dystrophic dendrites and axons. As a result, the entire complex forms a spherical structure with a diameter of approximately 200 μm which can inflame the surrounding area of the brain by initiating many downstream events (Blessed et al., 1968).

1.2.1.2. Neurofibrillary tangles

The NFTs on the other hand are composed of intracellular deposits of tau, a microtubule-associated protein, which aggregates to form paired helical filaments (PHFs) that consist of two 10 nm filaments twisted around each other to form a double helix (Kidd, 1963). These filaments are abundant inside the nerve cells and occupy most of the cytoplasm (Puglielli, 2008). Hyperphosphorylation of tau protein results in its disassembling from the microtubule and instead forming the NFTs. As hyperphosphorylated tau protein is present inside the nerve cells, the efficacy of axonal transport is impaired jeopardising the function of neurons and synapses (Iqbal

et al., 2005) resulting in many synaptic defects and memory impairments (Cowan et al., 2010).

The brain of an AD patient exhibits global structural atrophy particularly in the hippocampus and temporal lobes (Figure 1.2.). Neuropathological changes of the disease include the loss of brain weight, dysfunction and degeneration of neurons and synapses, enlargement of ventricles, and widespread oxidative damage (Markesbery, 1997) and death of cholinergic neurons resulting in many downstream inflammatory responses (Rozemuller et al., 1986; Wyss-Coray, 2006; McGeer et al., 2006).

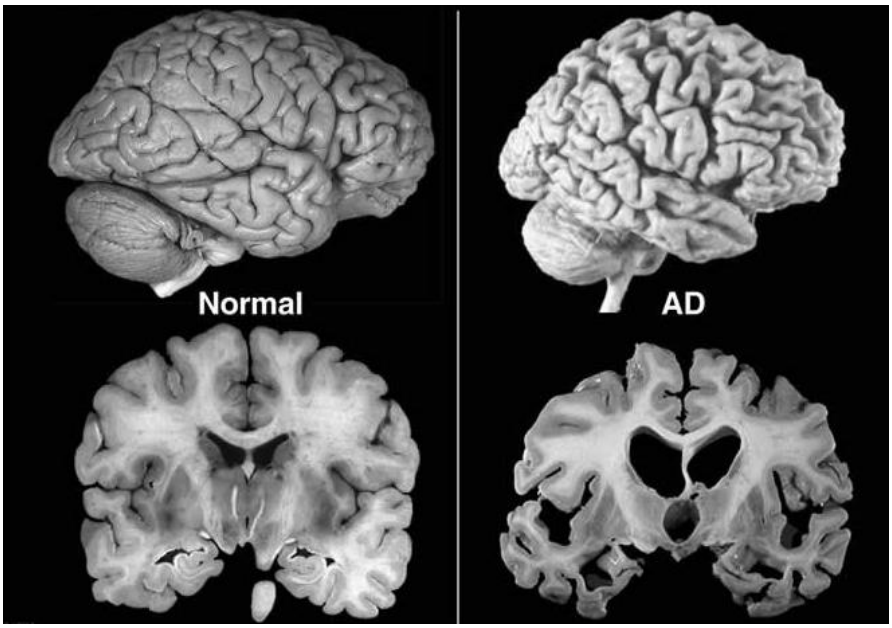

Figure 1.2. Comparison of a normal versus an Alzheimer brain.

Contrast image of a normal adult brain (left) with an Alzheimer's brain (right). During the progression of the disease, the structure of the brain becomes more damaged, showing marked diffuse cortical atrophy and enlargement of ventricles (Bird, 2008).

1.2.2. Neurological characterisation

The disease is clinically characterised by an insidious and vague onset along with progressive deterioration of selective cognitive domains, in particular short-term memory (primary/active memory). Specifically, memory decline initially establishes as a loss of episodic memory, which is considered as a subtype of declarative

(explicit) memory (LaFerla et al., 2007). Explicit memory with procedural (implicit) memory form the long term memory, which is severely affected during the late stage of AD.

Due to the progressive nature of the disease, typical signs that characterise the disease include agnosia, the lack of recognition of objects; apraxia, the inability to make voluntary movements; and aphasia, the loss of the capability to speak and poor word recognition. Alzheimer's patients often experience a plethora of cognitive symptoms due to the loss of cognitive function (the aptitude to think and reason clearly). These symptoms include disorientation, heighted aggression, agitation, impaired judgment, mood swings, sleep disturbances and hallucinations (Blennow et al., 2006).

1.2.3. Clinical determination for disease progression

The progression of AD and other dementias is commonly divided into three stages as defined by the mini-mental state examination (MMSE) score and include early, mild-moderate and late-severe stages. Nevertheless, neurodegeneration in AD is thought to start 20 – 30 years before the clinical onset and the appearance of overt clinical symptoms (Davies et al., 1988). The symptoms only appear after the plaque and NFT deposition reaches a certain critical threshold. Conversely, during the preclinical stage termed as mild cognitive impairment (MCI) (Eckerström et al., 2013), individuals show greater than expected memory deficits, yet not severe enough to be diagnosed with dementia. This presymptomatic stage is a transitional stage between normal ageing and AD where individuals can either be stable or go on to develop the disease with a conversion rate of 10 – 15% per year (Petersen, 2004). Ultimately, during the early stage of the disease, minor changes are detectable in behaviour due to the limited loss of cognitive function. On the contrary, as the disease advances to the moderate and severe stages, the changes become more discernible due to the loss of functional independence and increased behavioural problems. In consequence of these facts, the estimated life expectancy following initial diagnosis is around 8 years, depending on the individual's age.

1.3. Alzheimer's disease as amyloidosis

Numerous diseases, including AD, are characterised by the misfolding of one or more proteins which contribute, over a period of time, to extensive degeneration in specific brain regions, leading to the corresponding clinical and pathognomic features of each disease. These neurodegenerative diseases belong to a wider group of diseases termed as amyloidoses in which the central pathological characteristic is the deposition and accumulation of insoluble fibrillary proteins. Once formed, amyloid deposits remain resistant to proteolytic degradation; a process that normally allows the effective clearance of proteins from the organism and subsequently result in cell damage, organ dysfunction and ultimately death (Ghiso and Frangione, 2002).

Characterised by the presence of localised amyloid deposits and aggregates in the brain and the central nervous system (CNS), AD is actually the most frequent type of amyloidosis in humans (Wisniewski et al., 1997; Selkoe, 2001). The deposition of the insoluble and mature amyloid fibrils in AD is a consequence of misfolding from native α-helix/random coil soluble peptides to β-sheet structure, 7 – 10 nm in width (Figure 1.3.), with low molecular weight and ability to bind to dyes Congo red and ThT (Thioflavin T) (Gosal et al., 2006; Soto, 2003). Both Aβ and tau proteins are aggregated in AD composing parenchymal amyloid deposits in the form of amyloid/senile plaques and intraneuronal cytoplasmic deposits of NFTs, respectively.

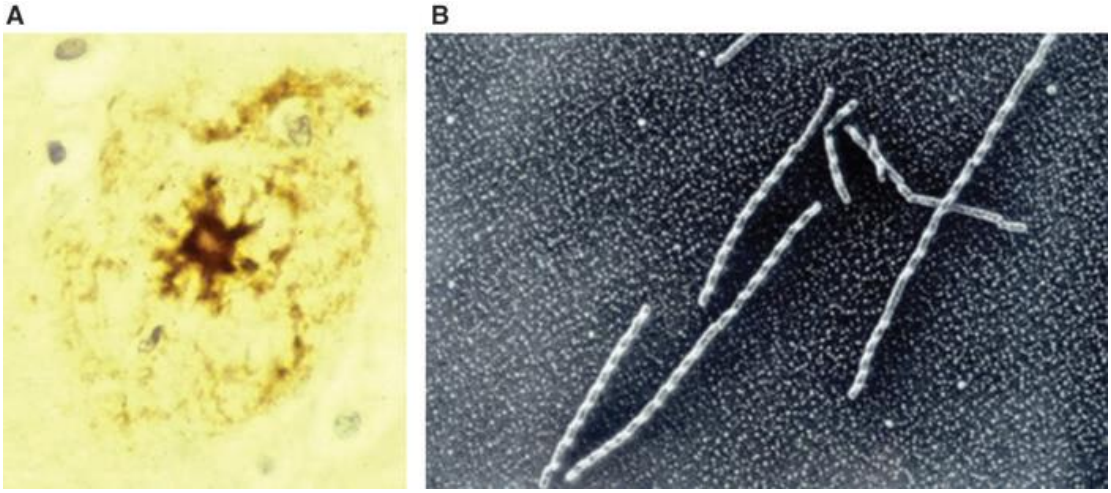

Figure 1.3. Aϐ fibrils and senile plaque formation.

A. The Aϐ peptide can be detected by in-vivo immunostaining at the core (centre) of the senile plaque. B. The in-vitro assembly of Aϐ into 10 nm (in diameter) fibrils as detected by electron microscopy with rotary metal shadowing (courtesy of Dr. David Howlett – King's College, London, U.K.) (Allsop, D., and Mayes, J., 2014).

1.3.1. Aβ and Amyloid precursor protein

The Aβ which is involved in AD as the main component of the amyloid plaques, is a 36 – 43 amino acid residue peptide and is produced by the internal proteolytic cleavage of both N- and C- terminal domains of a larger type I integral membrane glycoprotein called amyloid precursor protein (APP). The gene encoding the APP protein is located on chromosome 21 (Kang et al., 1987; Goldgaber et al., 1987; Robakis et al., 1987). The Aβ peptide sequence arises from fragments of exons 16 and 17 and contains a C-terminal hydrophobic tail composed of 12 – 14 residues that are derived from the intramembranous portion of APP, while the remaining resides are located outside of the membrane (Blennow et al., 2006; Barnham et al., 2003).

Aβ is produced constitutively during normal cell metabolism (Haass et al., 1992). Proteolytic cleavage of APP by α-secretase between residues 16 – 17 of the Aβ region prevents the formation of Aβ peptide; however initial cleavage by β-secretase and sequential processing of the resulting peptide by γ-secretase leads to the generation of Aβ (Figure 1.4.) Normally, APP in 90% of the neuronal cells undergoes the non-proteolytic pathway, denoting that the α-secretase pathway is predominant in APP processing (Selkoe, 2001; Blennow et al., 2006).

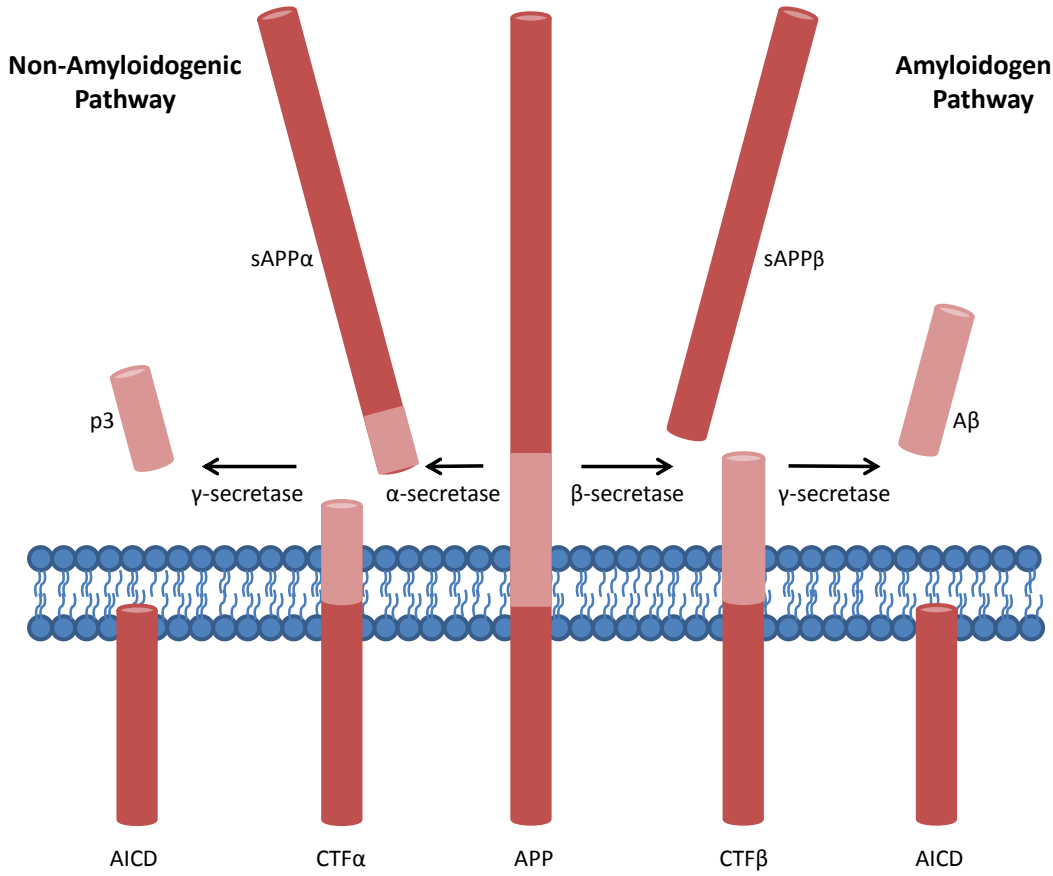

Figure 1.4. Proteolytic processing of APP.

In the non-amyloidogenic pathway (left-hand side) the APP is cleaved by α-secretase generating a large soluble sequence (sAPPα) and the C-terminal fragment (CTF) α (CTFα). Further processing of the CTFα sequence and cleavage by γ-secretase generates the p3 fragment and the amyloid precursor protein intracellular domain (AICD); neither of which are involved in amyloid plaque formation. However, in the amyloidogenic pathway (right-hand side), initial cleavage of APP by β-secretase results in the sAPPβ and CTFβ fragments, while further cleavage of CTFβ by γ-secretase provokes the production of AICD and Aβ which is implicated in the senile plaque formation. Imbalanced cleavage of APP through the amyloidogenic pathway, and inadequate Aβ degradation and clearance result in the formation of amyloid plaques (adapted from La Ferla et al., 2007).

Under physiological conditions, the Aβ peptide produced through the amyloidogenic pathway is cleared from the brain through degradarion by several peptidases including the insulin-degrading enzyme (IDE), neprilysin, and the endothelin-converting enzyme 1 (ECE1) (Carson and Turner, 2002). Additionally, the low-density lipoprotein (LDL) and the receptor for advanced glycation endproducts (RAGE)

mediate the balanced efflux and influx, respectively, of Aβ across the BBB in order to remove the excess peptide from the brain (Tanzi et al., 2004). Therefore, AD can also be described as an imbalanced between Aβ productin and clearance.

1.3.2. Amyloid cascade hypothesis

Aβ is produced from APP processing as a monomer, yet it can rapidly aggregate and assemble into multimeric protein complexes with various molecular weights, ranging from dimers or trimers to higher order assemblies including protofibrils and mature fibrils (Figure 1.5.). Two forms of Aβ peptide are mainly produced, Aβ40 (amino acid residues 1 – 40) and Aβ42 (amino acid residues 1 – 42). Cumulative evidence suggests that Aβ42 is more inclined to aggregation as it undergoes more accelerated formation of Aβ oligomers, larger intermediate assemblies such as the protofibrils, and more insoluble mature amyloid fibrils (Jarrett et al., 1993; Iwatsubo et al., 1994).

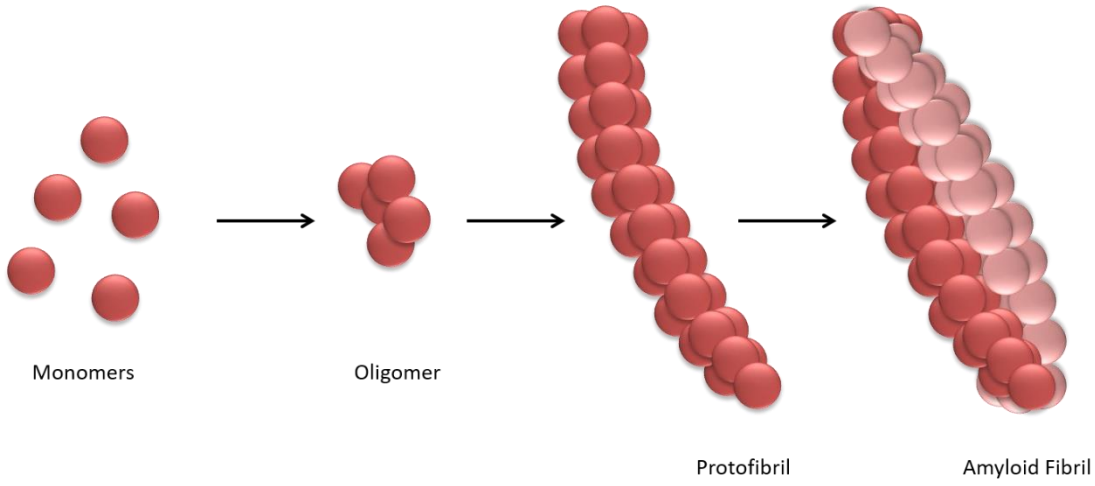

Figure 1.5. Aβ assembly and aggregation.

Aβ exists in multiple states. Monomeric molecules can aggregate into oligomeric and protofibrilar complexes, that further form the mature amyloid fibrils present at the core of the senile plaques. The early soluble oligomeric forms of Aβ are considered as potent neurotoxic agents that result in the pathogenicity of AD (adapted from LaFerla et al., 2007).

The "amyloid cascade hypothesis" initially proposed that imbalanced production and/or clearance of Aβ insoluble mature fibrils are central to AD pathology. According to the hypothesis, Aβ mature fibrils are responsible for the initiation of a

cascade of events in AD brain leading to a number of downstream consequences including neuronal cell death, NFT formation, and its aggregation and accumulation in senile plaques (Hardy and Allsop, 1991). Even though this hypothesis offers a broad description of AD pathogenesis, it was thought that it is lacking in detail and was more recently revised (Hardy and Selkoe, 2002).

1.3.2.1. The "Oligomer hypothesis"

Hardy and Selkoe (Hardy and Selkoe, 2002) reviewed the amyloid cascade hypothesis and shifted the emphasis away from the mature amyloid fibrils. They presented evidence that smaller and more soluble aggregates that embody a diversity of molecules, referred to as oligomers, ADDLs (amyloid β-derived diffusible ligands) or protofibrils, are the neurotoxic species of Aβ. The "oligomer hypothesis" (Figure 1.6.) thus suggests that intermediate Aβ oligomers are more potent brain toxins than the larger mature fibrils (Klein et al., 2001; Hardy and Selkoe, 2002; Varvel et al., 2008), resulting in synaptic dysfunction in AD brains, potent memory and learning deficits (Chromy et al., 2003; Bitan et al., 2003), and play a critical role in the progression of cognitive impairment in AD (Tomic et al., 2009) and its pathogenicity (Kayed et al., 2003; Kayed et al., 2004).

1.3.2.2. Oligomers and Reactive Oxygen Species generation

Further evidence that the early oligomeric structures are the neurotoxic components in AD has included the fact that these molecules are able to generate reactive oxygen species (ROS). Elevated levels of redox-active transition metal ions, lipid peroxidation, DNA and protein oxidation and the introduction of carboxyl groups into proteins have been reported in a wide range of neurodegenerative diseases (Allsop et al., 2008; Riederer et al., 2013), including AD. With reference to AD, the oxidative brain damage has been reported to be predominantly an early event in the time course of the disease (Nunomura et al., 2001; Markesbery et al., 2005), and ROS have been reported to be generated at the initial stages of Aβ aggregation (Tabner et al., 2005). Particularly, biometal ions have been found at enriched levels in the amyloid cores of the senile plaques in AD patients (Lovell et al., 1998; Huang et al., 2004; Smith et al., 1997). The soluble non-fibrillar oligomers have also been reported to

generate hydrogen peroxide (H_2O_2) from molecular oxygen through electron transfer interactions that involve strongly bound redox-active metal ions such as copper, iron and zinc (Huang et al., 1999; Huang et al., 1999; Curtain et al., 2001; Opazo et al., 2003).

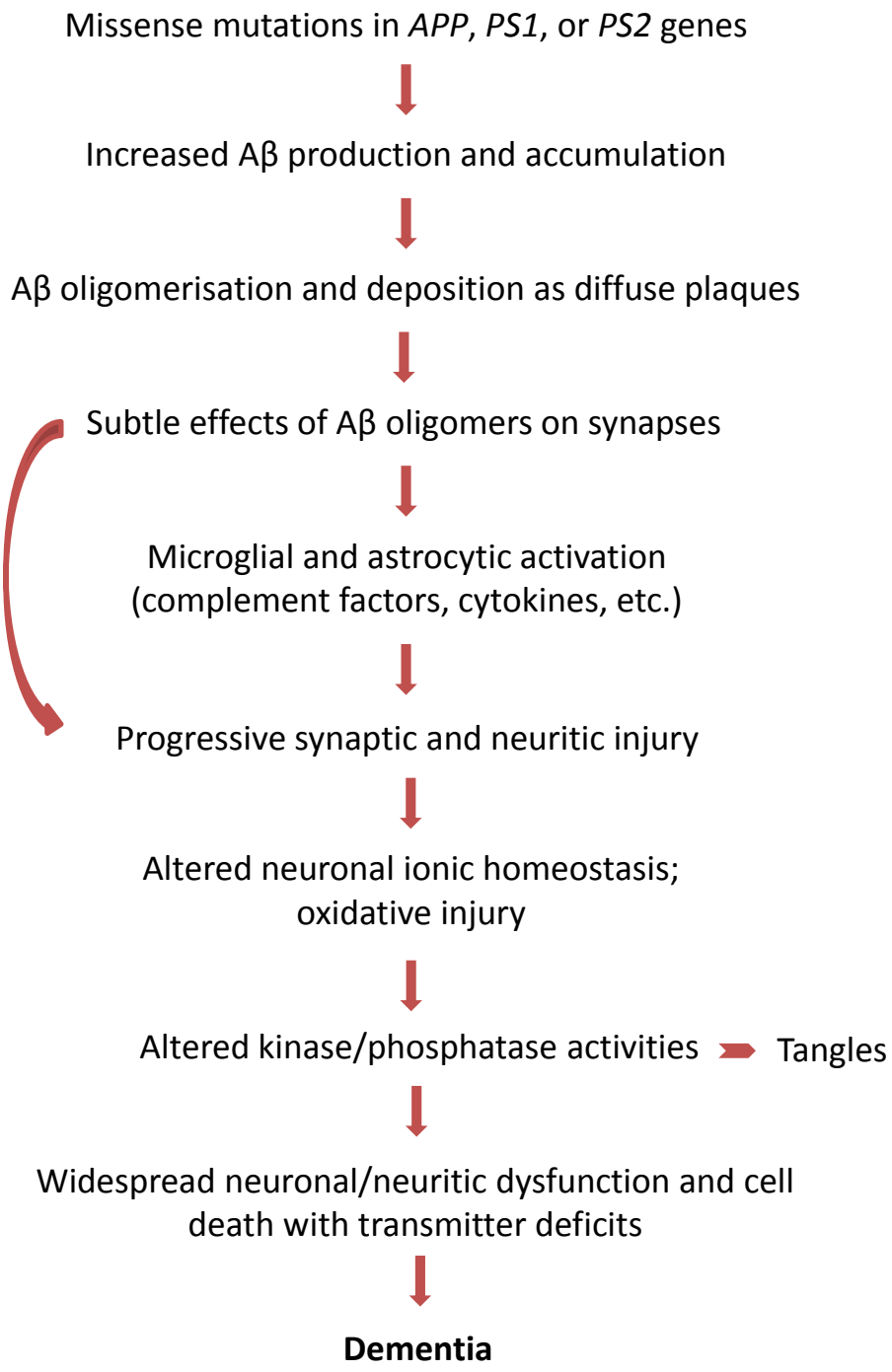

Figure 1.6. Oligomer cascade hypothesis.

Proposed sequence of the pathognomic events leading to Alzheimer's disease through the "oligomer hypothesis" cascade. The curved arrow indicates that the soluble oligomers of Aβ may not only activate the microglia and astrocytes, but also directly damage the synapses and neurites of neuronal cells (adapted from Hardy and Selkoe, 2002).

1.4. Sporadic and familial Alzheimer's disease

As the disease is strongly correlated with age, it is primarily characterised by two types; late-onset AD, which is the most common form of the disease and is defined by age at disease onset later than 65 years, and early-onset AD, which accounts for about 1 – 6% of all cases and the age at onset ranges from 30 to 65 years. From a genetic point of view though, the disease is mainly differentiated into familial cases that follow Mendelian inheritance and are predominantly linked with the early-onset disease, and sporadic cases which mainly appear as late-onset AD (Bekris et al., 2010), yet these two forms of the disease are clinically indistinguishable.

1.4.1. Familial Alzheimer's

The familial form of AD is a rare autosomal dominant disorder and is usually due to mutations in one of three principal genes; *APP* on chromosome 21, presenilin 1 (*PS1*) on chromosome 14 and presenilin 2 (*PS2*) on chromosome 1 (Bertram et al., 2010).

1.4.1.1. APP mutations

Currently, 25 pathogenic *APP* mutations have been associated with the familial form of the disease, yet they only account for less than 1% of AD cases (Lambert and Amouyel, 2007). These mutations either affect residues within the Aβ amino acid sequence that are important for its self-association and aggregation, or cluster around the β- and γ-secretase cleavage sites, where in both cases they result in increased levels of Aβ release, or promote its aggregation. More specifically, disease-causing mutations clustered around the β-cleavage site generate a better substrate for the production of Aβ40 (Mullan et al., 1992), while mutations around the γ-cleavage site, favour the production of the more toxic Aβ42 (Ghiso and Frangione, 2002).

Importantly, a coding mutation (A673T) in the *APP* gene was found to protect against the disease and the cognitive decline in non-AD elderly individuals. This mutation is a result of an amino acid substitution next to the site where β-secretase cleaves the APP protein. Data obtained by Jonsson and colleagues demonstrate that the resulted

mutation decreases the *in vitro* formation of Aβ by 40%, suggesting that inhibition of β-secretase APP cleavage site may protect against AD (Jonsson et al., 2012).

1.4.1.2. Presenilin mutations

Mutations in the highly homologous genes *PS1* and *PS2* account for the majority of familial AD cases (Rogaev et al., 1995; Sherrington et al., 1995; Sorbi et al., 1995). The proteins encoded by these genes determine γ-secretase action as they compromise the active site of the enzyme (Gandy, 2005). Subsequently, mutations on *PS1* and *PS2* genes can alter APP proteolysis and processing, increasing the levels of Aβ peptide generated and altering the ratio of Aβ42 to Aβ40 (Blennow et al., 2006; Schellenberg and Montine, 2012).

1.4.2. Sporadic Alzheimer's

On the other hand, the majority of all AD cases, about 95%, are considered to be sporadic and are strongly associated (about 35% of sporadic cases) with the apolipoprotein E (*APOE*) ε4 allele (Corder et al., 1993; Poirier et al., 1993) which accounts for much of the genetic risk and pathology in this form of the disease (Raber et al., 2004). Interestingly though, over 60% of all sporadic cases are not associated with the *APOE* ε4 allele, suggesting that other genetic and environmental factors can contribute to the determination of the disease. It has been identified that a rare variant of the *TREM2* gene is associated with late-onset sporadic AD (Guerreiro et al., 2013; Jonsson et al., 2013) and increases susceptibility to the disease with an odds ratio similar to that of the *APOE* ε4 allele (Jones, 2012; Niemitz, 2012; Neumann and Daly, 2013; Guerreiro et al., 2013; Jonsson et al., 2013).

1.4.2.1. Apolipoprotein E ε4 allele mutation

APOE is the major apolipoprotein expressed in the brain and exists in a polymorphic form; it is a constituent of lipoproteins which are involved in cholesterol homeostasis. In connection with AD, the *APOE* ε4 allele, located on chromosome 19, increases the risk of the disease by 3-fold in the heterozygote form and by 15-fold in homozygotes (Farrer et al., 1997), and also modifies the age of onset (Meyer et al., 1998) with each allele copy lowering the age of onset by approximately 10 years

(Corder et al., 1993). Even though the role of APOE in the predisposition of the disease is entrenched; the mechanism by which the protein is involved in the pathogenesis of AD is still unclear (Verghese et al., 2011). One possible mechanism suggested by Martins and colleagues (2006) proposes that the differences in the amino acid sequences of the three APOE isoforms (ε2, ε3 and ε4) induce a protein structure with altered functional properties resulting in abnormal cholesterol metabolism and defective redistribution of lipids, which would affect neuronal plasticity (Martins et al., 2006). Another potential mechanism of action described by Castano and colleagues (1995) suggests that based on the evidenced presence of APOE in both senile plaques and NFTs, APOE is associated with the conversion of monomeric Aβ to oligomeric and fibrillar forms that are deposited into plaques (Castano et al., 1995; Holtzman et al., 2000). In fact, the ε4 allele of the *APOE* gene plays a crucial role in AD as it is less effective in breaking down Aβ, thus increasing the risk of amyloid plaque formation and density (Corder et al., 1993) compared to the ε2 allele which has been linked with decreased risk for AD (Verghese et al., 2011).

1.4.2.2. TREM2 mutation

Encoding the triggering receptor expressed on myeloid cells (TREM) 2 protein, the *TREM2* gene is expressed throughout the CNS and particularly in white matter, as well as the hippocampus and neocortex, while the encoded protein is present on macrophages, dendritic cells, osteoclasts and microglia (Colonna, 2003; Bouchon et al., 2000). The TREM2 protein has two normal functions; it is involved in the regulation of phagocytic pathways responsible for the removal of neuronal debris and also suppresses various inflammatory responses through the repression of microglia-mediated cytokine production and secretion (Takahashi et al., 2007; Frank et al., 2008; Piccio et al., 2007). It has been demonstrated that a rare missense mutation in *TREM2* significantly increases the risk of AD by 3-fold. Considering the normal anti-inflammatory role of TREM2 protein in the brain, it is suspected that the mutated variant interferes with brain's ability to prevent the build-up of amyloid plaques (Guerreiro et al., 2013, Jonsson et al., 2013).

1.5. Risk factors

As a heterogeneous disorder, AD is associated with various risk factors that increase the frequency of its occurrence. Aside from ageing which is the most apparent risk factor, the disease is also linked with previous family history, even though only about 5% of cases have clear genetic linkage. As mentioned previously, the *APOE* ε4 and *TREM2* genotypes have been described as major risk factors for the development of sporadic AD.

1.5.1. Low brain reserve capacity

An alternative risk factor for the disease is the decreased reserve capacity of the brain which is determined by the number of neurons and their synaptic communications (Mayeux, 2003) and is described as the brain's resilience to pathological damage and changes. A low reserve capacity of the brain correlates with reduced brain size, low educational achievement, and low mental and physical activity later in life, along with other lifestyle-related strategies (Mayeux, 2003; Mortimer et al., 2003). Evidence provided by Jellinger in 2004, shows that head injuries can result in reduced brain reserve capacity, and thus are considered as a hazardous factor for the occurrence of AD (Jellinger, 2004). Additionally, epidemiological studies by Roberts and colleagues have also shown that multiple and repeated head trauma can lead to plaque and tangle formation (Roberts et al., 1990).

1.5.2. Type 2 Diabetes Mellitus

It has also been reported that impairments in insulin signalling and Type 2 Diabetes Mellitus (T2DM) are important risk factors associated with early-onset sporadic AD (Strachan, 2005; Haan, 2006; Luchsinger et al., 2004; Ristow, 2004; Biessels et al., 2006). Evidence suggests that hyperinsulinemia and insulin resistance, the hallmarks of T2DM, can lead to memory impairment (Ott et al., 1999; Kroner, 2009; Jiang et al., 2008), thus T2DM patients are predisposed to AD (Akter et al., 2011).

Other risk factors associated with AD include vascular diseases such as hypercholesterolaemia, hypertension, atherosclerosis, coronary heart disease and obesity (Mayeux, 2003).

1.6. Diagnosis of Alzheimer's disease

One of the main problems associated with AD is the limited availability of diagnostic methods and tools. The clinical diagnostic accuracy of the disease is around 80 – 90%. Diagnosis is performed based on the known clinical history of the individuals along with clinical, neurological and psychiatric examinations in order to exclude any other possible causes of dementia such as alcohol problems, head trauma or cerebrovascular dementia. Additionally, confirmation of genuine cognitive impairment is available through memory tests and rating scales such as the MMSE score.

Brain imaging (neuroimaging), computed tomography (CT) and magnetic resonance imaging (MRI) scans are sometimes used in the diagnosis of AD and can help with the exclusion of other causes of dementia such as brain tumours and strokes. The scans can also indicate neurodegeneration in the form of cerebral atrophy. It has also been identified that Pittsburgh Compound-B (PiB) can be used for imaging senile plaques in AD brains (Klunk et al., 2004). PiB is a radioactive analog of ThT which, when used in Positron Emission Tomography (PET) scans, can image amyloid plaques in the brain. Thus, PiB can potentially aid diagnosis of AD or be useful in clinical trials.

Still, a definitive diagnosis can only be made by examination of the brain post-mortem for the presence of senile plaques and NFTs (Blennow et al., 2006).

1.7. Therapy and treatment of Alzheimer's disease

AD is becoming gradually more common as the global population ages, yet development of drugs that prevent, delay the onset, slow the progression, or improve the symptoms of the disease has proven to be difficult. A study conducted by Cummings and colleagues examining data from a public website that records ongoing clinical trials, during the period between 2002 and 2012, identified 244 compounds in 413 AD clinical trials, of which; 151 (36.6%) were cognitive enhancers targeting the symptoms of the disease, 145 (35.1%) were small molecules with

disease-modifying potential, and 76 trials (18%) with immunotherapies; and an overall success rate of 0.4% (Cummings et al., 2014). Currently, four drugs are approved for AD treatment, which temporarily alleviate the symptoms of the disease and do not have a major impact on its progression, delineating the disease as an unmet medical and clinical need.

1.7.1. Acetylcholinesterase inhibitors

One approach implemented in symptomatic and palliative treatments for AD involves the acetylcholinesterase inhibitors which restore cholinergic activity through the inhibition of acetylcholinesterase. AD is associated with the loss of cholinergic neurons in the brain affecting the levels of the acetylcholine neurotransmitter (Lane et al., 2006). According to the cholinergic hypothesis in AD, degeneration of the cholinergic neurons, which are present in the basal forebrain nuclei, results in the disruption of the presynaptic cholinergic terminals, located in the hippocampus and neocortex, affecting the memory and consequently contributing to the cognitive decline present in AD (Terry and Buccafusco, 2003). Currently available acetylcholinesterase inhibitors approved for clinical use in AD, Donepezil, Rivastigmine and Galantamine, act by restoring both the levels and duration of action of acetylcholine, thus improving synaptic communication between nerve cells, and showing modest benefits in cognition and behaviour (Colovic et al., 2013). The acetylcholinesterase inhibitors are used to treat mild to moderate AD, however, these drugs show various adverse effects mainly with gastrointestinal symptoms, such as nausea, vomiting, diarrhoea, abdominal pain and dizziness (Inglis, 2002).

1.7.2. NMDA receptor antagonist

Another medication used for AD patients is Memantine, a NMDA (N-methyl-D-aspartate) receptor antagonist, which has demonstrated a modest effect on moderate-to-severe AD (Reisberg et al., 2003). More specifically, Memantine is administered to patients with moderate AD who have a contraindication to or are intolerant of acetylcholinesterase inhibitors, or those with severe AD. Memantine demonstrates a moderate decrease in clinical deterioration with minor effects on cognition, behaviour and mood of AD patients (Areosa et al., 2006). Despite years of

research on this drug, there is only slight evidence of any effect on mild AD (Schneider et al., 2011).

1.7.3. β- and γ-secretase inhibitors and modulators

Increasing knowledge regarding the molecular pathogenesis of AD has led to the development of drugs that interfere with the secretase activity in APP processing. These drug candidates can either inhibit Aβ production and consequently the aggregation of the peptide in the brain or increase Aβ clearance from the brain. The secretase modulators would either target the inhibition of β-secretase or γ-secretase; or stimulate the production of α-secretase. However, development of these inhibitors was proven difficult, especially for β-secretase or γ-secretase, as these secretases are involved in the clearance of multiple cell surface proteins – in addition to APP – thus resulting in various adverse side effects (Gandy, 2005).

More precisely, initial therapeutic approaches that targeted the inhibition of total Aβ peptide production by directly inhibiting the action of γ-secretase equivalently blocked the formation of all major Aβ variants (Anderson et al., 2005) – not only Aβ42 – and also the formation of the APP intracellular domain and Notch-1 receptor that plays a key role in the differentiation of multiple cell types (De Strooper et al., 1999). Semagacestat, a γ-secretase inhibitor that was tested in two Phase 3 clinical trials failed to show any effect on disease progression, compromised even more the performance of the patients on their daily activities as it induced further cognitive impairment (WWW, Lilly), and was also linked with an increased risk of skin cancer (Wagner et al., 2012). Further studies on drug candidates, called nonsteroidal anti-inflammatory drug (NSAID)-like compounds that modulate the levels of the enzyme activity instead of inhibiting its action, showed no potency and poor brain penetration (Weggen et al., 2001; Green et al, 2009). Regardless of the minimal properties of γ-secretase modulators, *R*-flurbiprofen (Tarenflurbil) was tested in three large phase clinical trials demonstrating no effect (Green et al., 2009).

On the other hand, inhibitors of β-secretase (BACE1) have been proven difficult to develop due to the large binding site of the enzyme. Additionally, because of the

numerous substrates that are cleaved by BACE1, inhibition of the enzyme may result in various side effects including impaired motor coordination (Cheret et al., 2013) and retinal pathology (Cai et al., 2012).

1.7.4. Immunotherapy and vaccine development

Studies associated with AD treatment using active and passive immunisation resulted in the development of various potential vaccine candidates for the disease. The idea of active Aβ immunisation was first proposed by Solomon and colleagues (Solomon et al., 1996; Solomon et al., 1997) suggesting that anti-Aβ antibodies can be used to prevent the mature fibril formation while also disaggregating any pre-existing fibrils. Schenk and colleagues then demonstrated that active immunisation against the full length of the peptide resulted in reduced load of amyloid plaques *in vivo* using AD transgenic mice (Schenk et al., 1999). Consequent studies proved that active Aβ immunisation promotes the generation of anti-Aβ antibodies able to bind on the amyloid plaques and reduce the cerebral Aβ load improving also cognition. The first active vaccine that was tested in clinical trials, AN1792, demonstrated reduction of Aβ deposition following autopsy of the responders' brains after several years, however, the drug itself failed to pass the trials as it resulted in the development of meningoencephalitis (Gilman et al., 2005).

The first approach of using passive immunisation was performed by Bard and colleagues (Bard et al., 2000) using an Aβ monoclonal antibody, 3D6 mAb, specific for the Aβ N-terminus. Systemic injection of the antibody in AD transgenic mice resulted in binding of the antibody onto amyloid plaques and induction of a Fc-receptor-mediated microglial phagocytosis of Aβ deposits following distribution and uptake of the antibody into the brain (Bard et al., 2000). The same antibody was then used to develop a humanised mAb, Bapineuzumab, that was tested in Phase 1, 2 and 3 clinical trials showing reduced Aβ load in PET scanning yet no other significant clinical benefits leading to the termination of the trials (Rinne et al., 2010). Further studies on Bapineuzumab demonstrated association with transient vasogenic oedema and microhaemorrhage with higher risk in AD patients with one or two *APOE* ε4 alleles (Sperling et al., 2012).

Another antibody reported for passive immunisation, m266, demonstrated low brain Aβ burden and increased levels of the protein in plasma suggesting that the antibody promotes Aβ clearance from the brain to blood (DeMattos et al., 2001). This antibody was used as a precursor for Solanezumab, an antibody tested in Phase 3 clinical trials showing no association with vasogenic oedema or microhaemorrhages but indeed increasing plasma Aβ (Farlow et al., 2012). However, in January 2017, Lilly terminated the study on Solanezumab failing to show positive results (WWW, ClinicalTrials.gov).

Currently on-going clinical trials on Gantenerumab and Crenezumab, show promising results (WWW, ClinicalTrials.gov). Gantenerumab, a fully humanised monoclonal antibody used in clinical studies (Bohrmann et al., 2012), binds to the fibrillar forms of Aβ and demonstrated 30% decrease of brain Aβ load in an antibody-dependent manner, using PET scanning (Ostrowitzki et al., 2012). Crenezumab demonstrated low possibility of causing inflammatory immune responses and reduced risk for brain microhaemorrhage and vasogenic oedema (Adolfsson et al., 2012; Garber, 2012).

However, one major confine of all clinical trial results is the placebo effect in which the placebo recipient demonstrates condition-related improvements due to psychological expectations rather than the treatment itself. This response, along with the long duration of clinical trials which promotes the deterioration of the conditions, result in the failure of many clinical studies (Ito et al., 2013).

1.8. The approach to an effective amyloid aggregation inhibitor

Many aggregation inhibitors have failed to progress in clinical studies. Tramiprosate (Alzhemed), an aggregation inhibitor that interferes with the binding of proteoglycans to Aβ, has failed in clinical trials as it did not demonstrate any beneficial effects (Anand, 2014). However, inhibition of the Aβ oligomerisation process is an attractive therapeutic approach for AD, as the early soluble oligomers are believed to be the neurotoxic agents that drive neurodegeneration and neuronal cell death. One of the strategies employed in order to develop novel drug candidates

was the use of peptide-based inhibitors that target the oligomeric state of Aβ aggregation process rather than the late fibrillar forms (Sciarretta et al., 2006).

1.8.1. The KLVFF region of Aβ

The central region of the Aβ peptide composed of amino acids 16 – 20, KLVFF, is crucial for the self-association and aggregation of the protein (Hilbich et al., 1992; Tjernberg et al., 1996). As a result, this pentapeptide sequence has been used as the lead compound to develop inhibitory agents of the Aβ aggregation process (Lowe et al., 2001; Zhang et al., 2003). Modified synthetic peptides based on this central sequence have been reported to prevent the conversion of monomeric Aβ to β-sheet-rich aggregated assemblies by binding to the homologous sequence in Aβ (Soto et al., 1996; Findeis et al., 1999; Ghanta et al., 1996; Gordon et al., 2001; Kokkoni et al., 2006; Watanabe et al., 2002). However, the design of these inhibitors was formulated on the inhibition of the late fibrillar mature aggregates rather than the early oligomeric assemblies and therefore they were only able to partially reverse the toxicity of Aβ.

1.8.2. OR1 and OR2 peptides

Austen and colleagues (Austen et al., 2008) designed peptide inhibitors of the oligomerisation assembly based on the corresponding KLVFF region of the Aβ peptide. Two synthetic inhibitors (Figure 1.7.) were initially developed, named OR1 (RGKLVFFGR) and OR2 (RGKLVFFGR-NH_2). Both modified peptides contained arginine (R) and glycine (G) amino acid residues (RG-/-GR) as a solubilising component (El-Agnaf et al., 2004) added to the N- and C- terminal ends of the peptides. The cationic arginine was added to the peptide through the glycine spacer to aid the solubility of the inhibitor and also to prevent it from self-aggregating. The glycine residues between the arginine molecule and the pentapeptide were added to facilitate the interaction between the inhibitor peptides and native Aβ. The two peptides were only differentiated by the replacement of the carboxyl terminus of the OR1 with an amide group at the C-terminus of the OR2 inhibitor to render it less charged. As the peptide sequence arose from an internal part of Aβ, it was thought best to introduce the amide group at the end of the OR2 inhibitor to design a peptide that would be

more likely to be recognised as if it was a part of the whole protein from which the sequence was chosen (Austen et al., 2008).

Data were obtained from ThT assay analysis and Transmission Electron Microscopy (TEM), showing that both OR1 and OR2 inhibitors were able to block the formation of Aβ mature aggregates. However, results from the enzyme-linked immunosorbent assay (ELISA) demonstrated that the OR2 inhibitor had a better inhibitory effect on Aβ soluble immature oligomer formation than the OR1 peptide. OR1 only had a slight blocking effect on oligomer formation at high concentrations signifying that it may act at a later point in the aggregation pathway than OR2 (Austen et al., 2008). As a control for their studies, the group also synthesised a modified KLVFF peptide alone containing an amide group at the C-terminus (KLVFF-NH_2) which showed no effect on the aggregation, possibly due to the absence of the flanking residues (RG- and -GR) in the amino acid sequence and thus affecting the peptide's tendency to self-aggregate (Austen et al., 2008). According to these results, blocking the C-terminus with an amide group was beneficial since OR2 is overall a more effective inhibitor of Aβ oligomer formation than OR1 (Austen et al., 2008).

Further investigation in cytotoxicity studies revealed that only the OR2 inhibitor was able to protect cultured human neuroblastoma (SH-SY5Y) cells from Aβ toxicity (Austen et al., 2008). Consistent with previous research (Lambert et al., 1998; Kim et al., 2003; Kayed et al., 2003; Clearly et al., 2005; El-Agnaf et al., 2000; El-Agnaf et al., 2001; El-Agnaf et al., 2003; El-Agnaf et al., 2006, ; Bucciantini et al., 2006; De Felice et al., 2004) the reported results provided clear evidence that the early non-fibrillar oligomers are the toxic species as the neuroprotective effects demonstrated by OR2 were due to the inhibition of the oligomeric assemblies rather than the late mature aggregates (Austen et al., 2008).

1.8.3. The retro-inverso OR2 peptide

Even though the OR2 peptide inhibitor was proven to be an effective inhibitor against the formation of early soluble oligomers, it was unlikely itself to be a viable drug candidate as it contains many sites for proteolytic attack in its peptide sequence

(Taylor et al., 2010). In order to overcome this flaw, yet retain the anti-aggregational properties of the inhibitor, Taylor and colleagues designed a retro-inverso version of the OR2 inhibitor (Figure 1.7.), named RI-OR2 (Ac-rGffvlkGr-NH_2) to transform it into a peptidomimetic (Taylor et al., 2010). Previous studies have demonstrated that retro-inverso peptides are able to maintain a topology, potency and selectivity similar to those of their "parent" molecule, and also have an improved bioavailability profile due to their enhanced stability to proteolysis (Chorev and Goodman, 1993; Chorev and Goodman, 1995). Additional studies suggest that retro-inverso peptide exhibit good blood-brain barrier (BBB) permeability (Taylor et al., 2000) and membrane translocation properties (Nickla et al., 2010).

The approach to develop a proteolytically stable retro-inverso peptide was achieved by replacing the natural L-amino acids with D-enantiomers (Poduslo et al., 1999; Findeis et al., 1999), and also by reversing the peptide bonds (Chorev and Goodman, 1993; Chorev and Goodman, 1995). Taylor and colleagues also retained the positioning of the two solubilising flanking residues, rG- and -Gr, and replaced the C-terminal amide group of OR2 with an N-terminal acetyl group in RI-OR2. This N-terminal acetyl group, CH_3CONH, has close chemical properties with $CONH_2$, as both are uncharged and unreactive, thus mimicking the original C-terminus of the OR2 inhibitor. As a result, the three-dimensional shape of the new inhibitor was maintained similar to the native molecule enabling the effective interaction between the retro inverted "ffvlk" in RI-OR2 peptide and the KLVFF sequence in Aβ (Taylor et al., 2010).

Stability experiments using individual proteolytic enzymes, and also exposure to human brain extract and blood plasma, confirmed that the RI-OR2 peptide is more stable to proteolysis than the OR2 inhibitor (Taylor et al., 2010). Additional studies on the RI-OR2 inhibitor demonstrated that the peptide is able to block the formation of Aβ oligomers and fibrils as verified by ThT assays, sodium dodecyl sulfate (SDS) polyacrylamide gel electrophoresis (PAGE) [SDS-PAGE] separation of stable oligomers, and atomic force microscopy (AFM). RI-OR2 was also assessed for cell toxicity in cultured SH-SY5Y cells using the MTT and lactate dehydrogenase (LDH)

assays, confirming its neuroprotective action against the toxic effects of pre-aggregated Aβ (Taylor et al., 2010). According to the data obtained by Taylor and colleagues (Taylor et al., 2010), the RI-OR2 inhibitor represented a suitable drug-like molecule for future development and testing in bioavailability studies and BBB penetration experiments.

1.8.4. The RI-OR2-TAT peptide inhibitor

Further development of the inhibitor was performed by the attachment of a retro-inverted version of the HIV protein transduction domain 'TAT' (Green and Loewenstein, 1988) to the RI-OR2 peptide to develop a cell-permeable and brain penetrant inhibitor, named RI-OR2-TAT (Ac-rGffvlkGrrrrqrrkkrGy-NH_2) (Figure 1.7.) (Parthsarathy et al., 2013). The incorporated sequence was attached on the RI-OR2 inhibitor in such a way as to maintain the protease resistance of the whole molecule, yet also to increase its bioavailability *in vivo*. Initial studies on the RI-OR2-TAT peptide determined that the inhibitor is able to interrupt the aggregation pathway at a very early point (Parthsarathy et al., 2013) by employing ThT assays, SDS-PAGE experiments and AFM (Taylor et al., 2010). However, RI-OR2-TAT showed inhibition of Aβ aggregation when present at a relatively high concentration of about 1:5 molar ratio of inhibitor to Aβ.

Moreover, a fluorescent version of RI-OR2-TAT, named Flu-RI-OR2-TAT, was tested for penetration in cultured neuroblastoma cells and demonstrated rapid entry – within minutes – into the cells. In contrast, Flu-RI-OR2 stayed mainly in the culture medium, indicating that the inverted TAT sequence attached on the RI-OR2 inhibitor is an effective transit peptide (Parthsarathy et al., 2013). Similar to previous studies that employ TAT as a targeting method into the brain (Dietz and Bahr, 2004; Repici et al., 2007; Ramanathan et al., 2001), Flu-RI-OR2-TAT was also able to penetrate across the BBB following its peripheral (i.p.) administration in APP/PS1 (APPswe/PS1ΔE9) transgenic mice. More specifically, the peptide demonstrated attachment to amyloid plaques – with high affinity – and to activated microglial cells. It also reduced β-amyloid oligomer formation, amyloid plaque load, oxidation and inflammation in the brain, and stimulated neurogenesis in the dentate gyrus (DG) of the hippocampus

when administrated at 100 nmol / kg / once per day over a period of 21 days (Parthsarathy et al., 2013).

To further develop the RI-OR2-TAT peptide inhibitor, Parthsarathy and colleagues (Parthsarathy et al., 2013) suggested that the effect of the RI-OR2-TAT inhibitor on the level of Aβ oligomerisation might be improved by the optimisation of the peptide sequence and/or by the use of an alternative dosing regimen.

OR1	**H_2N– R→ G→ K→ L→ V→ F→ F→ G→ R– COOH**
OR2	**H_2N– R→ G→ K→ L→ V→ F→ F→ G→ R– NH_2**
RI-OR2	**H_2N– r← G← k← l← v← f← f← G← r– Ac**
RI-OR2-TAT	**H_2N– y← G← r← k← k← r← r← q← r← r← r← r← G← k← l← v← f← f← G← r– Ac**

Figure 1.7. The structures of OR1, OR2, RI-OR2 and RI-OR2-TAT peptide inhibitors.

Demonstration of the amino acid sequences of the four peptide inhibitors. Uppercase letters represent L-amino acids while D-amino acids are in lowercase. There is no separate enantiomer of glycine (G) amino acid which is shown in uppercase. The direction of peptide bonds is indicated by the arrows (adapted from Taylor et al., 2010).

1.8.5. Peptide Inhibitor Nanoparticles

More recent studies have indicated a growing interest in the use of liposomes as carriers of therapeutic agents. The use of nanoliposome devices is an attractive strategy for drug delivery due to their remarkable characteristics such as their chemical and physical stability - they display good blood circulation times and are resistant to hydrolysis (Webb et al., 1995). They also show compatibility with living systems, and are biodegradable, since they are readily decomposed by biological agents (Torchilin, 2005). More importantly, liposomes can be multi-functionalised on their surface and are more efficient at recognising their molecular targets by decorating their surface with multi-ligand-nanosystems (Stukel et al., 2010).

Gregori, Taylor and colleagues (Gregori et al., 2017) have attached the RI-OR2-TAT peptide inhibitor onto the surface of synthetic nanoparticle scaffolds to form peptide inhibitor nanoparticles (PINPs) (Figure 1.8.). The liposomes were composed of a 1:1

ratio of sphingomyelin to cholesterol and the RI-OR2-TAT peptide was covalently attached to the surface of the liposome through a PEGylated lipid tail (Gregori et al., 2017). PINPs demonstrated high potency on the inhibition of Aβ aggregation at remarkably low concentrations with 50% inhibition at a molar ratio of about 1:2000 of liposome-bound peptide to Aβ, and they also rescued cultured human neuroblastoma cells from Aβ toxicity. Moreover, PINPS were efficient at crossing an *in vitro* BBB model, and also entered the brains of healthy mice with the C57/BL6 background, and protected against memory loss in the APPswe (Tg2576) transgenic mice model using the novel object recognition task (Gregori et al., 2017).

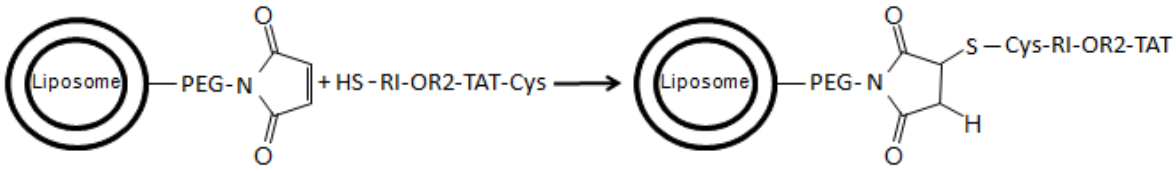

Figure 1.8. Preparation of PINPs.

PINPs are constructed through 'click' chemistry through a C-terminal cysteine residue added on the amino acid sequence of the RI-OR2-TAT peptide. The lipids are synthesised using equal molar ratio of sphingomyelin and cholesterol. The RI-OR2-TAT peptide is attached on the surface of the lipid nanoparticle through a lipid tail composed of DSPE, PEG (polyethylene glycol) and MAL (maleimide) (adapted from Gregori et al., 2017).

1.9. Scope of the thesis

A new version of the RI-OR2 peptide was developed by attaching *N*-acetylglucosamine (NAG), a stable analogue of glucose, to the RI-OR2 inhibitor, developing RI-OR2-NAG inhibitor. NAG, a monosaccharide derived from glucose, will be used as a transit molecule of the inhibitor by utilising the glucose transporters that are located at the BBB (GLUT1) and on the membranes of neurons (GLUT3) (Bell et al., 1990) and the NAG transporter (SLC35A3) expressed at the Golgi apparatus of the cells (Abeijon et al., 1996). The resulted peptide inhibitor, named RI-OR2-NAG will be tested for inhibition of Aβ aggregation using the ThT assay and for potential

toxic effects on cultured SH-SY5Y neuroblastoma cells using the MTS cell proliferation assay.

The overarching aim of this project is to compare the anti-aggregational properties and potency of the RI-OR2-NAG inhibitor relative to the previously developed RI-OR2-TAT inhibitor (Parthsarathy et al., 2013). The anti-aggregational properties of the two free peptides will be examined using the ThT assay, while the MTS assay will be employed to determine the effects of the peptides on the viability of cultured SH-SY5Y neuroblastoma cells. The two peptides will also be compared for their cell-penetrating properties using their fluorescent versions.

The hypothesis of this thesis project is that the RI-OR2-TAT, RI-OR2-NAG, and PINPs can penetrate a dynamic and intact BBB, and co-localise with major neuronal and glial cells following their peripheral administration in WT mice with the C57/BL6 background. This property of the peptides will be examined using confocal microscopy, visualising the cortex, hippocampus and DG of the mouse brains.

The three peptides will also be used in an attempt to study their bio-distribution and possible elimination routes in healthy mice. Luminex technology and ELISA systems are going to be applied in order to study the accumulation of the peptides in the brain, heart, lungs, stomach, liver, spleen, kidneys and small intestines of the mice following 1 h of peptide treatment, prior to tissue collection.

Chapter 2: Experimental Procedures

Unless otherwise stated, chemicals were purchased from Sigma-Aldrich/Sigma® Life Science (Dorset, UK) and antibodies were purchased from Abcam® (Cambridge, UK) and stored according to manufacturer's recommendations.

2.1. Preparation of peptides

2.1.1. Peptides and their fluorescent derivatives

The peptide inhibitors RI-OR2-TAT (Ac-rGffvlkGrrrrqrrkkrGy-NH_2), RI-OR2-TAT-Cys (Ac-rGffvlkrrrrqrrkkGyc-NH_2), RI-OR2-NAG (Ac-rGffvlkGrS(GlcNAc)-NH_2), and their fluorescent versions, Flu-RI-OR2-TAT (Flu-rGffvlkGrrrrqrrkkrGy-NH_2) and Flu-RI-OR2-NAG (5Flu-rGffvlkGrS(GlcNAc)-NH_2) used for the study were custom-made by Cambridge Peptides (Birmingham, UK). The purity of these peptides was determined as >95 % by HPLC – MS (high performance liquid chromatography – mass spectrometry).

2.1.2. Liposomes, peptide-liposomes (PINPs), and their fluorescent derivatives

2.1.2.1. Preparation of the lipid film

The PEGylated control liposomes (CL) and PINPs used in the study were custom-synthesized. The liposomes were composed of a matrix of sphingomyelin (egg, chicken)/cholesterol (plant derived) (Avanti® Polar Lipids, Inc., Alabama, USA), at a 1:1 molar ratio (47.5 molar % each) and mixed with 5 molar % of DSPE–PEG–MAL (1, 2-distearoyl-*sn*-glycero-3-phosphoethanolamine-N-poly(ethylene glycol)-maleimide (Laysan BIO, Inc., Alabama, USA). Following resuspension of the lipids in chloroform (VWR Chemicals, Leighton Buzzard, UK) to the required final volume, the chloroform solvent was first removed by evaporation under a gentle stream of nitrogen (N_2), followed by complete evaporation *in vacuo* using a round-bottomed flask attached to a rotary evaporator (SOGEVAC®, Leybold Vacuum, Valence, France) for about 1 h. The resulting lipid film was resuspended in PBS (phosphate buffered saline), pH 7.4, vortexed and sonicated until mixed completely. The lipid mixture was then subjected

to rapid changes of temperature by performing 5 cycles of freezing in liquid nitrogen for 15 sec and thawing at 42°C for 3 min, followed by sonication (U300H ultrasonic bath, Ultrawave, Cardiff, UK) for 5 min at 45°C. The lipid nanoparticle mixture was then extruded 10 times using a mini extruder (Figure 2.1.) (Avanti® Polar Lipids, Inc. from Stratech Scientific Ltd., Suffolk, UK) through a 100 nm nucleopore membrane (Whatman®, Little Chalfont, UK) and stored at 4°C for up to two weeks.

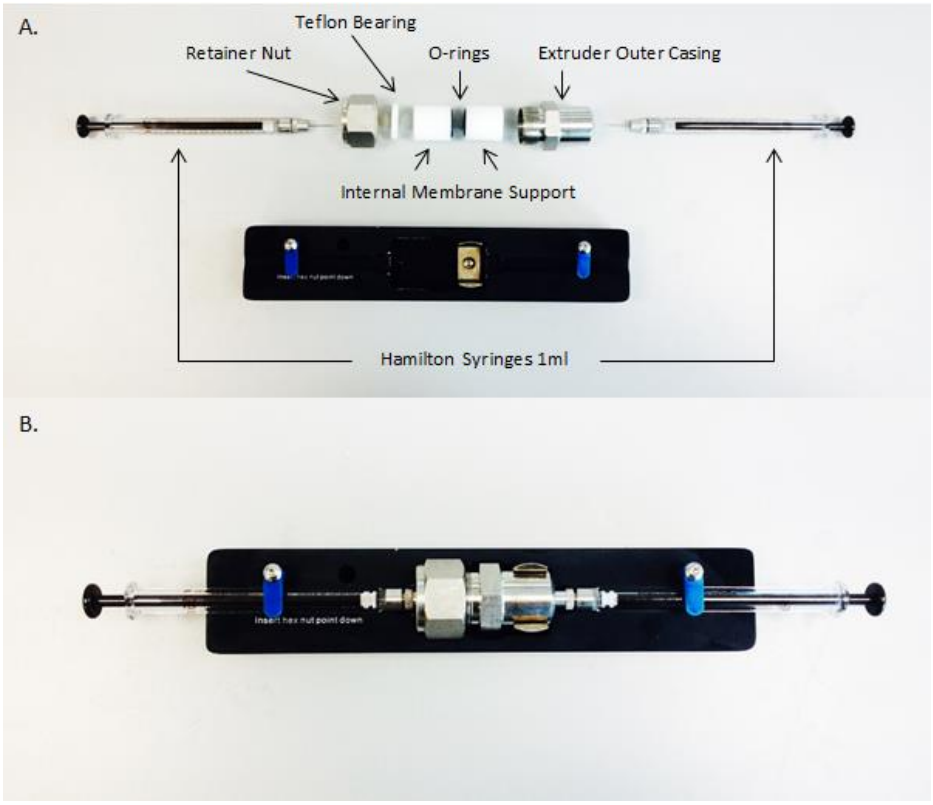

Figure 2.1.Mini extruder assembly.

For assembly of the mini extruder, two pre-wet filter supports were placed on the top of each of the internal membrane supports (with the O-rings facing up) and the 100 nm nucleopore membrane was secured in between them. The whole set up was inserted into the extruder outer casing and tightened with the retainer nut which already contains the teflon bearing. Once the sealed extruder outer casing was placed on the mini extruder base, the Hamilton syringes were attached.

The BODIPY-bound liposomes were designed using the same method, with the exception that BODIPY-cholesterol [23-(dipyrrometheneboron difluoride)-24-

norcholesterol] (Avanti® Polar Lipids, Inc., Alabama, USA) was added at 1 molar % of the total cholesterol present in the initial liposome mixture.

2.1.2.2. Attachment of RI-OR2-TAT onto the surface of the nanoliposomes

In order to covalently link the RI-OR2-TAT peptide to the liposomes by 'click chemistry', a cysteine residue was incorporated at the C-terminal end of the amino acid sequence of the peptide inhibitor, resulting in RI-OR2-TAT-Cys. The peptide was added at about 50 % molar ratio of the DSPE–PEG–MAL (in excess) in PBS, and incubated for 2 h at 37°C and then overnight (O/N) at RT (room temperature), on an end-over-end mixer (Stuart® equipment, Bibby Scientific Ltd., Stone, UK). Any unbound peptide was removed through centrifugation on an Optima™ L-100 XP Ultracentrifuge for 1 h at ~257 xg and 4°C [50k RPM (revolutions per minute) using the 70.1 Ti rotor] (Beckman Coulter, Inc., High Wycombe, UK). The supernatant was removed and the pellet of concentrated PINPs was resuspended in PBS, sonicated and vortexed until completely mixed. The final PINPs were stored at 4°C for up to two weeks.

The elution of the liposomes was assessed by dynamic light scattering (DLS), while the amount of peptide bound to the liposomes was quantified by BCA (bicinchoninic acid) assay (Smith et al., 1985). Determination of phospholipid recovery after extrusion and centrifugation was performed using the Wako LabAssay™ Phospholipid (Choline Oxidase–DAOS) method (Wako Pure Chemical Industries, Ltd. from Alpha Laboratories, Eastleigh, UK) (Takayama et al., 1977).

The concentrations of liposomes or peptide liposomes tested in this thesis refer to the total lipid content.

2.1.3. BCA assay for protein determination of peptide bound to liposomes

To determine the concentration of peptide bound to nanolipids, the BCA assay was performed using BSA (bovine serum albumin) as a standard. The working solution was prepared by mixing 50 parts of BCA solution with 1 part of copper (II) sulphate solution. The BSA standards - prepared in PBS - and the PINPs were added in

triplicate (5 µl/well) to a 96-well plate (ThermoFisher Scientific Nunc A/S from Life Technologies Ltd., Paisley, UK) along with 100 µl/well of working solution. The plate was left to stand for 30 min at 37°C, and then read at 562 nm (1.0 s) on a Wallac 1420 multilabel counter Victor^2 plate reader (PerkinElmer®, Massachusetts, USA).

2.1.4. Choline Oxidase – DAOS method for phospholipid determination

To determine the amount of phospholipid (sphingomyelin) present in PINPs following extrusion and centrifugation, the Wako LabAssay^{TM} Phospholipid Assay (Wako Pure Chemical Industries, Ltd. from Alpha Laboratories, Eastleigh, UK) was performed. The standards were prepared using the 'Standard Solution' provided in the kit. The 'Colour Reagent' was prepared by dissolving 1 vial of Chromogen substrate to 50 ml Buffer, both provided in the kit. To the plate, 2 µl/well of each standard and test peptide solution were added in triplicate, along with 300 µl/well of Colour Reagent. The plate was then incubated for 5 min in 37°C and then read at 562 nm (1.0 s) on a Wallac 1420 multilabel counter Victor^2 plate reader (PerkinElmer®, Massachusetts, USA).

2.2. Preliminary studies on RI-OR2-NAG peptide

2.2.1. Aβ deseeding

Recombinant Aβ42 was purchased from rPeptide (Stratech Scientific Ltd, Suffolk, UK). The freeze-dried peptide was dissolved at 1 mg/ml in 0.1 % (v/v) ammonium hydroxide (NH_4OH) and split into two aliquots in fresh glass vials. Following a 15 min incubation at RT, the solution was vortexed at high speed and sonicated at 12 microns peak to peak for four bursts of 30 sec. The solvent was then evaporated *in vacuo* by centrifugal concentration (Savant ISS110, SpeedVac Concentrator, ThermoFisher Scientific from Life Technologies Ltd., Paisley, UK) and the two aliquots were stored at -20°C for future use. Prior to use of the peptide in *in vitro* aggregation experiments, each Aβ42 aliquot was resuspended in 0.5 mg/ml trifluoroacetic acid (TFA) containing 5 % (v/v) thioanisole; vortexed at low speed and sonicated for 30 sec in glass vials with a chemically resistant Eppendorf lid (Eppendorf UK Ltd., Stevenage, UK). The solvent was then evaporated under a stream of oxygen-free

nitrogen ($N_{2)}$ gas and the resulting film was treated with 100 µl of 1,1,1,3,3,3-hexafluoro-2-propanol (HFIP), vortexed at high speed and sonicated for four bursts of 30 sec. The solvent was again evaporated *in vacuo* using the SpeedVac concentrator. Following the HFIP treatment, the peptide film was dissolved in 0.5 ml NH_4OH, vortexed at high speed and sonicated for four bursts of 30 sec and split into 100 µg aliquots which were dried in the centrifugal concentrator and stored at -20°C for future use.

2.2.2. ThT aggregation assay

2.2.2.1. Preparation of PB, PBS, and PB-2S solutions

To prepare and maintain the solutions at pH 7.4, the buffers were prepared in 0.81 % (v/v) of 1 M K_2HPO_4 (dipotassium phosphate monobasic acid) and 0.19 % (v/v) of 1 M KH_2PO_4 (monopotassium phosphate bibasic acid). To PBS and PB-2S (Phosphate buffered 2x saline) solutions, 0.15 M and 0.3 M NaCl (sodium chloride) were added respectively. The volume of the solutions was made to 100 ml with dH_2O.

2.2.2.2. Preparation of ThT dye

ThT powder was dissolved in PB (phosphate buffer) at a concentration of 15 mM and stored in 4°C in dark for a week. This stock solution was further diluted in PB-2S at a concentration of 60 µM for the purposes of the experiment.

2.2.2.3. Aβ and peptide treatment preparation

Aβ42 aliquots (100 µg each) were dissolved in 222 µl PB to yield a concentration of 100 µM. The peptide inhibitors RI-OR2-TAT and RI-OR2-NAG were prepared in PBS at 1:1, 1:2, 1:5 and 1:10 final molar ratios of peptide inhibitor to Aβ.

2.2.2.4. Preparation of ThT assay plate

The assays were conducted in 384-well black with clear-bottom microtiter plates (ThermoFisher Scientific Nunc A/S from Life Technologies Ltd., Paisley, UK). Controls (100 µM Aβ42, ThT and 50 µM of each peptide inhibitor) and sample conditions were added to the plates in triplicate to a final volume of 60 µl/well (Table 2.1.). The ThT fluorescence was monitored and read at λex = 442 nm and λem = 483 nm every 10

min for 48 h at 37°C following shaking of the plate using a BioTek Synergy 2 plate reader (BioTek UK, Swindon, UK).

CONDITIONS	100 µM Aβ42	ThT	Peptide inhibitors	PB	PBS
Aβ42 control	15 µl	15 µl	-	-	30 µl
ThT control	-	15 µl	-	15 µl	30 µl
Peptide inhibitor controls	-	15 µl	30 µl	15 µl	-
Sample conditions	15 µl	15 µl	30 µl	-	-

Table 2.1. Indication of the volumes added for each sample condition to the 384-well plate for the aggregation assay.

2.2.2.5. Analysis and statistics of ThT aggregation assay

The analysis of the aggregation experiment was performed using PRISM GraphPad software (GraphPad Software Inc., California, USA). Data collected at 24 h and 48 h from three independent experiments were averaged and analysed by applying one-way analysis of variance (ANOVA) using the *post hoc* Bonferroni's multiple comparisons test in the case of the control Aβ versus peptide treatment; and unpaired t-tests with Welch's correction [assuming different SDs (standard deviations)] for comparison between same concentrations of the RI-OR2-TAT and RI-OR2-NAG peptides. Outliers were checked using the GraphPad QuickCalcs: outlier calculator software (GraphPad Software Inc., California, USA). The analysis of the ThT assay is presented in Chapter 3, Sections 3.3.1. as mean ± SEM (standard error of mean) and a p value of ≤ 0.05 was considered as statistically significant.

2.2.3. Cell culture and maintenance of SH-SY5Y Human Neuroblastoma cell line

SH-SY5Y neuroblastoma cells (European Collection of Cell Cultures, Salisbury, UK) were habitually cultured in Dulbecco's Modified Eagle's Medium (DMEM) with 4.5 g/L glucose and L-glutamine (BioWhittaker® Lonza by Scientific Laboratory Supplies, Nottingham, UK) containing 0.1 % (v/v) FBS (Foetal Bovine Serum), and 0.01 % (v/v) PEN – STREP (Penicillin – Streptavidin). The cell cultures were maintained in T-75 flat flasks (ThermoFisher Scientific Nunc A/S from Life Technologies Ltd., Paisley, UK) at

37°C in a humidified incubator with 5 % CO_2 – 95 % room air and the medium was changed every other day. The cells were used for a maximum of 20 passages.

To maintain the cells in a viable state, a subculture/splitting process was performed twice per week. Following removal of the present growth medium, 5 ml of Trypsin EDTA (ethylenediaminetetraacetic acid) (BioWhittaker® Lonza by Scientific Laboratory Supplies, Nottingham, UK) were added to the T-75 flask of cells and incubated at 37°C for about 3 min until the cells were detached from the bottom of the flask. To the trypsinised cells, 10 ml of DMEM medium were added, and the solution was collected in a fresh tube and spun at 200 RCF for 3 min (Allegra X-30R Centrifuge with the SN 15D rotor, Beckman Coulter, Inc., High Wycombe, UK). The supernatant was removed and the pellet of cells was resuspended in 5 ml DMEM medium. 0.5 ml of this suspension was transferred to a new T-75 flask with 10 ml of fresh DMEM medium and incubated at 37°C in a humidified incubator for future use.

2.2.4. MTS cell proliferation assay

The MTS proliferation assays were conducted in 96-well plates (Costar®, Corning Inc. from Fisher Scientific, Loughborough, UK). Following subculture of SH-SY5Y cells, approximately 20,000 cells/well were transferred in a final volume of 100 µl of DMEM Medium. The cells were allowed to adhere to the bottom of the wells O/N at 37°C in a humidified incubator. Following incubation, the medium was replaced by either 100 µl of fresh DMEM in the control (untreated) samples, or 100 µl of DMEM containing 0.1 µM, 1 µM or 10 µM of RI-OR2-NAG, RI-OR2-TAT, PINPs or CL peptides; and the plate was incubated O/N at 37°C in a humidified incubator. To each well 100 µl of CellTiter96 Aqueous One Solution Cell Proliferation (MTS) assay (Promega, Southampton, UK) was added and left to stand for 3 h at 37°C in a humidified incubator. The proliferation of the cells was assessed on a Wallac 1420 multilabel counter Victor^2 plate reader (PerkinElmer®, Massachusetts, USA) at 490 nm (0.1 s).

2.2.4.1. Analysis and statistics of MTS proliferation assay results

Data collected from three independent experiments were averaged and assessed applying one-way ANOVA hypothesis followed by *post hoc* Bonferroni's multiple

comparison test. Outliers were calculated using the GraphPad QuickCalcs: outlier calculator software; and analysis was performed using the PRISM GraphPad software (GraphPad Software Inc., California, USA). The results are presented in Chapter 3, Section 3.3.2. as mean ± SEM and a p value of ≤ 0.05 was considered as statistically significant.

2.2.5. Cell penetration experiments

The experiments were conducted in 6-well plates (Costar®, Corning Inc. from Fisher Scientific, Loughborough, UK) containing autoclaved 22 x 22 mm coverslips (SuperFrost®, Menzel-Gläser from Life Technologies Ltd., Paisley, UK) at the bottom of each well. Following maintenance of SH-SY5Y cells under standard mammalian cell culture conditions and subculture of the cells, approximately 40,000 cells/well were added to a final volume of 1.5 ml of DMEM medium. The cells were incubated for 48 h at 37°C in a humidified incubator to allow their adherence on the coverslips. Following incubation, the medium was replaced with either 15 µl PBS in 1.5 ml DMEM medium for the control (untreated) cells, or 15 µl of PBS containing the tested peptide inhibitor in 1.5 ml DMEM for the treated cells; and incubated for 1 h at 37°C in a humidified incubator. The peptide inhibitors tested were fluorescently-tagged peptides, Flu-RI-OR2-TAT and Flu-RI-OR2-NAG, at 1 µM final concentration in DMEM growth medium. The coverslips were then placed onto the surface of autoclaved microscopy slides (SuperFrost®, Menzel-Gläser from Life Technologies Ltd., Paisley, UK) with a drop of Fluoroshield™ with DAPI histology mounting medium, and allowed to dry. The coverslips were then sealed and the penetration of the fluorescently labelled peptides was assessed on Zeiss LSM 510 confocal microscope (Carl Zeiss Ltd., Cambridge, UK), using multichannel filters and the 63x objective. The merged images of each condition are presented in Chapter 3, Section 3.3.3.

2.3. *In vivo* studies – C57/BL6 mice

2.3.1. Ethics statement

All animal regulated procedures were performed as part of authorised personal and project licenses; approved by the UK Home Office in accordance with the UK Animals (Scientific Procedures) Act 1986.

2.3.2. Animals

Wild type (WT) mice from APPswe/PS1ΔE9 breeding with C57BL/6 background were single housed a week prior to treatment injection in a temperature-controlled holding room (21.5°C ± 1) with 12:12 h light and dark cycle. Food and water were available *ad libitum*.

2.3.3. Drug treatment

A pilot study was performed using 25 female WT animals of age between 31 – 32 weeks old. The animals were organised in groups of five for study purposes. The groups included a control group – injected with 0.9 % NaCl (vehicle control), and four treatment groups injected with Flu-RI-OR2-TAT, Flu-RI-OR2-NAG, BODIPY-PINPs, and BODIPY-CL respectively. All animals were injected intraperitoneally (i.p.) at a dose of 100 nmol/kg for the free peptides and 4 µmol/kg in the case of the liposome-based peptides; with administration volume of 10 ml/kg. The dose, administration volume and duration of treatment were decided based on a previous study investigating the effects of Flu-RI-OR2-TAT on amyloid plaque load and other markers of brain pathology using the APP/PS1 transgenic mouse model (Parthsarathy et al., 2013).

2.3.4. Tissue collection

At the time of injection, 0 h, the animals were housed in a dark room. After 1 h, the animals were anaesthetised with 0.107 g/ml urethane at a dose of 0.7 ml/30 g, and transcardially perfused using PBS with heparin (20 units/ml). To determine if the peptides penetrate the BBB, to measure their intensities in the brain, and determine whether they co-localise with specific cells, the brains were recovered, sectioned through the sagittal plane and the left hemisphere (LH) was fixed in 4 % (w/v) ice-cold formaldehyde. Following fixation for 3 days, the formaldehyde-preserved LH

was transferred to 30 % (w/v) sucrose in PBS with 0.02 % (w/v) sodium azide (NaN_3), at 4°C for storage. To determine the distribution and elimination of the peptides, the right cerebral hemisphere (RH), along with the heart, lungs, liver, stomach, spleen, right and left kidneys, and small intestine were collected and snap-frozen in liquid nitrogen, and then stored at -80°C for future use.

2.4. Distribution of the peptides

2.4.1. Tissue homogenisation

Each tissue collected following the perfusion of the C57/BL6 mice (-80°C storage) was weighed and then incubated for 20 min in ice-cold homogenisation buffer (HB) [RIPA (Radioimmunoprecipitation assay) buffer with 10 µl/ml protease and phosphatase inhibitor cocktail (100x) and 10 µl/ml 0.5 M EDTA solution (100X)] (Halt™ Protease and Phospatatase inhibitor cocktail, Thermo Scientific from Fisher Scientific, Loughborough, UK) at a concentration of 3 µl/mg of tissue. Each sample tissue was then homogenised on ice using the LabGEN 7 series homogenizer (Cole-Parmer® Instrument Co. Ltd., London, UK). Following complete homogenization, the blade was rinsed with extra 2 µl/mg of tissue HB to a total final concentration of 5 µl/mg of tissue. The samples were then sonicated (U300H ultrasonic bath, Ultrawave, Cardiff, UK) for 5 min with 30 sec incubation intervals on ice and then maintained at constant agitation for 2 h at 4°C. Following incubation, the lysate samples were first centrifuged at 4750 RPM for 15 min (Allegra® X-15R Centrifuge with SX4750A ARIES™ rotor, Beckman Coulter, Inc., High Wycombe, UK) and the supernatant was centrifuged again at 14,000 RPM for further 15 mins (Heraeus Fresco 21 Centrifuge with 75003424 ClickSeal™ biocontainment rotor, Thermo Scientific from Fisher Scientific, Loughborough, UK). The lysate (supernatant) was collected, aliquoted and stored at -80°C for future use and the cell debris (pellet) was discarded.

2.4.2. BCA assay for total protein content quantification in tissue

To determine the total protein content of each tissue lysate, the BCA assay was performed (explained in Section 2.1.3.). The BSA standards prepared in HB and tissue lysate samples in HB were added at 5 µl/well in triplicate on the 96-well plate.

2.4.3. Concentration of antibodies

Antibodies used in Luminex experiments of concentration lower than 1 mg/ml were concentrated to 1 mg/ml using the Pierce® Concentrator, PES, 3K MWCO, 0.5 ml (Thermo Scientific from Fisher Scientific, Loughborough, UK). The concentration sample chamber was pre-rinsed with 500 µl dH_2O and centrifuged at 15,000 xg (Eppendorf centrifuge 5424 with FA-452411 rotor, Eppendorf UK Ltd., Stevenage, UK) until more than 400 µl of filtrate was produced. Any rinsing solution remaining in the collection tube and concentration chamber was discarded and the sample antibody was added to the concentration chamber. The sample was centrifuged 15,000 xg (Eppendorf centrifuge 5424 with FA-452411 rotor, Eppendorf UK Ltd., Stevenage, UK) until the desired concentration factor relative to the volume in concentration chamber was achieved.

2.4.4. Antibody biotinylation and conjugate purification

Detection antibodies used in Luminex experiments were biotinylated using the Biotin-XX Microscale protein labelling kit (Invitrogen by ThermoFisher Scientific from Life Technologies Ltd., Paisley, UK). A 1 M sodium bicarbonate solution was prepared by adding 1 ml of dH_2O to the vial of sodium bicarbonate provided in the kit; and vortexed until the reagent was fully dissolved. This reagent was stored at 3°C for up to two weeks, or to -20°C for longer storage. The required volume of antibody at 1 mg/ml was transferred to a reaction tube along with 1/10 volume of 1 M sodium bicarbonate and mixed by pipetting up and down numerous times. To a separate vial of biotin-XX (reactive biotin) provided in the kit, 10 µl of dH_2O were added and completely dissolved by pipetting up and down several times, yielding a concentration of 14.93 nmol/µl. The reagent was prepared immediately before use and any leftover was discarded. According to the equation (Equation 2.1.) that was presented in the kit's product information, the appropriate volume of reactive biotin was added to the reaction tube containing the pH-adjusted antibody and mixed thoroughly by pipetting up and down. The reaction mixture was incubated for 15 min at RT.

$$\frac{\left[\left(\frac{\mu g\ protein}{protein\ MW}\right) x1,000\right] xMR}{14.93} = \mu l\ reactive\ biotin - XX\ to\ add\ to\ sample$$

Equation 2.1. Equation used to calculate the volume of biotin solution.

The equation was used to calculate the amount of reactive biotin to be added to the reaction tube; where µg protein is the mass of protein to be labelled, protein MW is the molecular weight of protein in Da (150,000 in the case of antibodies), MR is the biotin to protein molar ratio (MR=18 for antibodies – information provided in the kit), and 14.93 is the concentration of reactive biotin stock (adapted from Biotin-XX Microscale protein labelling kit Product information).

To remove any unbound biotin from the mixture, protein desalting spin columns (ThermoFisher Scientific from Life Technologies Ltd., Paisley, UK) were used. The column was inverted to suspend the slurry and the bottom closure was twisted initially and removed once the cap was loosened. The column was placed in 1.5 ml microcentrifuge collection tube and centrifuged at 1,500 xg (Eppendorf centrifuge 5424 with FA-452411 rotor, Eppendorf UK Ltd., Stevenage, UK) for 1 min to remove excess liquid. To the tube, 400 µl of PBS-T [PBS with 0.05 % (v/v) Tween® 20] were added to the top of the column and centrifuged at 1,500 xg for 1 min. The process of buffer exchange was repeated three times. Following exchange of buffer, the column was placed in a fresh 1.5 microcentrifuge tube and the biotinylated antibody was added to the centre of the compacted resin bed and centrifuged at 1,500 xg for 2 min and the eluted purified biotinylated antibody was aliquoted and stored according to the manufacturer's recommendations.

2.4.5. BODIPY-PINPs peptide treatment with bee venom

To break down the phospholipids of the liposome, the PINPs solution was treated with 1 mg/ml Phospholipase A_2 from honey bee venom (Apis mellifera) at 10 % (v/v) of the lipid molarity. The reaction mixture was incubated for 20 min at 37°C and then stored at 3°C for up to two weeks.

2.4.6. Luminex-bead Immunoassay for tissue-specific peptide distribution

2.4.6.1. Primary antibody coupling to Luminex beads

Following vortexing and sonication of 1 vial of Luminex beads (COOH Beads 023 – 5.6 µm COOH microspheres, 1 ml at $1.25x10^7$ beads/ml) (Biol-Plex®, BIO-RAD Laboratories Ltd., Hertfordshire, UK), 33 µl of beads were transferred to a fresh coupling tube (Fisherbrand™ premium microcentrifuge tubes, Fisher Scientific, Loughborough, UK) with 50 µl of triton/activation buffer (Table 2.2.), and centrifuged at 10,000 RPM for 1 min (Eppendorf centrifuge 5424 with FA-452411 rotor, Eppendorf UK Ltd., Stevenage, UK). The supernatant was removed and the pellet of beads was washed using the Triton/activation buffer. To the pellet, 80 µl of activation buffer (Table 2.2.) were added and the bead mixture was vortexed and sonicated. To the tube, 10 µl of freshly prepared NHS (*N*-hydroxysuccinimide) buffer (Sulfo-NHS, Thermo Scientific from Fisher Scientific, Loughborough, UK) were added at 50 mg/ml in dH_2O along with 10 µl of fresh EDC [1-ethyl-3-(3-dimethylamino)propyl carbodiimide, hydrochloride] buffer (Pierce™ Premium-Grade EDC, Thermo Scientific from Fisher Scientific, Loughborough, UK) at 50 mg/ml in dH_2O, and the mixture was incubated for 30 min at RT in the dark on an end-over-end mixer (Stuart® equipment, Bibby Scientific Ltd., Stone, UK). After incubation, 100 µl of triton/coupling buffer (Table 2.2.) were added and centrifuged for an extra minute at 10,000 RPM. The supernatant was then removed and the pellet was washed twice with the Triton/coupling buffer as above. The pellet of beads was then resuspended in 500 µl of the primary antibody in coupling buffer (Table 2.2.) at final concentrations of 1 µg/ml in the case of anti-HIV1 tat [N3] (mouse monoclonal) antibody used in the Flu-RI-OR2-TAT peptide detection, and 3 µg/ml in the case of anti-O-GlcNAc CTD110.6 (mouse monoclonal) antibody (BioLegend, London, UK) used in the Flu-RI-OR2-NAG detection. The solution was then incubated for 2 h at RT in the dark in an end-over-end mixer. Following incubation, 100 µl of wash buffer (Table 2.2.) were added to the tube and the mixture was centrifuged for 1 min at 10,000 RPM. The supernatant was removed and the pellet was washed twice with the same buffer. The pellet of beads coupled to the primary antibody was then resuspended in 150 µl of blocking/storage buffer (Table 2.2.), and stored at 4°C until further use.

BUFFERS	COMPOSITION
Activation Buffer	0.1 M Sodium Phosphate monobasic pH 6.1
Triton/Activation Buffer	0.1 M Sodium Phosphate monobasic pH 6.1 with 0.025 % (v/v) Triton X-100
Coupling Buffer	50 mM MES hydrate of pH 5.0
Triton/Coupling Buffer	50 mM MES solution [2-(*N*-morpholino)ethanesulfonic acid)] of pH 5.0 with 0.025 % (v/v) Triton X-100
Wash Buffer	PBS with 0.025 % (v/v) Triton X-100
Blocking/Storage Buffer	PBS, 0.1 % (w/v) BSA, 0.02 % (v/v) Tween® 20 with 0.02 % (w/v) sodium azide

Table 2.2. The composition of Luminex bead coupling buffers.

2.4.6.2. Bead-based Luminex Assay Development

The assay was performed on a 96-well filter plate (MultiScreen$_{HTS}$ BV 1.2 µm filter plates, Merck Millipore from Life Technologies Ltd., Paisley, UK). The filter plate was initially pre-washed using 100 µl/well PBS-T and the solution was aspirated using a vacuum manifold (Dymax 5, Charles Austen Pumps Ltd., Surrey, UK). The primary antibody-coupled microspheres were diluted in 1:20 ratio in PBS-T, vortexed to remove any doublets and added at 25 µl/well to the plate. The plate was then agitated on a microplate shaker (Grant-bio, Grant Instruments Ltd., Cambridge, UK) for 5 min in dark and aspirated using the vacuum pump. To each well, 50 µl of peptide inhibitor standards were added in triplicate at concentrations ranging from 0.95 pM to 1 µM (and Blank control) in HB in the case of Flu-RI-OR2-TAT detection, and 0.24 nM to 1 µM (and Blank control) in HB in the case of Flu-RI-OR2-NAG detection, along with 50 µl of tissue lysates in triplicate at 1:5 volume ratio in HB; and the plate was agitated O/N at 3°C in the dark on a rocking shaker (Stuart®, gyro-rocker SSL3, Bibby Scientific Ltd., Stone, UK). Following incubation, the plate was aspirated, washed twice with 150 µl/well PBS-T, and aspirated again using the vacuum manifold. To each well, 50 µl of biotinylated secondary antibody, anti-fluorescein (biotin) (goat polyclonal) antibody, was added at 2 µg/ml in the Flu-RI-OR2-TAT assay and 0.125 µg/ml in the Flu-RI-OR2-NAG assay, diluted in PBS-T. The

plate was then agitated for 1 h at RT in the dark and then 50 µl/well of 4 µg/ml Streptavidin-RPE (R-phycoerythrin conjugate) (Molecular probes®, Life Technologies, Paisley, UK) was added, and the plate was agitated for further 30 min at RT in the dark. After incubation, the plate was aspirated, washed twice with 150 µl/well PBS-T, and aspirated again. The beads were then resuspended in 100 µl/well PBS-T, and agitated on a shaker for 1 min, at high speed, at RT in the dark. Finally, the plate was read in a Luminex® 200 xMAP™ Technology plate reader (Luminex Co., Texas, USA) using the xPONENT® 3.1 software. A schematic representation of the Luminex assay (sandwich reaction in each well) is shown in Figure 2.2.

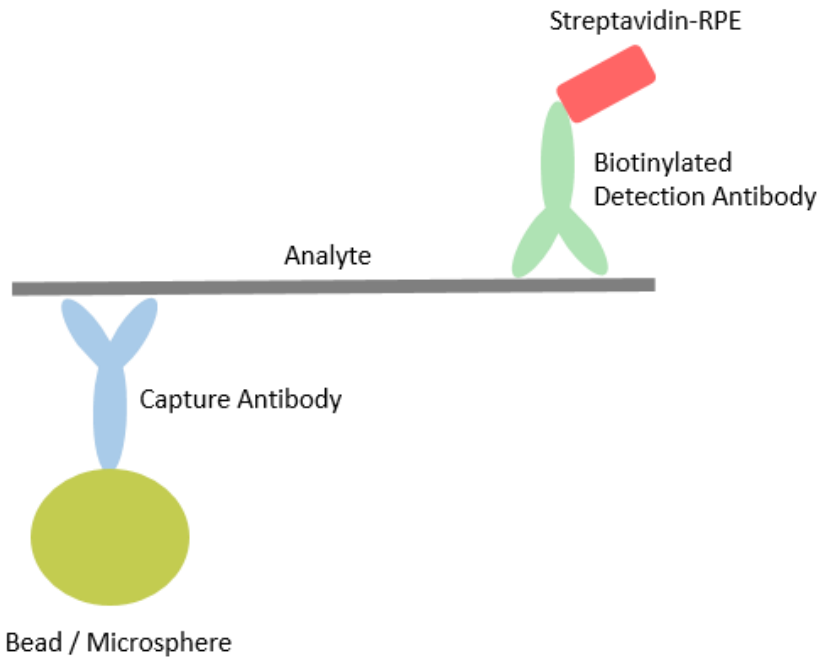

Figure 2.2. Luminex Sandwich Immunoassay.

Schematic representing the Luminex sandwich assay format. The capture and biotinylated detection antibodies are specific for each analyte of interest; streptavidin-RPE acts as a reporter molecule.

2.4.7. Luminex peptide-specific assay optimisation

Prior to the analysis of tissue lysates in Luminex-bead immunoassays, a variety of antibody combinations and antibody concentrations were used with fluorescent-tagged peptide inhibitor standards to optimise each peptide assay following the same protocol as presented in Section 2.4.6. The tables below show the antibodies

and antibody concentrations used for Flu-RI-OR2-TAT optimisation assays (Table 2.3), Flu-RI-OR2-NAG optimisation assays (Table 2.4) and PINPs optimisation assays (Table 2.5).

Flu-RI-OR2-TAT optimisation assay

ANTIBODY	Coupling concentrations tested (µg/ml)	Detection concentrations tested (µg/ml)
anti-HIV1 tat [N3] (mouse monoclonal) antibody	1, 2, 3	
anti-Fluorescein (Biotin) (goat polyclonal) antibody		0.5, 1, 2

Table 2.3. Table representing the concentrations (µg/ml) tested for detection and coupling antibodies for the Flu-RI-OR2-TAT assay optimisation.

Flu-RI-OR2-NAG optimisation assay

ANTIBODY	Coupling concentrations tested (µg/ml)	Detection concentrations tested (µg/ml)
anti-O-GlcNAc CTD110.6 (mouse monoclonal) antibody (BioLegend, London, UK)	1, 2, 3	
anti-Fluorescein (Biotin) (goat polyclonal) antibody		0.125, 0.25, 0.5, 1, 2
anti-O-Linked N-Acetylglucosamine [RL2] (mouse monoclonal) antibody	1, 2, 3	
Anti-O-GlcNAc RL2 (mouse monoclonal) antibody (BioLegend, London, UK)	1, 2, 3	

Table 2.4. Table representing the concentrations (µg/ml) tested for detection and coupling antibodies for the Flu-RI-OR2-NAG assay optimisation.

The same detection antibody was used for all the coupling antibodies tested.

BODIPY-PINPs optimisation assay

ANTIBODY	Coupling concentrations tested (µg/ml)	Detection concentrations tested (µg/ml)
anti-HIV1 tat [N3] (mouse monoclonal) antibody	1, 2, 3	
anti-Polyethylene glycol [PEG-2-128] (rabbit monoclonal) antibody		0.5, 1, 2
anti-Polyethylene glycol [PEG-B-47b] (Biotin) (rabbit monoclonal) antibody		0.5, 1, 2

Table 2.5. Table representing the concentrations (µg/ml) tested for detection and coupling antibodies for the BODIPY-PINPs assay optimisation.

The same coupling antibody was used for all the detection antibodies tested.

2.4.8. Luminex assay analysis

Data obtained from the assay optimisation experiments were analysed according to the signal to noise ratio (S/N) of each assay to determine the antibody concentrations to be used in the peptide detection; and are presented in Chapter 4. Analysis of each tissue-specific peptide detection was performed using one-way ANOVA hypothesis test followed by *post hoc* Bonferroni's multiple comparison test. The outliers were calculated using the GraphPad QuickCalcs: outlier calculator software (GraphPad Software Inc., California, USA). Data are presented in Chapter 5 as mean ± SEM of the total amount (moles) of peptide per tissue-specific protein content (mg) and a p value of ≤ 0.05 was considered as statistically significant.

2.4.9. Sandwich ELISA immunoassay for tissue-specific BODIPY-PINPs detection

96-well plates (ThermoFisher Scientific Nunc A/S from Life Technologies Ltd., Paisley, UK) were coated with 100 µl/well of diluted anti-HIV1 tat [N3] (mouse monoclonal) primary antibody in carbonate-bicarbonate buffer at a concentration of 3 µg/ml and left to incubate O/N at 3°C on a rocking shaker (Stuart®, gyro-rocker SSL3, Bibby

Scientific Ltd., Stone, UK). The coating solution was then removed and the plate was washed three times with 100 µl/well PBS-T. To the plate, 100 µl/well of blocking buffer [5 % (w/v) dry-milk in PBS-T] were added and incubated for 1 h at RT on a microplate shaker (Grant-bio, Grant Instruments Ltd., Cambridge, UK) in the dark. The blocking buffer was then removed, and 100 µl of BODIPY-PINPs standards (treated with bee venom) ranging from 7.81 nM to 1 µM (and blank control) in HB were added in triplicate to the plate along with tissue lysates prepared at a 1:5 volume ratio in HB. The plate was then agitated O/N at 3°C in the dark on a rocking shaker. Following incubation, the samples and controls were removed and the plate was washed three times with 100 µl/well PBS-T. In each well, 100 µl of diluted anti-polyethylene glycol [PEG-2-128] (rabbit monoclonal) secondary antibody were added to the plate at a concentration of 1 µg/ml, and the plate was incubated for 1 h at RT in the dark on a microplate shaker. To each well, 100 µl of Streptavidin-RPE (Molecular probes®, Life Technologies, Paisley, UK) was added to the plate and left to incubate for 30 min at RT in the dark. The detection solution was then removed and the wells were washed three times with 200 µl PBS-T. After washes, the wells were filled with 100 µl PBS-T, and the plate was read at λex = 546 λem = 578 nm using an average 25 reads/per well on a TECAN infinite M200 pro (Tecan Trading AG, Switzerland) plate reader, using Magellan V 7.0 software. A schematic representation of the ELISA assay (sandwich reaction in each well) is shown in Figure 2.3.

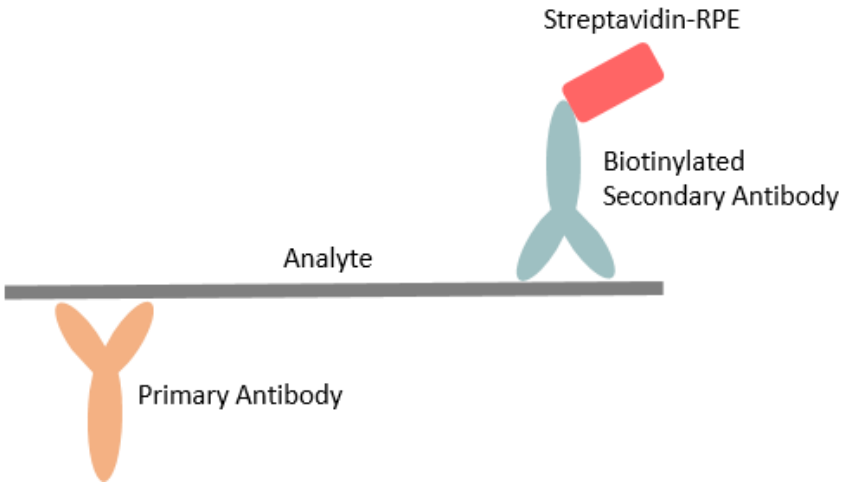

Figure 2.3. ELISA Sandwich Immunoassay.

Schematic representing the ELISA sandwich assay format. The primary and biotinylated secondary antibodies are specific for each analyte of interest; streptavidin-RPE acts as a reporter molecule with three excitation maxima at 496, 546, and 565 nm, and one emission maximum at 578 nm.

2.4.10. ELISA peptide-specific assay optimisation

The following table (Table 2.6) represents the antibodies, and antibody concentrations used for the optimisation of the BODIPY-PINPs assay, using only peptide standards with and without bee venom treatment, following the same protocol as described in Section 2.4.9.

BODIPY-PINPs optimisation assay

ANTIBODY	Primary antibody concentrations tested (µg/ml)	Secondary antibody concentrations tested (µg/ml)
anti-HIV1 tat [N3] (mouse monoclonal) antibody	1, 2, 3	
anti-Polyethylene glycol [PEG-2-128] (rabbit monoclonal) antibody		0.5, 1, 2, 5
anti-Polyethylene glycol [PEG-B-47b] (Biotin) (rabbit monoclonal) antibody		0.5, 1, 2

Table 2.6. Table representing the concentrations (µg/ml) tested for primary and secondary antibodies for the BODIPY-PINPs assay optimisation.

The same primary antibody was used for all the secondary antibodies tested.

2.4.11. Sandwich ELISA assay analysis

Data obtained from the BODIPY-PINPs assay optimisation are presented in Chapter 4, while analysis of each tissue-specific peptide detection are presented in Chapter 5. The analysis of both optimisation assays and tissue-specific peptide detection assays was performed as described in Section 2.4.8.

2.5. BBB penetration, intensity and co-localisation study

2.5.1. Brain sectioning

Following storage, the brains were transferred to 30 % (w/v) sucrose in PBS O/N, and then were snap-frozen with Shandon ENVI-RO-TECH^{TM} freezing spray (ThermoFisher Scientific from Life Technologies Ltd., Paisley, UK). Using the Bright model OTF cryostat with 5040 microtome (Bright Instruments, Luton, UK), 25 micron (µm) thick coronal sections of the brains were cut at anatomical regions of 1.10 mm to -4.04 mm Bregma (Franklin and Paxinos, 2008) with the first section taken at random and then every 12th section afterwards. The brain sections were preserved in cryoprotect

solution [30 % (v/v) Ethylene Glycol, 25 % (v/v) Glycerin, and 45 % (v/v) PBS] in a 24-well plate (Costar®, Corning Inc. from Fisher Scientific, Loughborough, UK) and stored at -20°C in the dark until further use.

2.5.2. Microscopy Slides Silanization

The silanizing reagent for coating of microscopy slides (SuperFrost®, Menzel-Gläser from Life Technologies Ltd., Paisley, UK) was prepared using 2 % (v/v) 3-amino-propylthieoxysilane in acetone. The staining rack holding slides was immersed in freshly prepared silanizing solution for 1 min. Following coating, the rack was transferred to a tank of water for an extra minute. The slides were then removed and allowed to air-dry.

2.5.3. Immunostaining of floating brain tissue sections

The immunostaining procedure was performed in a fresh 24-well plate (Costar®, Corning Inc. from Fisher Scientific, Loughborough, UK) and all solutions were added at 1 ml/well. The brain sections stored in cryoprotect solution were initially washed 3 times in TBS (Tris-buffered saline) of pH 8 for 5 min and then incubated in 1X citrate buffer at 90°C for 30 min to retrieve the antigens. Following 3 x 5 min washes, the sections were permeabilised for 15 min at RT in 0.3 % (v/v) Triton X-100 in TBS and then blocked in 5 % (v/v) goat serum with 1 % (w/v) BSA for 1 h at RT. The primary antibodies of interest were then added at 1:500 dilution and incubated O/N in a cold room (3°C) and dark on a rocking shaker (Stuart®, gyro-rocker SSL3, Bibby Scientific Ltd., Stone, UK). For the co-localisation study the sections were examined using cell-specific markers for neurons using anti-NeuN (Rabbit polyclonal) antibody, astrocytes using anti-GFAP (Rabbit polyclonal) antibody, or activated microglia using anti-Iba-1 (Rabbit polyclonal) antibody.

The brain sections were then washed 3 times in TBS for 10 min and then stained with goat anti-rabbit Alexa Fluor 594 conjugate secondary antibody (AlexaFluor®, ThermoFisher Scientific from Life Technologies Ltd., Paisley, UK) at 1:1,000 dilution, for 1 h in dark at RT. Following 3 x 10 min washes, the tissue sections were placed on silanized slides and allowed to air-dry. The slides were then mounted using

Fluoroshield™ with DAPI histology mounting medium and sealed with a coverslip (SuperFrost®, Menzel-Gläser from Life Technologies Ltd., Paisley, UK).

All sections were visualised on a Zeiss LSM 880 confocal microscope (Carl Zeiss Ltd., Cambridge, UK), using multichannel filters, and the images were merged using the Zen lite Blue 2012 software (Carl Zeiss Ltd., Cambridge, UK). For quantification, 3 digital photographic images per section were taken from the cortex (area close to the hippocampal formation), DG and cornus ammonis (CA) region 1 (CA1) (referred to as hippocampus) areas with a 40X objective, with a minimum of 15 sections visualised per animal. For the cell-specific co-localisation study, images were also taken with a 63X objective. Image analysis for the BBB penetration and intensity study was performed using 8-bit converted images in ImageJ [National Institutes of Health (NIH), USA]. Images analysis for the co-localisation study was performed using 8-bit separated-channels images in Fiji (Fiji is just ImageJ) (NIH, USA).

2.5.4. Statistics of Immunohistochemical Study

Collected data obtained from ImageJ for the BBB penetration and intensity study were analysed as mean Normalised Intensities (Equation 2.2.) applying one-way ANOVA hypothesis test in the case of control versus peptide treatment; and two-way ANOVA in case of peptide versus brain region and conditions using the PRISM GraphPad software (GraphPad Software Inc., California, USA). Outliers were detected using the GraphPad QuickCalcs: outlier calculator software (GraphPad Software Inc., California, USA). The tests were then further analysed by *post hoc* Bonferroni's multiple comparison test and are presented in Chapter 6 as mean ± SEM and a p value of ≤ 0.05 was considered as statistically significant.

$$\textbf{Normalised Intensity} = \frac{\textbf{Intensity of sample} - \textbf{Black intensity}}{\textbf{White intensity} - \textbf{Black intensity}}$$

Equation 2.2. Normalised Intensity equation.

Equation applied to normalise the averaged mean values of the intensities for each peptide. The "black intensity" was calculated from an image acquired with a shutter in front of the camera (i.e. black image – no light). The "white intensity" was calculated from an image acquired with the shutter open but no sample present. The two images were acquired using the same conditions as for data acquisition. The two values are most commonly represented as 0 for black intensity and 255 for white intensity demonstrating the maximum pixel value in an 8-bit image (adapted from Vojnovic and Barber, 2005).

2.5.5. Analysis of the Co-localisation study

8-bit images of separated channels from the images taken by the 63X objective were analysed by built-in plugins provided in Fiji (NIH, USA). The images were first compared using the "Colocalization Test" plugin to obtain the PSF (Point Spread Function) of the image and the Costes' p-value, where a p-value of ≥0.95 was considered statistically significant for colocalization between the two channel intensities. The colocalization of the images was also expressed using scatterplots of colocalized pixel maps using the "Colocalization Threshold" plugin. Finally, for each image, the Pearson's correlation coefficient (Rr), Manders' overlap coefficient (R), Manders' colocalization coefficients (M1 and M2), and Manders' thresholded colocalization coefficients (tM1 and tM2) were calculated using the "Coloc2" plugin. The qualitative - image based - approaches; and quantitative, including threshold-based and intensity-based, approaches are presented in Chapter 7.

Chapter 3: RI-OR2-NAG as a potential peptide inhibitor of Aβ aggregation process

3.1. Introduction

3.1.1. Amyloid aggregation as a target for novel treatments for AD

Cumulative evidence supports the hypothesis that Aβ oligomerisation and fibrillogenesis are the primary and crucial pathogenic events in AD (Hardy and Selkoe, 2002). Early nonfibrillar intermediate aggregates, known as soluble oligomers, are likely to be the pathogenic components that are at least partly responsible for neurodegeneration and neuronal cell death in the brains of affected individuals (Klein et al., 2001; Hardy and Selkoe, 2002; Chromy et al., 2003; Bitan et al., 2003; Kayed et al., 2003; Kayed et al., 2004; Varvel et al., 2008; Tomic et al., 2009). Thus, the development of drugs that directly inhibit the very early stages of the Aβ aggregation process, rather than the late stages of amyloid fibril formation, is now considered to be a viable therapeutic approach for slowing the progression of the disease, or even halting the pathogenic events of AD.

3.1.2. Different versions of RI-OR2 peptide as potential inhibitors

Taylor and colleagues developed a proteolytically stable retro-inverso peptide, RI-OR2, which demonstrated inhibition of Aβ aggregation and rescued SH-SY5Y neuroblastoma cells from Aβ-induced toxicity (Taylor et al., 2010). Parthsarathy and colleagues improved the RI-OR2 peptide by attaching a 'TAT' transit sequence onto its carboxyl terminus, to give RI-OR2-TAT (Parthsarathy et al., 2013). The incorporation of the retro-inverted version of the HIV-1 TAT sequence onto the peptide was aimed at targeting it into cells and into the brain (Parthsarathy et al., 2013). The TAT sequence has previously been shown to enable a variety of different molecules to cross the BBB (Dietz and Bähr, 2004; Repici et al., 2007); an activity that was retained in the retro-inverso version of the TAT sequence (Ramanathan et al., 2001; Zhang et al., 2009). In our inhibitor, the retro-inverso TAT sequence was incorporated so that the protease resistance of RI-OR2 is maintained, which should result in good *in vivo* bioavailability (Parthsarathy et al., 2013).

The effects of RI-OR2-TAT on the extent of Aβ aggregation and other associated components of AD brain pathology could be improved by using a more brain-selective delivery mechanism, ideally in combination with a more potent inhibitor. An approach that was suggested by Parthsarathy and colleagues to increase the potency of RI-OR2-TAT against Aβ aggregation, was to attach the peptide onto the surface of lipid nanoparticles, to produce a multivalent inhibitor (Parthsarathy et al., 2013). The resulting peptide inhibitor nanoparticles (PINPs) (Gregori et al., 2017) have been studied as part of this project. Another approach taken here is to use NAG as an alternative targeting mechanism to TAT, to develop a new version of the RI-OR2 aggregation inhibitor. This new peptide inhibitor, RI-OR2-NAG, could potentially have an enhanced ability to penetrate across the BBB more selectively than TAT by utilising the glucose transporters located at the BBB and nerve cell membranes (Bell et al., 1990), and the NAG transporters found at the Golgi complex of cells (Abeijon et al., 1996).

In this Chapter, the effect of the RI-OR2-NAG peptide on Aβ aggregation and cell proliferation and its ability to penetrate into cells, was examined. The data obtained were compared with the RI-OR2-TAT peptide, which has already demonstrated anti-aggregational properties, no effect on the survival of SH-SY5Y cells, and penetration into cultured SH-SY5Y neuroblastoma cells. In the case of the cell proliferation experiments, PINPs and CL were also examined.

3.1.3. *N*-acetylglucosamine

NAG is a monosaccharide and a derivative of glucose and is abundant at the surface of mammalian cells, but is also present in the extracellular matrix, where it is involved in insulin signalling, cell cycle control and many other essential processes (reviewed by Konopka, 2012). Glucose transporters (GLUT) are structurally characterised by twelve membrane-spanning helices with their amino- and carboxy-terminals exposed on the cytoplasmic side of the biological cell membrane (Oka et al., 1990; Hebert and Carruthers, 1992; Cloherty et al., 1995). The glucose transporters are expressed in a variety of cell membranes, including barrier tissues such as the BBB (GLUT1), and in neurons (GLUT3) (Bell et al., 1990). The NAG

transporter (SLC35A3), belongs to the solute carrier (SLC) family 35 nucleotide sugar transporters and is characterised by ten transmembrane helices with their C- and N-terminals exposed to the cytosol (reviewed by Ishida and Kawakita, 2004). SLC35A3 is ubiquitously distributed in tissues as it is found in the Golgi apparatus of mammalian cells (Abeijon et al., 1996).

3.1.4. Introduction to the ThT spectroscopic assay

ThT (Figure 3.1.) is a benzothiazole salt which is used regularly in experimental procedures for visualisation and quantification of fibrillization of Aβ and other amyloid aggregates. Upon binding to amyloid fibrils, ThT exhibits a shift in its excitation maximum (from 385 nm to 450 nm) and emission maximum (from 445 nm to 482 nm) (Naiki et al., 1989; LeVine, 1993). ThT is only able to bind to the end-product of the aggregation process, the mature fibrils, due to the cross-β-structure that they display (Naiki et al., 1989; LeVine, 1995).

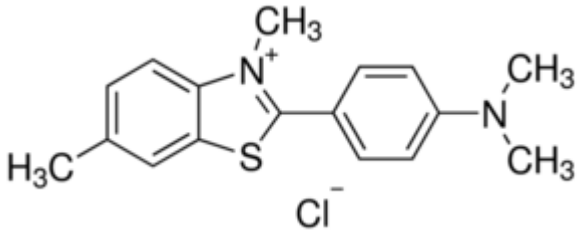

Figure 3.1. The structure of Thioflavin T.

(Adapted from LeVine, 1993)

The ThT assay measures changes in fluorescence intensity of ThT upon binding to the mature fibrils. It can be used to monitor the assembly over time of Aβ into fibrils, with this process typically exhibiting sigmoidal growth kinetics (Ferrone et al., 1985; Ferrone et al., 1985; Ferrone, 1999). The initial state of this growth is characterised as a flat region referred as the lag phase which is followed by a steep transition zone known as the growth or elongation phase. Following the latter phase, there is another flat region called the plateau phase (Arosio et al., 2015). The lag phase corresponds to the early nucleation steps involved in Aβ assembly which occur before fibril formation as displayed in the rapid growth phase. In the final plateau phase, the monomer concentration is thought to reach an equilibrium where no

more assemblies are being formed. It is, however, worth noting that the process of Aβ aggregation is ongoing through these phases (Ferrone et al., 1985; Ferrone et al., 1985; Ferrone, 1999; Cohen et al., 2012). For the assay, synthetic Aβ42 was 'deseeded' so that the starting point for aggregation was as close to monomeric peptide as possible in these types of experiments.

3.1.5. Introduction to the cell proliferation assay

3.1.5.1. SH-SY5Y human neuroblastoma cell line

The SH-SY5Y cell line that was used for these experiments is a widely used in vitro cell model in neuroscience research as it possesses many functional and biochemical properties of normal neurons (Biedler et al., 1978; Ross et al., 1983). SH-SY5Y is a human-derived cell line that was originally subcloned from the SK-N-SH cell line that was isolated from a bone marrow biopsy of a four-year-old female with neuroblastoma cancer (Biedler et al., 1973). The homogenous neuroblast-like SH-SY5Y cell line exhibits proliferative properties for long-term periods thus it can be used as a model for neurodegenerative disorders for a variety of studies that can include neuronal differentiation, neurotoxicity and neuroprotection.

3.1.5.2. The MTS proliferation and viability assay

The MTS assay is a colorimetric method that is widely used in proliferation or cytotoxicity experiments to determine the number of viable cells. Using a colorimetric reaction, the assay measures the potential of cells to bio-reduce the MTS tetrazolium compound [3-(4,5-dimethylthiazol-2-yl)-5-(3-carboxymethoxyphenyl)-2-(4-sulfophenyl)-2H-tetrazolium] into a formazan product (Figure 3.2.) which is soluble in the medium solution (Barltrop et al., 1991). The reaction occurs through NADPH or NADH which is produced by dehydrogenase enzymes present in metabolically active cells (Berridge and Tan, 1993). Thus, the resulted formazan product is directly proportional to the number of viable cells.

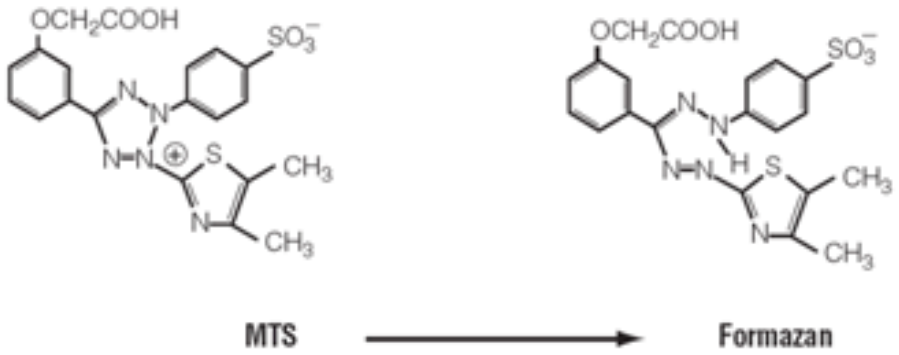

Figure 3.2. Structures of MTS tetrazolium and its coloured formazan product.

(WWW, Promega)

3.1.6. Determination of cell penetration

As the initial steps of Aβ aggregation may start inside cells (Friedrich et al., 2010), it is of primary importance for the new candidate peptide inhibitors to enter neuronal cell and block the very early stages of aggregation. The 'TAT' sequence of the RI-OR2-TAT peptide has previously been shown to be an effective transit peptide, as a fluorescent version of this inhibitor, Flu-RI-OR2-TAT, demonstrated rapid entry into cultured SH-SY5Y human neuroblastoma cells, within 10 min of incubation, in contrast to the fluorescent version of the original RI-OR2 peptide (Taylor et al., 2010), Flu-RI-OR2, that was not able to enter cells and remained in the culture medium (Parthsarathy et al., 2013).

3.2. Methods

3.2.1. Thioflavin-T assay

The ThT assays were employed to examine the effects of the RI-OR2-NAG peptide inhibitor on Aβ aggregation and fibril formation. The aggregation of Aβ into ThT-positive amyloid fibrils was monitored by the incubation of the deseeded Aβ peptide with inhibitor, in the continuous presence of ThT dye. The fluorescent absorbance of ThT-bound fibrils (λex = 442 nm and λem = 483 nm) was recorded every 10 min for a period of 48 h on a BioTek Synergy 2 plate reader (BioTek UK, Swindon, UK) at 37°C. The results presented are compared with those obtained with the RI-OR2-TAT peptide inhibitor.

Data obtained from the ThT aggregation assays for control Aβ versus peptide treatment were analysed, using one-way ANOVA and *post hoc* Bonferroni's multiple comparisons test, whereas unpaired t-tests with Welch's correction (assuming different SDs) were used for comparison between the levels of Aβ aggregation obtained at the same concentrations of RI-OR2-TAT and RI-OR2-NAG. Assay data are presented as mean ± SEM (n = 3) for 24 h and 48 h incubation periods, and a p-value of ≤ 0.05 was considered to be statistically significant.

3.2.2. MTS cell proliferation assay

Cultured SH-SY5Y human neuroblastoma cells were treated with 0.1, 1, and 10 μM of RI-OR2-TAT, RI-OR2-NAG, PINPs and CL for 24 h to determine their effect on cell proliferation. In the case of PINPs and CL, the concentrations refer to total lipid content. Cell proliferation was assessed using the CellTiter96 Aqueous One Solution Cell Proliferation (MTS) assay (Promega, Southampton, UK). Following a 3 h incubation, the plate was read at 490 nm (0.1 s) on a Wallac 1420 multilabel counter Victor^2 plate reader (PerkinElmer®, Massachusetts, USA).

Cell proliferation results were analysed using one-way ANOVA followed by *post hoc* Bonferroni's multiple comparison test. The results are presented as mean ± SEM (n = 3) and a p-value of ≤ 0.05 was considered to be statistically significant.

3.2.3. Cell penetration experiment

Assessment of peptide penetration was performed followed a 1 h incubation of 1 μM fluorescently-tagged peptides, Flu-RI-OR2-TAT and Flu-RI-OR2-NAG, with SH-SY5Y cultured cells. The cells were visualised on Zeiss LSM 510 confocal microscope (Carl Zeiss Ltd., Cambridge, UK), using multichannel filters and the 63x objective.

3.3. Results

3.3.1. RI-OR2-NAG peptide inhibits the formation of Aβ fibrils *in vitro*

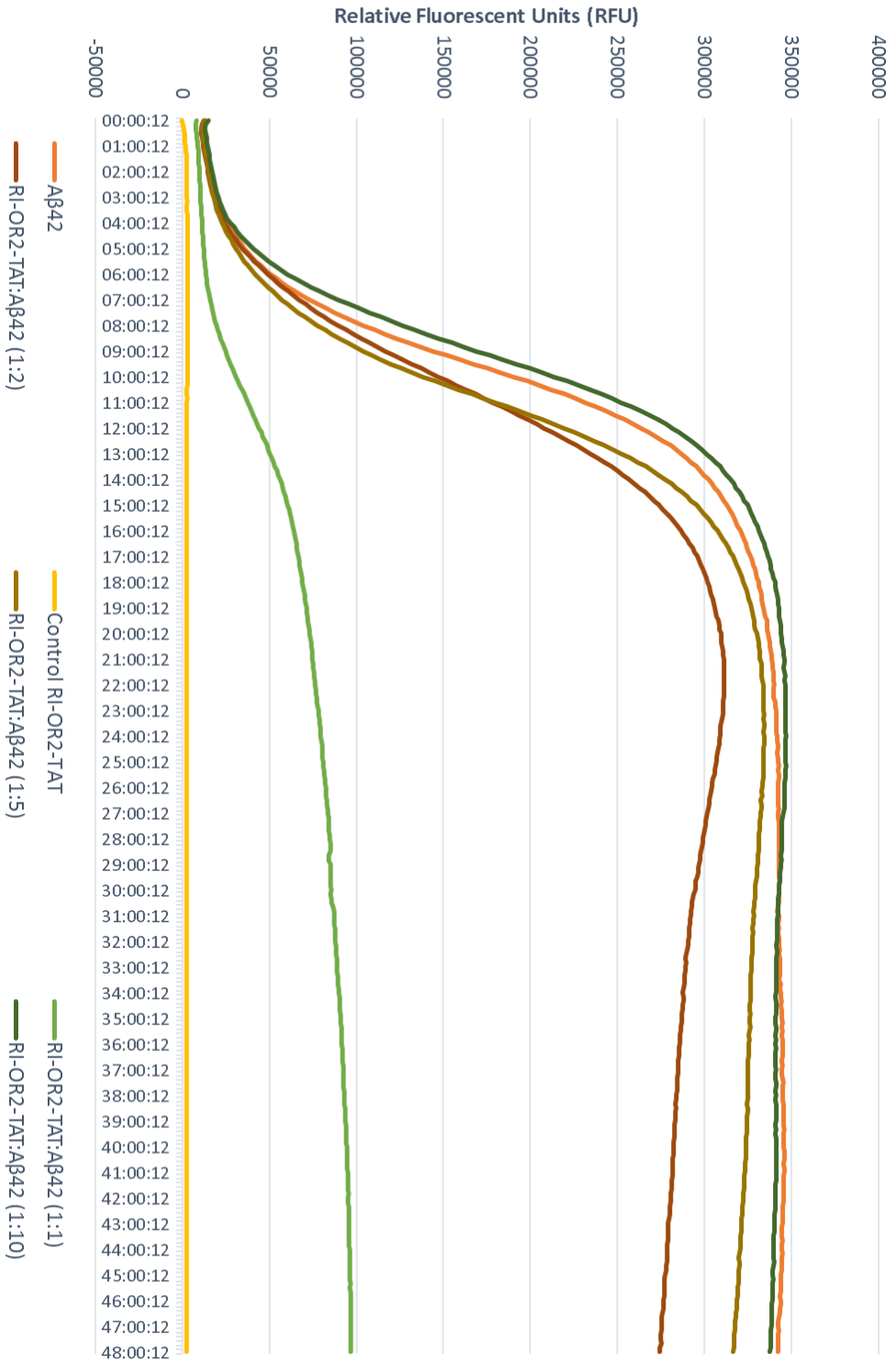

Figure 3.3. Macroscopic aggregation curve of Aβ with RI-OR2-TAT.

Graph demonstrating the lag phase (0 – 5 h), growth phase (6 – 23 h), plateau phase (24 – 48 h) of RI-OR2-TAT alone and synthetic Aβ42 alone or in the presence of RI-OR2-TAT peptide at different molar ratios.

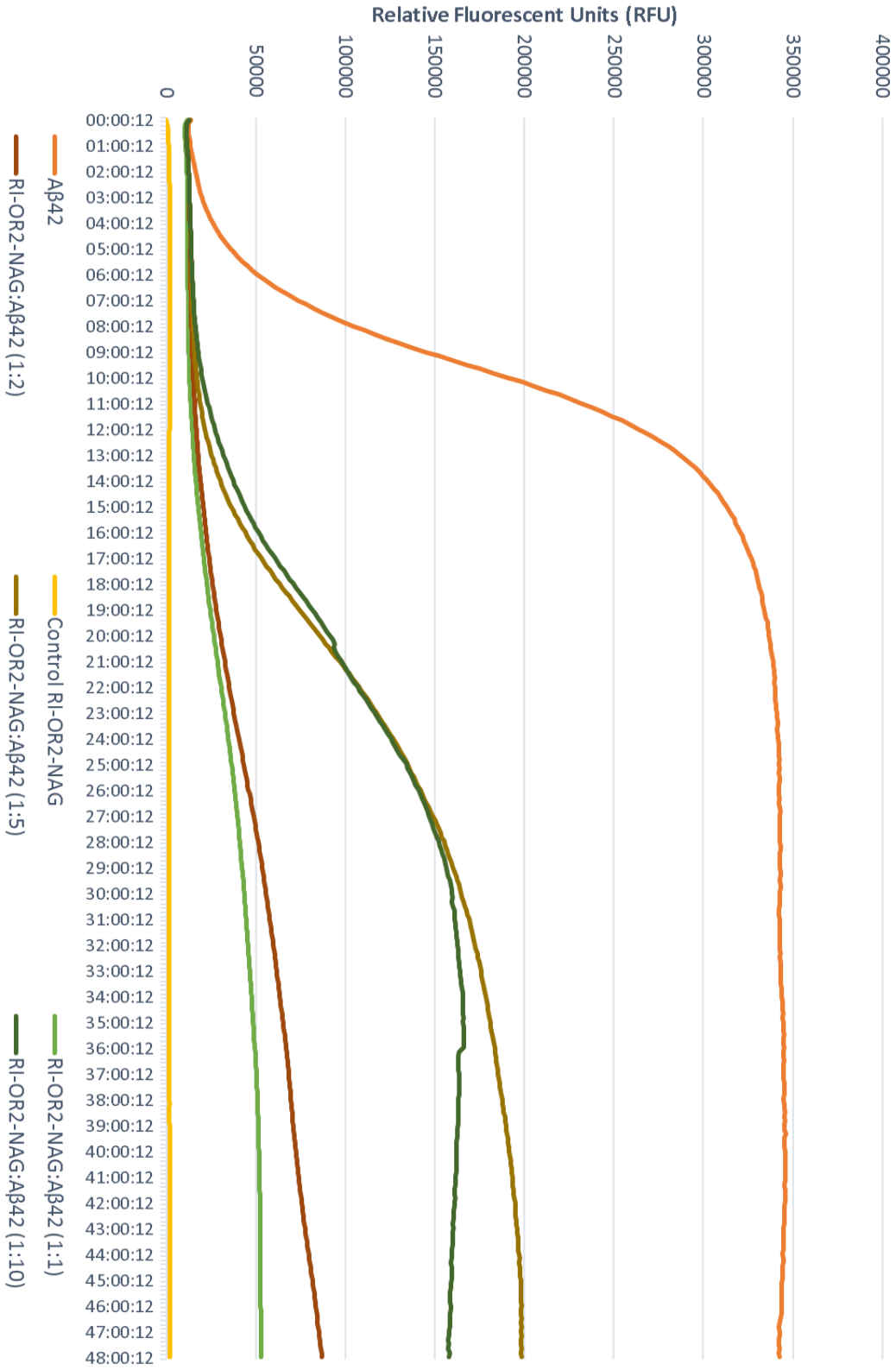

Figure 3.4. Macroscopic aggregation curve of Aβ with RI-OR2-NAG.

Graph demonstrating the lag phase (0 – 5 h), growth phase (6 – 23 h), plateau phase (24 – 48 h) of RI-OR2-NAG alone and synthetic Aβ42 alone or in the presence of RI-OR2-NAG peptide at different molar ratios.

Both peptides, RI-OR2-TAT and RI-OR2-NAG, when incubated alone, show no tendency to self-aggregate. When Aβ was incubated in the presence of each of these peptides, there was a decrease in the ThT fluorescence signal, indicating inhibition of Aβ aggregation. The maximum ThT fluorescence signal, representing the point where most of the monomeric peptide has been converted into mature fibrils, was observed at around 24 h of co-incubation between Aβ and each peptide.

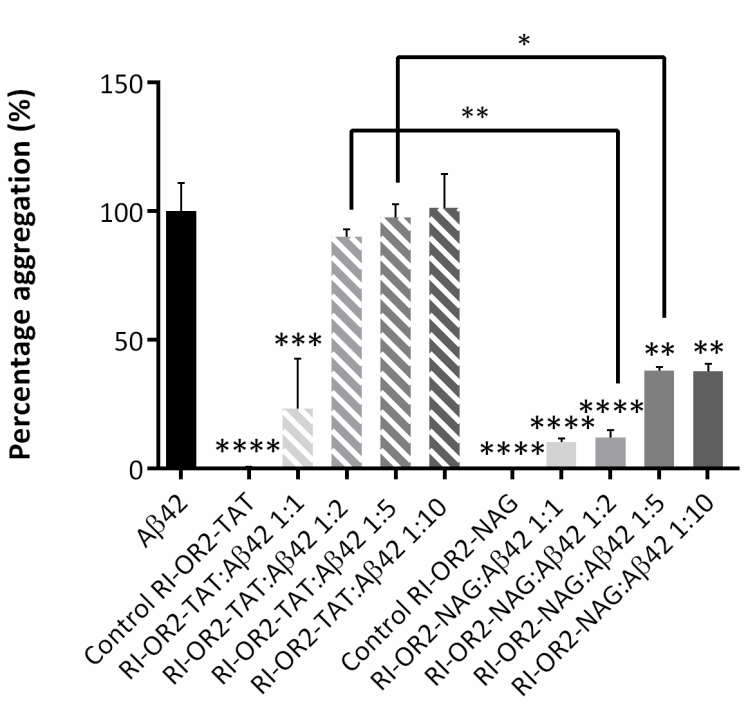

Figure 3.5. Inhibition of Aβ fibrils at 24 h by RI-OR2-TAT and RI-OR2-NAG peptides.

*Graph representing the data obtained from the ThT assay at 24 h of incubation of Aβ in the presence of RI-OR2-TAT and RI-OR2-NAG peptide inhibitors as percentage of aggregation (fluorescence signal of ThT-bound Aβ fibrils). The results are presented as mean ± SEM. * indicates p ≤ 0.05, ** indicates p ≤ 0.01, *** indicates p ≤ 0.001, **** indicates p ≤ 0.0001.*

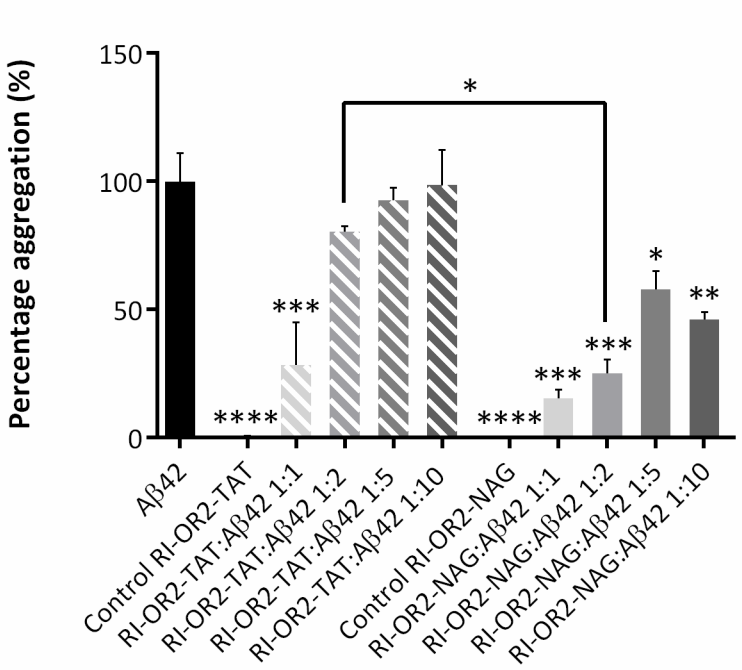

Figure 3.6. Inhibition of Aβ fibrils at 48 h by RI-OR2-TAT and RI-OR2-NAG peptides.

*Data obtained from the ThT assay at 48 h of incubation of Aβ in the presence of RI-OR2-TAT and RI-OR2-NAG peptide inhibitors are represented as percentage of aggregation (fluorescence signal of ThT-bound Aβ fibrils). The results are presented as mean ± SEM. * denotes p ≤ 0.05, ** denotes p ≤ 0.01, *** denotes p ≤ 0.001, **** denotes p ≤ 0.0001.*

The ThT assay results clearly show inhibition of mature Aβ fibril formation by the RI-OR2-NAG peptide. In the presence of RI-OR2-NAG at 1:1, 1:2, 1:5 and 1:10 molar ratios (inhibitor: Aβ), the aggregation of Aβ was significantly decreased at both 24 h and 48 h of co-incubation. More importantly, the novel RI-OR2-NAG peptide demonstrated a better inhibitory effect than the RI-OR2-TAT peptide, which has previously demonstrated inhibition of Aβ fibrilization at 1:1, 1:2, 1:4, and 1:10 molar ratios (Parthsarathy et al., 2013). This was further supported by comparing equimolar concentrations of the two inhibitory peptides. RI-OR2-NAG demonstrated better inhibition than RI-OR2-TAT at 1:2 and 1:5 molar ratios after 24 h of incubation, and at 1:2 molar ratio after 48 h of incubation.

3.3.2. RI-OR2-NAG peptide demonstrates no toxic effect on cells

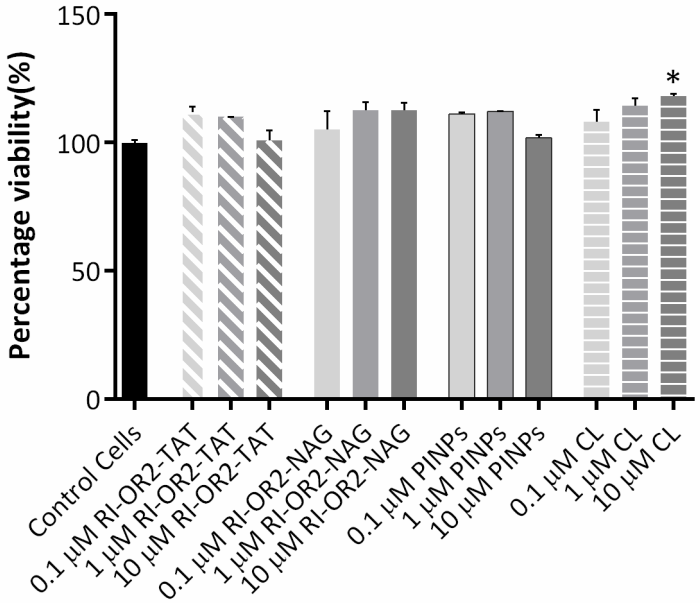

Figure 3.7. The effects of RI-OR2-TAT, RI-OR2-NAG, PINPs and CL on cell proliferation.

*Graph presenting the effect of the test peptides on the proliferation of SH-SY5Y cells following 24 h incubation, expressed as a percentage relative to control (untreated) cells. Cell proliferation was assessed using the MTS assay. The results are expressed as mean ± SEM. * indicates $p \leq 0.05$.*

Exposure to RI-OR2-TAT, RI-OR2-NAG, PINPs and CL alone for 24 h showed no toxic effect on SH-SY5Y cells. On the contrary, cells co-incubated with 10 µM CL demonstrated a significant increase in proliferation. Even though the rest of the data do not show any significant effect, they do suggest a concentration-dependent increase in cell proliferation, especially for CL, signifying a possible effect on stimulation of neurogenesis.

3.3.3. Flu-RI-OR2-NAG penetration into cultured SH-SY5Y neuroblastoma cells

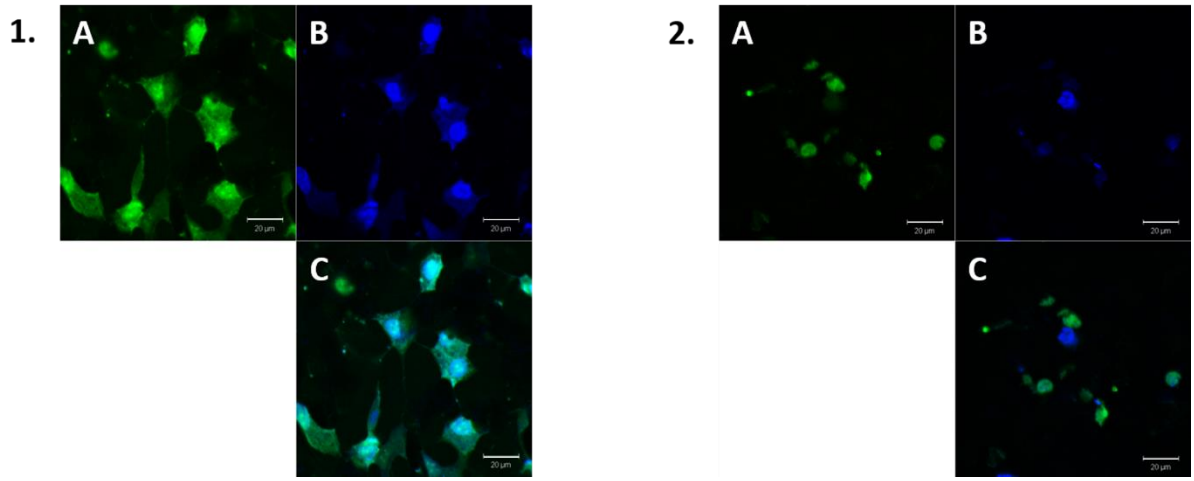

Figure 3.8. Flu-RI-OR2-TAT and Flu-RI-OR2-NAG cell penetration.

Demonstration of cell penetration of the fluorescent peptides Flu-RI-OR2-TAT and Flu-RI-OR2-NAG into cultured SH-SY5Y neuroblastoma cells. Image 1 demonstrates penetration of Flu-RI-OR2-TAT, whereas image 2 represents penetration of Flu-RI-OR2-NAG. A, Fluorescein (peptide) detection (488 nm); B, DAPI (cell nucleus) detection (405 nm); C, merged image of A and B. Scale bars = 20 µm.

Image acquisition of fluorescently labelled RI-OR2-TAT demonstrated penetration of the peptide inside the cultured cells at 1 h of incubation. Flu-RI-OR2-NAG, at 1 h of incubation, also penetrates inside the cells but not in their nuclei. The fluorescence is detected close to the cells' nuclei possibly in the cytoplasm.

3.4. Discussion

This Chapter presents preliminary studies on the development of a new Aβ aggregation inhibitor peptide as a potential treatment for AD, alongside previously studied peptides and PINPs (Gregori et al., 2017). These same inhibitors are examined further in the subsequent Chapters of this thesis.

3.4.1. Anti-aggregational properties of RI-OR2-NAG

Data obtained from the ThT aggregation assays demonstrate inhibition of Aβ fibrillization by both RI-OR2-TAT and RI-OR2-NAG (Figures 3.3., 3.4.). RI-OR2-TAT was

shown previously to be an effective inhibitor of Aβ aggregation at 1:1, 1:2, 1:4, and 1:10 molar ratios of peptide inhibitor to Aβ, after 48 h of co-incubation (Parthsarathy et al., 2013). In the experiments presented here, the results were analysed at 24 h and 48 h incubation when the elongation of Aβ into fibrils reached a maximum (end of growth phase and entrance to the plateau phase). At both 24 h and 48 h of co-incubation (Figures 3.5., 3.6.), RI-OR2-TAT inhibited Aβ aggregation when present at a 1:1 molar ratio, while RI-OR2-NAG inhibited aggregation at all ratios tested (i.e. at 1:1, 1:2, 1:5, 1:10 molar ratios). The difference between the results presented by Parthsarathy and colleagues and those presented here may be attributed to the use of different batches of Aβ peptide, and possibly variability resulting from slight differences in the preparation and de-seeding of the peptides. The Aβ peptide is notoriously variable and extremely sensitive, for example, to temperature, which influences its aggregation rate.

At 24 h of co-incubation (Figure 3.5.), the presence of RI-OR2-NAG resulted in a decrease of around 90% in fibril formation when incubated at 1:1 and 1:2 molar ratios of inhibitor to Aβ, and around 62% when incubated at 1:5 and 1:10 molar ratios. At 48 h of co-incubation (Figure 3.6.), the presence of RI-OR2-NAG resulted in 85% inhibition of fibril formation at 1:1 molar ratio, and 75% inhibition at 1:2 molar ratio. At 1:5 and 1:10 molar ratios, these values were deceased to 42% and 54% inhibition, respectively. Statistical comparison between equal concentrations of RI-OR2-TAT and RI-OR2-NAG showed that the RI-OR2-NAG peptide exhibits a better inhibitory effect than RI-OR2-TAT at 1:2 and 1:5 molar ratios of inhibitor to Aβ at 24 h incubation, and at 1:2 molar ratio at 48 h incubation.

In future studies, the effects of RI-OR2-NAG on early Aβ oligomer formation should also be examined. Examples of previously employed techniques for oligomer detection include the “double-antibody” approach using 6E10 – 6E10 (Yang et al., 2005; Ward et al., 2000), 4G8 – 4G8 (LeVine, 2004), and 3D6 – 3D6 (82E1 – 82E1) (Xia et a., 2009), based on the multiple epitopes available for these antibodies on multimeric/oligomeric Aβ. Parthsarathy and colleagues tested the RI-OR2-TAT peptide in a 6E10-6E10 sandwich immunoassay (Taylor et al., 2010), for its ability to

inhibit oligomeric forms of Aβ. RI-OR2-TAT induced a reduction in immunoassay signal at 2:1 and 1:1 molar ratios of inhibitor relative to Aβ42, at 4 h and 8 h of incubation, indicating inhibition of oligomer formation (Parthsarathy et al., 2013). A similar type of study could be employed in the case of RI-OR2-NAG.

3.4.2. The effect of RI-OR2-NAG on cultured neuroblastoma cells

Data from the MTS cytotoxicity assay indicate no toxic effect on SH-SY5Y neuroblastoma cells of any of the peptides (RI-OR2-TAT and RI-OR2-NAG) or nanoliposomes (PINPs and CL) under the conditions tested (Figure 3.7.). Similarly, the RI-OR2-TAT peptide has previously shown no toxic effect on cultured SH-SY5Y cells, as demonstrated by MTS and LDH assays, except when incubated at a higher concentration of 200 µM (Taylor et al., 2010).

Interestingly, the presence of 10 µM CL resulted in a significant 18% increase in cell viability (Figure 3.7.), which can be attributed to the control liposomes added to the cell culture medium. The presence of cholesterol and sphingomyelin in CL may have supplemented the lipid content of the medium, favouring the growth of the cells (Savonnière et al., 1996). Even though the other conditions did not demonstrate any significant effect, the data do show an increase in the viability of the cells when incubated with the peptides, including the RI-OR2-NAG peptide with its glucose derivative. This is an interesting observation because previous studies on APP/PS1 transgenic mice have shown that RI-OR2-TAT administration, at 100 nmoles/kg/once per day over 21 days, results in a substantially increased number of young nerve cells in the dentate gyrus (DG) of the hippocampus (Parthsarathy et al., 2013). It is possible that this peptide rescues the neuronal stem cells present in this region of the brain from the toxic effects of Aβ, but a directly stimulatory effect on the viability of these cells is also possible. One of the aims of this present study is to determine whether the peptide inhibitors can be detected *in vivo* in the DG of the mouse brain (Chapter 6).

3.4.3. Penetration of RI-OR2-NAG into cultured neuroblastoma cells

RI-OR2-TAT was previously assessed using cultured SH-SY5Y cells for its penetration properties. The fluorescence signal of the fluorescein-tagged peptide, Flu-RI-OR2-TAT, was detected inside cells following a 10 min incubation with 1 μM concentration of the peptide, in contrast with fluorescently-labelled RI-OR2 peptide which remained in the culture medium (Parthsarathy et al., 2013). Confocal imaging of cells exposed to Flu-RI-OR2-TAT and Flu-RI-OR2-NAG revealed a build up of fluorescence inside the cells following 1 h incubation with 1 μM of these peptides (Figure 3.8.). The RI-OR2-TAT fluorescence was observed throughout all cell compartments, whereas fluorescence from the RI-OR2-NAG peptide was detected in the cytoplasm, close to the nucleus of the cells. This is possibly explained by the location of the NAG transporters in the Golgi apparatus of the cells.

There was, however, a definite difference between the intracellular fluorescence intensity levels of the two peptides, with Flu-RI-OR2-TAT being more intense that Flu-RI-OR2-NAG. This could be due to different levels of fluorescence output from the peptides themselves or to slower diffusion of the RI-OR2-NAG peptide into the cells, via the glucose transporters located in the cell membrane. Further experiments would be required to investigate these possibilities, including staining of the Golgi apparatus inside the cells (Terasaki et al., 2001) to evaluate co-localisation of the RI-OR2-NAG peptide in this region of the cell, and time-course experiments to assess how the build up of fluorescence intensity varies with cell incubation time.

3.5. Conclusions

Understanding the pathological and molecular events that lead to the initiation of Aβ aggregation and its accumulation, is crucial for the development of effective treatments for AD. This Chapter presented three anti-aggregation peptides, with more focus on a novel peptide, RI-OR2-NAG, as possible treatments for the disease. Taking everything into consideration, the RI-OR2-NAG peptide appears to be a better inhibitor of Aβ aggregation than the RI-OR2-TAT peptide, as it induced better inhibitory properties at lower concentrations in the presence of Aβ. It also showed

no toxic effects on cultured cells. The data presented in this Chapter show encouraging results for future development of RI-OR2-NAG as a potential therapeutic agent for AD.

Chapter 4: Peptides Detection - Assay Development

4.1. Introduction

4.1.1. The importance of assay development

Determination of analyte concentration and distribution is a core and fundamental practice in the process of drug discovery and development. Various measurement systems and analytical methods can be designed to evaluate the effects of a target substance on processes of interest, including those at cellular, biochemical and molecular levels. These procedures allow the qualitative assessment or quantitative measurement of the investigative molecule in biological samples.

In this Chapter, the development and optimisation of peptide-specific assays is explored using both Luminex technology and conventional ELISA systems. The optimised assays were subsequently used for the quantitative estimation of Flu-RI-OR2-TAT, Flu-RI-OR2-NAG and BODIPY-PINPs in tissues collected from WT mice with C57/BL6 background. Data from the actual tissue-specific peptide detection are presented in Chapter 5.

4.1.2. Luminex Technology

The Luminex analyser utilises a combination of technologies, including flow cytometry, bead microspheres, lasers, avalanche photodiodes (APDs) and a photomultiplier tube, to deliver a multilateral platform for developing and performing sensitive and specific immunoassays.

Based on uniquely identifiable microsphere bead sets, the Luminex system allows detection of target analytes in samples. Currently there are 100 bead sets available, with each set being internally dyed with red and infrared fluorophores of varying intensities. This precise colour code system provides a unique characteristic or 'spectral signature' for each bead set, for its specific identification. Thus, monoplex and multiplex assays can be performed using the Luminex system, which offers simultaneous detection of up to 100 analytes in a single well or reaction.

There are two inbuilt lasers in the Luminex analyser; a red laser which excites the internal classification dyes of the beads at a wavelength of 635 nm, and a green laser which excites a reporter molecule attached on the surface of the beads, via the biological molecule, at a wavelength of 532 nm. The fluorescent intensity emitted by the coded beads is then measured by the APDs, which identify and classify the bead set. The emission intensity of the reporter molecule is measured by the photomultiplier tube, determining the level of analyte captured onto the microspheres and generating a quantifiable measurement. In these assays, biotinylated detection antibodies and 4 µg/ml of STREP-RPE were used as the detection - reporter system (refer to Figure 2.2.).

4.1.3. The reporter system

STREP is a bacterial-derived protein with extremely high affinity for binding to biotin (Green, 1975). The crystal structure of the two bound molecules was first reported in 1989 by Hendrickson and colleagues (Hendrickson et al., 1989) and Weber and colleagues (Weber et al., 1989). Due to the remarkably strong non-covalent interaction of these two molecules, this complex is extensively used in science. RPE, on the other hand, is an intensely bright phycobiliprotein derived from red algae (Ficner and Huber, 1993), with absorption maxima at 496, 546 and 565 nm, and fluorescence emission maximum at 578 nm.

By applying a biotinylated antibody as detection, RPE and other labelled streptavidin complexes have been widely used as a detection - reporter system to localise antigens on cells and tissues, and to detect biomolecules in immunoassays.

4.1.4. Luminex-bead sandwich immunoassay

For the purposes of this project, Luminex-bead sandwich immunoassays were developed for each peptide. The analytes of interest, in this case the fluorescently-labelled peptides, were captured using analyte-specific antibodies conjugated on a particular bead set. The captured analytes were then detected by employing biotinylated antibodies specific to each peptide. STREP-RPE (reporter molecule) was

added to the mixture to determine the level of analyte bound to the bead-antibody reaction.

4.2. Methods

4.2.1. Flu-RI-OR2-TAT peptide Luminex assay development

A Luminex assay for detection of the RI-OR2-TAT peptide was developed by utilising the 'TAT' sequence of the peptide and the fluorescein molecule attached to the peptide as epitope recognition sites. For the optimisation of the Flu-RI-OR2-TAT detection assay, 1, 2, and 3 μg/ml of anti-HIV1 tat [N3] primary antibody were coupled to the beads. For detection, 0.5, 1 and 2 μg/ml of anti-fluorescein (biotin) secondary antibody were used. STREP-RPE at 4 μg/ml was added as the reporter molecule. A range of peptide concentrations (244 pM to 1 μM, and a blank control) diluted in HB were tested and the intensities and signal to noise ratios for each capture and detection combination were compared.

4.2.2. Flu-RI-OR2-NAG peptide Luminex assay development

Similar to the development of the Flu-RI-OR2-TAT Luminex assay, the Flu-RI-OR2-NAG assay was generated by exploiting the 'NAG' sequence on the peptide and the fluorescein molecule attached. In order to develop an assay for detection of the Flu-RI-OR2-NAG peptide, three different primary antibodies were coupled to the surface of the Luminex beads, at concentrations of 1, 2, 3 μg/ml. The captured peptide was detected using anti-fluorescein (biotin) secondary antibody concentrations of 0.125, 0.25, 0.5, 1, 2 μg/ml, followed by the 4 μg/ml STREP-RPE reporter system. Flu-RI-OR2-NAG peptide concentrations diluted in HB ranging from 1.95 nM to 1 μM, and a blank control, were tested in the antibody titration experiments, and the signal to noise ratios of each antibody combination were compared.

4.2.3. BODIPY-PINPs peptide ELISA assay development

An ELISA assay was developed for detection of PINPs. Two biotinylated antibodies were tested as candidate detection components: anti-polyethylene glycol [PEG-B-47b] (biotin) (rabbit monoclonal) antibody at concentrations of 0.5, 1, and 2 μg/ml;

and anti-polyethylene glycol [PEG-2-128] (rabbit monoclonal) antibody at 0.5, 1, 2, and 5 μg/ml. In each case, anti-HIV1 tat [N3] antibody was employed as the capture antibody, at concentrations of 1, 2, and 3 μg/ml (similar to those employed for the Flu-RI-OR2-TAT Luminex assay). Bee venom-treated BODIPY-PINPs were added at a concentration range of 15.63 nM to 1 μM, diluted in HB, along with blank controls.

4.2.4. Signal to noise ratio

The developed assays for the three peptides were analysed based on the S/N ratio which is defined as the ratio of MFI (Median Fluorescent Intensity) signal power to the background signal. The data obtained from the S/N ratio are plotted against each peptide concentration examined, and are also presented in tables in this Chapter's Results Section (Section 4.3.).

4.3. Results

4.3.1. Flu-RI-OR2-TAT peptide Luminex assay development

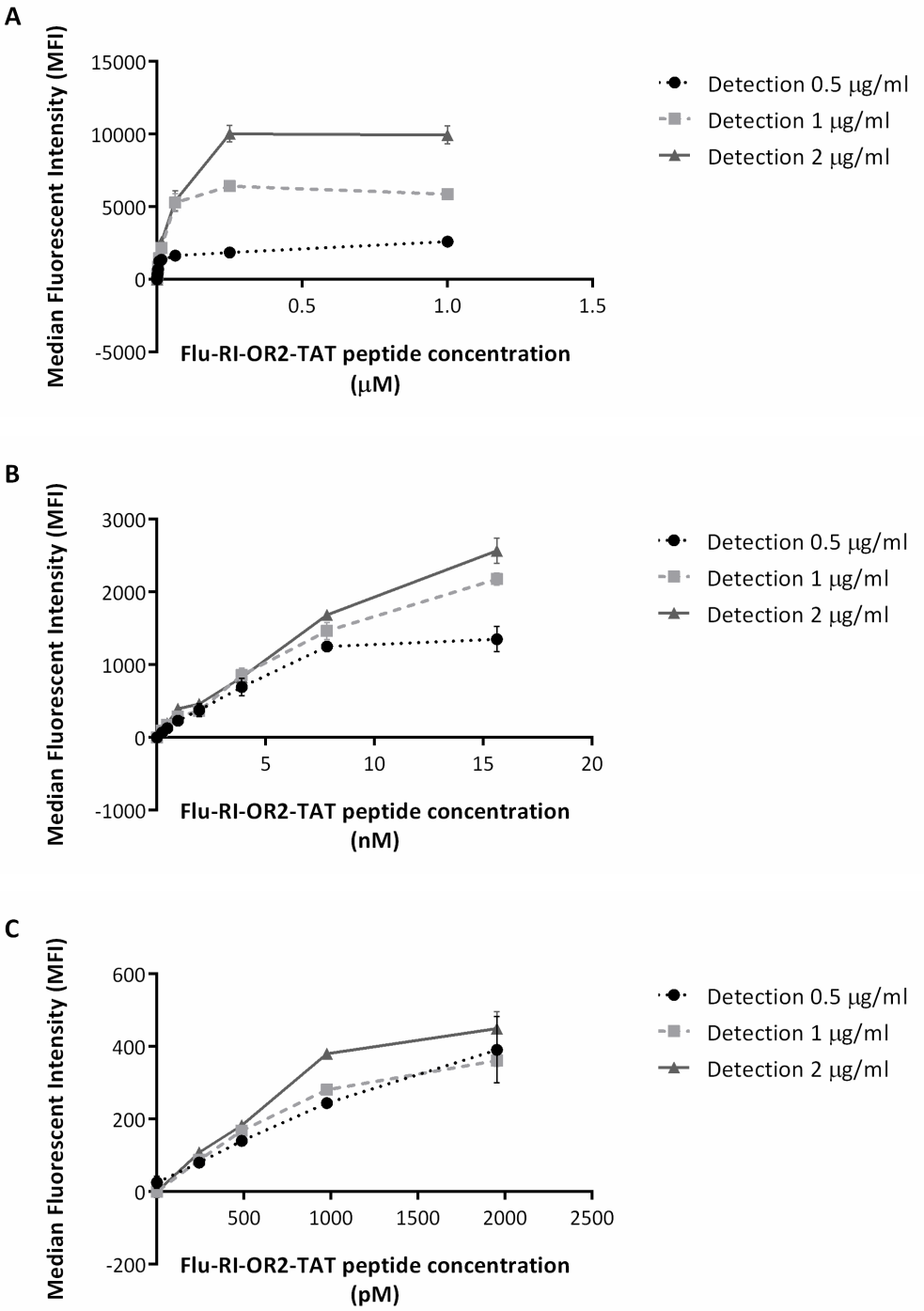

Figure 4.1. Flu-RI-OR2-TAT Luminex assay optimisation – Coupling 1 µg/ml.

Luminex beads coupled with 1 µg/ml anti-HIV1 tat [N3] antibody were reacted with HB blank controls and Flu-RI-OR2-TAT concentration ranges: (A) 244 pM to 1 µM, (B) 244 pM to 15.63 nM, and (C) 244 pM to 1953 pM. Biotinylated detection anti-fluorescein (biotin) antibody of 0.5, 1, and 2 µg/ml and 4 µg/ml STREP-RPE were used as the detection – reporter

system for the assay. The figure presents the mean ± SEM (n = 3) of median fluorescent intensity (MFI) signal.

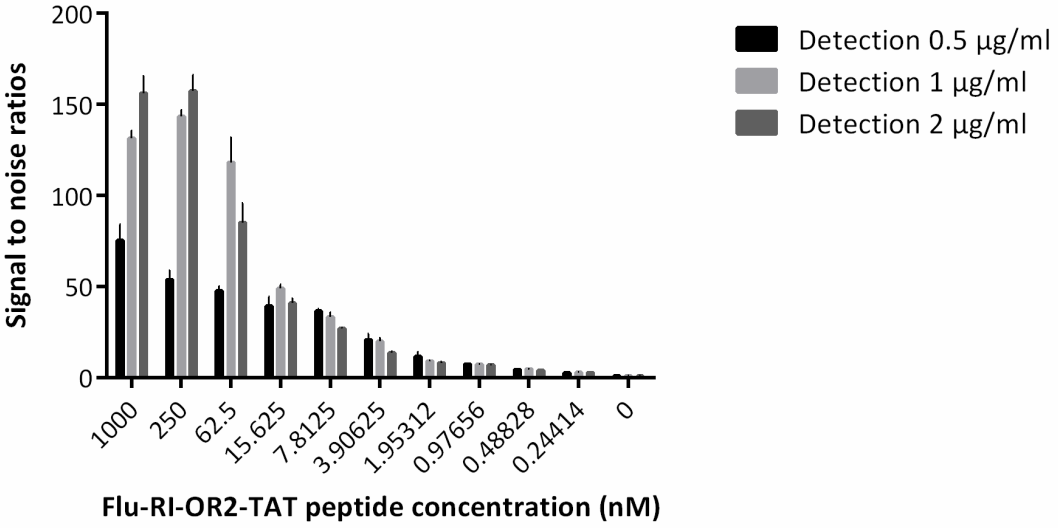

Figure 4.2. Signal to noise ratios of Flu-RI-OR2-TAT assay optimisation – Coupling 1 µg/ml.

The figure presents the signal to noise ratios of the MFI values obtained from the antibody titrations for development of the Flu-RI-OR2-TAT Luminex assay. Luminex beads coupled with 1 µg/ml anti-HIV1 tat [N3] antibody were reacted with HB blank controls and Flu-RI-OR2-TAT peptide (244 pM to 1 µM). Biotinylated detection anti-fluorescein (biotin) antibody at 0.5, 1, and 2 µg/ml and 4 µg/ml STREP-RPE were used as detection – reporter system for the assay. The figure represents the mean ± SEM (n = 3) of MFI signals obtained for the antibody concentrations.

Flu-RI-OR2-TAT	Detection antibody (µg/ml)		
(nM)	***0.5***	***1***	***2***
1000	75.39	131.35	156.16
250	53.99	143.33	157.42
62.5	47.89	118.23	85.33
15.63	39.59	49.31	41.07
7.81	36.80	33.46	27.32
3.91	20.85	20.04	13.95
1.95	11.79	9.19	8.22
0.98	7.59	7.40	7.14
0.49	4.63	4.91	4.05
0.24	2.92	3.12	2.89
0	1	1	1

Table 4.1. Flu-RI-OR2-TAT signal to noise raw MFI values – Coupling 1 µg/ml.

Table presenting the raw MFI values of the signal to noise ratio results of 1 µg/ml anti-HIV1 tat [N3] antibody coupled to Luminex microspheres and detected with 0.5, 1, and 2 µg/ml of anti-fluorescein (biotin) antibody, as demonstrated in Figure 4.2.

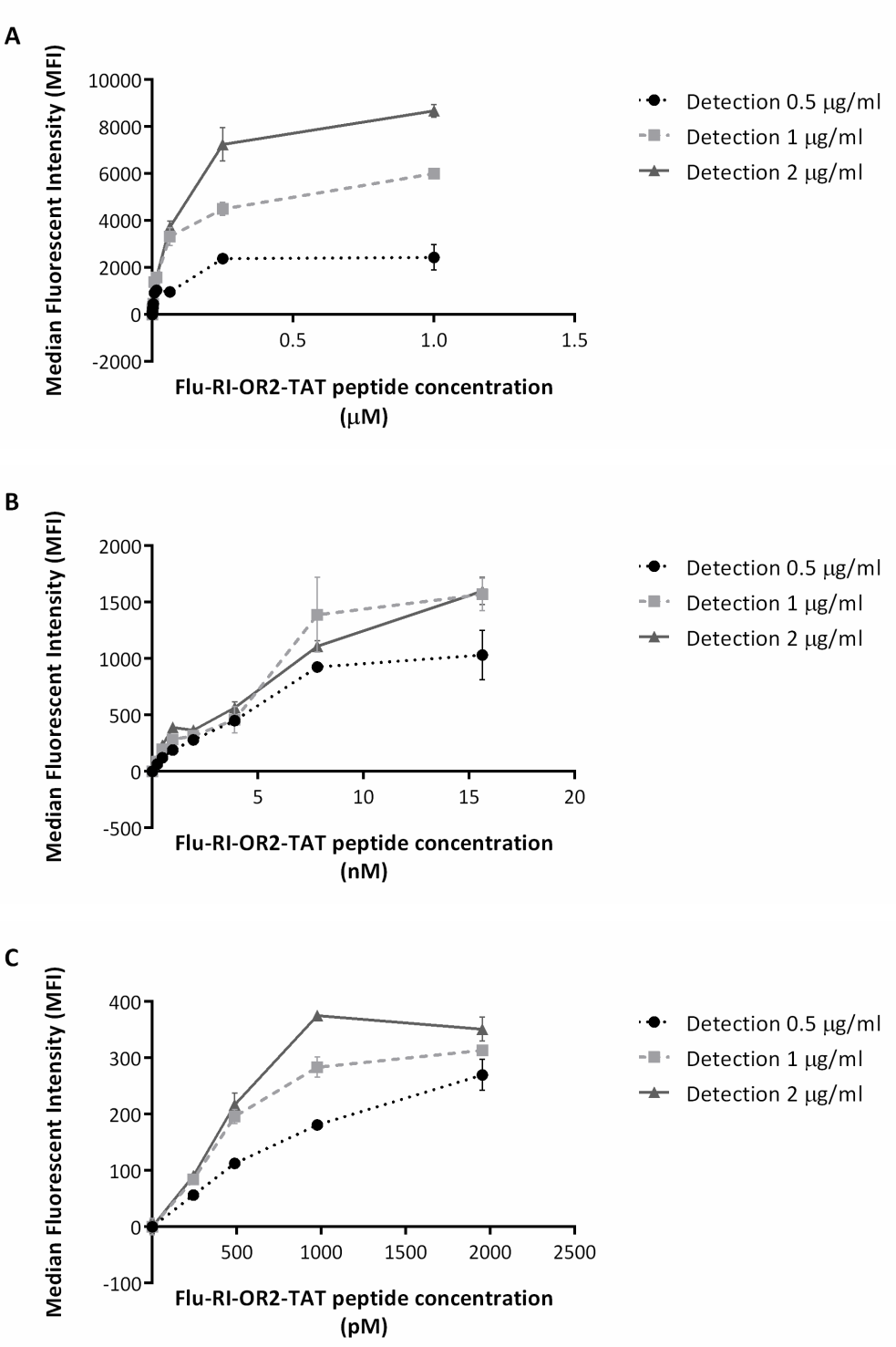

Figure 4.3. Flu-RI-OR2-TAT Luminex assay optimisation – Coupling 2 µg/ml.

Luminex beads coupled with 2 µg/ml anti-HIV1 tat [N3] antibody were reacted with HB blank controls and Flu-RI-OR2-TAT concentration ranges: (A) 244 pM to 1 µM, (B) 244 pM to 15.63 nM, and (C) 244 pM to 1953 pM. Biotinylated detection anti-fluorescein (biotin) antibody of 0.5, 1, and 2 µg/ml and 4 µg/ml STREP-RPE were used as the detection – reporter

system for the assay. The figure presents the mean ± SEM (n = 3) of median fluorescent intensity (MFI) signal.

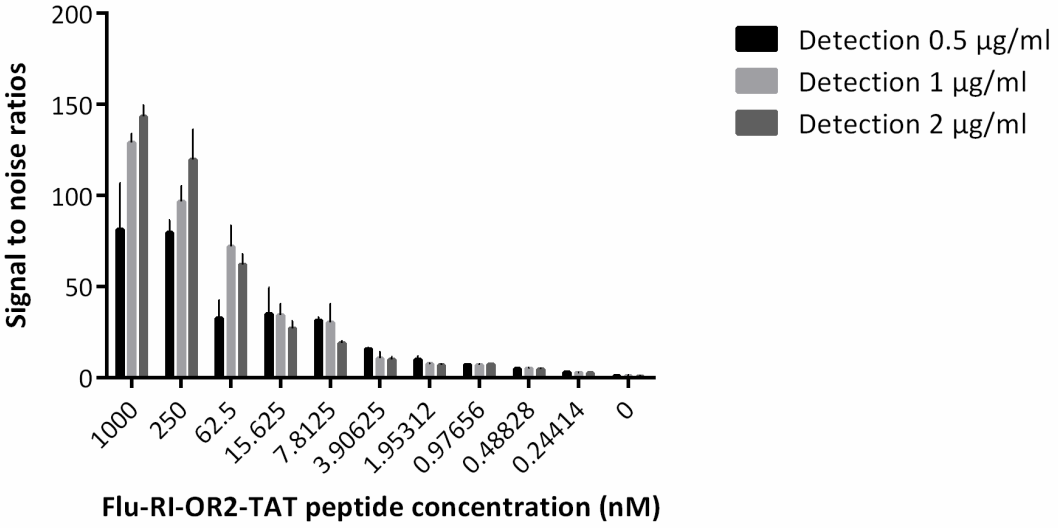

Figure 4.4. Signal to noise ratios of Flu-RI-OR2-TAT assay optimisation – Coupling 2 µg/ml. *The figure presents the signal to noise ratios of the MFI values obtained from the antibodies titration for the development of the Flu-RI-OR2-TAT Luminex assay. Luminex beads coupled with 2 µg/ml anti-HIV1 tat [N3] antibody were reacted with HB Blank controls and Flu-RI-OR2-TAT peptide (244 pM to 1 µM). Biotinylated detection anti-Fluorescein (Biotin) antibody of 0.5, 1, and 2 µg/ml and 4 µg/ml STREP-RPE were used as detection – reporter system for the assay. The figure represents the mean ± SEM (n = 3) of MFI signals.*

Flu-RI-OR2-TAT	Detection antibody (µg/ml)		
(nM)	***0.5***	***1***	***2***
1000	81.38	129.18	143.45
250	79.73	96.95	119.93
62.5	32.82	72.08	62.18
15.63	35.03	34.52	27.24
7.81	31.53	30.64	19.20
3.91	15.87	10.79	10.30
1.95	10.22	7.73	7.01
0.98	7.29	7.09	7.41
0.49	5.04	5.22	4.81
0.24	3.18	2.84	2.74
0	1	1	1

Table 4.2. Flu-RI-OR2-TAT signal to noise raw MFI values – Coupling 2 µg/ml.

Table representing the raw MFI values of the signal to noise ratio results of 2 µg/ml anti-HIV1 tat [N3] antibody coupled to Luminex beads and detected with 05, 1, and 2 µg/ml of anti-Fluorescein (Biotin) antibody as demonstrated in Figure 4.4.

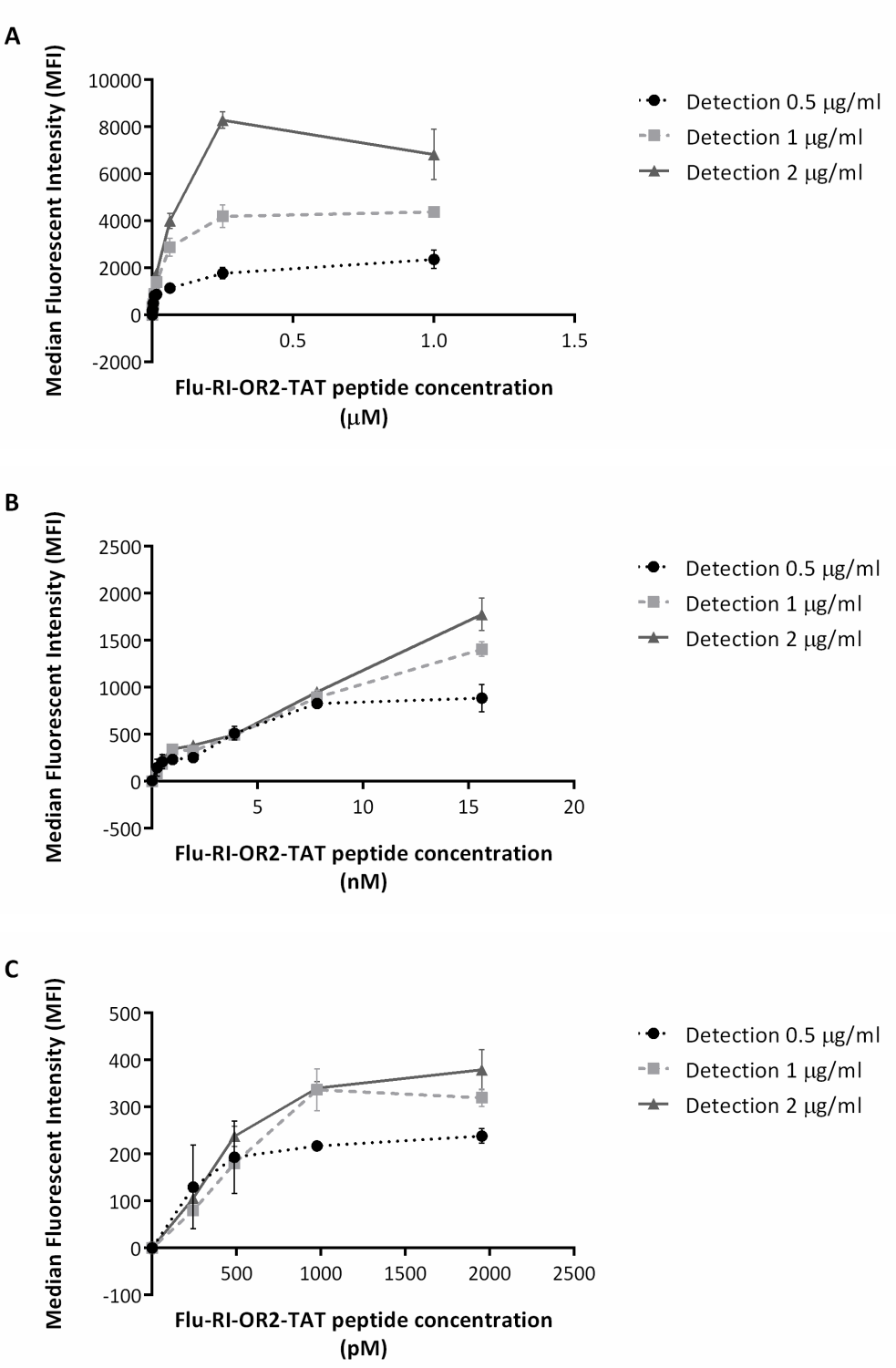

Figure 4.5. Flu-RI-OR2-TAT Luminex assay optimisation – Coupling 3 µg/ml.

Luminex beads coupled with 3 µg/ml anti-HIV1 tat [N3] antibody were reacted with HB blank controls and Flu-RI-OR2-TAT concentration ranges: (A) 244 pM to 1 µM, (B) 244 pM to 15.63 nM, and (C) 244 pM to 1953 pM. Biotinylated detection anti-fluorescein (biotin) antibody of 0.5, 1, and 2 µg/ml and 4 µg/ml STREP-RPE were used as the detection – reporter

system for the assay. The figure presents the mean ± SEM (n = 3) of median fluorescent intensity (MFI) signal.

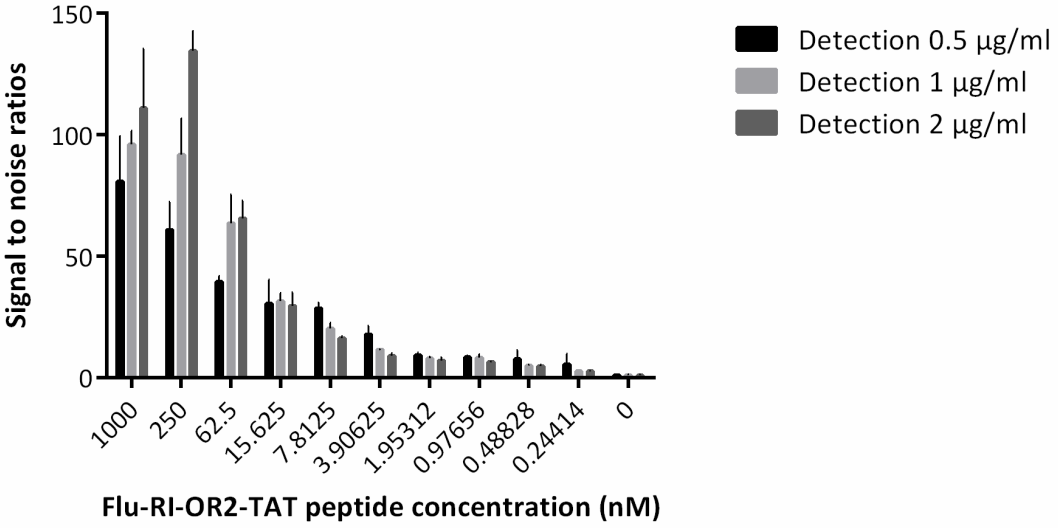

Figure 4.6. Signal to noise ratios of Flu-RI-OR2-TAT assay optimisation – Coupling 3 µg/ml. *The figure represents the signal to noise ratios of the MFI values obtained from the antibodies titration for the development of the Flu-RI-OR2-TAT Luminex assay. Luminex beads coupled with 3 µg/ml anti-HIV1 tat [N3] antibody were reacted with HB Blank controls and Flu-RI-OR2-TAT peptide (244 pM to 1 µM). Biotinylated detection anti-Fluorescein (Biotin) antibody of 0.5, 1, and 2 µg/ml and 4 µg/ml STREP-RPE were used as detection – reporter system for the assay. The figure represents the mean ± SEM (n = 3) of MFI signals.*

Flu-RI-OR2-TAT	Detection antibody (µg/ml)		
(nM)	***0.5***	***1***	***2***
1000	80.97	96.18	111.05
250	60.88	91.97	134.66
62.5	39.63	63.65	65.66
15.63	30.67	31.53	29.63
7.81	28.73	20.39	16.34
3.91	17.97	11.72	9.00
1.95	9.32	8.04	7.19
0.98	8.61	8.41	6.56
0.49	7.80	5.02	4.90
0.24	5.65	2.84	2.78
0	1	1	1

Table 4.3. Flu-RI-OR2-TAT signal to noise raw MFI values – Coupling 3 µg/ml.

Table showing the raw MFI values of the signal to noise ratio results of 3 µg/ml anti-HIV1 tat [N3] antibody coupled to Luminex microspheres and detected with 0.5, 1 and 2 µg/ml of anti-fluorescein antibody, as demonstrated in Figure 4.6.

Analysis of the measured MFI signals of the Flu-RI-OR2-TAT antibody titration experiments involving nine different combinations of capture (anti-HIV1 tat [N3]) and detection (anti-fluorescein (biotin)) antibodies, revealed that Luminex beads coated with 1 µg/ml of capture antibody and detected using 2 µg/ml of biotinylated secondary antibody (Figure 4.1.) gave the best signal to noise ratios (Figure 4.2., Table 4.1.) and sensitivity of peptide detection. This antibody combination was used to investigate the distribution of the Flu-RI-OR2-TAT peptide in various mouse tissues, following acute i.p. dosing of the WT mice in Chapter 5, Section 5.3.1.

4.3.2. Flu-RI-OR2-NAG peptide Luminex assay development

4.3.2.1. Bead coupling using the anti-O-linked N-acetylglucosamine [RL2] antibody

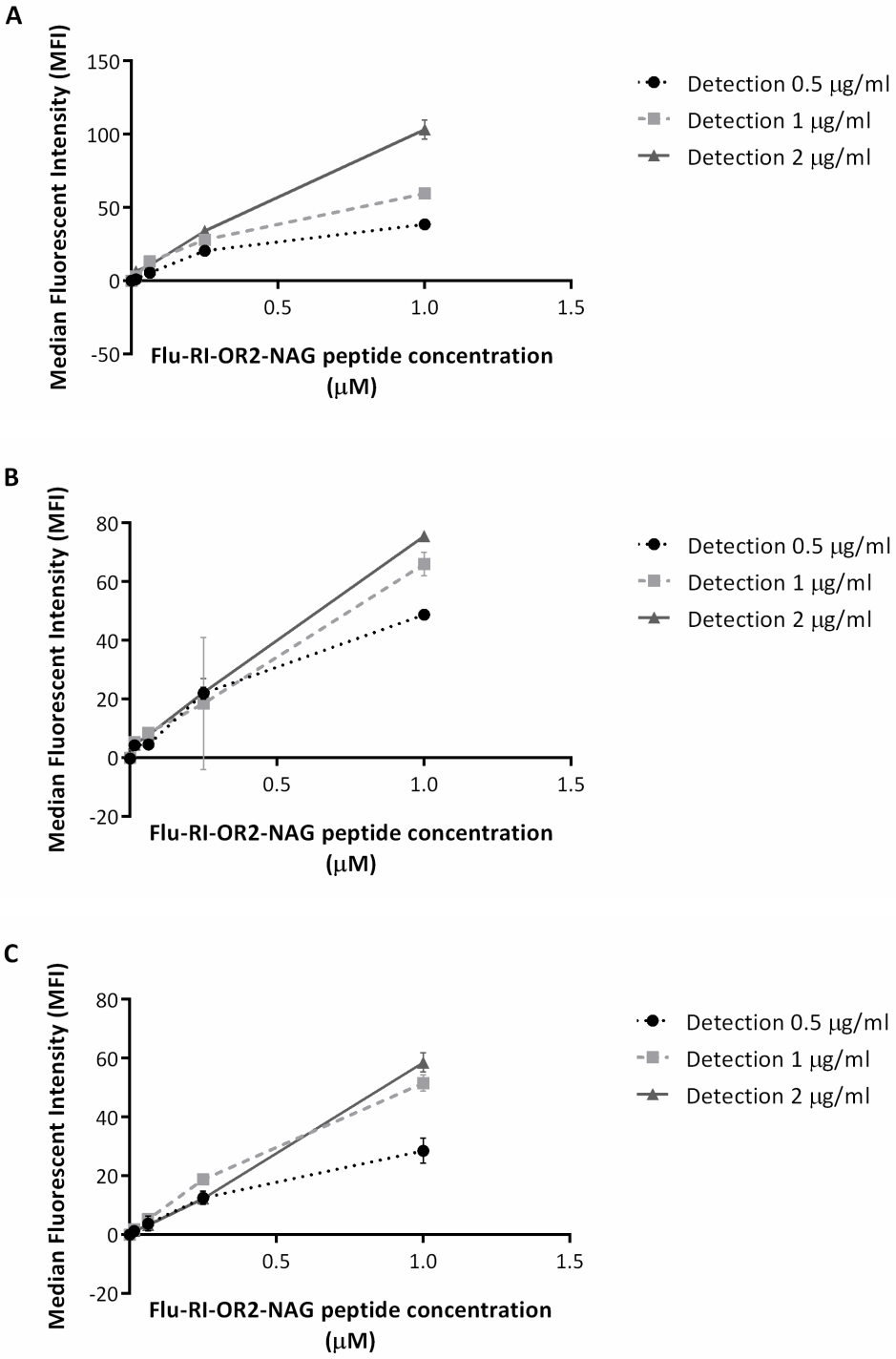

Figure 4.7. Anti-O-linked N-acetylglucosamine [RL2] antibody titration.

Luminex microspheres coupled with (A) 1 µg/ml, (B) 2 µg/ml and (C) 3 µg/ml of anti-O-linked N-acetylglucosamine [RL2] antibody were reacted with HB blank controls and Flu-RI-OR2-NAG peptide concentrations ranging from 15.63 nM to 1 µM. Biotinylated detection using the anti-fluorescein (biotin) antibody at 0.5, 1, and 2 µg/ml and 4 µg/ml STREP-RPE reporter were

used as the detection – reporter system for the assay. The figure represents the mean ± SEM (n = 3) of MFI signals obtained at these antibody concentrations.

The MFI signals detected using the anti-O-linked N-acetyglucosamine [RL2] antibody as coupling molecule and the anti-Fluorescein (Biotin) antibody as detection molecule did not generate very high MFI signals in any of the combinations tested compared to the Flu-RI-OR2-TAT assay. Thus, alternative coupling antibodies were considered.

4.3.2.2. Bead coupling using the anti-O-GlcNAc RL2 (mouse monoclonal) antibody

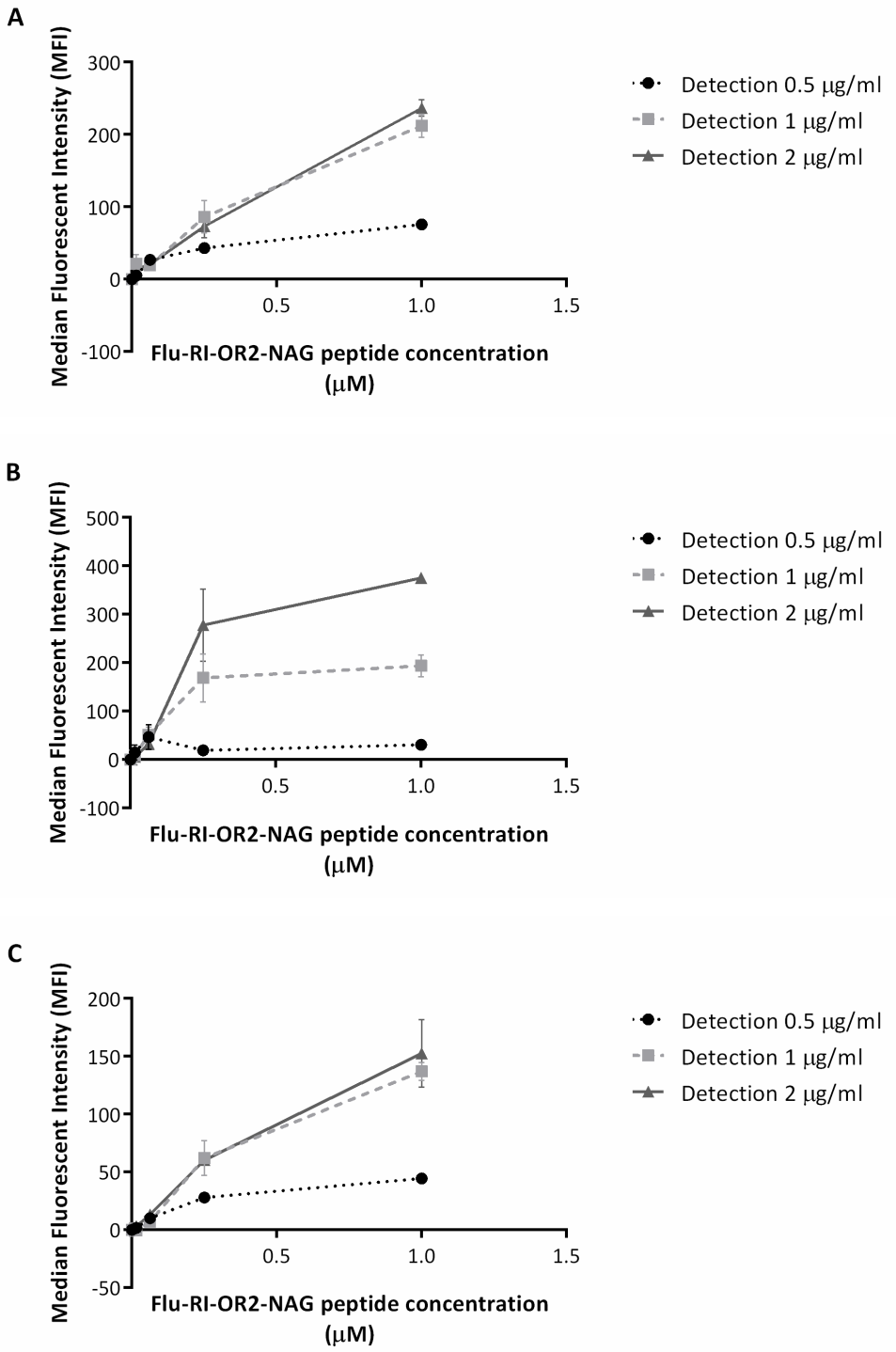

Figure 4.8. Anti-O-GlcNAc RL2 (mouse monoclonal) antibody titration.

Luminex beads coupled with (A) 1 µg/ml, (B) 2 µg/ml and (C) 3 µg/ml of anti-O-GlcNAc RL2 (mouse monoclonal) antibody were reacted with HB blank controls and Flu-RI-OR2-NAG peptide concentrations ranging from 15.63 nM to 1 µM. Biotinylated detection using the anti-fluorescein (biotin) antibody at 0.5, 1, and 2 µg/ml and 4 µg/ml STREP-RPE reporter molecule

were used as the detection – reporter system for the assay. The figure represents the mean ± SEM (n = 3) of MFI signals obtained for these antibody combinations.

The MFI signals detected using the anti-O-GlcNAc RL2 (mouse monoclonal) antibody as coupling molecule were improved compared to the signals observed using the anti-O-Linked N-Acetylglucosamine [RL2] antibody. However, the MFI signals generated in this assay are not as high as in the assay developed for detection of the Flu-RI-OR2-TAT assay.

4.3.2.3. Bead coupling using the anti-O-GlcNAc CTD110.6 (mouse monoclonal) antibody

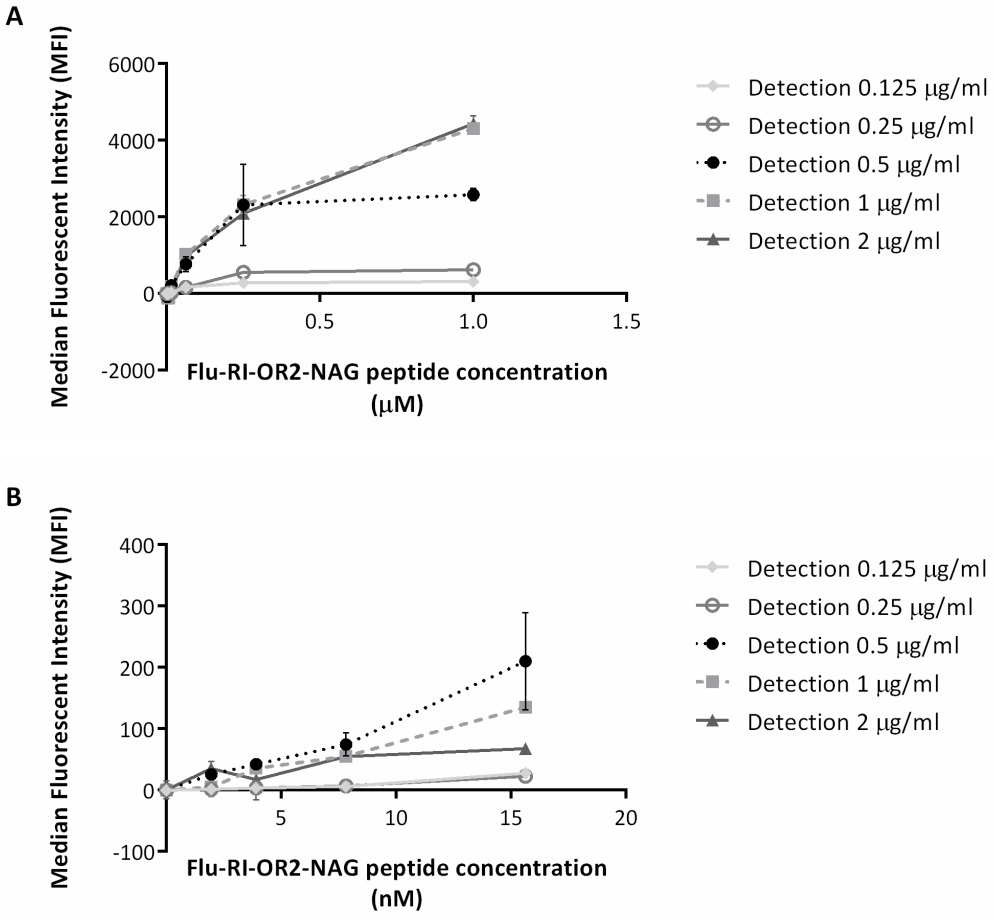

Figure 4.9. Anti-O-GlcNAc CTD110.6 (mouse monoclonal) antibody – Coupling 1 µg/ml.

Luminex beads coupled with 1 µg/ml of anti-O-GlcNAc CTD110.6 (mouse monoclonal) antibody were reacted with HB blank controls and Flu-RI-OR2-NAG concentration ranges (A) 1.95 nM to 1 µM and (B) 1.95 nM to 15.63 nM. Biotinylated detection anti-fluorescein (biotin) antibody of 0.125, 0.25, 0.5, 1, and 2 µg/ml and 4 µg/ml STREP-RPE were used as detection –

reporter system for the assay. The figure represents the mean ± SEM (n = 3) of MFI signals obtained for these antibody concentrations.

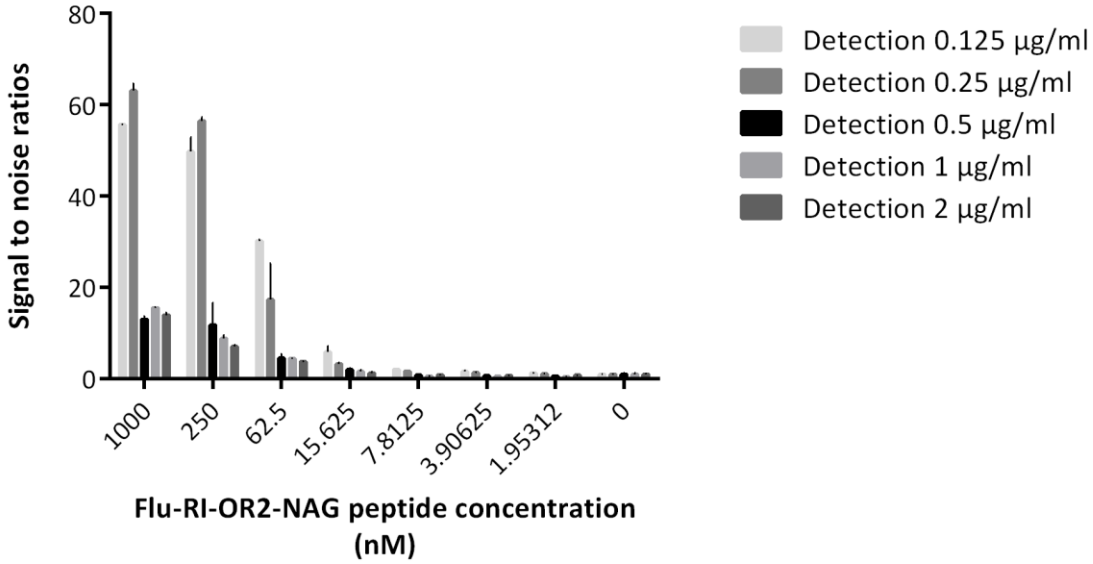

Figure 4.10. Signal to noise ratios of Flu-RI-OR2-NAG assay optimisation – Coupling 1 µg/ml.

The figure represents the signal to noise ratios of the MFI values obtained from the antibodies titration for the development of the Flu-RI-OR2-NAG Luminex assay. Luminex beads coupled with 1 µg/ml anti-O-GlcNAc CTD110.6 (mouse monoclonal) antibody were reacted with HB Blank controls and Flu-RI-OR2-NAG peptide (1.95 nM to 1 µM). Biotinylated detection anti-Fluorescein (Biotin) antibody of 0.125, 0.25, 0.5, 1, and 2 µg/ml and 4 µg/ml STREP-RPE reporter molecule were used as detection – reporter system for the assay. The figure represents the mean ± SEM (n = 3) of MFI signals.

Flu-RI-OR2-NAG (nM)	**Detection antibody (µg/ml)**				
	0.125	***0.25***	***0.5***	***1***	***2***
1000	55.70	63.08	13.01	15.59	13.99
250	49.74	56.53	11.78	8.86	7.13
62.5	30.26	17.40	4.57	4.47	3.87
15.63	5.87	3.28	2.01	1.63	1.32
7.81	2.09	1.70	0.85	0.65	0.87
3.91	1.65	1.35	0.70	0.58	0.76
1.95	1.30	1.13	0.62	0.48	0.82
0	1	1	1	1	1

Table 4.4. Flu-RI-OR2-NAG signal to noise raw MFI values – Coupling 1 µg/ml.

Table showing the raw MFI values of the signal to noise ratio results for 1 µg/ml anti-O-GlcNAc CTD110.6 (mouse monoclonal) antibody coupled to Luminex bead and detected by 0.125, 0.25, 0.5, 1 and 2 µg/ml of anti-fluorescein (biotin) antibody, as demonstrated in Figure 4.10.

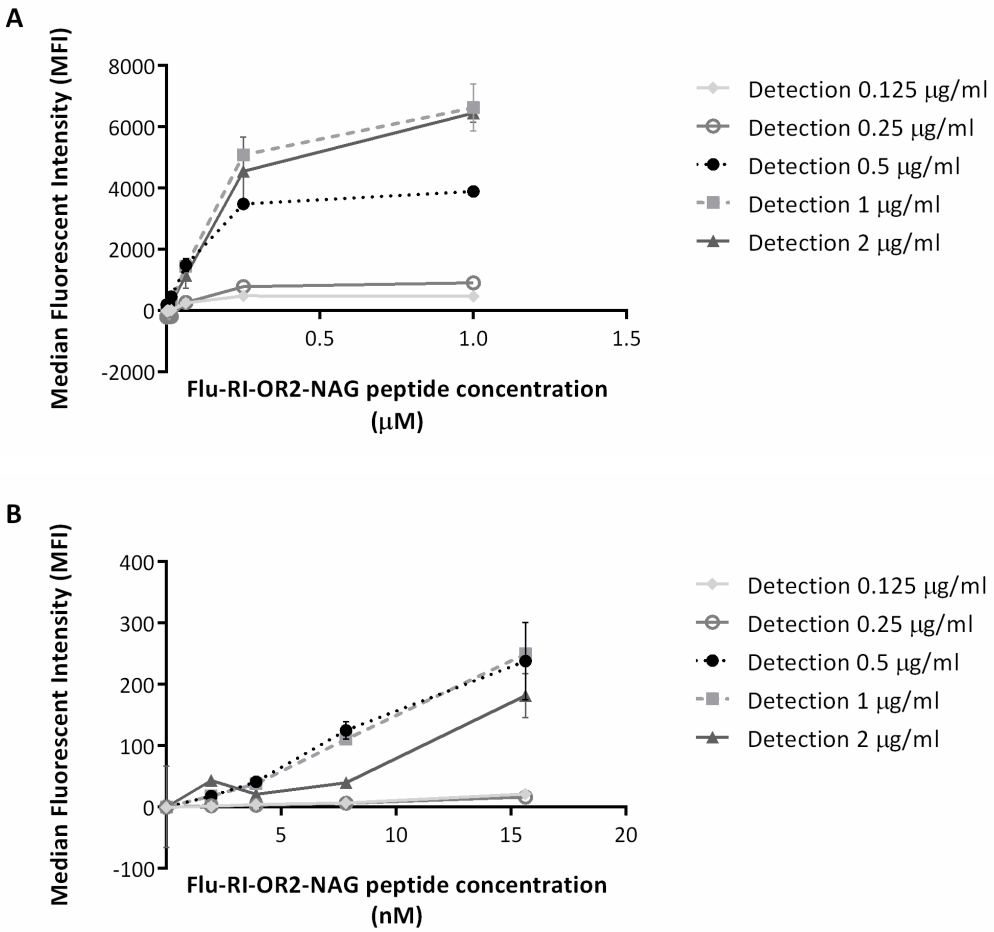

Figure 4.11. Anti-O-GlcNAc CTD110.6 (mouse monoclonal) antibody – Coupling 2 µg/ml.

Luminex beads coupled with 2 µg/ml of anti-O-GlcNAc CTD110.6 (mouse monoclonal) antibody were reacted with HB blank controls and Flu-RI-OR2-NAG concentration ranges (A) 1.95 nM to 1 µM and (B) 1.95 nM to 15.63 nM. Biotinylated anti-fluorescein antibody at 0.125, 0.25, 0.5, 1, and 2 µg/ml and 4 µg/ml STREP-RPE were used as detection – reporter system for the assay. The figure represents the mean ± SEM (n = 3) of the MFI signals.

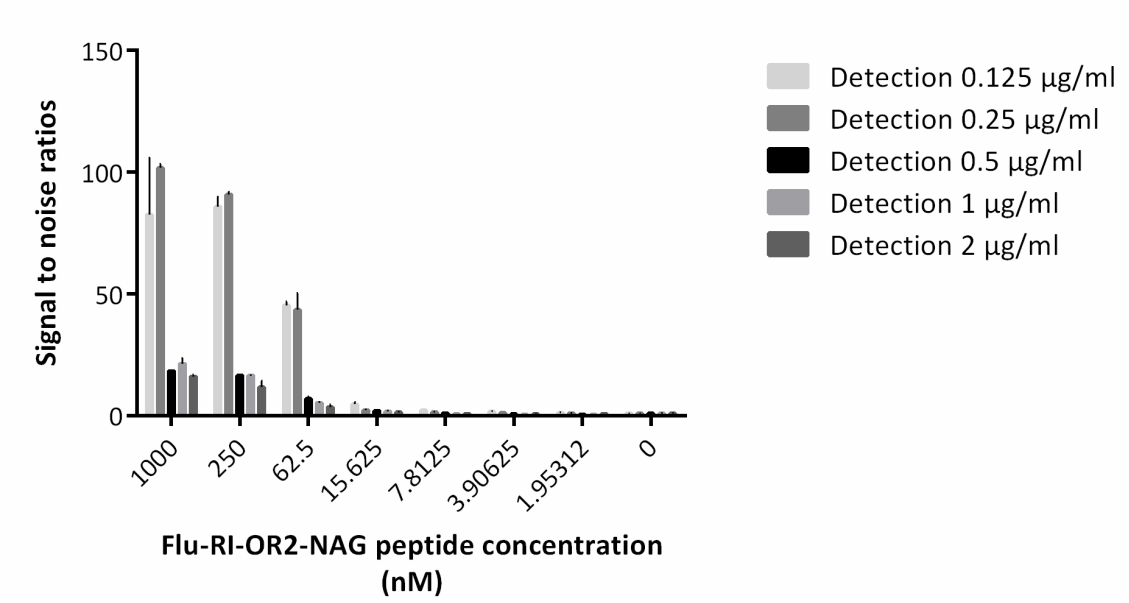

Figure 4.12. Signal to noise ratios of Flu-RI-OR2-NAG assay optimisation – Coupling 2 µg/ml.

The figure shows the signal to noise ratios of the MFI values obtained from the antibodies titration for the development of the Flu-RI-OR2-NAG Luminex assay. Luminex beads coupled with 2 µg/ml anti-O-GlcNAc CTD110.6 (mouse monoclonal) antibody were reacted with HB Blank controls and Flu-RI-OR2-NAG peptide (1.95 nM to 1 µM). Detection with biotinylated anti-Fluorescein antibody of 0.125, 0.25, 0.5, 1, and 2 µg/ml, and 4 µg/ml STREP-RPE reporter molecule were used as detection – reporter system for the assay. The figure represents the mean ± SEM (n = 3) of MFI signals.

Flu-RI-OR2-NAG (nM)	**Detection antibody (µg/ml)**				
	0.125	***0.25***	***0.5***	***1***	***2***
1000	82.70	101.82	18.43	21.38	16.25
250	85.96	90.98	16.51	16.65	11.76
62.5	45.48	43.50	7.05	5.44	3.70
15.63	4.78	2.48	2.21	1.91	1.60
7.81	2.26	1.59	1.16	0.79	0.89
3.91	1.83	1.27	0.76	0.56	0.85
1.95	1.30	1.20	0.65	0.50	0.90
0	1	1	1	1	1

Table 4.5. Flu-RI-OR2-NAG signal to noise raw MFI values – Coupling 2 µg/ml.

Table representing the raw MFI values of the signal to noise ratio results of 2 µg/ml anti-O-GlcNAc CTD110.6 (mouse monoclonal) antibody coupled to Luminex microspheres and detected by 0.125, 0.25, 0.5, 1 and 2 µg/ml of anti-Fluorescein (Biotin) antibody as demonstrated in Figure 4.12.

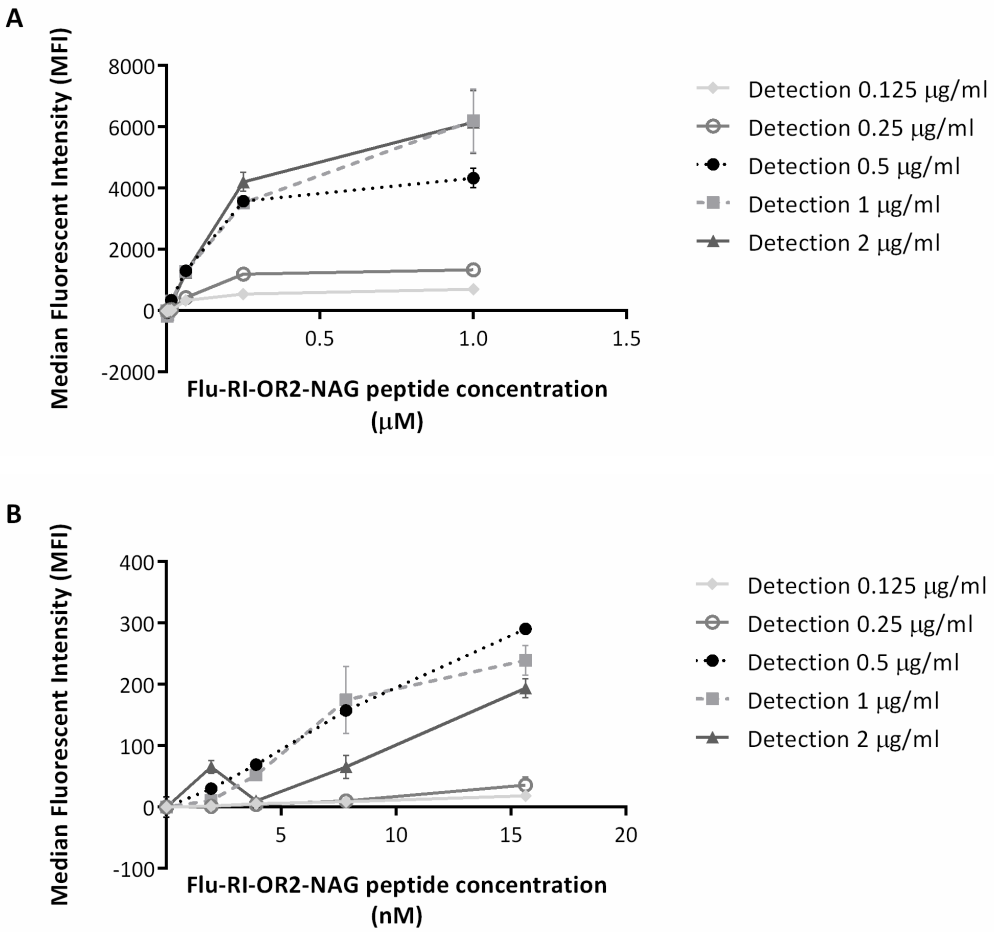

Figure 4.13. Anti-O-GlcNAc CTD110.6 (mouse monoclonal) antibody – Coupling 3 µg/ml.

Luminex beads coupled with 3 µg/ml of anti-O-GlcNAc CTD110.6 (mouse monoclonal) antibody were reacted with HB Blank controls and Flu-RI-OR2-NAG concentrations ranges (A) 1.95 nM to 1 µM and (B) 1.95 nM to 15.63 nM. Biotinylated anti-Fluorescein antibody of 0.125, 0.25, 0.5, 1, and 2 µg/ml and 4 µg/ml STREP-RPE were used as detection – reporter system for the assay. The figure represents the mean ± SEM (n = 3) of MFI signals.

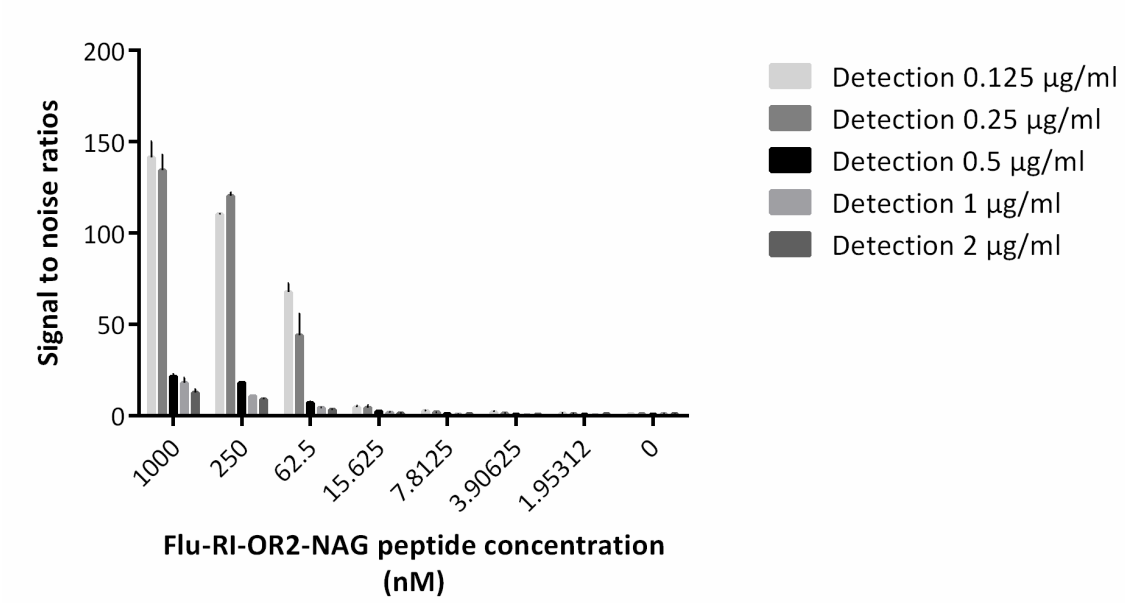

Figure 4.14. Signal to noise ratios of Flu-RI-OR2-NAG assay optimisation – Coupling 3 µg/ml.

The figure demonstrated the signal to noise ratios of the MFI values obtained from the antibodies titration for the development of the Flu-RI-OR2-NAG Luminex assay. Luminex beads coupled with 3 µg/ml anti-O-GlcNAc CTD110.6 (mouse monoclonal) antibody were reacted with HB Blank controls and Flu-RI-OR2-NAG peptide (1 µM to 1.95 nM). Biotinylated anti-fluorescein antibody of 0.125, 0.25, 0.5, 1, and 2 µg/ml, and 4 µg/ml STREP-RPE reporter molecule were used as detection – reporter system for the assay. The figure represents the mean ± SEM (n = 3) of MFI signals of the antibody combinations.

Flu-RI-OR2-NAG (nM)	**Detection antibody (µg/ml)**				
	0.125	***0.25***	***0.5***	***1***	***2***
1000	141.60	134.35	21.59	18.09	12.73
250	110.40	120.43	18.05	10.71	9.01
62.5	67.95	44.18	7.19	4.55	3.38
15.63	4.70	4.60	2.64	1.87	1.43
7.81	2.80	2.00	1.31	0.96	1.05
3.91	2.10	1.45	0.89	0.62	0.95
1.95	1.40	1.15	0.70	0.51	1.05
0	1	1	1	1	1

Table 4.6. Flu-RI-OR2-NAG signal to noise raw MFI values – Coupling 3 µg/ml.

Table representing the raw MFI values of the signal to noise ratio results at 3 µg/ml anti-O-GlcNAc CTD110.6 (mouse monoclonal) antibody coupled to Luminex beads and detected by 0.125, 0.25, 0.5, 1, and 2 µg/ml anti-fluorescein (biotin) antibody, as demonstrated in Figure 4.14.

The anti-O-GlcNAc CTD110.6 (mouse monoclonal) antibody to the Flu-RI-OR2-NAG peptide gave much higher signals than the two previous antibodies tested, and so this was the capture system chosen for the study of this peptide in mouse tissues (Chapter 5, Section 5.3.2.). In order to decide on the best combination of anti-O-GlcNAc CTD110.6 capture and anti-Fluorescein detection antibody concentrations, the signal to noise ratio of each antibody combination was examined. The best signal was obtained using the capture antibody at 3 µg/ml and the detection antibody at 0.125 µg/ml (Figures 4.13., 4.14., Table 4.6.).

4.3.3. BODIPY-PINPs peptide ELISA assay development

The original idea was to develop and optimise a Luminex-bead immunoassay for detection of the BODIPY-PINPs peptide by utilising the 'TAT' sequence of the peptide attached to the liposome and the 'PEG' molecule of the lipid tail as possible epitope detection sites. Administration of the peptide into live organisms will presumably result at some stage in the breakdown of the liposome and release of the free peptide, possibly following its delivery to the brain. The BODIPY-PINPs were treated

with bee venom to break up the nanoliposome membrane so that the peptide molecule, still attached covalently to lipid, would be released and could be detected and measured. This system might also allow detection of the peptide-lipid combination that would be present in the mouse tissues examined in Chapter 5.

Unfortunately, development of a Luminex assay for detection of the peptide-lipid component of the BODIPY-PINPs was not feasible as the tested antibody system was not generating any signal at all. Thus, an attempt was made to develop an ELISA assay to be used in the investigation of this peptide in the mouse tissues.

4.3.3.1. System detection using the anti-polyethylene glycol [PEG-B-47b] (biotin) antibody

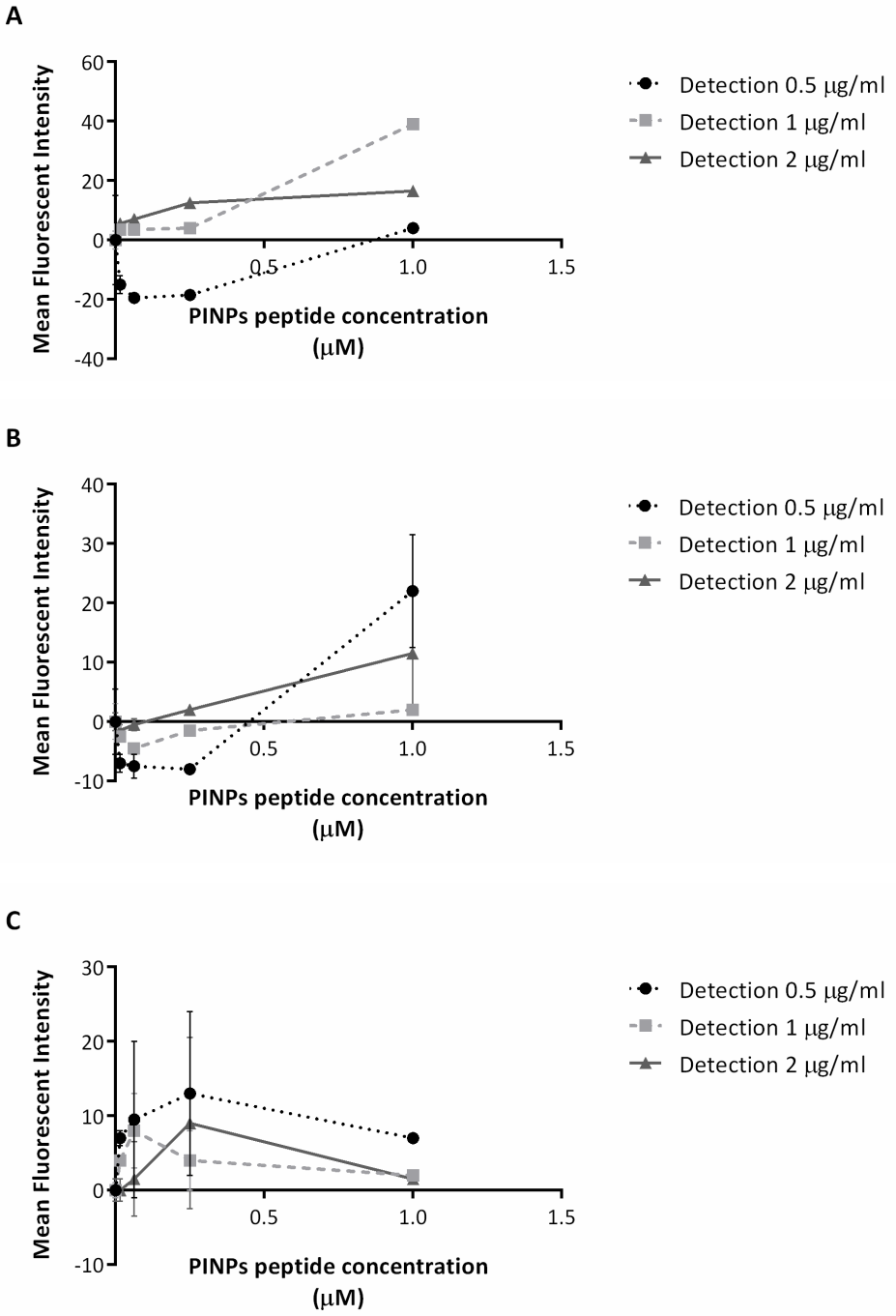

Figure 4.15. Anti-polyethylene glycol [PEG-B-47b] (biotin) antibody titration.

Microtiter ELISA plates coated with (A) 1 µg/ml, (B) 2 µg/ml and (C) 3 µg/ml of anti-HIV1 tat [N3] antibody were reacted with HB blank controls and BODIPY-PINPs concentrations over the range of 15.63 nM to 1 µM, with biotinylated detection using anti-polyethylene glycol [PEG-B-47b] (biotin) antibody at 0.5, 1, and 2 µg/ml, and 4 µg/ml STREP-RPE as the detection

– reporter system. The figure shows mean ± SEM (n = 3) of fluorescent intensity (FI) signals for these antibody combinations.

The mean FI data observed from using the anti-polyethylene glycol [PEG-B-47b] (biotin) antibody as the detection molecule for this assay showed poor sensitivity, in great contrast to the large dose-dependent MFI signals obtained for the optimised Flu-RI-OR2-TAT and Flu-RI-OR2-NAG peptide assays. An alternative detection antibody, anti-polyethylene glycol [PEG-2-128] (rabbit monoclonal) antibody, was therefore tested in an effort to generate an improved assay for detection of the BODIPY-PINPs peptide.

4.3.3.2. System detection using the anti-polyethylene glycol [PEG-2-128] antibody

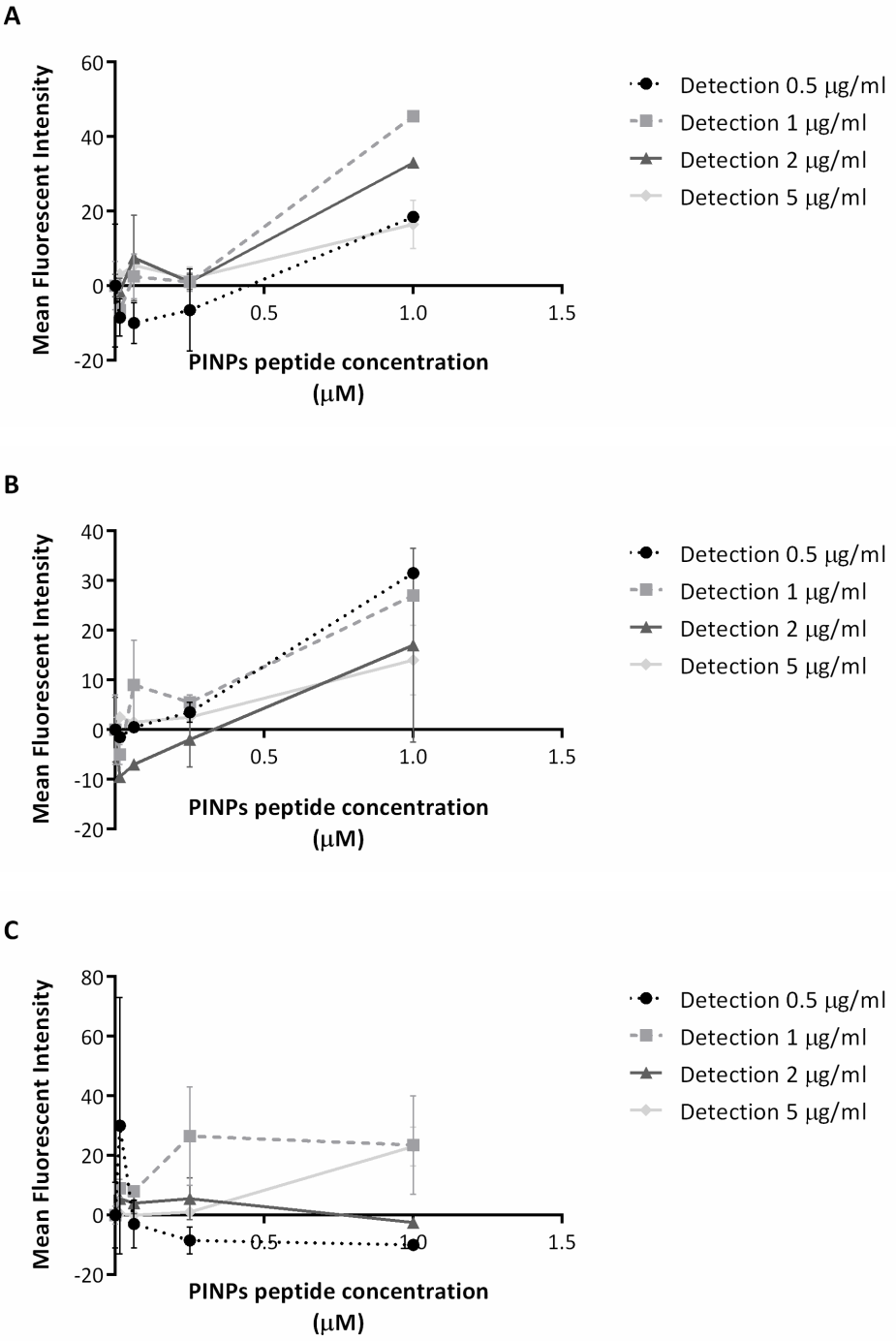

Figure 4.16. Anti-polyethylene glycol [PEG-2-128] antibody titration.

Microtiter ELISA plates coated with (A) 1 µg/ml, (B) 2 µg/ml and (C) 3 µg/ml of anti-HIV1 tat [N3] antibody were reacted with HB blank controls and BODIPY-PINPs concentrations over the range of 15.63 nM to 1 µM, with biotinylated detection using anti-polyethylene glycol [PEG-2-128] (biotin) antibody at 0.5, 1, 2 and 5 µg/ml, and 4 µg/ml STREP-RPE as the detection – reporter system. The figure shows mean ± SEM (n = 3) of fluorescent intensity (FI) signals for these antibody combinations.

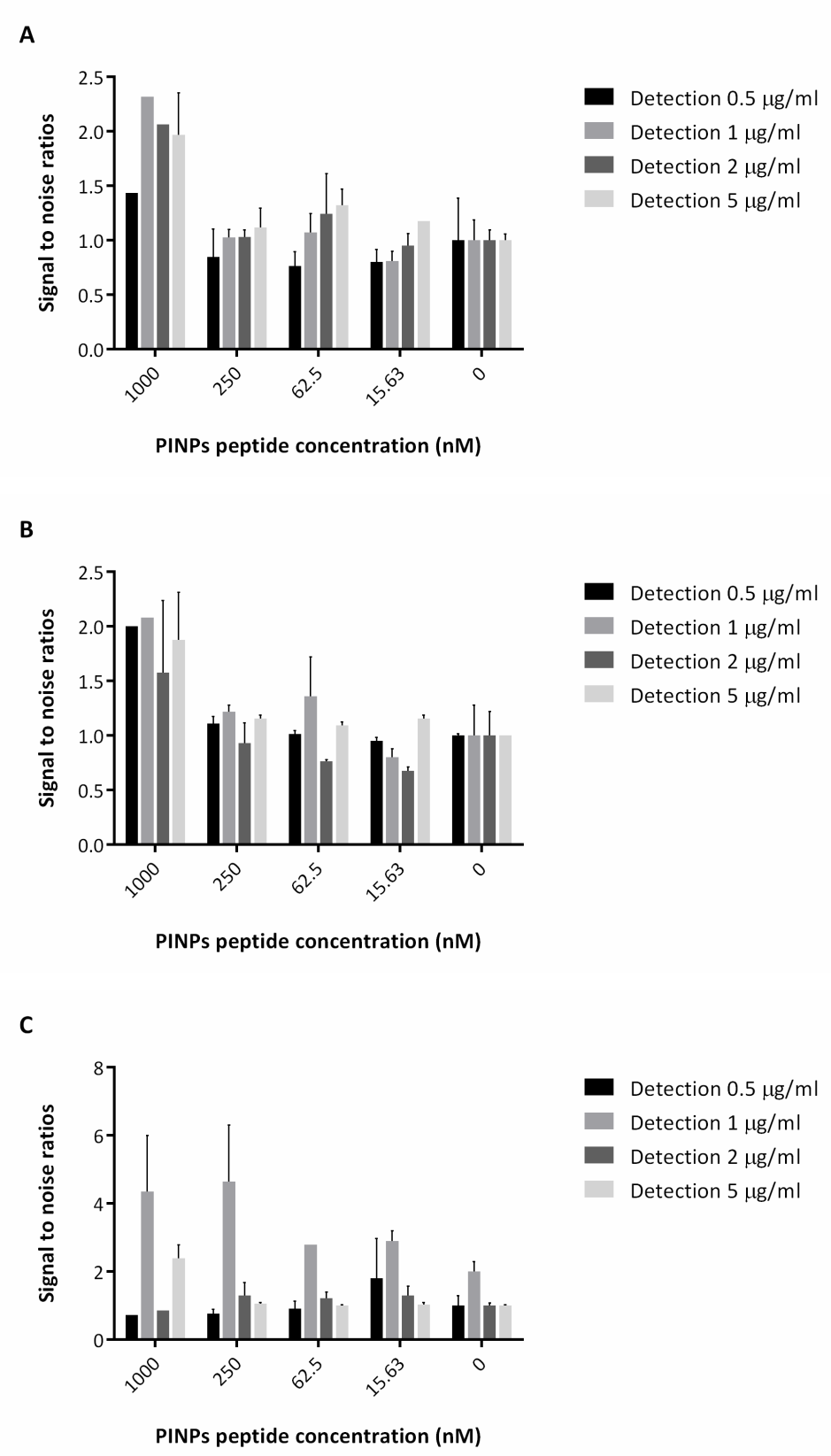

Figure 4.17. Signal to noise ratios of PINPs assay optimisation.

The figure demonstrated the signal to noise ratios of the mean FI values obtained from the antibodies titration for the development of the PINPs ELISA assay. Microtiter ELISA plates

coated with (A) 1 µg/ml, (B) 2 µg/ml and (C) 3 µg/ml of anti-HIV1 tat [N3] antibody were reacted with HB blank controls and BODIPY-PINPs concentrations over the range of 15.63 nM to 1 µM, with biotinylated detection using anti-polyethylene glycol [PEG-2-128] (biotin) antibody at 0.5, 1, 2 and 5 µg/ml, and 4 µg/ml STREP-RPE as the detection – reporter system. The figure shows mean ± SEM (n = 3) of fluorescent intensity (FI) signal to noise ratios for these antibody combinations.

Comparing the two antibodies used as detection molecules in the process of developing an assay for the BODIPY-PINPs, the anti-polyethylene glycol [PEG-2-128] antibody demonstrated higher mean FI values. Even though this assay did not generate very high signals compared to the assay developed for detection of the Flu-RI-OR2-TAT, an attempt was made to use the combination of 3 µg/ml anti-HIV1 tat [N3] antibody as the capture reagent and 1 µg/ml of anti-polyethylene glycol [PEG-2-128] antibody as the detection molecule (Figure 4.16. – C), in the effort to investigate the bio-distribution of BODIPY-PINPs in the mouse tissues collected (Chapter 5, Section 5.3.3.). Even though the raw mean FI signals demonstrate higher readings using alternative combinations, this system shows a better ratio of the signal's strength relative to background, even at the lowest concentration of peptide tested (Figure 4.17. – C).

4.4. Discussion

This Chapter has explored the development and optimisation of Luminex assays for detection of the Flu-RI-OR2-TAT and Flu-RI-OR2-NAG peptides; and an ELISA assay for detection of the BODIPY-PINPs peptide. These assays were used in the following Chapter (Chapter 5) to examine the bioavailability and distribution of these peptides in several different mouse tissues, 1 h after their peripheral administration, although it was realised that the ELISA assay for BODIPY-PINPs may not be fit for this purpose.

4.4.1. Luminex versus ELISA assays

Immunoassays have allowed major advances in laboratory research and diagnostics, and have been widely employed in the process of drug development. They permit

specific and sensitive detection of numerous different analytes in biological samples, and have become a routine part of clinical and pharmaceutical investigations. ELISA assays have been long used as the main tool to detect and quantify analytes in biological samples. However, as discussed by Baker and colleagues (Baker et al., 2012), they have multiple limitations that are mostly associated with the technical application of the method. Examples of these limitations include the relatively large amounts of sample required for binding to the available antibody sites; and the non-specific binding and increased background effects seen due to the large surface area of the plate wells, and the hydrophobic binding of capture antibody to the solid phase of the wells (Baker et al., 2012).

The new and emerging Luminex technology has overcome some of the limitations mentioned above by increasing the flexibility of the assays, allowing reduced amounts of antibody and sample volumes to be employed, and delivering a lower cost system (Baker et al., 2012). Most importantly, the Luminex platform has enabled multiplexing applications from a single sample, in contrast to ELISA assays that are limited to detection of one analyte in each reaction.

4.4.2. Luminex assays detecting the Flu-RI-OR2-TAT and Flu-RI-OR2-NAG peptides

The development of a Luminex assay for the quantification of Flu-RI-OR2-TAT was effectively performed using a combination of antibodies that bind to the available 'TAT' and fluorescein antigen sites of the peptide. The developed Flu-RI-OR2-TAT assay demonstrated efficient and sensitive detection of this peptide, down to picomolar concentration levels.

The Flu-RI-OR2-NAG assay was developed by utilising the 'NAG' site of the peptide and, in a similar way to the Flu-RI-OR2-TAT assay, the fluorescein molecule attached to the peptide. This Luminex assay was optimised to detect nanomolar concentrations of the free peptide in HB. Even though this range would be considered sensitive enough for most applications, it may not be sufficient for quantifying the Flu-RI-OR2-NAG peptide in mouse tissue samples where peptide penetration is particularly low. However, this was examined in detail in the following

Chapter (Chapter 5). Further optimisation and validation of this assay, including the use of alternative antibodies for the NAG site, or different antibodies that target fluorescein, may improve the sensitivity of the Flu-RI-OR2-NAG assay.

4.4.3. ELISA assay for detection of BODIPY-PINPs

The original idea was to develop and optimise a Luminex assay for quantification of the BODIPY-PINPs peptide by employing the 'TAT' sequence of the free peptide and the PEG molecule of the lipid tail. Unfortunately, this was not possible, and an alternative ELISA assay was developed.

There are a few possible reasons that can be offered as to why the BODIPY-PINPs Luminex assay did not work, although it should be noted that none of these explanations was proven experimentally:

1. The phospholipase A_2 from honey bee venom may not have broken down the cholesterol and sphingomyelin lipid membranes of the BODIPY-PINPs very effectively. If the liposomes remained largely intact, this would obstruct the interaction of the antibodies with their corresponding antigen binding sites.
2. Even if the phospholipase A_2 was effective at breaking down the lipid membranes, the disintegrated free lipids would be viscous and so could readily adhere to the filters present at the bottom of the assay plate wells, so interfering with the Luminex reaction.
3. Monoclonal or polyclonal antibodies can be used for developing an immunoassay system. However, polyclonal antibodies are more commonly used as the capture component because they bind through multiple antigenic sites and so can effectively capture more of the analyte molecule than monoclonal antibodies which only recognise one single epitope of the analyte molecule. In the BODIPY-PINPs assay, both of the antibodies used for capture and detection were monoclonal, and the use of polyclonal antibodies was not explored.
4. Tween® 20 was used at 0.05 % (v/v) concentration in the wash buffer of the assays. However, Tween® 20 and other polyoxyethylene detergents can interfere with immunoassays when used with anti-PEG products as the

detergent itself contains PEG polymers which may interfere with binding of the antibodies to their correct antigen sites (Saifer et al., 2014).

5. When designing a sandwich immunoassay it is important to consider that the capture and detection antibodies must recognize two different non-overlapping epitopes. More specifically, the epitope recognised by the detection secondary antibody should not be altered or interfered with by binding of the antigen to the capture antibody. In the case of the BODIPY-PINPs assay, both epitope sites are located on the C-terminal end of the peptide which, considering also the viscous properties and the size of the lipids, may have affected the binding of the anti-PEG antibodies to their epitope sites.
6. Poor biotinylation of the anti-polyethylene glycol [PEG-2-128] (rabbit monoclonal) antibody may offer an explanation. This antibody was supplied at a concentration of 0.593 mg/ml preserved in 0.01 % sodium azide, and constituted in 40 % Glycerol, 0.05 % BSA, and 59 % PBS. For optimal biotinylation, it is suggested to use 1 mg/ml of antibody in a buffer that does not contain primary amines or carriers such as BSA. The BSA and glycerol present as antibody constituents may have interfered with biotinylation of the antibody. Additionally, the anti-polyethylene glycol [PEG-2-128] antibody initially underwent a buffer exchange step and was then concentrated to 1 mg/ml prior to biotin-labelling. It is possible that some of the interfering components were not completely removed from the mixture during this buffer exchange step, and also that some of the antibody was lost. Equally important, the purification process that follows biotinylation of the antibody usually yields 60 – 90 % of purified labelled protein, thus, there is the possibility that some of the labelled antibody was lost through this process also.

These limitations would apply to both the Luminex-bead and ELISA immunoassays for the BODIPY-PINPs and can reasonably explain the failure to develop a suitable Luminex assay for this system. However, a low sensitivity ELISA was developed for detecting the peptide-lipid component of the BODIPY-PINPs and it was decided to

attempt to employ this assay for examination of the bioavailability and distribution of this molecule in subsequent experimental investigations (Chapter 5).

4.5. Conclusions

The development of diagnostic methods is extremely important in research and especially in the process of discovering candidate drugs for the treatment of various diseases. This Chapter has presented the development, optimisation and suggestions for improvement, of immunoassays for detection of three possible drug-related peptides. Equally important, as we are hoping that these drugs will be able to enter human clinical trials for treatment of AD, I suggest that further modifications of these assays could enable the detection of these peptides in human biological samples (e.g. in blood plasma) for investigation of and correlation with various indicators of disease.

In this project, these assays were applied in order to investigate the bioavailability and distribution of the peptides concerned in the brain, heart, lungs, stomach, liver, spleen, right and left kidneys and small intestine in the following Chapter (Chapter 5). These tissues were collected from WT mice with C57/BL6 background, one hour after peripheral administration of the peptides.

Chapter 5: A pilot study to investigate the distribution of the peptides

5.1. Introduction

5.1.1. Pharmacokinetics and pharmacodynamics in drug design and development

The study of pharmacokinetics and pharmacodynamics in drug design and development is crucial. The fields of clinical pharmacology, pharmacokinetics and pharmacodynamics are focused on predicting the effects of chemical substances, including potential pharmaceutical drugs, in living organisms (Csajka and Verotta, 2006). Pharmacokinetic studies analyse the effect of the organisms on the drug's fate by examining the route of the drug through the body, whereas pharmacodynamics examine the biochemical and physiological effects of drugs on the living organism (Meibohm and Derendorf, 1997).

This Chapter is focused on preliminary studies on the pharmacokinetics of the three peptide-based inhibitors, RI-OR2-TAT, RI-OR2-NAG, and PINPs. Fluorescent versions of these inhibitors were injected intra-peritoneally at a dose of 100 nmol/kg in the case of free peptides and 4 µmol/kg (total lipids) for the peptide-decorated nanoliposomes, with an administration volume of 10 ml/kg in WT mice with C57/BL6 background. Tissue samples were removed for analysis after 1 h.

5.1.2. Introduction on pharmacodynamics

Pharmacodynamics explain the effects of the drug on cellular and molecular processes. Tissues differentiate chemical messenger signals through receptors located on cell membranes or in the intracellular fluid. Upon binding of an exogenous compound to each receptor, a chemical signal is transduced to the cells which initiates a downstream response of biological events. The affinity and efficacy of a drug is dependent on the chemical structure of the compound relative to the receptor, whereas the pharmacologic effect of the drug is associated with the duration of binding between the compound (ligand) and receptor (WWW, MSD Manual: Professional/Clinical Pharmacology/Pharmacodynamics). Ideally drugs

should bind with high affinity on specific receptors to minimize undesirable side-effects.

5.1.3. Introduction on pharmacokinetics

Pharmacokinetic studies of a chemical substance involve the analysis of the chemical metabolism of a drug in an attempt to determine the journey of the drug in the body following its administration up to the time that it is completely eliminated from the organism (Csajka and Verotta, 2006). The pharmacokinetic properties of a substance are therefore associated with the mechanisms of absorption, bioavailability, distribution, metabolism and excretion of the drug, and are greatly affected by the route of administration and the dose of the administered drug (Bryant and Knights, 2014).

5.1.3.1. Route of administration

In pre-clinical studies, the route of administration of therapeutic substances plays a crucial role in determining the pharmacokinetic properties of the drug of interest. Based on the target action of the substance, the route of administration can be classified as local or systemic. Systemic administration can also be classified as enteral where the drug is administered through the gastrointestinal tract or parenteral where the application of administration occurs outside of the digestive tract (Turner et al., 2011).

Parenteral administration methods are usually preferred in pre-clinical studies because of the ease of their application and the beneficial effects they have on the bioavailability of the substances as they avoid the first-pass effect of hepatic metabolism (Turner et al., 2011). Intravenous administration of substances is the most efficient route of delivery as it avoids the absorption process that must occur prior to distribution of the drug using alternative parenteral methods. However, as application of this method is challenging when using small rodents, the peptides investigated in this Chapter were administered intraperitoneally. The intraperitoneal method involves the administration of substances into the abdominal body cavity.

5.1.3.2. Absorption

Drugs administered non-intravenously need to be absorbed into the circulation to be distributed into the tissues. The major factors affecting the absorption of administered substances are their physiochemical properties, dosage and formulation, and route of administration of the drug. Transcellular movement of drugs is facilitated through several processes that include passive diffusion, facilitated or active diffusion, active transport and pinocytosis (WWW, MSD Manual: Professional/Clinical Pharmacology/Pharmacokinetics).

Absorption of substances following intraperitoneal administration occurs through the mesenteric vessels that release blood into the hepatic portal vein and then pass through the liver (Lukas et al., 1971). At the site of liver, exogenous substances undergo the first pass effect of metabolism (pre-systemic metabolism) whereby the concentration/bioavailability of the drug might be reduced in order to be absorbed and reach the systemic circulation (Rowland, 1972; Pond and Tozer, 1984). Therefore, a disadvantage associated with this method of administration is that substances may undergo metabolism through the hepatic system before reaching the circulation for distribution (Turner et al., 2011).

5.1.3.3. Bioavailability

The term bioavailability refers to the percentage fraction of dose that enters the systemic circulation and reaches the site of action following administration of a given dosage of a drug (Shargel and Yu, 1999). Medicines administered intravenously exhibit 100% bioavailability as they remain unchanged and active, whereas drugs administered by alternative routes, usually have decreased bioavailability due to either incomplete absorption or first-pass metabolism through the hepatic system where they are initially metabolised by the liver before entering the general circulation (Griffin, 2009).

5.1.3.4. Distribution

Once in the circulation of the blood, drugs are distributed to the body's tissues. Each organ and tissue receives different amounts of the drug, and also the total time that

the drug remains in each tissue and organ varies. These variabilities in the distributional properties of a drug are attributed to the differences in blood flow and perfusion of organs, tissues and blood-plasma protein binding, regional pH content and vascular permeability of tissue and cell membranes. Drugs are more easily distributed in highly perfused areas like liver, kidneys and heart, whereas poorly vascularized organs such as muscle and fat exhibit slower distribution rates (WWW, MSD Manual: Professional/Clinical Pharmacology/Pharmacokinetics). Equally important is the degree of binding between the drug and proteins in plasma and tissues. When in circulation, drugs can transport freely or bind to various blood components. However, only unbound drugs in circulation are free to passively diffuse to the site of action.

5.1.3.5. Metabolism and biotransformation

Metabolism and excretion of drugs occurs concurrently with distribution. As mentioned earlier, the liver is the primary organ of drug metabolism. Drugs are metabolised by various processes that include oxidation, reduction, hydrolysis and conjugation with endogenous substances in order to excrete the substance from the organism (WWW, MSD Manual: Professional/Clinical Pharmacology/Pharmacokinetics). Most commonly there are two phases in the metabolism of drugs; phase I metabolism where the exogenous substances are oxidised by the cytochrome P-450 enzyme superfamily (Danielson, 2002), and phase II where the drugs are conjugated to water-soluble compounds by UPD-glucuronosyltransferases and are secreted in bile and eliminated in urine (King et al., 2000).

5.1.3.6. Excretion

Drugs are eliminated from the organism following their distribution and metabolism, either in an unaltered state as the parent drug or in modified forms as metabolites. The major route of elimination is through the urine via the kidneys, which excrete water-soluble substances, however, other elimination pathways also exist that include tears, saliva, perspiration, respiration, hair, milk, bile and faeces.

Most metabolic unbound drug compounds are eliminated through renal filtration in the glomerular endothelium and are not reabsorbed back into circulation though tubular reabsorption like most water and metabolites (WWW, MSD Manual: Professional/Clinical Pharmacology/Pharmacokinetics). On specific occasions, drugs and their metabolites combine with bile juices and enter the biliary excretion process. Through this process, drugs enter the intestines and can either be excreted with any unabsorbed material through the faeces or be reabsorbed into the circulation (enterohepatic cycling) though the intestinal mucosa and eventually be eliminated though the kidneys (Roberts et al., 2002).

5.2. Methods

Brain, heart, lungs, stomach, liver, spleen, right and left kidneys, and small intestinal tissues, were collected after 1 h from three groups of mice, each comprised of 5 animals, which were injected with 100 nmol/kg of Flu-RI-OR2-TATot Flu-RI-OR2-NAG, or 4 µmol/kg (total lipids) of BODIPY-PINPs. Tissues were homogenised in 5 µl/mg of tissue HB. The total protein content for each lysate was determined using the BCA assay.

The tissue-specific distribution of each peptide was then determined by applying the developed Luminex-bead assays to investigate the levels of Flu-RI-OR2-TAT and Flu-RI-OR2-NAG peptides, and the ELISA assay developed for detection of BODIPY-PINPs peptide (Chapter 4). The results obtained from the tissue-specific peptide distribution are analysed using one-way ANOVA hypothesis followed by Bonferroni's *post hoc* multiple comparison test and are presented as the total amount (moles) of peptide per tissue-specific protein content (mg).

5.2.1. Flu-RI-OR2-TAT tissue-specific peptide distribution

A Luminex-bead sandwich immunoassay specific for detecting the Flu-RI-OR2-TAT peptide was then applied to determine the concentration of the peptide present in each tissue of interest. For the assay, 1 µg/ml of anti-HIV1 [N3] antibody was coupled to Luminex beads, and bound peptide was detected using 2 µg/ml of anti-fluorescein

(biotin) antibody, and 4 μg/ml STREP-RPE, which were applied as the recognition element. Analysis of the assay is presented as mean ± SEM (n = 5), and a p-value of ≤ 0.05 was considered to be statistically significant.

5.2.2. Flu-RI-OR2-NAG tissue-specific distribution

Similarly to the Flu-RI-OR2-TAT peptide detection, a Luminex assay was applied to investigate the amount of Flu-RI-OR2-NAG peptide in the tissue extracts. Luminex beads were coupled with 3 μg/ml of anti-O-GlcNAc CTD110.6 (mouse monoclonal) antibody and the bound peptide was detected using 0.125 μg/ml of anti-fluorescein (biotin) antibody, with 4 μg/ml of STREP-RPE as the recognition system for the assay. Analysis of the Flu-RI-OR2-NAG peptide (pmoles) is presented as mean ± SEM (n = 5) and a p-value of ≤ 0.05 was considered to be statistically significant.

5.3.3. BODIPY-PINPs tissue-specific peptide distribution

In order to detect the BODIPY-PINPs peptide in the several tissues collected, an ELISA assay was developed, although the sensitivity of this assay is poor compared to the Luminex assays developed for the two free peptides. Microtiter plates were coated with 3 μg/ml of primary anti-HIV1 tat [N3] antibody, and 1 μg/ml of anti-Polyethylene glycol [PEG-2-128] (rabbit monoclonal) antibody along with 4 μg/ml STREP-RPE were added as the detection – reporter system to measure the fluorescence signal of RPE. Analysis of the BODIPY-PINPs peptide (nmoles) is presented as mean ± SEM (n = 5) and a p-value of ≤ 0.05 was considered to be statistically significant.

5.3. Results

5.3.1. Flu-RI-OR2-TAT tissue-specific peptide distribution

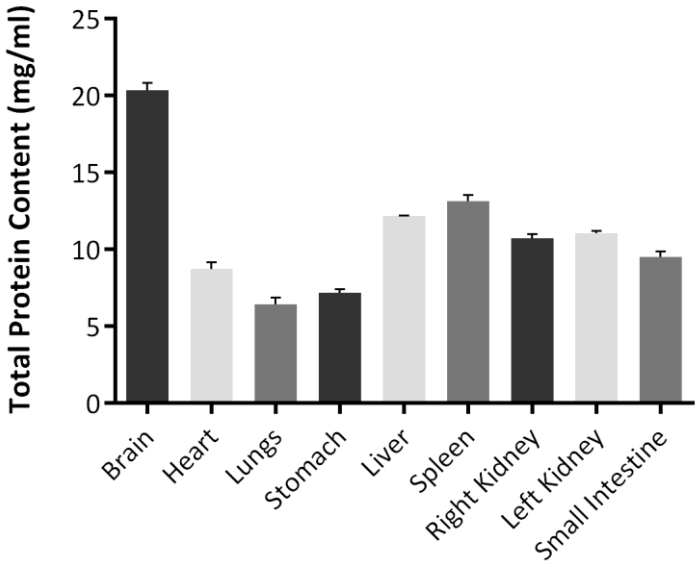

Figure 5.1. Protein concentration in tissue extracts from mice injected with Flu-RI-OR2-TAT. *The figure presents the average total protein content (mg/ml) of tissue extracts prepared following i.p. injection of the Flu-RI-OR2-TAT peptide in five WT mice with C57/BL5 background. Each tissue was homogenised in HB at 5 µl/mg of tissue and analysis of the protein concentration was determined with the BCA assay. The results are presented as mean ± SEM (n = 5).*

The total protein content of tissue homogenates (Figure 5.1.) of mice injected with 100 nmol/kg Flu-RI-OR2-TAT peptide varies from about 6 mg/ml in lungs to about 20 mg/ml in brains. The precise protein content (mg) of each tissue extract was determined according to the volume of lysate in HB (Table 5.1.).

Tissue	Homogenate Volume (µl)	Tissue-specific protein content (mg)
Brain	1265	25.60
Heart	900.4	7.78
Lungs	1647.9	10.26
Stomach	2492.2	17.85
Liver	5543.2	67.36
Spleen	568.8	7.40
Right Kidney	955.8	10.21
Left Kidney	803.7	8.85
Small Intestine	3672.1	34.87

Table 5.1. Protein content in tissue extracts injected with Flu-RI-OR2-TAT.

The table presents the average tissue-specific protein content (mg) of 5 mice injected i.p. with 100 nmol/kg Flu-RI-OR2-TAT. The amount of protein in each tissue homogenate was calculated according to the average volume of tissue extracts prepared in 5 µl/mg HB.

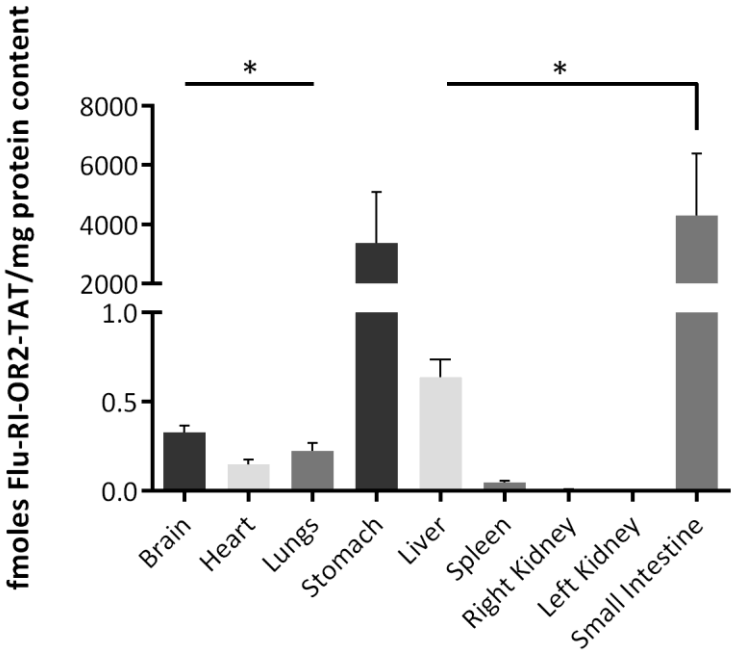

Figure 5.2. Flu-RI-OR2-TAT peptide concentration in mouse tissue extracts.

The figure represents the total amount (fmoles) of Flu-RI-OR2-TAT detected in the tissue lysate samples in relation to tissue-specific protein content (mg). Luminex-beads were

*coupled with 1 µg/ml of anti-HIV1 [N3] antibody, and the bound sample was detected using 2 µg/ml of anti-fluorescein (biotin) antibody with 4 µg/ml of STREP-RPE as the reporter molecule. Results are presented as mean ± SEM (n = 5). * indicates* $p \leq 0.05$*. The levels of Flu-RI-OR2-TAT peptide were significantly higher in small intestine compared to all tissues except stomach.*

The results presented (Figure 5.2.) demonstrate that most of the Flu-RI-OR2-TAT peptide is found in the small intestine compared to the brain, heart, lungs, liver, spleen and kidney tissues, following peripheral administration and distribution of the peptide for 1 h. High amounts of the peptide are also located in the stomach tissue of the mice. The data indicate that a possible route of excretion of the Flu-RI-OR2-TAT peptide is the faeces, supported also by the absence of the peptide in the kidneys signifying that elimination of the peptide does not occur through the urine. However, the assumptions relative to the excretion of the peptide cannot be confidently concluded until further investigation of other pharmacokinetic parameters including the peptide's half-life and excretion rate. The exact amount (fmoles) of Flu-RI-OR2-TAT was determined by investigating the total protein content (mg) in each tissue extract (Table 5.2.).

Tissue	Tissue-specific protein content (mg)	Flu-RI-OR2-TAT fmoles/mg protein	Total amount of Flu-RI-OR2-TAT (fmoles) per tissue-specific protein content
Brain	25.60	0.327	8.37
Heart	7.78	0.149	1.16
Lungs	10.26	0.223	2.29
Stomach	17.85	3373.253	60212.57 (60.21 pmoles)
Liver	67.36	0.637	42.91
Spleen	7.40	0.048	0.36
Right Kidney	10.21	0.009	0.09
Left Kidney	8.85	0.005	0.04
Small Intestine	34.87	4298.117	149875.34 (149.88 pmoles)

Table 5.2. Total amount (fmoles) of Flu-RI-OR2-TAT in tissue extracts.

The table presents the total amount of Flu-RI-OR2-TAT (fmoles) present in each tissue homogenate sample by taking into account the tissue-specific protein content (mg).

The total amount of drug recovered in these tissues is approximately 210 pmoles (Table 5.2.), from the average 2624 pmoles originally administered in the 5 mice of the group (8% recovery). The average original dose was calculated by taking into consideration the 100 nmol/kg administered to the mice relative to their body weight. There are a few possible reasons for the low recovery of the drug, however, it should be noted that none of these has been proven experimentally:

1. A large amount of the drug dose is in the blood circulation of the mice and was removed following the perfusion of the mouse body.
2. Part of the drug has already been excreted from the organisms through either the faeces or urine.
3. The Flu-RI-OR2-TAT remains at the site of the injection and is not distributed around the body; or its distribution is very slow.

4. The drug is distributed in other tissues in the mouse body which were not examined in this study.

5.3.2. Flu-RI-OR2-NAG tissue-specific distribution

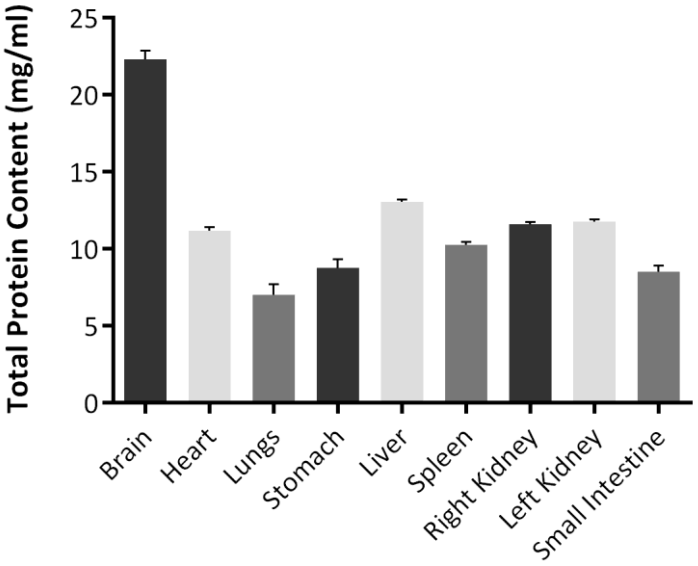

Figure 5.3. Protein concentration in tissue extracts from mice injected with Flu-RI-OR2-NAG.

The figure presents the total protein content (mg/ml) of tissue extracts prepared following i.p. injection of the Flu-RI-OR2-NAG peptide in five WT mice with C57/BL6 background. Each tissue was homogenised in HB at 5 µl/mg of tissue and analysis of the protein concentration was determined BCA assay. The results are presented as mean ± SEM (n = 5).

The total protein content of tissue homogenates (Figure 5.3.) of mice injected with 100 nmol/kg Flu-RI-OR2-TAT peptide varies from about 7 mg/ml in lungs to about 22 mg/ml in brains. The exact protein content (mg) of each tissue extract was determined according to the volume of lysate in HB (Table 5.3).

Tissue	Homogenate Volume (µl)	Tissue-specific protein content (mg)
Brain	1261.8	27.97
Heart	690.1	7.68
Lungs	1456.2	9.80
Stomach	2012.1	17.56
Liver	5571.2	72.53
Spleen	462.8	4.75
Right Kidney	937.3	10.84
Left Kidney	774.9	9.10
Small Intestine	3551.1	30.16

Table 5.3. Protein content in tissue extracts injected with Flu-RI-OR2-NAG.

The table presents the tissue-specific protein content (mg) of 5 mice injected i.p. with 100 nmol/kg Flu-RI-OR2-NAG. The amount of protein in each tissue homogenate was calculated according to the volume of tissue extract prepared in 5 µl/mg HB.

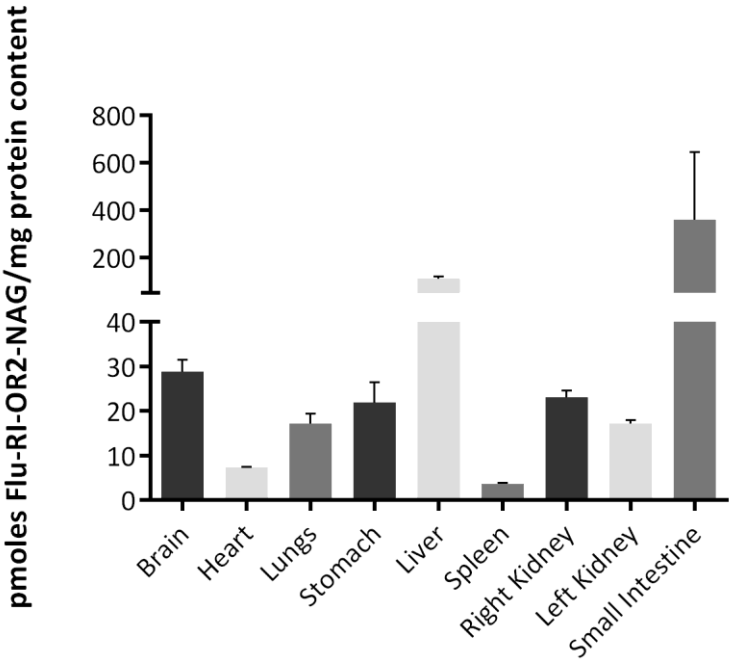

Figure 5.4. Flu-RI-OR2-NAG peptide concentration in mouse tissue extracts.

The figure represents the total amount (pmoles) of Flu-RI-OR2-NAG detected in the tissue lysate inn relation to tissue-specific protein content (mg). Luminex-beads were coupled 3

µg/ml of anti-O-GlcNAc CTD110.6 (mouse monoclonal) antibody, and the bound sample was detected using 0.125 µg/ml of anti-fluorescein (biotin) antibody with 4 µg/ml of STREP-RPE as the reporter molecule. Results are presented as mean ± SEM (n = 5).

Even though statistical analysis of the samples shows no significant difference between the distribution of the Flu-RI-OR2-NAG peptide in the mouse tissue extracts (Figure 5.4.), high quantities of the peptide were apparently detected in the small intestines of the mice, indicating a possible route of clearance, similar to that of the Flu-RI-OR2-TAT peptide. Further examination on pharmacokinetic factors, including the peptide's half-life, can accurately determine the exact route of elimination of the Flu-RI-OR2-NAG peptide. The exact amount (pmoles) of Flu-RI-OR2-NAG was determined by investigating the total protein content (mg) in each tissue extract (Table 5.4).

Tissue	Tissue-specific protein content (mg)	Flu-RI-OR2-NAG pmoles/mg protein	Total amount of Flu-RI-OR2-NAG (pmoles) per tissue-specific protein content
Brain	27.97	28.77	804.70
Heart	7.68	7.28	55.91
Lungs	9.80	17.21	168.66
Stomach	17.56	21.96	385.62
Liver	72.53	109.73	7958.72 (7.96 nmoles)
Spleen	4.75	3.57	16.96
Right Kidney	10.84	23.08	250.19
Left Kidney	9.10	17.17	156.25
Small Intestine	30.16	359.08	10829.85 (10.83 nmoles)

Table 5.4. Total amount (pmoles) of Flu-RI-OR2-NAG in tissue extracts.

The table represents the total amount of Flu-RI-OR2-NAG (pmoles) present in each homogenate sample compared to the tissue-specific protein content (mg).

The total amount of drug recovered in these tissues is approximately 20.63 nmoles (Table 5.4.), whereas the original average dose administered in the 5 mice of this group was calculated to be only 2.66 nmoles. This indicates an unacceptable over-recovery of peptide, and suggests that the assay developed for Flu-RI-OR2-NAG (Chapter 4, Section 4.3.2.) is not reliable enough to detect the peptide in the mouse tissues. The false-positive data obtained from this assay can be attributed to the incabability of the Luminex equipment to appropriately detect particular antibodies coupled to the microspheres (personal communication with Dr. Kurimun Ismail). Even though the pattern of peptide detection may be correct, any assumption relative to the actual concentrations calculated, should be made with caution.

5.3.3. BODIPY-PINPs tissue-specific peptide distribution

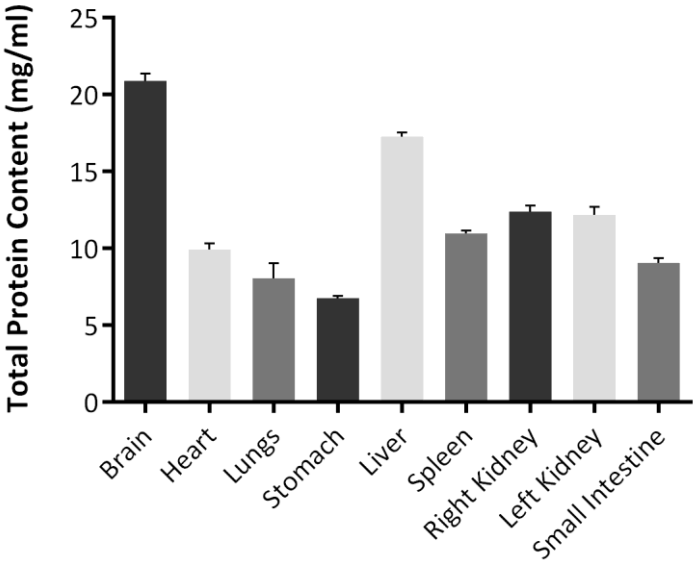

Figure 5.5. Protein concentration in tissue extracts from mice injected with BODIPY-PINPs. *The figure presents the total protein content (mg/ml) of tissue extracts prepared following i.p. injection of the BODIPY-PINPs peptide in five WT mice with C57/BL6 background. Each tissue was homogenised in HB at 5 µl/mg of tissue and analysis of the protein concentration was determined BCA assay. The results are presented as mean ± SEM (n = 5).*

The total protein content of tissue homogenates (Figure 5.5.) of mice injected with µmol/kg BODIPY-PINPs varies from about 6.8 mg/ml in lungs to about 20 mg/ml in

brains. The actual protein content (mg) of each tissue extract was determined according to the volume of lysate in HB (Table 5.5.).

Tissue	Homogenate Volume (µl)	Tissue-specific protein content (mg)
Brain	1304.5	27.20
Heart	721	7.13
Lungs	1271.1	9.44
Stomach	2555.4	17.26
Liver	6285.5	108.56
Spleen	545.9	5.97
Right Kidney	807.4	10.16
Left Kidney	898.1	10.86
Small Intestine	3141.2	28.39

Table 5.5. Protein content in tissue extracts injected with BODIPY-PINPs.

The table presents the tissue-specific protein content (mg) of 5 mice injected i.p. with 4 µmol/kg BODIPY-PINPs. The amount of protein in each tissue homogenate was calculated according to the volume of tissue extract prepared in 5 µl/mg HB.

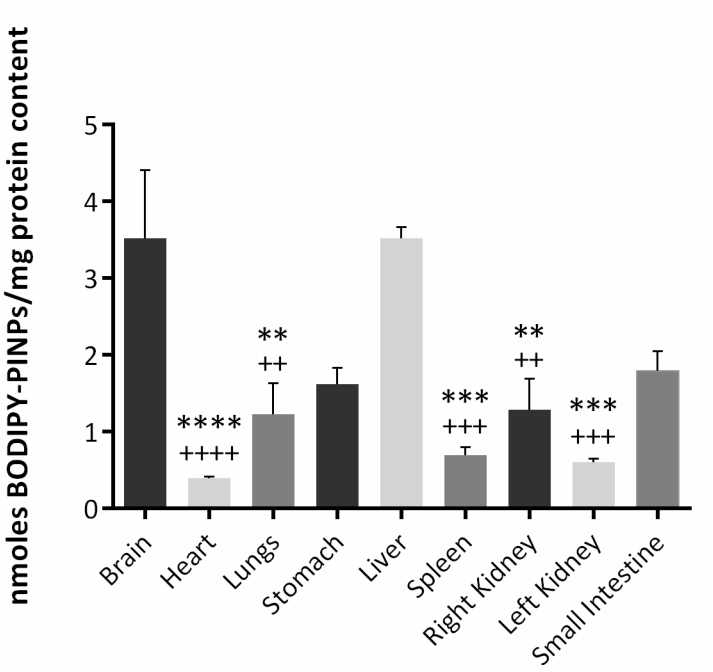

Figure 5.6. BODIPY-PINPs peptide concentration in mice tissue extracts.

*The figure represents the total amount (nmoles) of BODIPY-PINPs detected in the tissue lysate samples in relation to tissue-specific protein content (mg). 3 µg/ml of primary anti-HIV1 tat [N3] antibody were coated on the wells of the plate, and the bound peptide was detected using 1 µg/ml of anti-Polyethylene glycol [PEG-2-128] (rabbit monoclonal) antibody. 4 µg/ml of STREP-RPE was used as the reporter molecule. Results are presented as mean ± SEM (n = 5). Significant results relative to the amount (nmoles) of BODIPY-PINPs in the brain extract are presented as: ** denoting p ≤ 0.01, *** denoting p ≤ 0.001, **** denoting p ≤ 0.0001; while significant results relative to the amount (nmoles) of peptide in the liver extract are presented as: ++ indicating p ≤ 0.01, +++ indicating p ≤ 0.001, ++++ indicating p ≤ 0.0001.*

Statistical analysis of the BODIPY-PINPs peptide distribution following 1 h incubation (Figure 5.6.) shows that most of the peptide is apparently found in the brain and liver extracts of the mice, demonstrating significantly higher results compared to the heart, lungs, spleen and kidney lysates. High signals were also obtained from the small intestine, suggesting also a possible route of peptide elimination. The exact amount (nmoles) of Flu-RI-OR2-NAG was determined by investigating the total protein content (mg) in each tissue extract (Table 5.6.).

Tissue	Tissue-specific protein content (mg)	BODIPY-PINPs nmoles/mg protein	Total amount of FBODIPY-PINPs (nmoles) per tissue-specific protein content
Brain	27.20	3.52	95.74
Heart	7.13	0.39	2.78
Lungs	9.44	1.23	11.61
Stomach	17.26	1.62	27.96
Liver	108.56	3.52	382.13
Spleen	5.97	0.69	4.12
Right Kidney	10.16	1.28	13.01
Left Kidney	10.86	0.60	6.52
Small Intestine	28.39	1.79	32.92

Table 5.6. Total amount (nmoles) of BODIPY-PINPs in tissue extracts.

The table represents the total amount of BODIPY-PINPs (nmoles) present in each homogenate sample compared to the tissue-specific protein content (mg).

The total amount of drug recovered in these tissues is approximately 577 nmoles (Table 5.6.). The original average dose administered in 5 mice was calculated to be 110.8 nmoles in relation to the body weight of the mice. This means that the data generated from the assay developed for detection of the BODIPY-PIPs peptide (Chapter 4, Section 4.3.3.), are likely to be due to a very high level of background interference, and should not be trusted.

5.4. Discussion

Using intravenous administration of Evans Blue, the one-pass blood circulation time of mice was investigated, resulting in complete staining of the mouse body at 15 sec (Debbage et al., 1998). Perfusion of mice in this study was conducted 1 h following

i.p. administration of the peptides or peptide-liposomes, which should provide sufficient time for them to be absorbed and enter the circulation of the mice and then be distributed throughout the body tissues.

The dosage of the 'free' peptides (100 nmol/kg), with administration volume (10 ml/kg) and duration of treatment (1 h) was decided based on a previous study of Flu-RI-OR2-TAT where the effects of this peptide on amyloid plaque load and other markers of brain pathology were investigated using APP/PS1 transgenic mice (Parthsarathy et al., 2013). The administration dose (4 µmol total lipid/kg) of the BODIPY-PINPs was formulated using the same administration volume and duration of treatment. This particular dose of total lipid was chosen so that the dose expressed as concentration of peptide available on the surface of the liposomes (i.e. 100 nmol/kg or 2.5% of total lipids) is approximately the same as in the experiments with the 'free' peptides (Gregori et al., 2017). However, I suggest that further investigation of the peptides administration dose and duration of treatment can provide more in-depth details on the fate of the inibitors within the organism. More specifically, determination of the maximum administration dose can improve the effects of the peptides in the brain in future studies while also avoiding any side effects; whereas investigation on the duration of treatment can provide more detailed information on the pharmacokinetic properties of the three peptides.

Following the development of Luminex-bead assays for detection of Flu-RI-OR2-TAT and Flu-RI-OR2-NAG peptides and an ELISA assay detecting the levels of BODIPY-PINPs peptide (Chapter 4), this Chapter presents some preliminary studies on the pharmacokinetics of the three peptides of interest.

5.4.1. Flu-RI-OR2-TAT peptide distribution

The assay developed for the Flu-RI-OR2-TAT peptide (Chapter 4, Section 4.3.1.), detecting picomolar concentrations of the peptide, has effectively demonstrated the distribution of the peptide within the different tissues collected. Following intraperitoneal administration of 100 nmol/kg of Flu-RI-OR2-TAT for 1 h, the peptide was mostly found in the small intestines of the mice. High levels of the peptide were

also detected in the stomach. This highly skewed distribution and high sensitivity of the assay suggest that the data are likely to be reliable. However, the overall recovery of the drug is relatively low. This could be due to the majority of the drug remaining at, or close to, the site of the injection, or due to accumulation in blood, or other tissues not sampled here.

A possible explanation for this distribution is that the peptide is initially absorbed though the liver as the primary lymphatic organ located in the abdomen, and following the hepatic first-pass effect, the peptide is then distributed throughout the mouse body, where it accumulates in the stomach. Following distribution and metabolism, the peptide is likely to be secreted into the gastrointestinal tract through the bile where it can be excreted though the faeces or reabsorbed back into the systemic circulation by the gastric mucosa, resulting in enterohepatic circulation.

This interpretation is supported by the fact that drugs administered to animals that have a molecular mass exceeding 600 g/mol (600 Da) are usually eliminated through biliary excretion (WWW, MSD Manual: Veterinary/Pharmacology/Pharmacology Introduction). Similarly, drugs administered to humans that exceed a molecular mass of 300 g/mol and contain both polar and lipophilic amino acid groups in their biochemical structure are likely to be excreted in bile into the small intestine and then be eliminated from the organism or enter the enterohepatic cycle (WWW, MSD Manual: Professional/Clinical Pharmacology/Pharmacokinetics). Both of these statements support the above theory regarding the distribution and excretion of the peptide, because the molecular mass of Flu-RI-OR2-TAT (~2979 g/mol) exceeds these limits mentioned above.

Interestingly, as the primary target tissue of the peptide is the brain, this pilot study also demonstrates effective accumulation of Flu-RI-OR2-TAT in the brain, and effective penetration of the BBB of WT mice. Even though the mice were perfused with saline prior to collection of the samples, there is a possibility that the peptide is found within the cerebral blood vessels, rather than in the brain tissue itself. The

penetration of the peptides through the BBB and their accumulation in the brain is further investigated in Chapter 6.

5.4.2. Flu-RI-OR2-NAG peptide distribution

The assay developed for Flu-RI-OR2-NAG in Chapter 4, Section 4.3.2. detects nanomolar concentrations of the peptide, and given the dose of 100 nmol/kg the assay should be sensitive enough to detect this peptide in at least some of the mouse tissues sampled. Signals above background were obtained from the tissue extracts, especially in the case of the small intestine, which gave the highest signal. As there was no observed statistical significance in tissue distribution, and a calculated over-recovery of the peptide, these results should be interpreted with a great deal of caution, and it can only be tentatively concluded that the majority of RI-OR2-NAG is found in the small intestine.

Similar to Flu-RI-OR2-TAT, the detection of Flu-RI-OR2-NAG in the small intestine may indicate a possible route of excretion. The molecular mass of the Flu-RI-OR2-NAG peptide (~1727 g/mol) also exceeds the two limits discussed in the previous section (Section 5.4.1.), supporting the possibility that the peptide is secreted through the bile into the small intestine where it may undergo elimination or re-absorption into the systemic circulation. Additionally, the Flu-RI-OR2-NAG peptide was also detected in relatively large amounts in the liver and kidney extracts of the 5 mice examined, indicating that it may have been re-absorbed in the circulation, and following further distribution and metabolism, it may be partially eliminated through renal excretion.

Notably, the Flu-RI-OR2-NAG peptide may also have been detected in the brain, which is the primary target of the peptide's action, indicating that is able to penetrate the BBB, possibly by utilising the glucose (Bell et al., 1990) and *N*-acetylglucosamine (Abeijon et al., 1996) transporters located there. This property of the peptide will be further examined in Chapter 6 of this thesis.

5.4.3. BODIPY-PINPs peptide distribution

The development of a suitable assay for sensitive detection of the BODIPY-PINPs (Chapter 4, Section 4.3.3.) proved to be very difficult and presented many problems and limitations, as discussed in Chapter 4, Section 4.4.3. The very high signals obtained with the BODIPY-PINPs peptide ELISA, suggest that there may be considerable and unacceptable background interference with this assay. The data from this assay are, therefore, not believable. By detection of fluorescence, Chapter 6 investigates the ability of BODIPY-PINPs to cross the BBB and accumulate in brain areas that are predominantly affected in AD.

A small pilot study was also conducted by Quotient Bioresearch (Rushden) Ltd., in order to investigate the biodistribution of PINPs in three C57/BL6 mice. The cholesterol component of the liposomes decorated with RI-OR2-TAT peptide was radioactively labelled (^{14}C), and the peptide-liposomes were administered intravenously (tail vein) at the same dose (4 μmol/kg) and volume (10 ml/kg) as the study presented in this Chapter. The amount of radioactivity in various tissues (brain, liver, kidneys, lungs, spleen), was assessed using quantitative whole body autoradiography (QWBA), and the peptide's concentration in blood was measured by liquid scintillation counter. The results from this study demonstrated that 0.49 %/g of the dose was found in the brain and 0.952 %/g in the blood after 15 min of administration, supporting the fact that the lipid-peptide does penetrate through the BBB (with approximately 50% brain: blood ratio). However, after this 15 min period, most of the peptide (92 %/g) was detected in the lungs. At 60 min post-injection, the concentration of peptide in several tissues was generally decreased, yet higher amounts were still observed in the lungs (Gregori et al., 2017). This effect of the peptide was attributed to the clearance of the peptide-liposomes by the mononuclear phagocyte system in the lungs and other tissues (spleen, liver) where the peptide was also found in large concentrations (Gregori et al., 2017).

The data between this previous study and the one reported here do not appear to be compatible. Presumably due to the poor sensitivity and reliability of the BODIPY-PINPs peptide ELISA assay, but also the difference in the detection element of the

peptide could also be a factor. A major reason also explaining the incompatibility between the two studies is the difference in the administration sites. In the Quotient study the peptide was administered intravenously resulting in complete bio-availability in the circulation of the mice, whereas in the study presented in this Chapter, the peptides were applied i.p. where they exhibit an initial biotransformation (metabolism) prior to their tissue distribution due to the first pass effect in the liver.

Finally, the Quotient study was focused on the lipid component of PINPs rather than the peptide component, and so further studies using labelled peptide will be required to examine the detailed tissue distribution of the peptide component of the PINPs.

5.4.4. General limitations and further considerations on the study

One of the purposes of this Chapter was to compare the distributions of the three peptides in each of the tissues collected. However, due to the limitations of some of the assay systems employed, particularly the ELISA system, this was not entirely feasible.

Another major confine of the study was the inaccessibility to equipment and lack of experience to investigate intravenous application of the peptides, which is difficult in mice. For these reasons, a more convenient intraperitoneal administration route was employed, where absorption of the peptides is facilitated by the large surface area present in the abdominal cavity. Intravenous application of the peptides would have enabled immediate administration of unchanged peptides into the circulation, avoiding the absorption and first pass metabolism effects that could have decreased their bioavailability (Griffin, 2009). For the same reasons, collection of blood samples was not accomplished, which could have increased understanding of the distribution, bioavailability and elimination of the peptides. As an alternative, the terminal bleed procedure (collection of blood from the heart prior perfusion) can be applied in future studies.

As improvements to the study, investigation of alternative administration sites as well as variable treatment durations should be undertaken. Intravenous application of the peptides would enable comparisons of their bioavailability in tissues, as the bioavailability of compounds administered directly in the blood circulation is 100% (Shargel and Yu, 1999). It would be particularly interesting to study intranasal administration as a possible delivery route for immediate absorption into the brain, avoiding the need to penetrate the BBB, which may improve the levels of peptides detectable in the brain. Examination of variable durations of treatment can permit determination of half-life, elimination rate, clearance and absorption rates of the peptides which are all important factors in drug pharmacokinetic studies.

5.5. Conclusions

This Chapter has described preliminary experiments that attempt to study the biodistribution of Flu-RI-OR2-TAT, Flu-RI-OR2-NAG and BODIPY-PINPs peptides, and their possible routes of elimination and excretion. As a result of limitations observed in the sensitivity of some of the assays, accurate and reliable estimation of the peptide concentrations in tissues was not always possible. However, in the case of Flu-RI-OR2-TAT, the pattern of tissue distribution is likely to reflect the actual distribution of the peptide in the tissues concerned. Further suggestions on the improvement and optimisation of the Flu-RI-OR2-NAG and BODIPY-PINPs assays, as well as additional considerations on the study of peptide distribution have been proposed in Chapter 4 and in this Chapter, respectively.

To summarise, the Flu-RI-OR2-TAT peptide, 1 h post-injection, shows effective distribution around the body of the mice, and possible secretion through the bile into the small intestine, where it can either be excreted though the faeces or re-absorbed into the circulation. In the case of Flu-RI-OR2-NAG, clear assumptions cannot be made due to the over-recovery of the peptide in the assay. However, comparison of the distribution pattern within the tissues suggests that the peptide may be excreted through the bile secretion.

Signals for all three peptides were detected in the brains of WT mice, suggesting an ability to cross the BBB. Penetration across the BBB is of primary importance as treatments for AD should be principally targeted to the brain of patients in order to minimise or avoid unwanted side-effects. The ability of Flu-RI-OR2-TAT, Flu-RI-OR2-NAG and BODIPY-PINPs to enter the brain, and their distribution therein, will be examined further in Chapter 6.

Chapter 6: Blood-Brain Barrier penetration and deposition of the peptides

6.1. Introduction

Previously published data by Parthsarathy and colleagues (Parthsarathy et al., 2013) have shown that the RI-OR2-TAT peptide is able to cross the BBB and bind to amyloid plaques and activated microglia cells in the cerebral cortex of APP/PS1 Alzheimer's transgenic mice, followed peripheral administration. Data from the same research also demonstrated that the RI-OR2-TAT peptide inhibitor is able to reduce amyloid plaque deposition, oxidation and inflammation, yet also stimulate neurogenesis in the brains of the same mouse model of AD (Parthsarathy et al., 2013).

In this study, the ability of the peptides to penetrate through the BBB of WT mice with a C57/BL6 background following i.p. administration of 100 nmol/kg of free peptides, and 4 μmol/kg (total lipids) of peptide-decorated liposomes and undecorated control liposomes, was investigated. WT mice have an intact BBB, whereas this may not be the case for Alzheimer's transgenic mice (APP/PS1) where the BBB is disrupted and its transport proteins are impaired (Banks, 2012; Erickson and Banks, 2013). Thus, with a therapeutic focus, it is of high importance to determine whether the peptide inhibitors are able to cross a functioning and integral BBB. The accumulation of the peptides was also assessed in brain areas (cortex – close to the hippocampal formation, CA1 of the hippocampus, and DG) that are pathologically primarily affected in AD.

6.1.1. Introduction on hippocampus, cortex and the dentate gyrus

6.1.1.1. Cerebral cortex

The cerebral cortex is the outer layer of neuronal tissue of the brain and has a key role in various important brain functions, including memory, thought, consciousness, language, attention and perceptual awareness. The two main pathophysiological features of AD, the neuritic plaques and neurofibrillary tangles, are mainly found in the frontal and temporal lobe structures of the cortex, close to the hippocampus, as

well as in other cortical areas of the brain (Morgan, 2011). Additionally, AD brains exhibit marked diffused cortical atrophy and enlargement of ventricles (Bird, 2008) which both correlate with the reduced weight of the brain in diseased individuals.

6.1.1.2. Hippocampus

The hippocampus is one of the major components of the brain in humans and vertebrates and it is located underneath the cerebral cortex. The hippocampus belongs to the limbic system of the brain, which supports a variety of functions and emotions. The hippocampus specifically is involved in the stabilisation and unification of information between short-term and long-term memory, and is also responsible for spatial navigation (Eichenbaum, 2013; Leuner and Gould, 2010). This brain region is one of the first sites that suffers damage in AD as it is associated with memory loss and disorientation which are primary symptoms of the disease.

The hippocampus of the brain is composed of several compartments that include the subiculum complex, the hippocampus proper (CA1, CA2, CA3 and CA4 areas) and the DG. Based on the idea that some of the brain areas are more susceptible in AD and exhibit neuronal dysfunction from the very early stages of the disease, Padurariu and colleagues have demonstrated a significant decrease in neuronal density in the CA1 and CA3 areas of the hippocampus proper in AD brains, particularly in the CA1 area, compared with age-matched control brains (Padurariu, 2012).

6.1.1.3. The dentate gyrus

The DG is one of the components of the hippocampal formation system along with the hippocampus proper and subiculum (Amaral and Lavenex, 2007; Insausti and Amaral, 2012), and is involved in the creation of new episodic memories and promotes environmental and spatial exploration (Saab et al., 2009). The DG has been identified as the sole site of the hippocampal formation system where a population of stem cells is located facilitating the process of neurogenesis (Deng et al., 2010; Aimone et al., 2010) and indicating a mechanism of plasticity (Derrick, 2007; Saabet al., 2009). This region of stem cells was apparently stimulated, or rescued from Aβ

toxicity, in the presence of RI-OR2-TAT peptide in transgenic Alzheimer's mouse experiments (Parthsarathy et al., 2013).

6.1.2. Overview of Blood-Brain and Blood-Cerebrospinal Fluid Barriers

The brain is the most sensitive and tightly controlled tissue in the human body. The co-occurrence of the BBB and blood-cerebrospinal fluid barrier (B-CSFB) serves to separate the peripheral circulation from the CNS and maintain its homeostasis. The anatomical unit of the B-CSFB is epithelial cells of the choroid plexus (Wolburg et al., 2001) that are responsible for control of the molecular exchange between blood and cerebrospinal fluid, while the functional unit of the BBB is the cerebrovascular endothelial cells of brain capillaries (Abbott et al., 2010) that control the exchange of molecules between the blood and the brain interstitial fluid.

Tight junctions between the epithelial cells and endothelial cells in the B-CSFB and BBB, respectively, form semi-permeable barriers that regulate the entry of blood-borne substances into the CNS, preserving the chemical composition of the brain and protecting its functional processes (Spuch and Navarro, 2011). There is also a third barrier formed by the avascular arachnoid epithelium that completely encloses all of the CNS compartments, however, it is thought that this does not have a significant role in nutrient exchange between blood and CNS (Kandel et al., 2000).

The backbone of the tight junctions formed between the endothelial cells in BBB consists of the transmembrane proteins occludin, claudins and junctional adhesion molecules, and are responsible for interacting with other cytoplasmic proteins (Tietz and Engelhardt, 2015). More precisely, occludin plays a crusial role in the function of the BBB as it is involved in the redox regulation (Blasig et al., 2011) and stability (Medina et al., 2000) of the tight junctions. Claudin-3 and claudin-5 are involved in the formation of the tight junctions and the integrity of the BBB (Luissint et al., 2012); whereas the junctional adhesion molecules facilitate the assaembly of the tight junctions even though they are not essential in their formation (Bazzoni, 2011).

More specifically, the BBB is comprised of a complex of capillary endothelial cells, pericytes (Balabanov and Dore-Duffy, 1998; Armulik et al., 2010), astrocytes (Abbott, 2002) and extracellular matrix that act as a diffusion barrier for transport of substances in and out of the brain and aid communication between the CNS and periphery (Banks, 2012). Figure 6.1. illustrates the potential routes by which nutrients, minerals, molecules and ions are transported across the BBB.

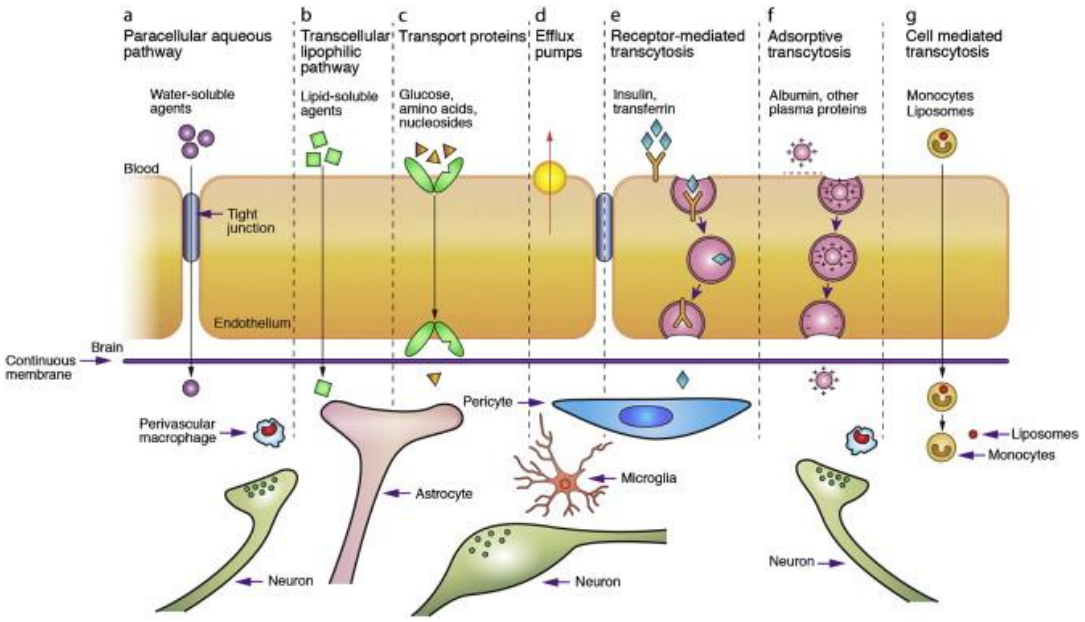

Figure 6.1. Possible routes of molecular transport across the BBB.

Transport pathways "a" to "f" are used commonly used to move solute molecules across the BBB, while pathway "g" is used to transport monocytes, macrophages and drugs (including liposome-based drugs). The transport of molecules is regulated by the tight junctions of endothelial cells and endogenous transporters (Chen and Liu, 2012 – adapted from Abbott et al., 2006).

Only certain molecules with lipophilic and polar properties can diffuse to the CNS from the blood. It has actually been reported that approximately 98% of small molecules and almost all macromolecules do not cross the BBB (Pardridge, 2005). Due to the highly restrictive properties of the BBB, the transport of therapeutic molecules and neuropharmaceutical agents to the CNS has proved to be limited and ineffective.

6.1.3. Blood-Brain Barrier and drug delivery

One of the huge challenges in the development of effective drugs for AD is the presence of the BBB. As a compartment of the CNS, the BBB creates a strictly controlled and unique extracellular fluid environment by the presence of multiple endothelium interacting cells, which function as an anatomical, metabolic and transport barrier to the free movement of solute molecules between blood and brain (Begley, 2004). For this reason, various potential drugs have failed to proceed to clinical trials, despite the advances in drug discovery, as insufficient quantities were transferred to the CNS, so having little impact on the disease even though they were proven to be effective at their site of action *in vitro* (Begley, 2004; Spuch and Navarro, 2011).

Consequently, alternative strategies have been employed including the use of prodrugs, direct administration of drugs into the brain, and modulations of the BBB by osmotic opening of tight junctions to overcome the limitation of BBB permeability (Begley, 2004; Banks, 2012). Amongst these, nanotechnology-based approaches are considered effective for significant delivery of drugs to the CNS.

6.1.4. Targeted delivery of nanoliposomes through the Blood-Brain Barrier

Nanoparticles are currently widely used in diagnostics and therapeutics as they possess important and unique features of which the most apparent are given below (Gelperina et al., 2005; Tassa et al., 2010).

1. Nanoparticles are developed using both biocompatible and biodegradable materials.
2. They are characterised by high stability both in circulation and shelf life.
3. Nanoparticles can be multi-functionalised by attaching various ligands to their surface.
4. Drugs can be incorporated on their surface or in the core of the particle to avoid degradation, improve bioavailability, and minimise any potential side effects by reducing the dosing frequency.

5. The nanoparticle/drug system can be incorporated though various administration routes and can be applied in solid dosage forms (Schmidt and Bodmeier, 1999; Sham et al., 2004; Tsapis et al., 2002).

Among these promising delivery systems, liposomes have been developed as nanomedical devices that, further to the above described features, are also characterised by their unique compatibility with both hydrophobic and hydrophilic drugs, low toxic effect, avoidance of immune system activation and targeted delivery of drugs to the site of action (Chen et al., 2010). Their naturally occurring outer layer increases permeability across membranes and biological barriers, while specifically sphingomyelin and cholesterol stabilize the liposomal structure (Szoka and Papahadjopoulos, 1980). Hydrophilic agents may be entrapped inside the aqueous core or attached on the surface, while hydrophobic drugs can be loaded into the phospholipid bilayer (Spuch and Navarro, 2011). Finally, the addition of PEG on the surface of the nanoliposomes prevents vesicle aggregation, increases stability and bioavailability, and provides "stealth properties" to the device which extend the blood circulation time of the liposomes as it makes them invisible to the mononuclear phagocyte system that is responsible for the rapid clearance of liposomes from the blood stream (Gabizon et al., 1994; Drummond and Kirpotin, 2007).

6.2. Methods

Five animals were injected i.p. with either 100 nmol/kg Flu-RI-OR2-TAT or Flu-RI-OR2-NAG; or 4 µmol/kg BOIPY-PINPs or BODIPY-CL peptides. After 1 h, the LH of the brains was collected, fixed in 4 % (w/v) formaldehyde, and coronally sliced (25 micron) at anatomical regions 1.10 mm to -4.04m bregma. The brain slices were stained with anti-NeuN, anti-GFAP and anti-Iba-1 antibodies and counterstained with DAPI. All brain sections were visualised with confocal microscopy, and 3 digital images per animal were taken at 40X objective from the cortex, DG and CA1 region of the hippocampus.

Analysis of the images' intensities was performed using Image J software and by applying one-way ANOVA in the case of control (injected with vehicle) versus peptide treatment; and two-way ANOVA in the case of peptide versus brain region. The data were further analysed using the *post hoc* Bonferroni's multiple comparison test and are presented as mean ± SEM. A p value of ≤ 0.05 was considered as statistically significant.

6.3. Results

6.3.1. Confocal Images of peptides and vehicle control

6.3.1.1. Flu-RI-OR2-TAT peptide

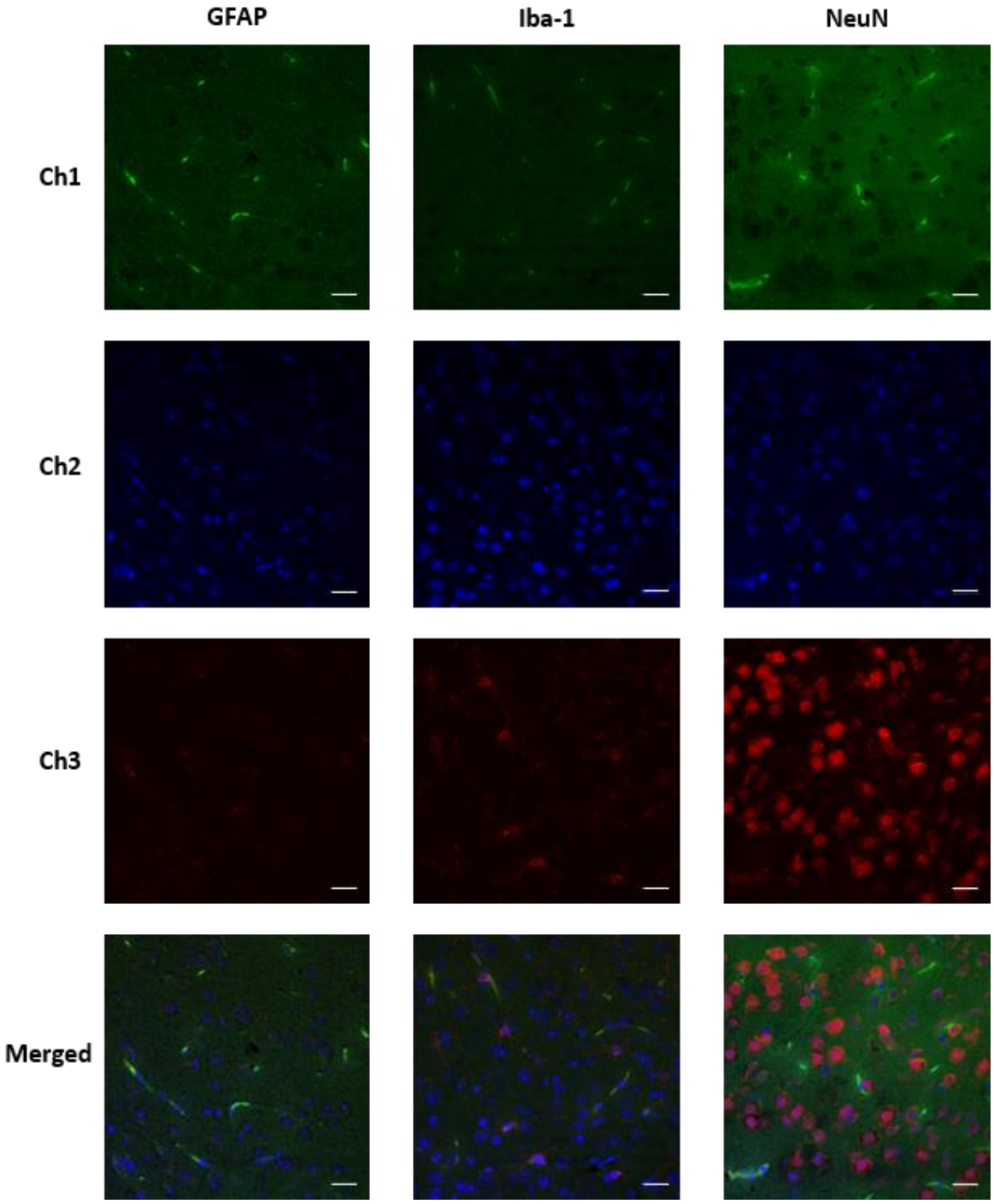

Figure 6.2. Confocal images of Flu-RI-OR2-TAT in cortex.

Brain sections stained with markers for astrocytes (anti-GFAP), activated microglia (anti-Iba-1), and neurons (anti-NeuN), and counterstained with DAPI (nucleus). Ch1 refers to the green

fluorescence of the peptide, Ch2 is DAPI nucleus staining, Ch3 is the neuronal cell marker, and Merged refers to the merged images of Ch1, Ch2 and Ch3. Scale Bar = 20 µm.

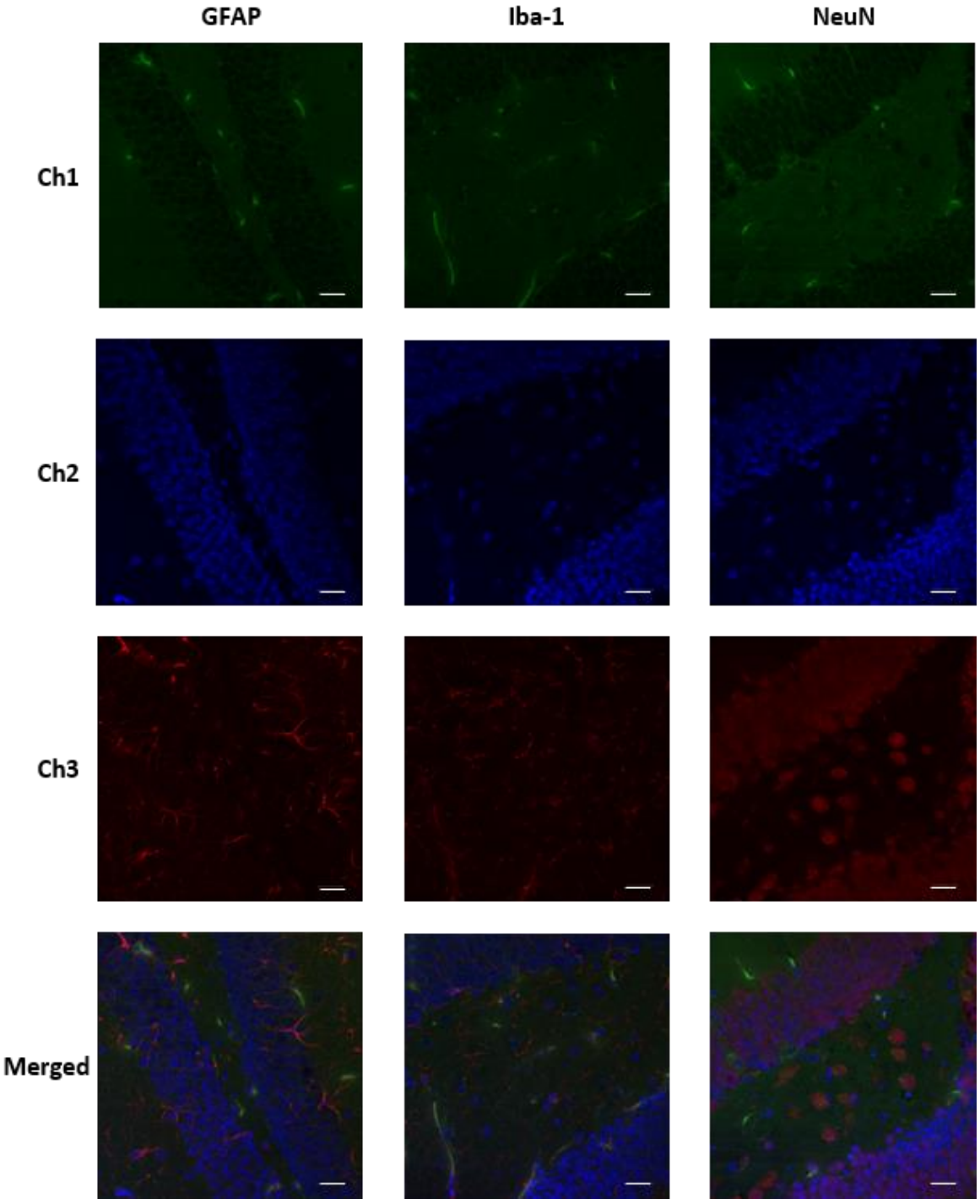

Figure 6.3. Confocal images of Flu-RI-OR2-TAT in dorsal dentate gyrus.

Brain sections stained with markers for astrocytes (anti-GFAP), activated microglia (anti-Iba-1), and neurons (anti-NeuN), and counterstained with DAPI (nucleus). Ch1 refers to the green fluorescence of the peptide, Ch2 is DAPI nucleus staining, Ch3 is the neuronal cell marker, and Merged refers to the merged images of Ch1, Ch2 and Ch3. Scale Bar = 20 µm.

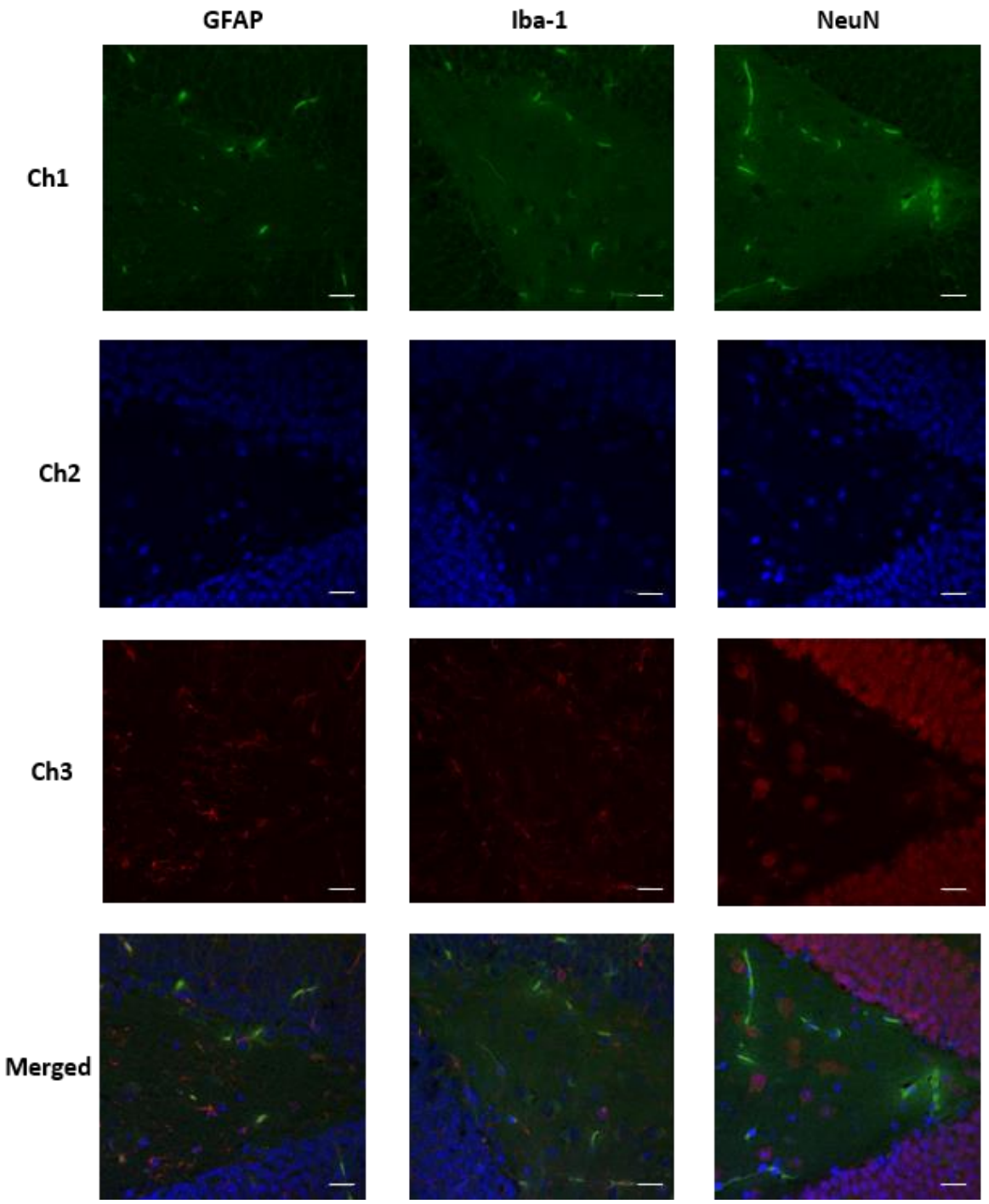

Figure 6.4. Confocal images of Flu-RI-OR2-TAT in ventral dentate gyrus.

Brain sections stained with markers for astrocytes (anti-GFAP), activated microglia (anti-Iba-1), and neurons (anti-NeuN), and counterstained with DAPI (nucleus). Ch1 refers to the green fluorescence of the peptide, Ch2 is DAPI nucleus staining, Ch3 is the neuronal cell marker, and Merged refers to the merged images of Ch1, Ch2 and Ch3. Scale Bar = 20 µm.

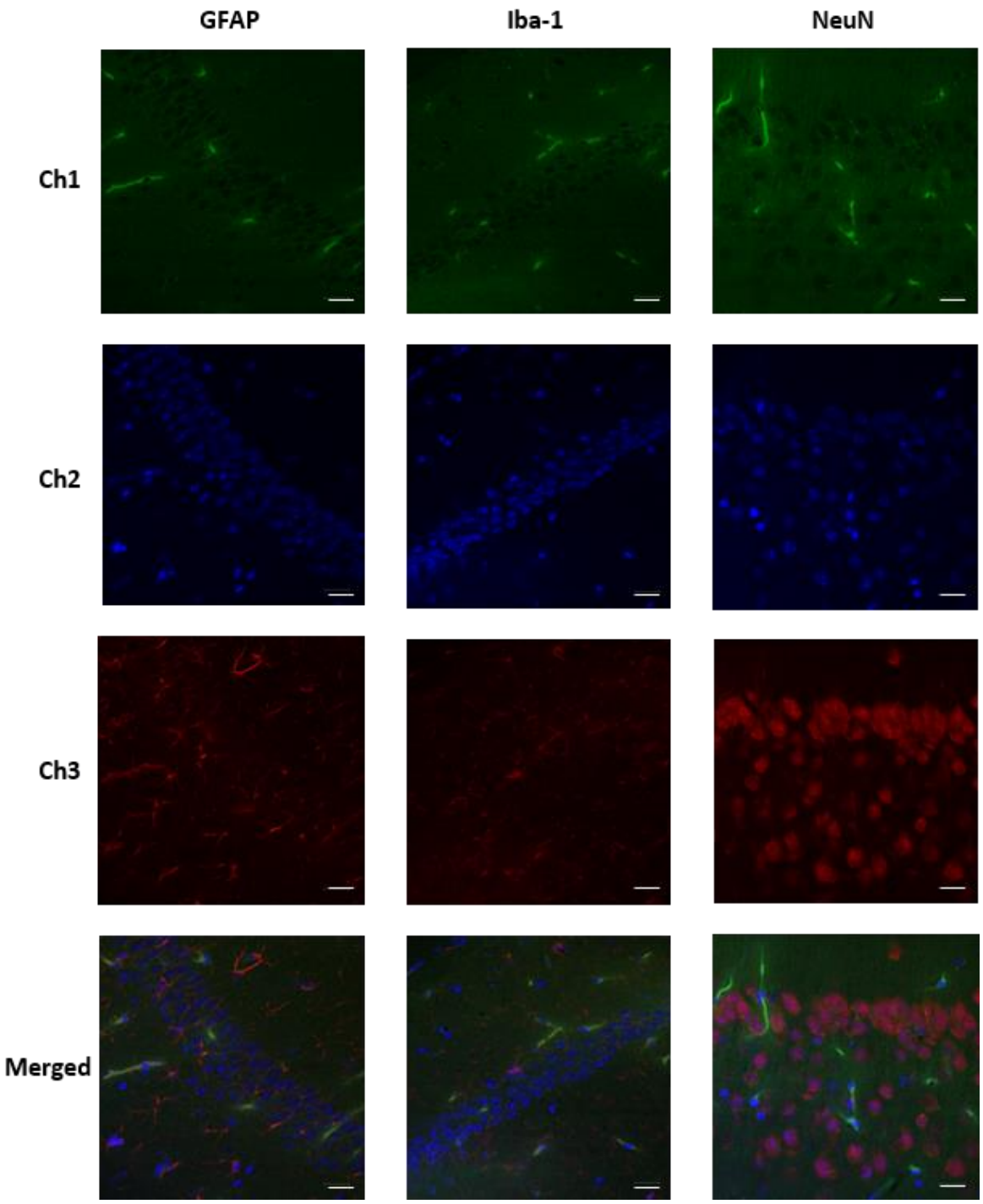

Figure 6.5. Confocal images of Flu-RI-OR2-TAT in CA1 region of the hippocampus.

Brain sections stained with markers for astrocytes (anti-GFAP), activated microglia (anti-Iba-1), and neurons (anti-NeuN), and counterstained with DAPI (nucleus). Ch1 refers to the green fluorescence of the peptide, Ch2 is DAPI nucleus staining, Ch3 is the neuronal cell marker, and Merged refers to the merged images of Ch1, Ch2 and Ch3. Scale Bar = 20 µm.

6.3.1.2. Flu-RI-OR2-NAG peptide

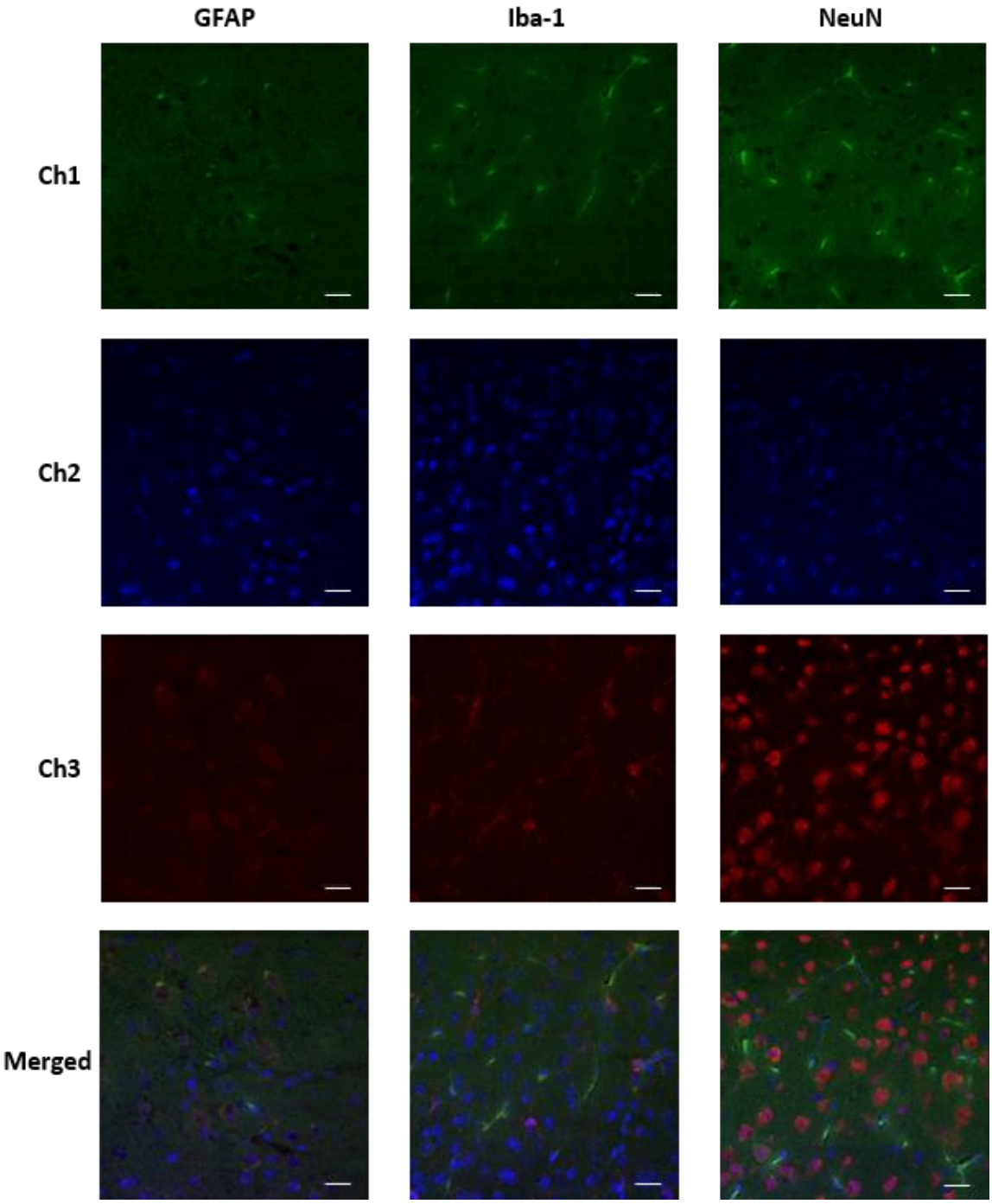

Figure 6.6. Confocal images of Flu-RI-OR2-NAG in cortex.

Brain sections stained with markers for astrocytes (anti-GFAP), activated microglia (anti-Iba-1), and neurons (anti-NeuN), and counterstained with DAPI (nucleus). Ch1 refers to the green fluorescence of the peptide, Ch2 is DAPI nucleus staining, Ch3 is the neuronal cell marker, and Merged refers to the merged images of Ch1, Ch2 and Ch3. Scale Bar = 20 µm.

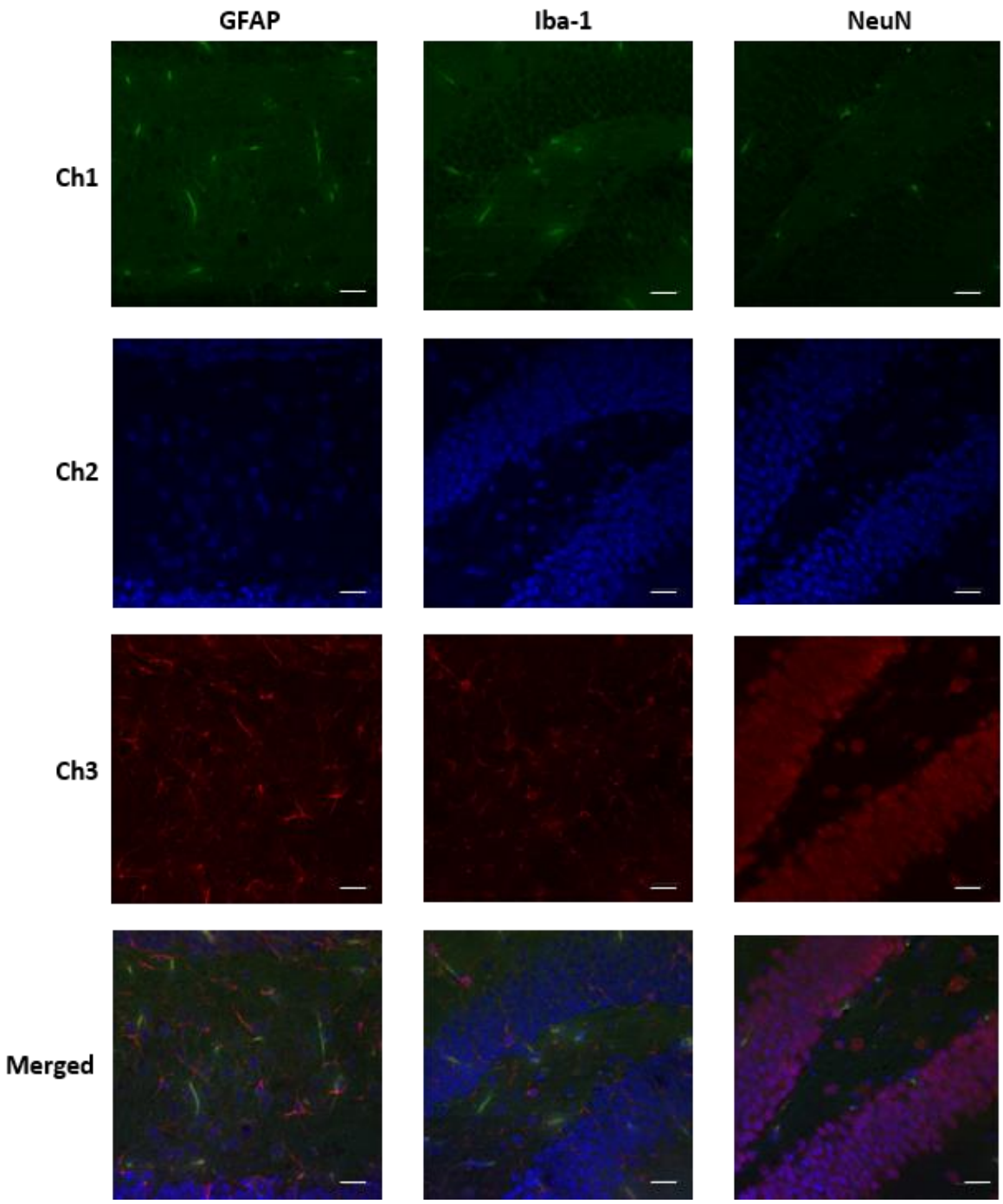

Figure 6.7. Confocal images of Flu-RI-OR2-NAG in dorsal dentate gyrus.

Brain sections stained with markers for astrocytes (anti-GFAP), activated microglia (anti-Iba-1), and neurons (anti-NeuN), and counterstained with DAPI (nucleus). Ch1 refers to the green fluorescence of the peptide, Ch2 is DAPI nucleus staining, Ch3 is the neuronal cell marker, and Merged refers to the merged images of Ch1, Ch2 and Ch3. Scale Bar = 20 µm.

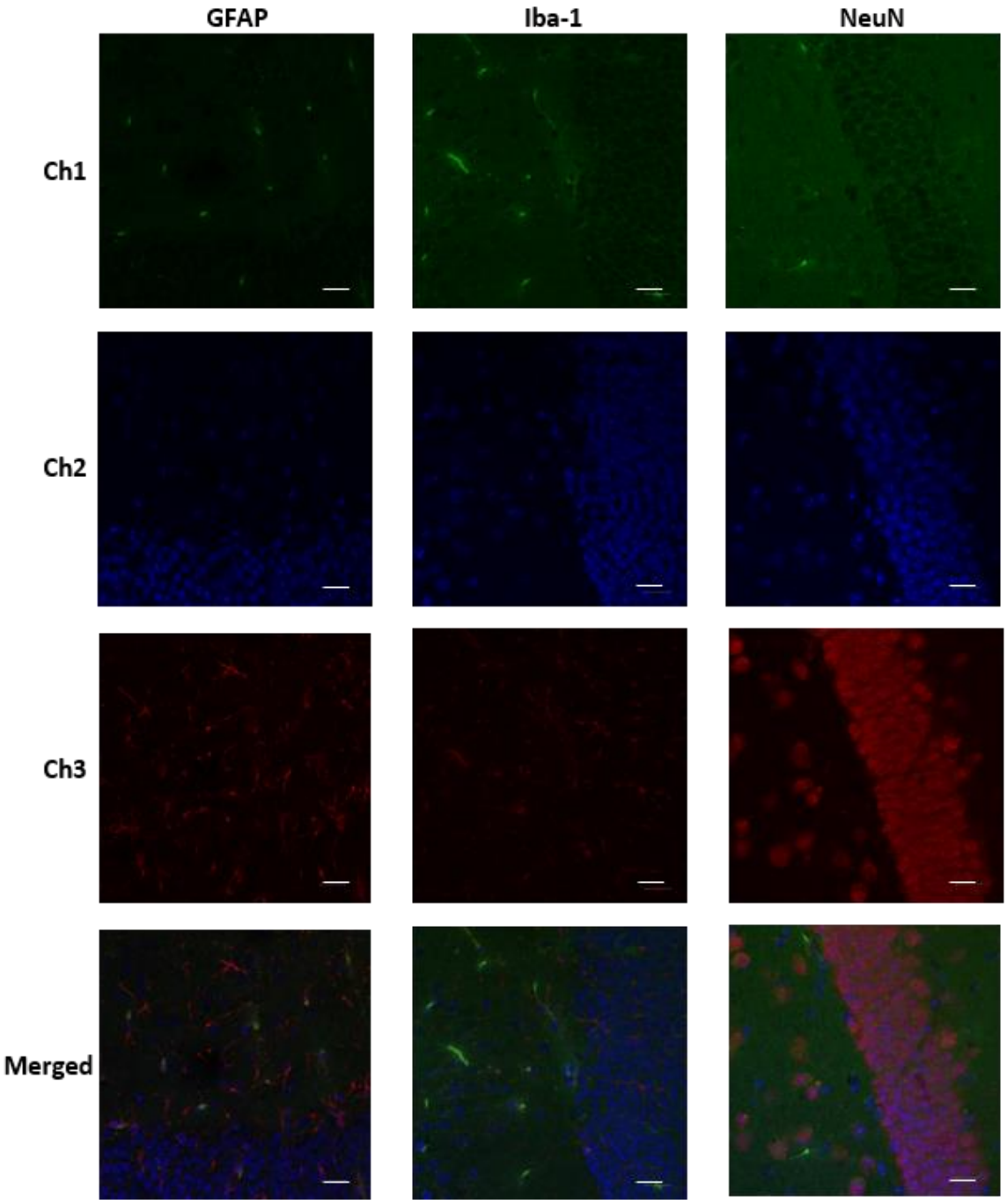

Figure 6.8. Confocal images of Flu-RI-OR2-NAG in ventral dentate gyrus.

Brain sections stained with markers for astrocytes (anti-GFAP), activated microglia (anti-Iba-1), and neurons (anti-NeuN), and counterstained with DAPI (nucleus). Ch1 refers to the green fluorescence of the peptide, Ch2 is DAPI nucleus staining, Ch3 is the neuronal cell marker, and Merged refers to the merged images of Ch1, Ch2 and Ch3. Scale Bar = 20 µm.

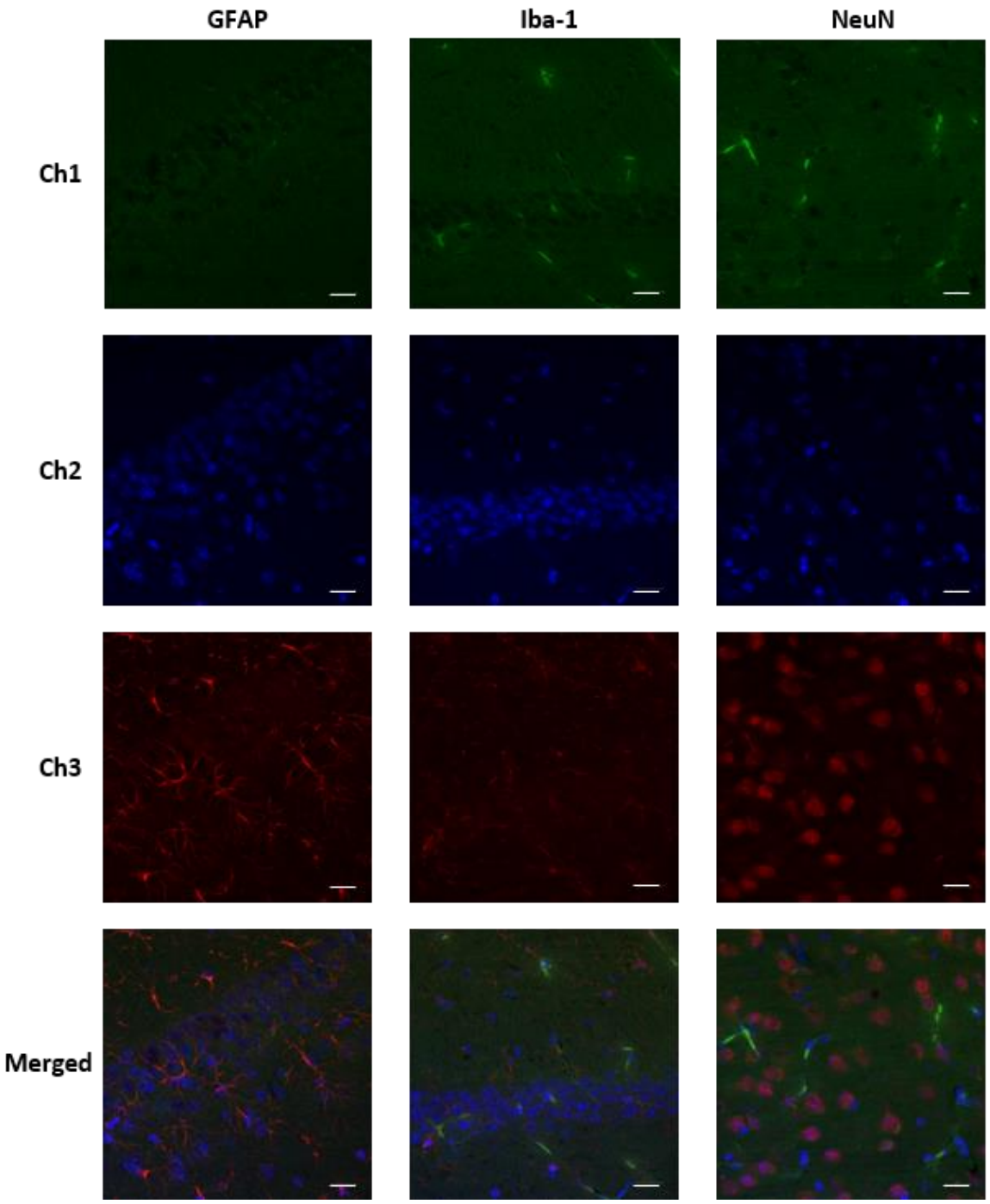

Figure 6.9. Confocal images of Flu-RI-OR2-NAG in CA1 region of the hippocampus.

Brain sections stained with markers for astrocytes (anti-GFAP), activated microglia (anti-Iba-1), and neurons (anti-NeuN), and counterstained with DAPI (nucleus). Ch1 refers to the green fluorescence of the peptide, Ch2 is DAPI nucleus staining, Ch3 is the neuronal cell marker, and Merged refers to the merged images of Ch1, Ch2 and Ch3. Scale Bar = 20 µm.

6.3.1.3. BODIPY-PINPs

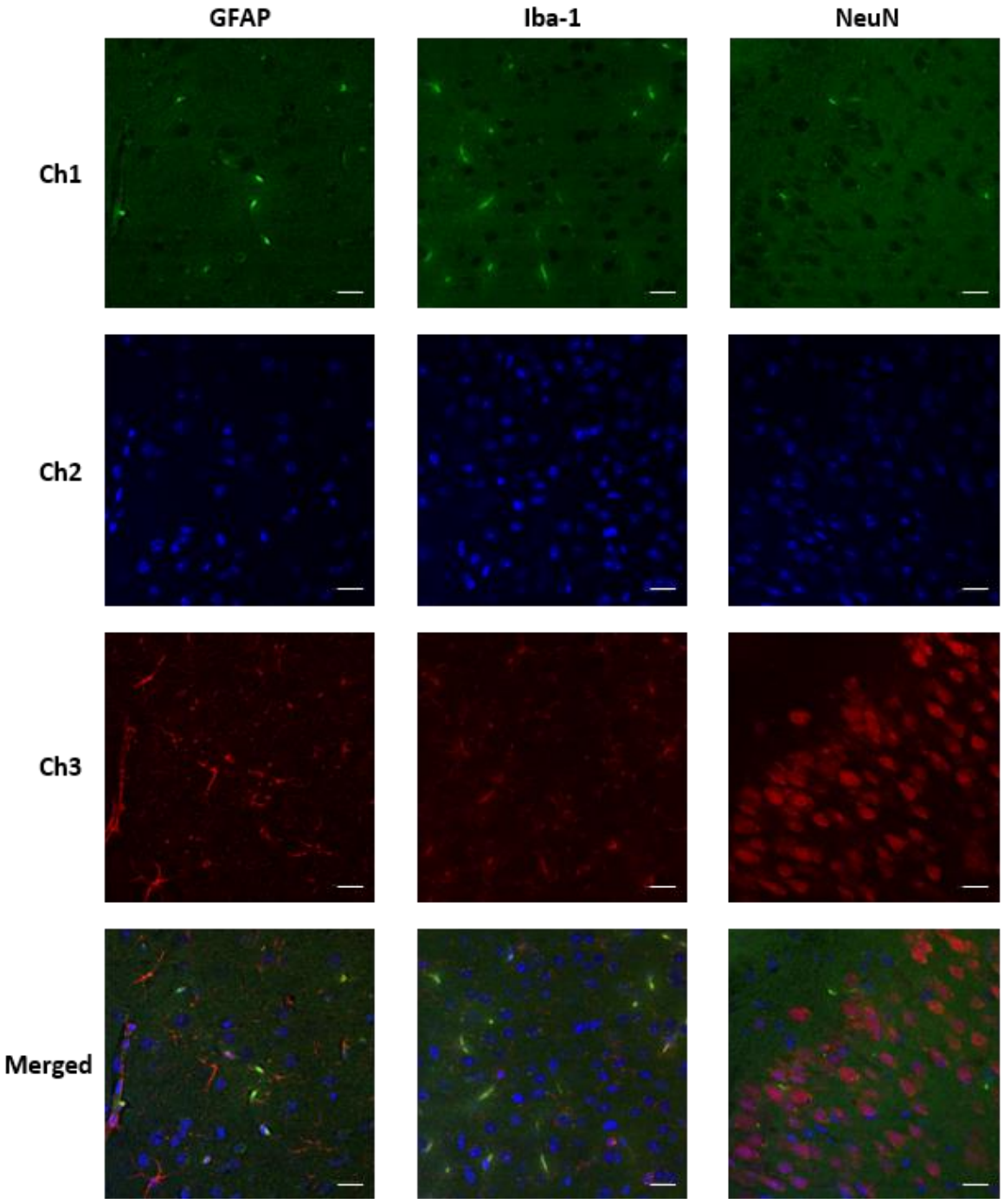

Figure 6.10. Confocal images of BODIPY-PINPs in cortex.

Brain sections stained with markers for astrocytes (anti-GFAP), activated microglia (anti-Iba-1), and neurons (anti-NeuN), and counterstained with DAPI (nucleus). Ch1 refers to the green fluorescence of the peptide, Ch2 is DAPI nucleus staining, Ch3 is the neuronal cell marker, and Merged refers to the merged images of Ch1, Ch2 and Ch3. Scale Bar = 20 µm.

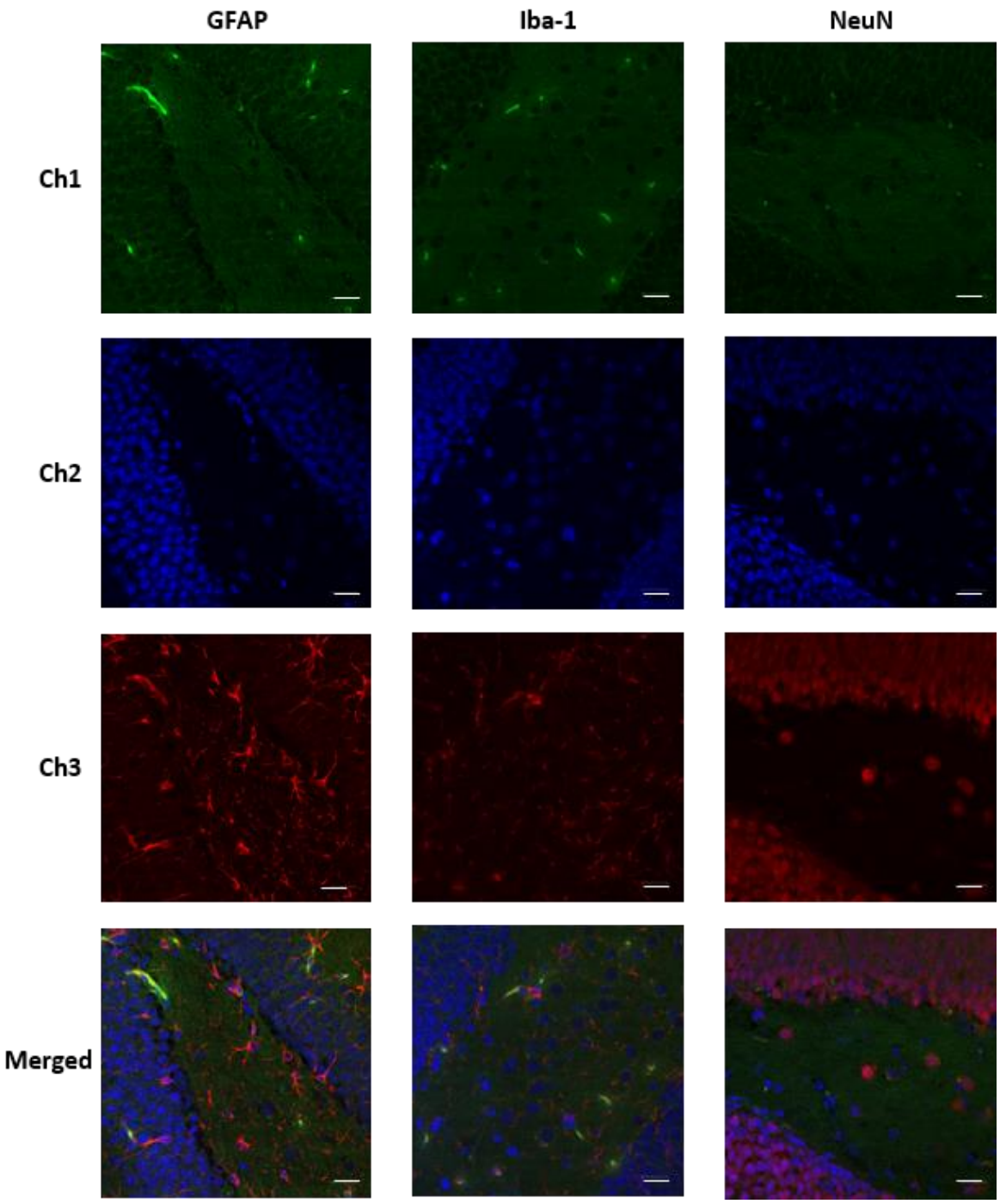

Figure 6.11. Confocal images of BODIPY-PINPs in dorsal dentate gyrus.

Brain sections stained with markers for astrocytes (anti-GFAP), activated microglia (anti-Iba-1), and neurons (anti-NeuN), and counterstained with DAPI (nucleus). Ch1 refers to the green fluorescence of the peptide, Ch2 is DAPI nucleus staining, Ch3 is the neuronal cell marker, and Merged refers to the merged images of Ch1, Ch2 and Ch3. Scale Bar = 20 µm.

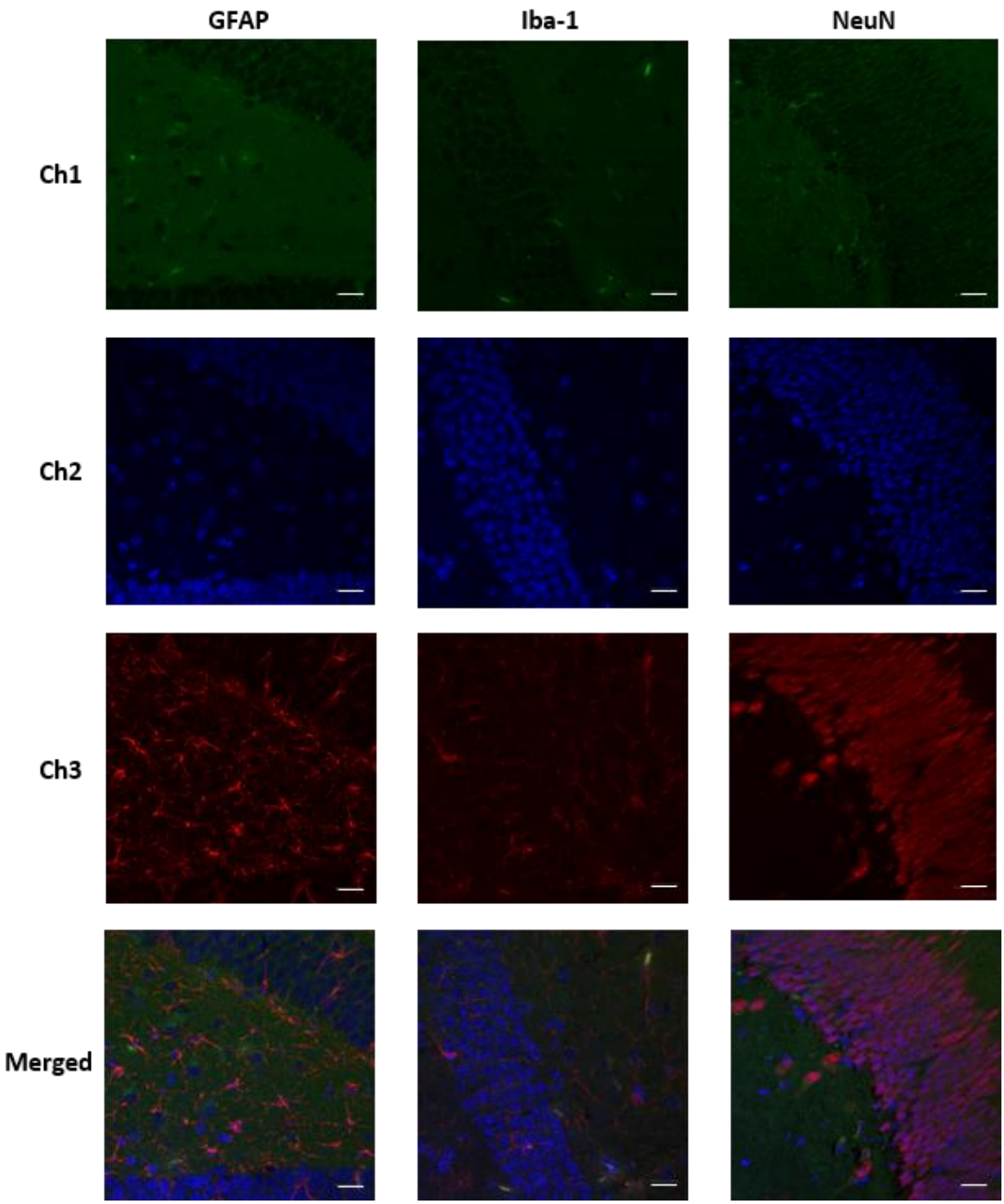

Figure 6.12. Confocal images of BODIPY-PINPs in ventral dentate gyrus.

Brain sections stained with markers for astrocytes (anti-GFAP), activated microglia (anti-Iba-1), and neurons (anti-NeuN), and counterstained with DAPI (nucleus). Ch1 refers to the green fluorescence of the peptide, Ch2 is DAPI nucleus staining, Ch3 is the neuronal cell marker, and Merged refers to the merged images of Ch1, Ch2 and Ch3. Scale Bar = 20 µm.

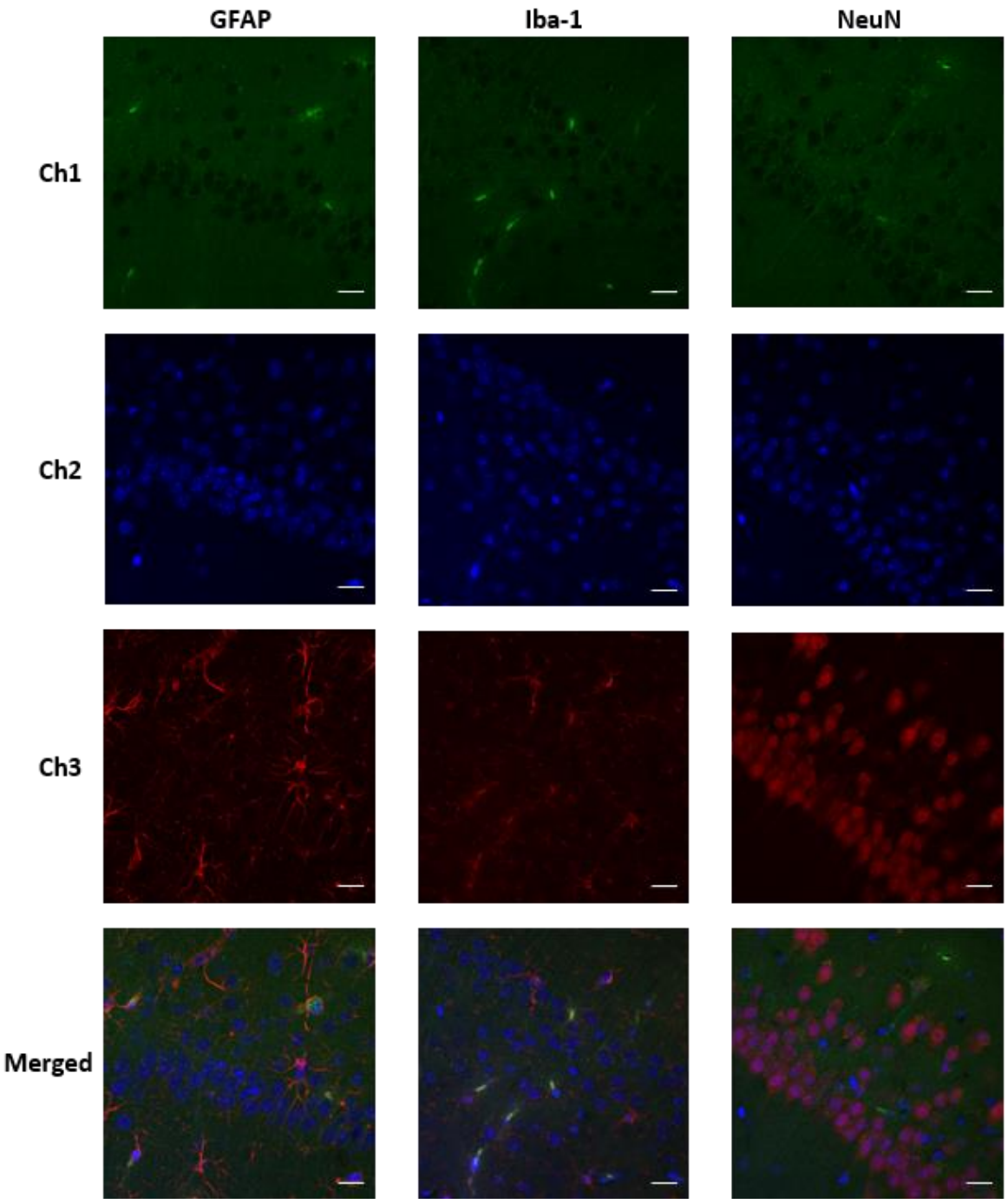

Figure 6.13. Confocal images of BODIPY-PINPs in CA1 region of the hippocampus.

Brain sections stained with markers for astrocytes (anti-GFAP), activated microglia (anti-Iba-1), and neurons (anti-NeuN), and counterstained with DAPI (nucleus). Ch1 refers to the green fluorescence of the peptide, Ch2 is DAPI nucleus staining, Ch3 is the neuronal cell marker, and Merged refers to the merged images of Ch1, Ch2 and Ch3. Scale Bar = 20 µm.

6.3.1.4. BODIPY-Control Liposomes

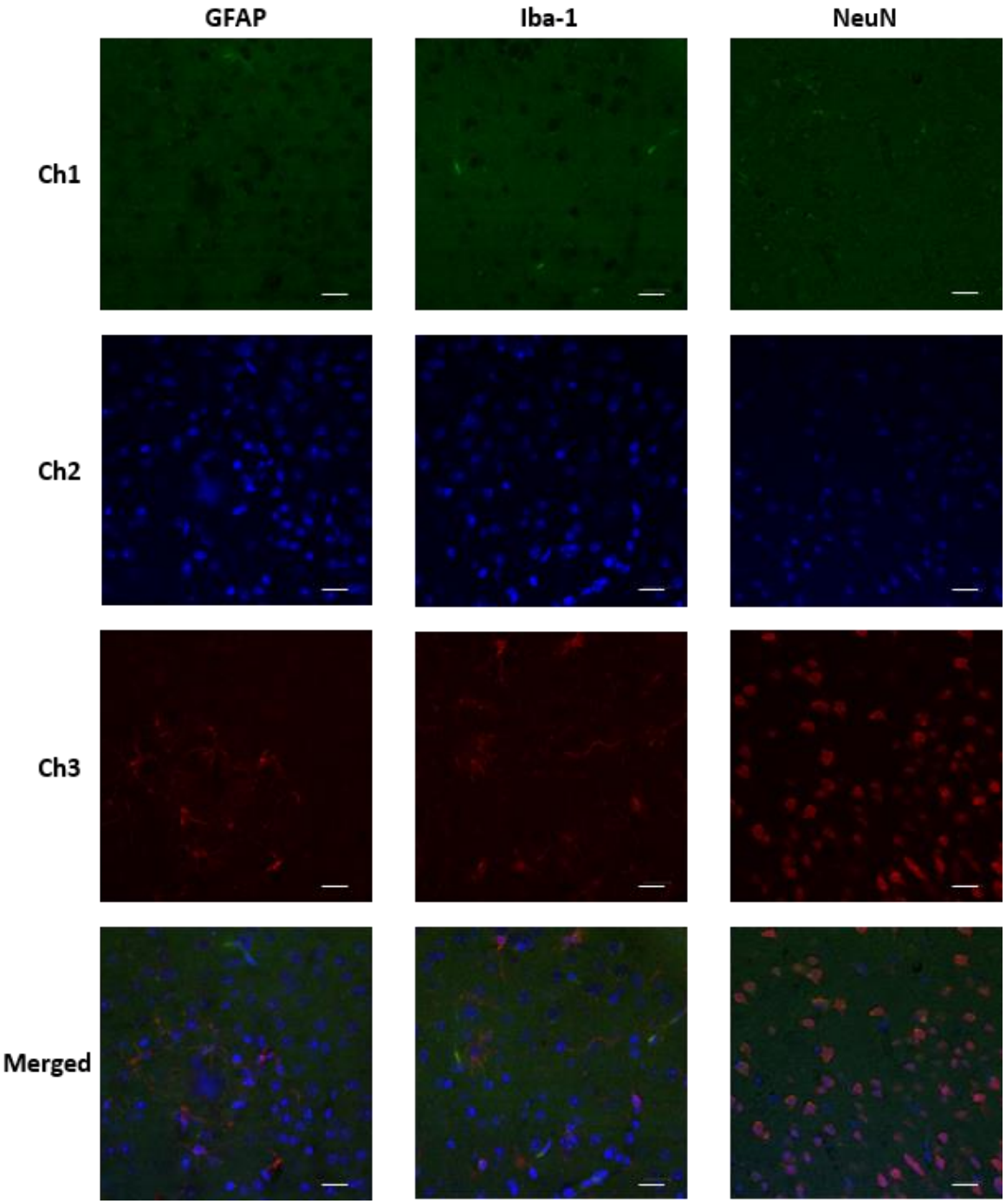

Figure 6.14. Confocal images of BODIPY-CL in cortex.

Brain sections stained with markers for astrocytes (anti-GFAP), activated microglia (anti-Iba-1), and neurons (anti-NeuN), and counterstained with DAPI (nucleus). Ch1 refers to the green fluorescence of the peptide, Ch2 is DAPI nucleus staining, Ch3 is the neuronal cell marker, and Merged refers to the merged images of Ch1, Ch2 and Ch3. Scale Bar = 20 µm.

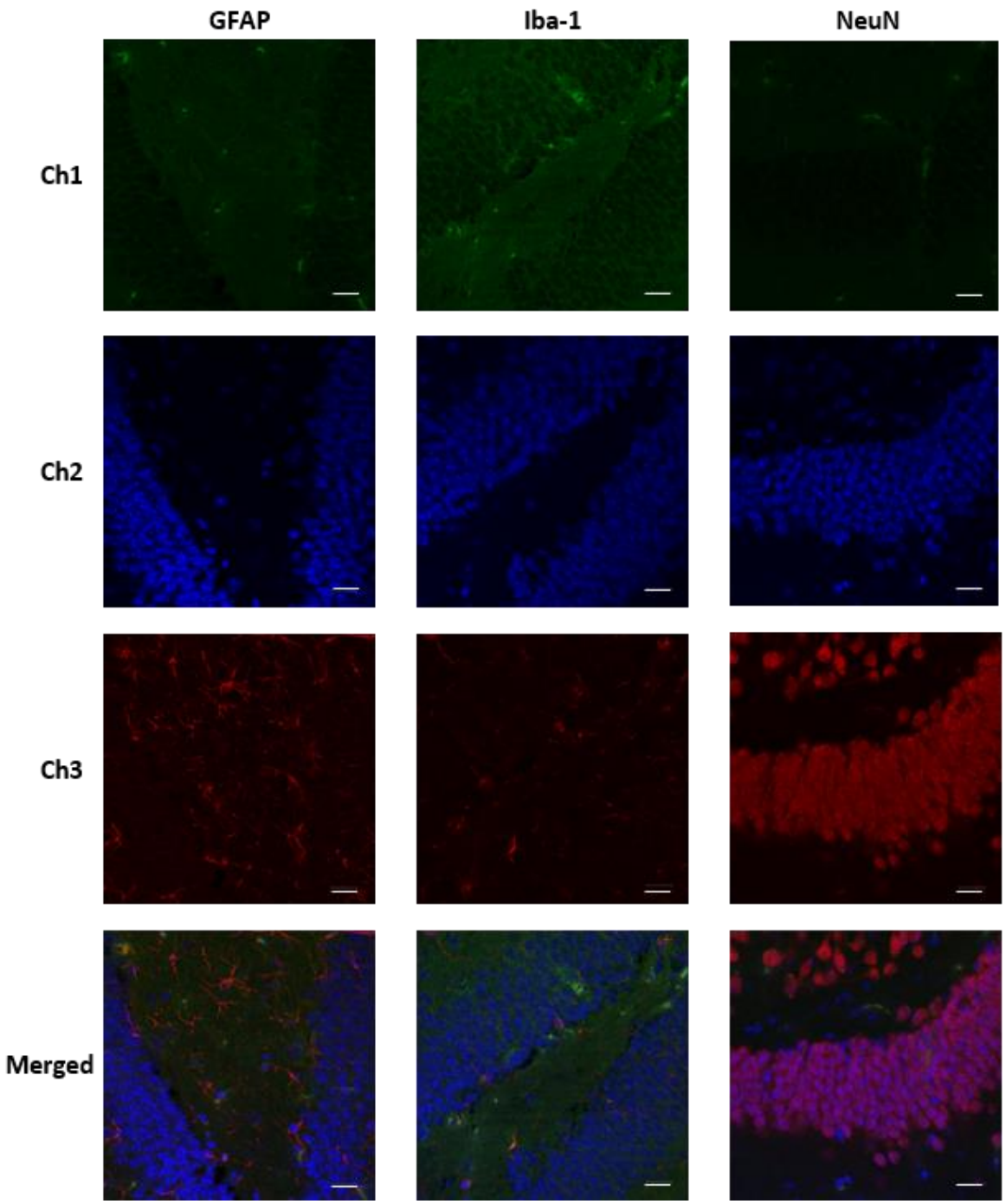

Figure 6.15. Confocal images of BODIPY-CL in dorsal dentate gyrus.

Brain sections stained with markers for astrocytes (anti-GFAP), activated microglia (anti-Iba-1), and neurons (anti-NeuN), and counterstained with DAPI (nucleus). Ch1 refers to the green fluorescence of the peptide, Ch2 is DAPI nucleus staining, Ch3 is the neuronal cell marker, and Merged refers to the merged images of Ch1, Ch2 and Ch3. Scale Bar = 20 µm.

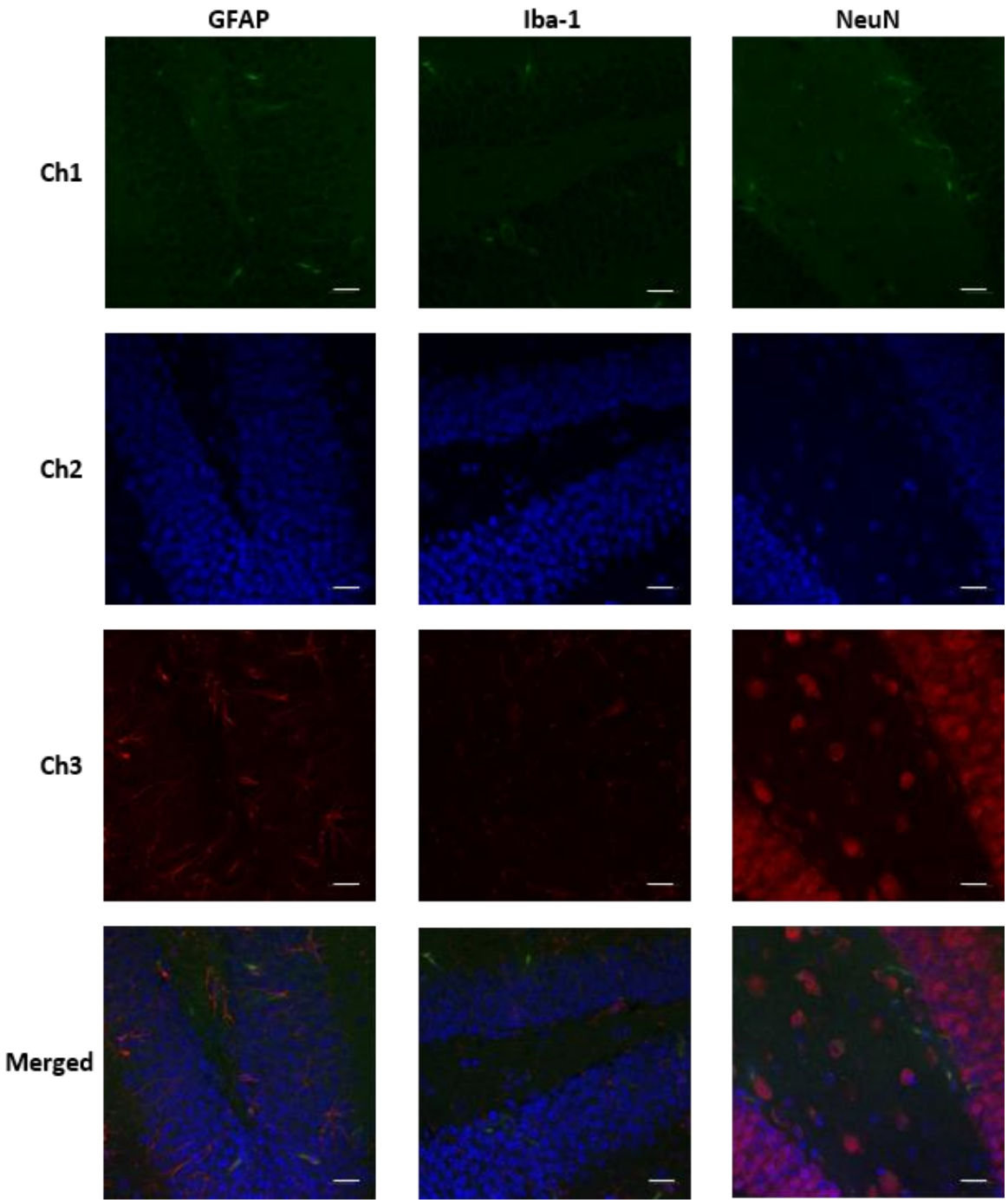

Figure 6.16. Confocal images of BODIPY-CL in ventral dentate gyrus.

Brain sections stained with markers for astrocytes (anti-GFAP), activated microglia (anti-Iba-1), and neurons (anti-NeuN), and counterstained with DAPI (nucleus). Ch1 refers to the green fluorescence of the peptide, Ch2 is DAPI nucleus staining, Ch3 is the neuronal cell marker, and Merged refers to the merged images of Ch1, Ch2 and Ch3. Scale Bar = 20 µm.

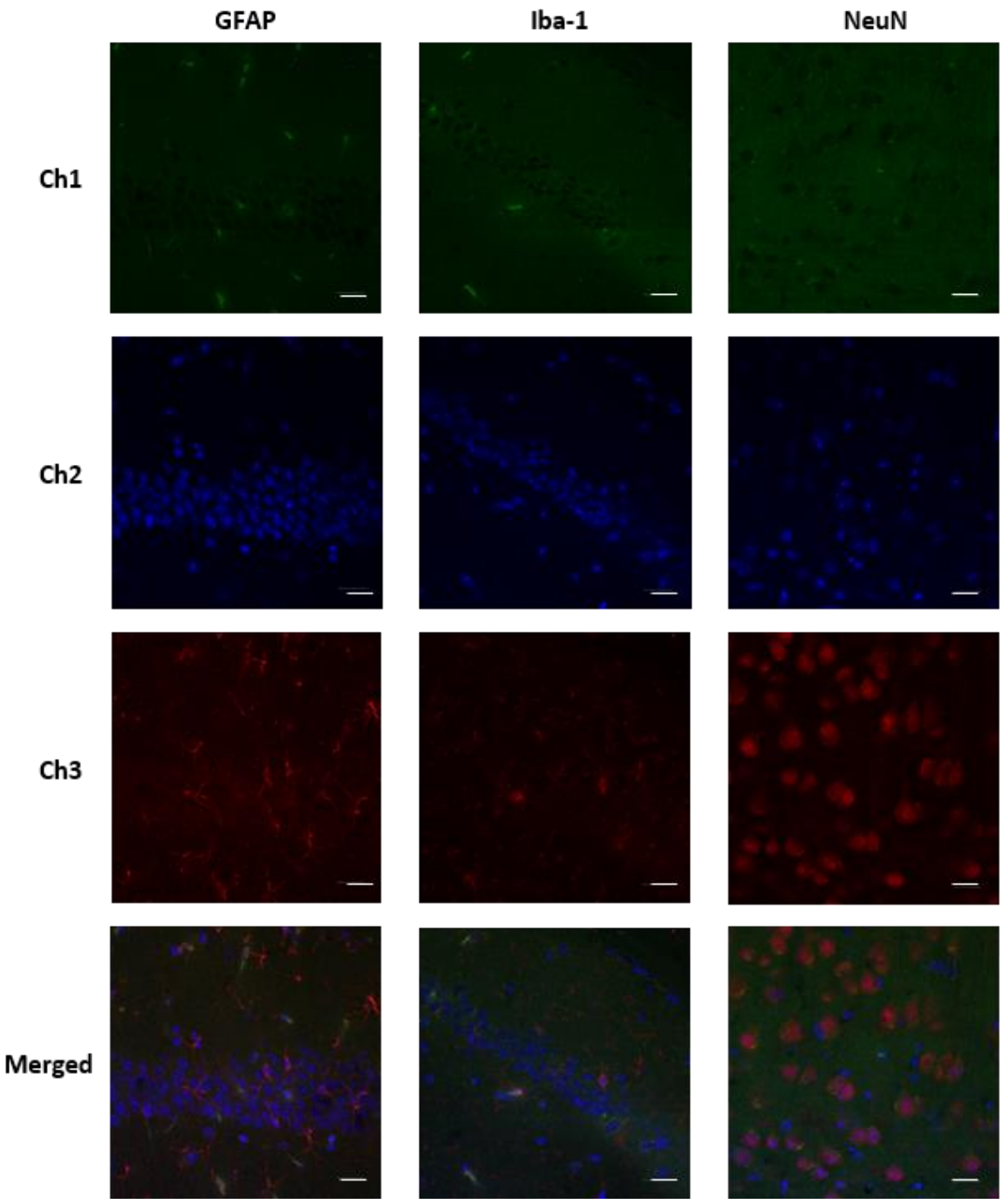

Figure 6.17. Confocal images of BODIPY-CL in CA1 region of the hippocampus.

Brain sections stained with markers for astrocytes (anti-GFAP), activated microglia (anti-Iba-1), and neurons (anti-NeuN), and counterstained with DAPI (nucleus). Ch1 refers to the green fluorescence of the peptide, Ch2 is DAPI nucleus staining, Ch3 is the neuronal cell marker, and Merged refers to the merged images of Ch1, Ch2 and Ch3. Scale Bar = 20 µm.

6.3.1.5. Vehicle control

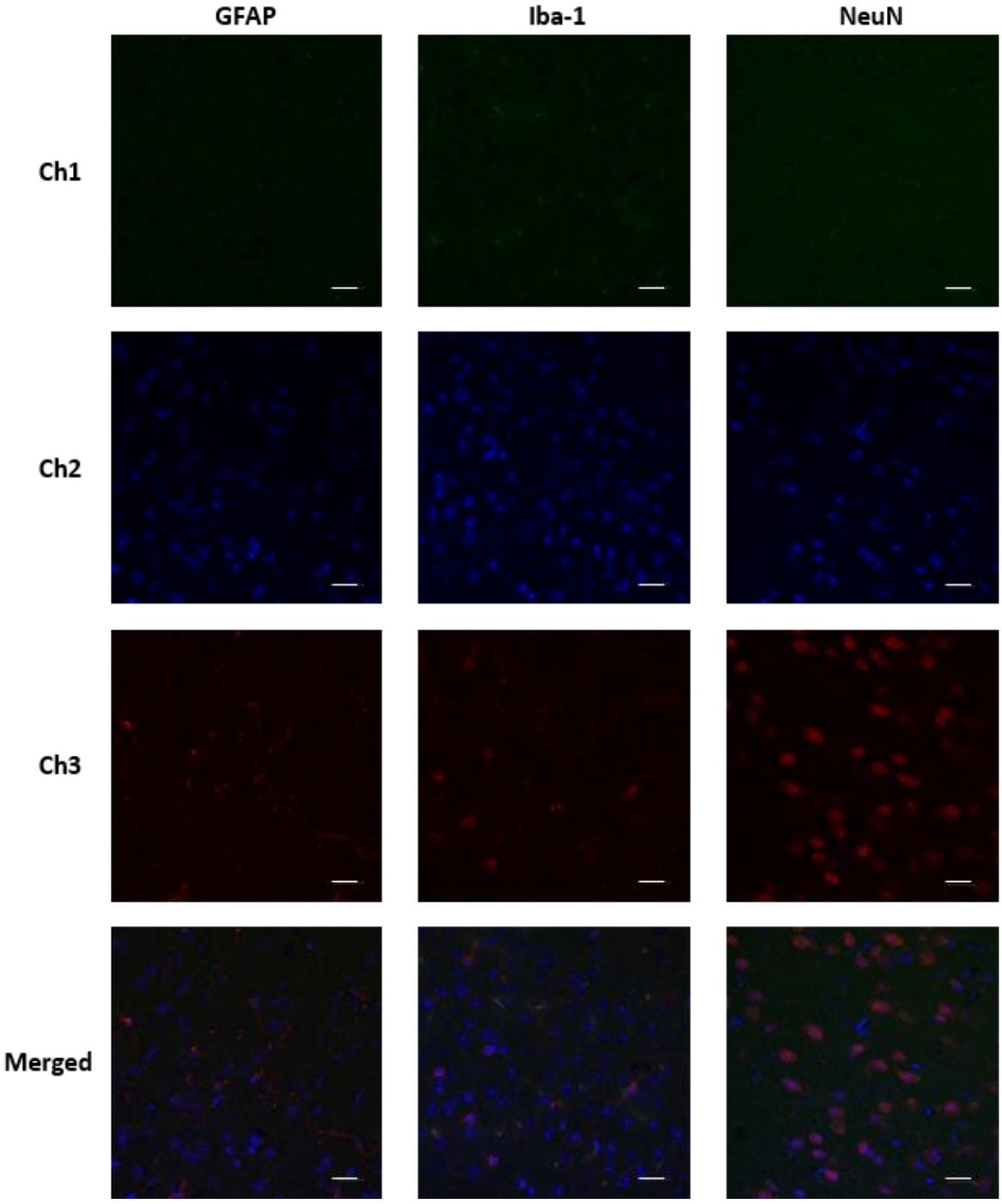

Figure 6.18.Confocal images of vehicle control in cortex.

Brain sections stained with markers for astrocytes (anti-GFAP), activated microglia (anti-Iba-1), and neurons (anti-NeuN), and counterstained with DAPI (nucleus). Ch1 refers to the background fluorescence of the vehicle control peptide, Ch2 is DAPI nucleus staining, Ch3 is the neuronal cell marker, and Merged refers to the merged images of Ch1, Ch2 and Ch3. Scale Bar = 20 µm.

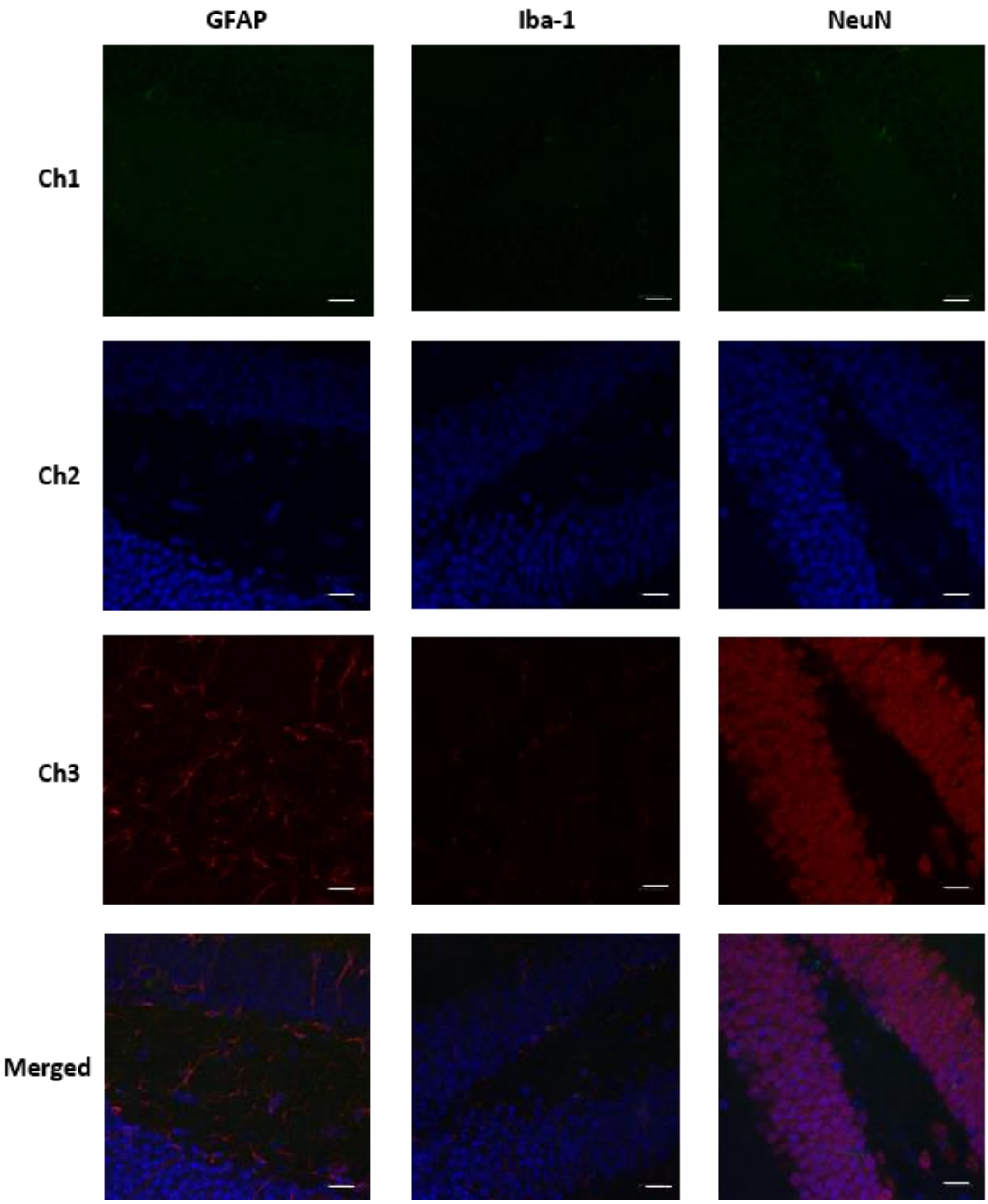

Figure 6.19. Confocal images of vehicle control in dorsal dentate gyrus.

Brain sections stained with markers for astrocytes (anti-GFAP), activated microglia (anti-Iba-1), and neurons (anti-NeuN), and counterstained with DAPI (nucleus). Ch1 refers to the background fluorescence of the vehicle control peptide, Ch2 is DAPI nucleus staining, Ch3 is the neuronal cell marker, and Merged refers to the merged images of Ch1, Ch2 and Ch3. Scale Bar = 20 µm.

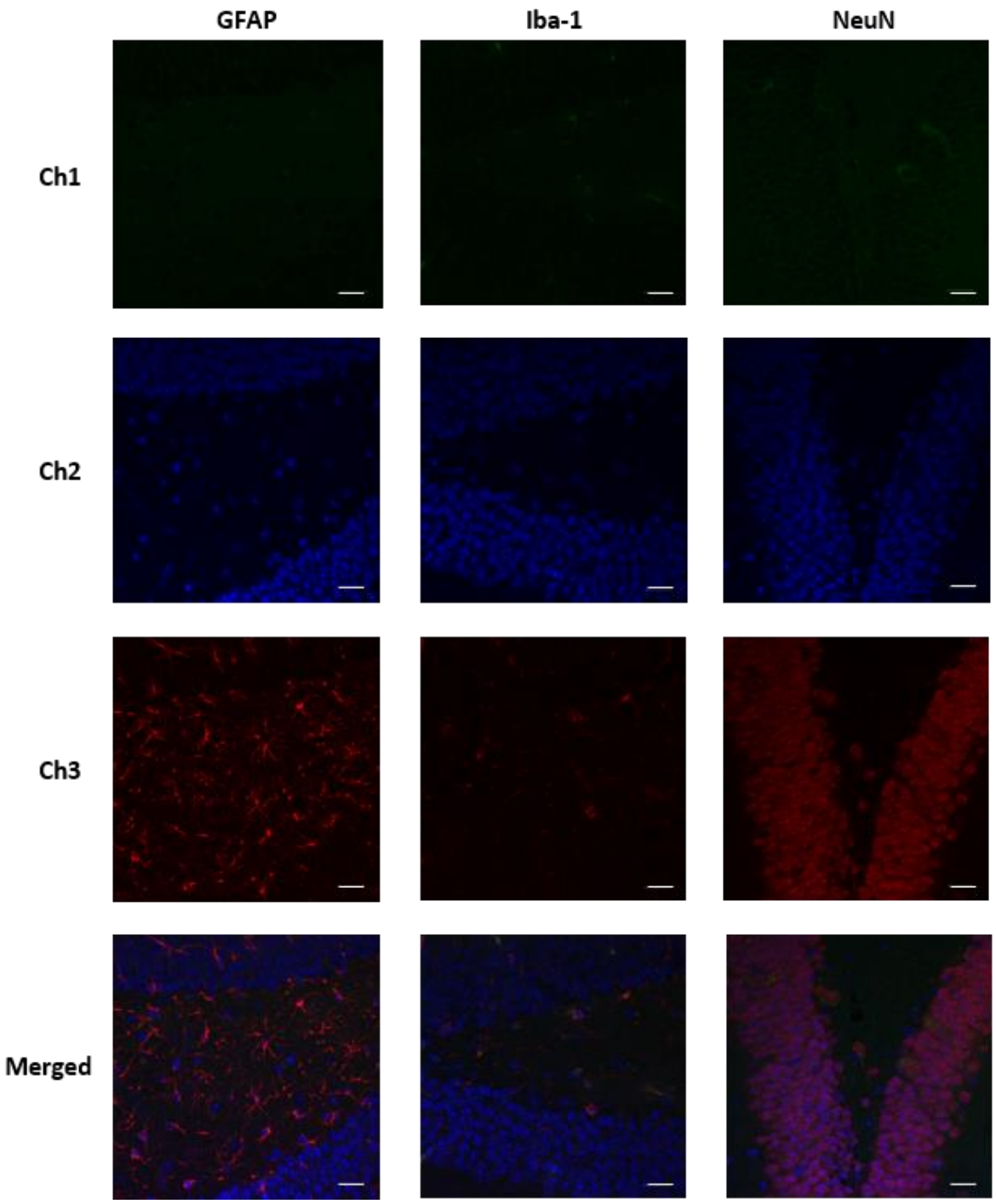

Figure 6.20. Confocal images of vehicle control in ventral dentate gyrus.

Brain sections stained with markers for astrocytes (anti-GFAP), activated microglia (anti-Iba-1), and neurons (anti-NeuN), and counterstained with DAPI (nucleus). Ch1 refers to the background fluorescence of the vehicle control peptide, Ch2 is DAPI nucleus staining, Ch3 is the neuronal cell marker, and Merged refers to the merged images of Ch1, Ch2 and Ch3. Scale Bar = 20 µm.

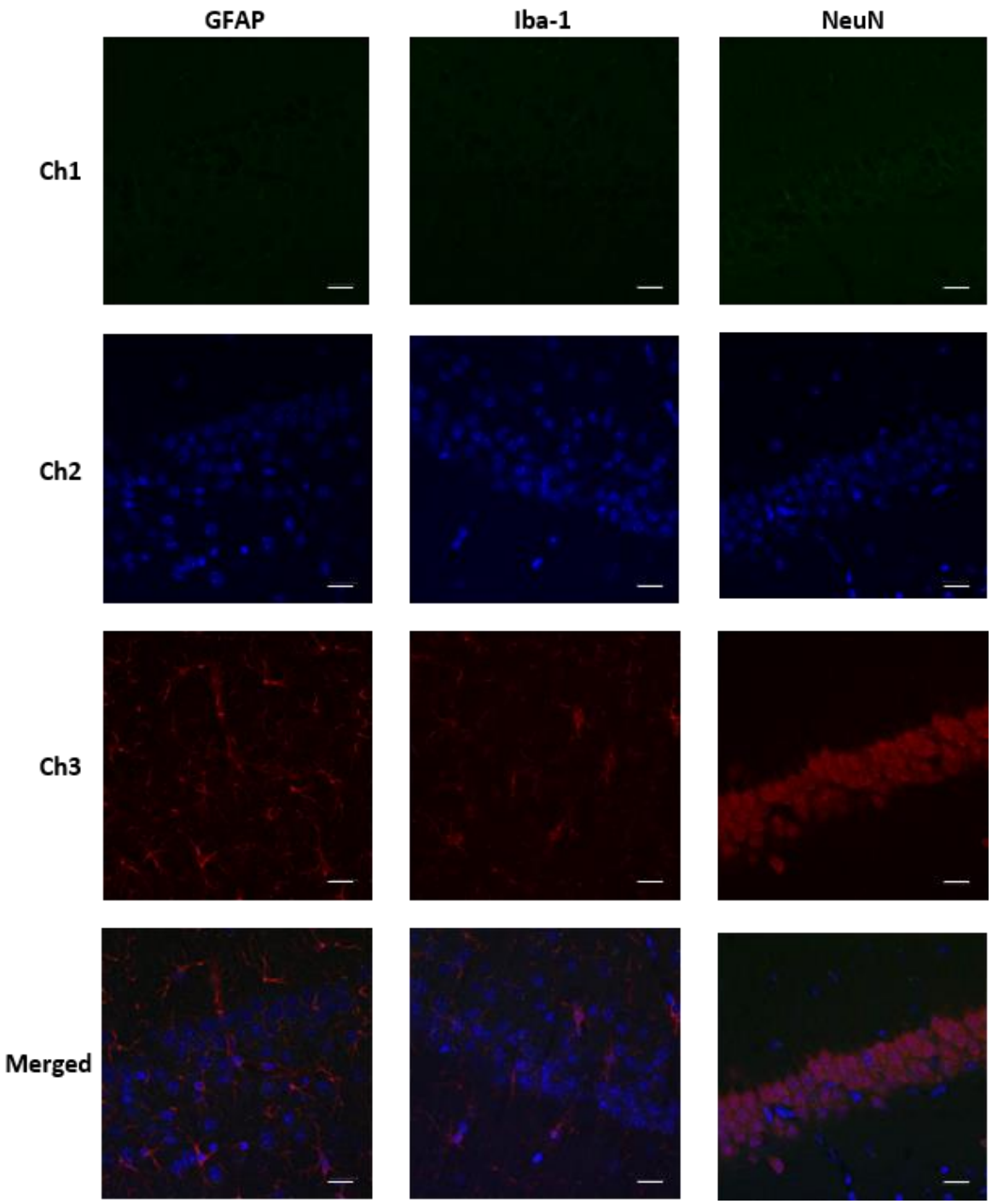

Figure 6.21. Confocal images of vehicle control in CA1 region of the hippocampus.

Brain sections stained with markers for astrocytes (anti-GFAP), activated microglia (anti-Iba-1), and neurons (anti-NeuN), and counterstained with DAPI (nucleus). Ch1 refers to the background fluorescence of the vehicle control peptide, Ch2 is DAPI nucleus staining, Ch3 is the neuronal cell marker, and Merged refers to the merged images of Ch1, Ch2 and Ch3. Scale Bar = 20 µm.

6.3.2. Total mean normalised intensity of the peptides

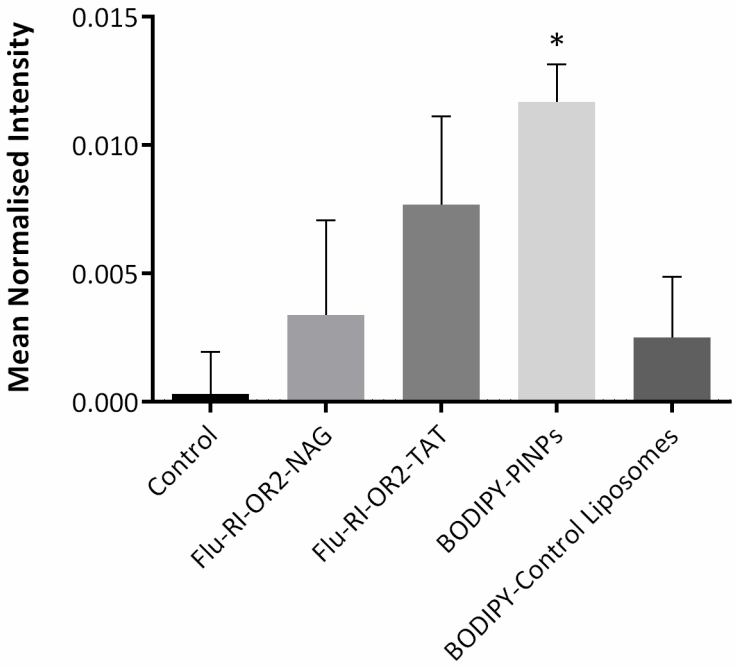

Figure 6.22. Total mean normalised intensity of the peptides in brain.

*The figure illustrates the total mean normalised intensity of the peptides in the cortex, CA1 and DG areas of the brain 1 h after peripheral administration (10 ml/kg) of 100 nmol/kg of free peptides and 4 µmol/kg of peptide-decorated and undecorated liposomes. The graph is presented as mean ± SEM (n = 5). Control mice were injected with 0.9 % NaCl (vehicle control). * indicates p ≤ 0.05 compared to control.*

One hour after peripheral administration of the peptides or peptide-liposomes, all of them demonstrated penetration across the BBB and deposition into the mouse brains, compared to the control mice that were injected with vehicle control. The BODIPY-PINPs peptide demonstrates significantly higher levels in the brain compared to the vehicle control indicating that attachment of the peptide to the nanoliposome device facilitates the transport of the peptides across the BBB, supported also by the observed intensity difference between the BODIPY-PINPs and the undecorated BODIPY-CL peptides.

6.3.3. Mean normalised peptide intensities in each brain region

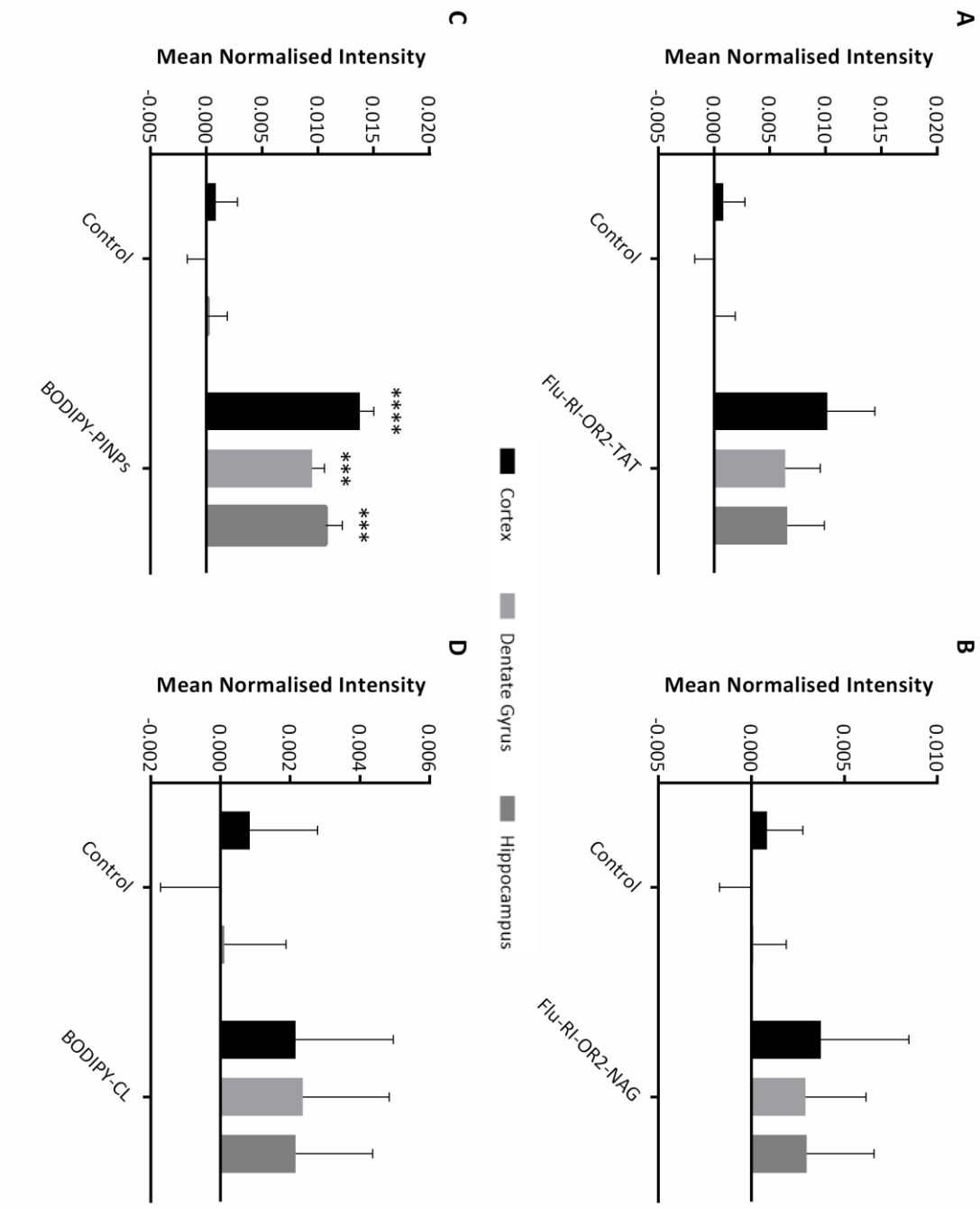

Figure 6.23. Normalised intensities of the peptides in each brain region.

*The figure represents the mean normalised intensities of (A) Flu-RI-OR2-TAT, (B) Flu-RI-OR2-NAG, (C) BODIPY-PINPs and (D) BODIPY-CL in the cortex, DG and CA1 of the hippocampus, compared to the vehicle control (normalised based on the brain region). The peptides were administered at 100 nmol/kg for the free peptides and 4 µmol/kg for the liposome peptides. The figure represents the mean ± SEM (n=5). *** indicates p ≤ 0.001, **** indicates p ≤ 0.0001 compared to control.*

All the peptides show deposition into the various brain regions compared to the vehicle control. The BODIPY-PINPs peptide demonstrates highly significant results compared to the control peptide for all the regions examined.

6.3.4. Mean normalised regional intensities of each peptide

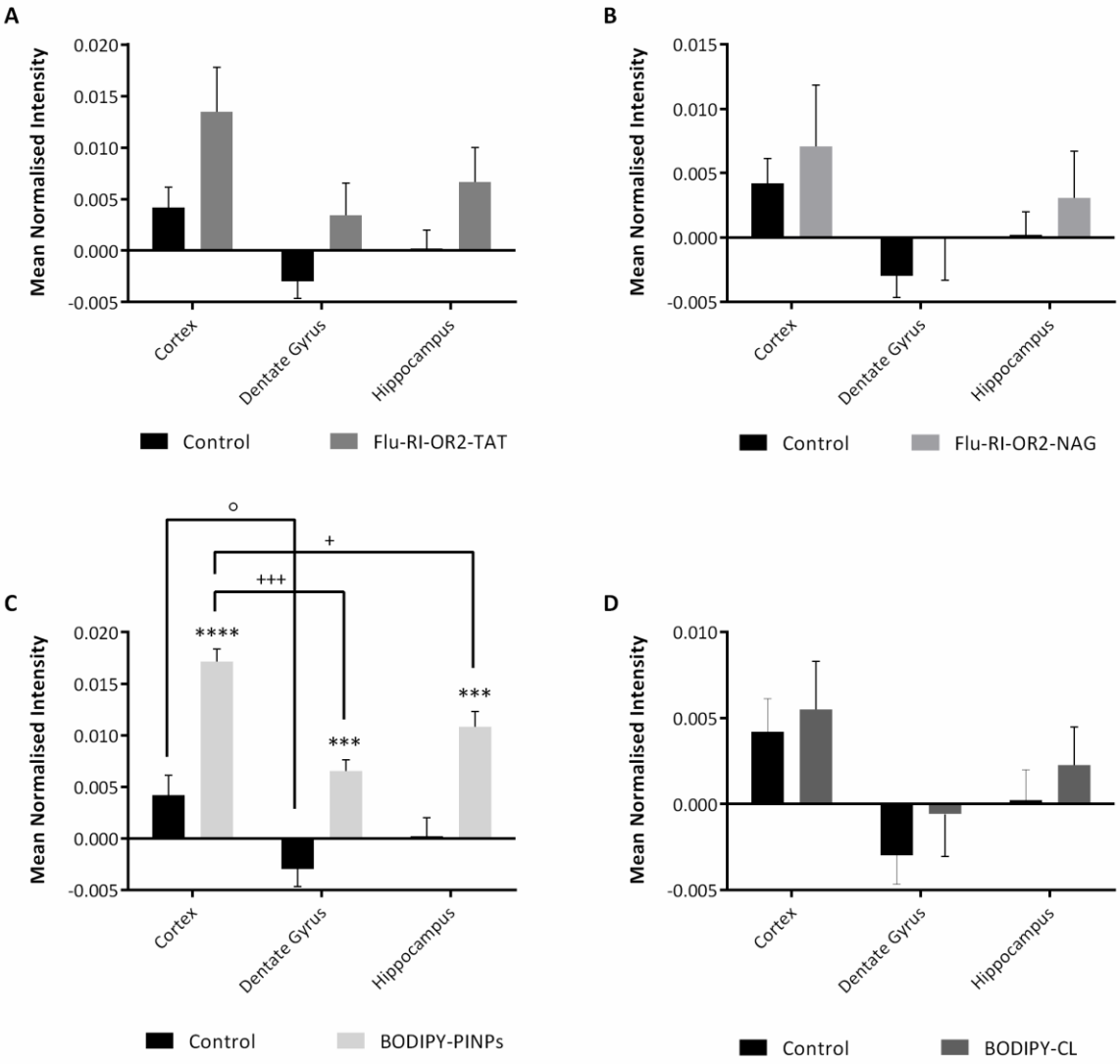

Figure 6.24. Normalised regional intensities of each peptide.

*The figure represents the intensities in each brain region examined for (A) Flu-RI-OR2-TAT, (B) Flu-RI-OR2-NAG, (C) BODIPY-PINPs, and (D) BODIPY-CL compared to the vehicle control regional intensities (normalised based on the average of the vehicle control). The peptides were administered at 100 nmol/kg for the free peptides and 4 µmol/kg for the liposome peptides. The figure represents the mean ± SEM (n=5) and statistical analysis was performed between control versus treatment; and region vs region for each condition. *** indicates p ≤*

*0.001 (control vs treatment), **** indicates p ≤ 0.0001 (control vs treatment), + indicates p ≤ 0.05 (region vs region), +++ indicates p ≤ 0.001 (region vs region), ° indicates p ≤ 0.05 (region vs region).*

The peptides demonstrate increased fluorescence compared to the vehicle control for each brain region. Comparison between the brain regions for each peptide treatment show significant differences for the BODIPY-PINPs peptide that exhibit increased deposition in the cortex of the brains relevant to the dentate gyrus and the CA1 of the hippocampus. Significant difference is also observed in the control treatment between the cortex and the dentate gyrus regions of the brains.

6.3.5. Comparison of the peptides in dorsal and ventral dentate gyrus

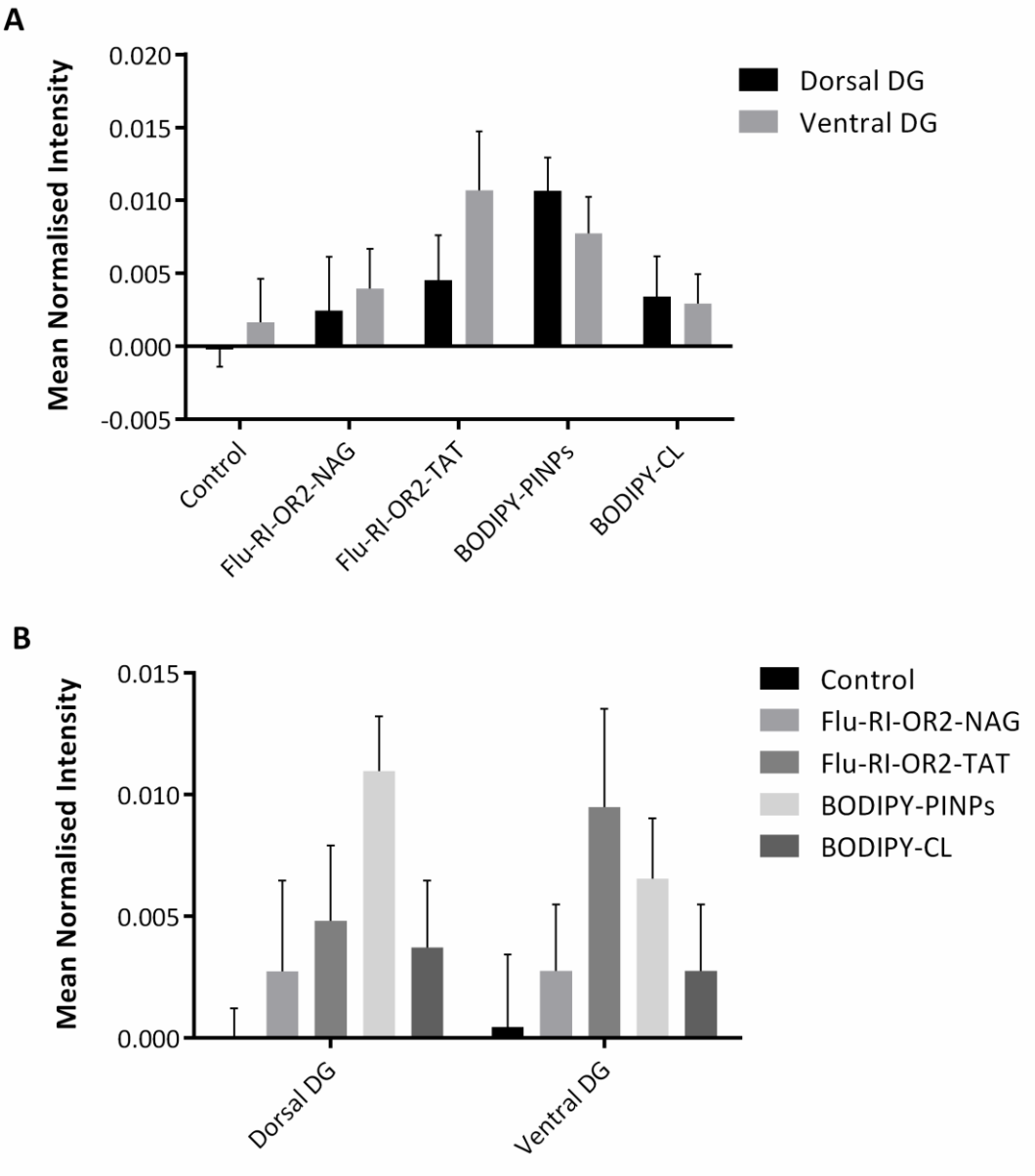

Figure 6.25. Normalised peptide and regional intensities in dorsal and ventral dentate gyrus.

The figure represents the normalised (A) peptide intensities (normalised based on the brain region) and (B) regional intensities (normalised based on the average of the vehicle control) in dorsal and ventral DG of the mice brains. The figure is presented as mean ± SEM (n=5).

The first figure demonstrates the differences in the deposition of the peptides in the dorsal and ventral DG of the mouse brains. Even though no significant difference was observed, the free peptides were found mostly in the ventral DG whereas the

liposome-bound peptides were found more in the dorsal DG of the brain. The second figure shows a comparison between the peptide differences in each DG compartment. Comparison of the peptides' intensities in the dorsal DG demonstrates that the BODIPY-PINPs peptide is found in increased levels compared to the other peptides, in contrast to the ventral DG where the Flu-RI-OR2-TAT peptide seemed to be present at higher levels than the other peptides examined.

6.3.6. Deposition of the peptides in the brains (Percentage normalised intensities)

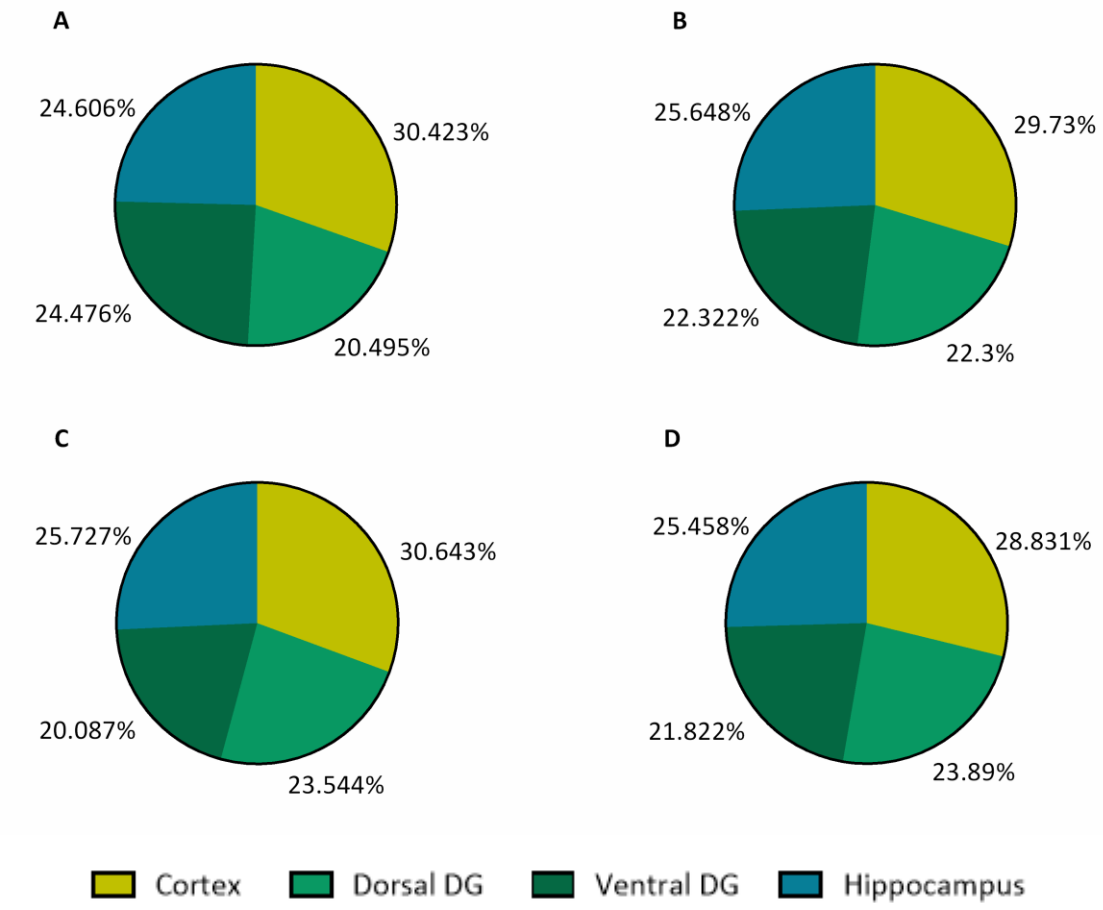

Figure 6.26. Percentage normalised intensities of the peptides in brain.

The figure demonstrates pie charts of the percentage total mean intensity of the (A) Flu-RI-OR2-TAT, (B) Flu-RI-OR2-NAG, (C) BODIPY-PINPs and (D) BODIPY-CL in the cortex, dorsal and ventral DG and CA1 of the hippocampus.

The mean normalised intensities of the four peptides were calculated as percentages and presented as pie charts. With respect to the DG, the peptide intensities were correlated to the longitudinal plane of the sections and are presented as dorsal and

ventral DG. All of the peptides seem to be deposited at higher levels in the cortex of the brains relative to the other brain regions examined. Similar intensity levels are observed in the other brain regions for each of the peptides examined.

6.4. Discussion

One major problem associated with the treatment of various neurodegenerative diseases, including AD, is the inability of potential drugs to penetrate across the BBB and accumulate in the brain in sufficient amounts to achieve the desired effect (Begley, 2004). This Chapter presents the ability of our candidate peptides to penetrate across the BBB and accumulate in major brain areas that are primarily involved in the pathology of AD. The Flu-RI-OR2-TAT, Flu-RI-OR2-NAG and BODIPY-PINPs peptides all demonstrated BBB passage and were found in the cortex, hippocampus and dentate gyrus areas of the brain.

6.4.1. Flu-RI-OR2-TAT brain deposition

The Flu-RI-OR2-TAT peptide was previously investigated in a BBB penetration study using APP/PS1 Alzheimer's transgenic mice (Parthsarathy et al., 2013). However, as the BBB in AD, and in these mice, is disrupted (Banks, 2012; Erickson and Banks, 2013), it was decided to investigate whether the peptide is able to cross an integral and functional BBB. The Flu-RI-OR2-TAT peptide indeed demonstrated penetration of the intact BBB in WT mice when they were examined 1 h after i.p. administration.

Flu-RI-OR2-TAT was found in the cortex of the mouse brains, which is possibly the primary region of the brain where amyloid plaques are observed. The Flu-RI-OR2-TAT peptide was also detected in similar amounts (based on intensity quantification) in the hippocampus and the DG of the brain. Even though the number of young neurons present in the DG was not calculated in this project, the fact that the peptide was detected in this brain region further supports the data observed by Parthsarathy and colleagues where the peptide stimulated neurogenesis demonstrating the ability to reverse the toxic effect of Aβ in the brain (Parthsarathy et al., 2013).

In the case of the hippocampus, there is a particular interest in the CA1 area, which has demonstrated significant neurodegeneration in the initial stages of the disease, as demonstrated by Padurariu and colleagues (Padurariou et al., 2012). Flu-RI-OR2-TAT was found in both in the CA1 and DG regions of the brain, indicating that this peptide may be able to prevent neuronal dysfunction in the CA1 region of the hippocampus as well.

The accumulation of the peptide in cellular sites and vascular capillaries is further investigated in Chapter 7.

6.4.2. BODIPY-PINPs brain deposition

The BODIPY-PINPs peptide demonstrates significant results in the BBB penetration study, demonstrating that the attachment of the peptide on the liposome results in an improved peptide inhibitor. For comparison purposes, I have also included undecorated control liposomes, which in general show limited penetration and deposition in the brain, indicating that the RI-OR2-TAT peptide on the liposome facilitates the transport of the peptide across the BBB and accumulation in the brain.

A similar study on the BBB penetration properties of PINPs was performed using an artificial BBB model composed of a hCMEC/D3 cell monolayer where the PINPs demonstrated enhanced permeability compared to undecorated control liposomes (Gregori et al., 2017). This study, further supports the fact that the BODIPY-PINPs are able to cross the BBB, an ability that is maintained from the initial free RI-OR2-TAT peptide (Parthsarathy et al., 2013).

Similar to the Flu-RI-OR2-TAT peptide, the BODIPY-PINPs were located more in the cortex of the brain compared to the CA1 area of the hippocampus and DG. As previously explained, this supports the idea that the peptide can facilitate the generation of young new neuronal cells in the brain, and protect against neuronal dysfunction and amyloid plaque formation in the diseased brains, so providing a candidate peptide for the treatment of AD.

6.4.3. Flu-RI-OR2-NAG brain deposition

The results obtained from study investigating the ability of the Flu-RI-OR2-NAG peptide to cross the BBB demonstrate that the peptide can penetrate into the brain, although with much lower efficacy compared to the Flu-RI-OR2-TAT and BODIPY-PINPs peptides. These results show that the peptide potentially utilises the *N*-acetylglucosamine transporters on neuronal cells and the glucose transporters at the BBB, but the NAG moiety on the peptide is not as effective as a transport modulator as the HIV1 virus TAT sequence that was previously incorporated onto the RI-OR2 peptide.

The Flu-RI-OR2-NAG peptide also seems to locate more into the cortex of the brains. The localisation of the peptide in CA1 of the hippocampus, and the DG, however, suggest that this peptide could be useful therapeutically, and possibly stimulate neurogenesis and protect against neuronal damage in a similar way to RI-OR2-TAT and PINPs.

The efficacy of the Flu-RI-OR2-NAG peptide, including its ability to penetrate across the BBB, could be improved by attaching the peptide onto the surface of synthetic nanoliposomes, in a similar way to the PINPs, to generate a more effective multivalent peptide.

6.4.4. Comparison of the dorsal-ventral DG peptide deposition

The variety of processes controlled by the hippocampus, including not only involvement in episodic memory and spatial navigation (Eichenbaum, 2013; Leuner and Gould, 2010), but also implementation of emotional responses (Bannerman et al., 2004), changes in hormonal levels (Lathe, 2001) and detection of novel stimuli (Knight, 1996), have been related to different regions along the longitudinal axis of the hippocampus. Several studies on the dorsal and ventral regions of the hippocampus have demonstrated that the areas are functionally heterogeneous. The dorsal portion of the hippocampus is involved in learning and spatial memory, whereas the ventral region is involved in emotion, behaviour and anxiety (Amaral and Witter, 1989; Moser and Moser, 1998; Fanselow and Dong, 2010).

As the DG is part of the hippocampal formation it should not be considered as a homogeneous structure, as variations in the cellular content of the DG can be associated with the differential properties of the dorsoventral axis of the hippocampus (Fanselow and Dong, 2010). A study by Fuster-Matanzo and colleagues demonstrated that the functional differences between the two DG poles are linked to the time variation of the appearance of cognitive and behavioural decline symptoms in various neurodegenerative diseases (Fuster-Matanzo et al., 2011). Similarly, Kheirbek and Hen suggested that the granule cells present in the DG may contribute to different functions associated with learning and emotion (Kheirbek and Hen, 2011).

Based on these studies I decided to investigate whether the peptides are extensively deposited in either of the two poles of the DG. The results obtained from our study demonstrated that the Flu-RI-OR2-TAT and Flu-RI-OR2-NAG peptides are found mainly in the ventral DG, whereas the BODIPY-PINPs are found more in the dorsal DG. These differences between the peptides suggest the RI-OR2-TAT and RI-OR2-NAG peptides can improve the behavioural changes that occur in patients with AD; while PINPs peptide can recover the cognitive deficits of the disease. However, as the peptides are detected in both regions of the dorsoventral axis of the DG (Figure 6.25.), this outcome suggests that the peptides may affect both of these functional processes of the hippocampus. Further investigation of the distribution of these peptides within the DG, along with behavioural tests that involve APP/PS1 transgenic mice, are necessary to confirm such a finding.

6.5. Conclusions

The results generated from this study demonstrate that Flu-RI-OR2-TAT, Flu-RI-OR2-NAG and BODIPY-PINPs are able to cross an intact and functional BBB and accumulate in the cortex and hippocampus of the brain, regions that are primarily affected in AD, as well as in the DG which contains a neuronal stem cell population.

A main restriction of this study is the limited number of animals used, which also explains the large error bars in some of the graphs presented. However, the pattern observed in the total normalised intensities of the peptides correlates with other studies presented in this thesis, or published by our research group. Examples include the ability of Flu-RI-OR2-TAT to penetrate across the BBB in APP/PS1 transgenic mice (Parthsarathy et al., 2013), or an artificial BBB in the case of PINPs (Gregori et al., 2017). Additionally, the lower fluorescence intensity observed with the Flu-RI-OR2-NAG peptide compared to the Flu-RI-OR2-TAT peptide was also observed in the cell penetration experiments presented in Chapter 3, Section 3.3.3.

One major finding of this Chapter is that the liposome-attached RI-OR2-TAT peptide has an enhanced ability to cross the BBB compared to the RI-OR2-TAT free peptide and control undecorated liposomes. Moreover, focusing on the therapeutic abilities of the peptides, their accumulation in the DG of the brain suggests that they may be able to stimulate neurogenesis in diseased brains, or reverse the toxic effects of Aβ on neuronal stem cells, as well as improving both cognition and memory. This finding also correlates with the ability of the peptides to enhance cell viability and proliferation, in studies presented in Chapter 3, Section 3.3.2. using cultured SH-SY5Y neuroblastoma cells.

Chapter 7: Co-localisation of peptides with neuronal and glial markers

7.1. Introduction

7.1.1. The study of co-localisation

The study of co-localisation can provide basic evidence on the structural and functional characteristics of two antigens of interest. The co-existence of a signal at a particular pixel location when examining multichannel fluorescence microscopy images provides an initial clue of spatial overlap between the two fluorescent antigens (Zinchuk et al., 2007).

There are many techniques used to identify the co-localisation of two biological phenomena, which can be divided into qualitative and quantitative methods. The qualitative approach involves the presentation of a merged image where co-localisation is demonstrated by the colour change on colocalised pixels between two fluorescent channels. The quantitative approach involves the statistical analysis of the degree of co-localisation where the frequency of coincidental objects and the interdependence of the two different channels is calculated (Manders et al., 1993).

7.1.2. Introduction on co-localisation analysis

Qualitative analysis can provide initial insights into co-localisation estimation. Merged fluorescent images, colocalised pixel maps and scatterplots of pixel intensities of each channel's image demonstrate to some degree the co-localisation of two objects (Dunn et al., 2011). On the other hand, quantitative co-localisation analysis results in the generation of multiple coefficients that describe the degree of co-localisation between two objects (Demandolx and Davoust, 1997). These coefficients estimate the degree of co-localisation using specially developed algorithms that have different sensitivity and applicability (Zinchuk et al., 2007).

7.1.2.1. Pearson's correlation coefficient (Rr)

Pearson's correlation coefficient is widely used in pattern recognition and determines the covariance and correlation of signal intensities between the two channels. Pearson's coefficient is not sensitive to the intensity of the background nor to the intensity of the overlapping signals. Statistical values of Pearson's coefficient ranges from -1 to 1, where 0 indicates no significant or random correlation, -1 indicates total negative correlation and 1 refers to total positive correlation (Manders et al., 1992; Manders et al., 1993; Zinchuk et al., 2007; Dunn et al., 2011).

7.1.2.2. Costes' p-value

The Costes' method calculates the Pearson's correlation coefficient of the two channel images and then tests the result in trials where the channel 1 image is compared to the channel 2 image with scrambled pixel values. This process occurs 200 times to stimulate random overlap between the two images. The Costes' p-value is then generated, indicating the probability of real co-localisation in the original image. In this study, the test must be passed at 95% confidence level to proceed to further statistical analysis using alternative methods (Costes et al., 2004).

7.1.2.3. Manders' overlap coefficient (R)

Manders' overlap coefficient refers to the overlap of signals between the two channels and therefore represents the true degree of co-localisation. Manders' overlap coefficient is sensitive to the differences in background intensities but not to the overlapping pixel intensities. Its values range from 0 to 1, where 0 means no overlapping pixels, and 1 indicates high co-localisation (Manders et al., 1992; Manders et al., 1993; Zinchuk et al., 2007; Dunn et al., 2011).

7.1.2.4. Manders' colocalization coefficients (M1 and M2)

M1 and M2 colocalization coefficients demonstrate the input of each channel's image to the pixels of interests. More specifically, M1 describes the number of above background pixels in the channel 1 image that overlap with above background pixels in the channel 2 image. Respectively, M2 refers to the number of above background pixels in channel 2 image that overlap with above background pixels in channel 1

image. Thus, M1 and M2 are not sensitive to overlapping pixel intensities but they are sensitive to background intensity. The coefficients' values range from 0 to 1 and can be expressed as a percentage where a value of 1 in both channels indicates 100% co-localisation (Manders et al., 1992; Manders et al., 1993; Zinchuk et al., 2007; Dunn et al., 2011).

7.1.2.5. Manders' thresholded colocalization coefficients (tM1 and tM2)

This method of analysis is based on Costes' p-value. Following determination of the p-value, the method generates a scatterplot from the two analysed images and a regression line between the two channels pixel distribution. The Pearson's correlation coefficient is calculated for all colocalised pixels on the regression line; until the Pearson's value reaches 0 indicating the threshold values for each channel of certain images. Following determination of the threshold, the M1 and M2 values are calculated yet, this time the pixels below threshold are ignored (Manders et al., 1993; Dunn et al., 2011).

7.1.2.6. Scatterplots

Two-dimensional scatterplots can also be generated by computer software upon analysis of co-localisation and demonstrate the distribution of the pixels according to each image examined. The pixels intensity scale for the channel 1 image is presented on the x-axis whereas the pixels intensity of the channel 2 image is represented on the y-axis. Each pixel's intensity value is used as point coordinate on the graph. Thus, the more points at a specific location on the scatterplot, the brighter the location becomes.

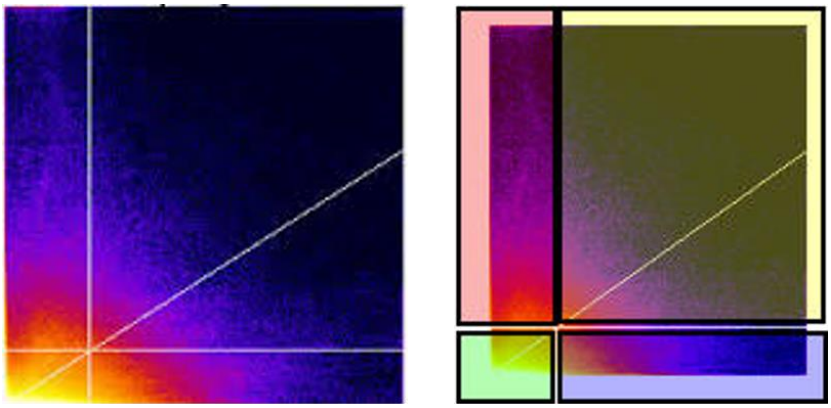

Figure 7.1. Example of a 2D scatterplot.

The figure demonstrates (A) an example of a scatterplot designed by the alignment of pixels from two fluorescent images, and (B) the four quadrants of a scatterplot. The red quadrant indicates channel 1 pixels below threshold and channels 2 pixels above threshold. The green quadrant demonstrates channel 1 and channel 2 pixels below threshold. The blue quadrant shows channel 1 pixels above threshold and channel 2 pixels below threshold. The yellow quadrant indicates channel 1 and channel 2 pixels above threshold. The regression line reflects the ratio of the fluorescence between the two channels' pixels (WWW, Image J: Colocalization analysis).

7.1.3. Introduction to neuronal cells

7.1.3.1. Neurons

Neurons are the basic component of signalling in the brain that process information through electrical signals or action potentials by the formation of synapses between two neuronal cells. They are composed of the cell body (soma), dendrites, and an axon that ends at the presynaptic terminals. The cell body of the neurons is responsible for the metabolic processes associated with the cell while the dendrites and the axon are responsible for signal transmission. More specifically, the many dendrites on the soma of the neuron are responsible for receiving incoming information, whereas the axon transmits the signal to the synapse to communicate with a postsynaptic neuronal cell (Tanapat, 2013).

7.1.3.2. Glial cells

Macroglial and microglial cells of the brain are responsible for the structural and metabolic support of the neurons and maintenance of CNS homeostasis (Jessen and Mirsky, 1980). The macroglial cells are classified as astrocytes, oligodendrocytes, ependymal cells and radial glia. Astroglial cells support the metabolic balance of extracellular ions and are involved in the exchange of substances in the brain by assisting the BBB endothelial cells (Abbott, 2002). On the other hand, ependymal cells form the epithelial layer that surrounds the choroid plexus, thus maintaining the B-CSFB. Oligodendrocytes are responsible for the production of myelin that shields and protects the neuronal axons and the formation of action potentials. Finally, radial glia facilitate the migration of new neurons formed in the hippocampus and have been also identified as precursor cells of both neurons and glial cells (Campell and Gotz, 2002; Steindler, 2012).

As specialised macrophages, microglia are associated with the immune functioning of the CNS. They present antigens on their cell-surface and secrete cytokines (Eglitis and Mezey, 1997), and are involved in phagocytic procedures protecting neurons in the CNS and interfering with the progression of various diseases (Wake et al., 2013). Adult microglial cells have been identified to regulate synaptic elimination, cell death, neurogenesis and neuronal surveillance and plasticity (Eyo and Dailey, 2013). Thus, microglial deficiency may result in several psychiatric but also neurological disorders (Wake et al., 2013), including AD.

7.1.4. Neuronal and glial cells markers

7.1.4.1. anti-GFAP: Astrocytes

Antibodies specific towards glial fibrillary acidic protein (GFAP) have been used as markers for astrocytes. GFAP is a class-III intermediate filament that provides support to the astroglia by the formation of a network that controls their function, shape and movement (Eng et al., 2000).

7.1.4.2. anti-Iba-1: Activated Microglia

Ionized calcium binding adaptor molecule 1 (Iba-1) mRNA is specifically expressed in microglia (Imai et al., 1996; Ito et al., 1998), thus antibodies targeting this protein have been used in immunocytochemical and immunohistochemical studies to identify activated microglial cells. This macrophage-specific calcium binding protein embodies the actin-bundling activity and is involved in the membrane disruption and phagocytic properties of activated microglia (Ohsawa et al., 2004).

7.1.4.3. anti-NeuN: Neurons

Antibodies recognising Neuronal Nuclei (NeuN) protein have been widely used in immunohistochemistry as a tool to identify neurons in the CNS (Mullen et al., 1992). NeuN has been identified as Fox-3, a protein that is expressed exclusively in neurons and is involved in the regulation of mRNA alternative splicing and neuronal cell differentiation (Kim et al., 2009).

In this Chapter, brain sections from WT mice were stained with anti-GFAP, anti-Iba-1, and anti-NeuN antibodies and counterstained with DAPI, and visualised on a Zeiss LSM confocal microscope and images of the sections were acquired using the 63X objective. The analysis of co-localisation is presented, with both qualitative and quantitative approaches.

7.2. Methods

Fluorescent images acquired using confocal microscopy were converted into 8-bit images and analysed for co-localisation between neuronal cell markers (red – Channel 1) and fluorescent peptides (green – Channel 2) using plugins in Image J software. The “Colocalization Test” was used to obtain the Costes’ p-value. The “Colocalization Threshold” was used to generate a colocalised pixel map and a scatterplot of colocalization of the two channels. Finally, the “Coloc 2” plugin was used to calculate the Pearson’s correlation coefficient (Rr), Manders’ overlap coefficient (R), Manders’ colocalization coefficients (M1 and M2), and Manders’ thresholded colocalization coefficients (tM1 and tM2).

7.3. Results

7.3.1. Co-localisation of Flu-RI-OR2-TAT with cell markers in cortex, DG and hippocampus

7.3.1.1. Evaluation of co-localisation with astrocytes (anti-GFAP)

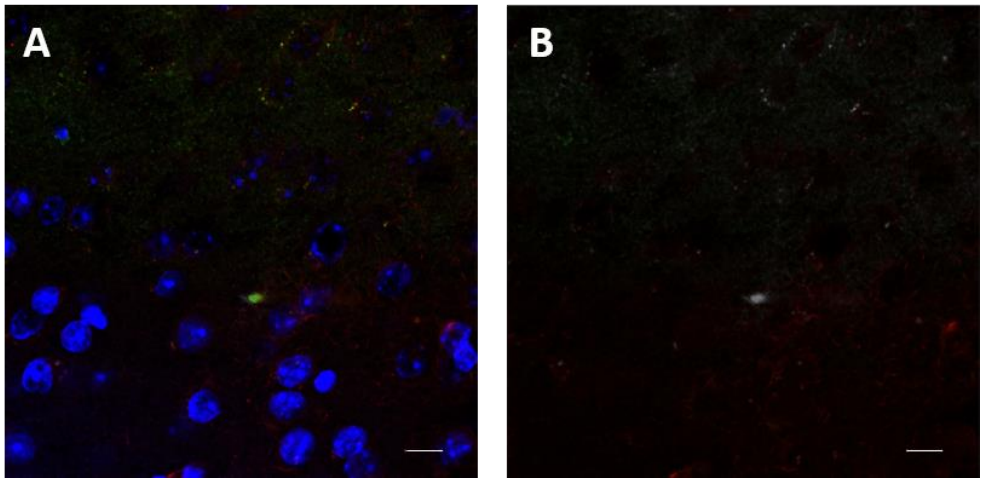

Figure 7.2. Co-localisation of Flu-RI-OR2-TAT with astrocytes in cortex.

The figure illustrates the (A) confocal image analysed, (B) pixel map where colocalised pixels are shown as white. SB = 10 µm.

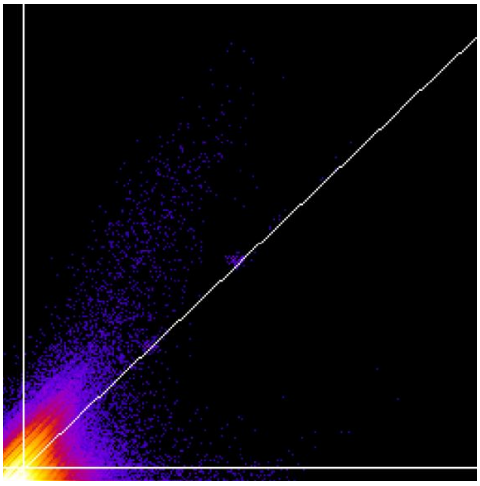

Figure 7.3. Scatterplot of colocalised pixel map of Flu-RI-OR2-TAT with astrocytes in cortex.

The scatterplot illustrates the threshold of the red channel on x-axis and the threshold of the green channel on y-axis. The intensity of a given pixel in channel 1 is used as an x-coordinate whereas the corresponding pixel's intensity in channel 2 is represented as the y-coordinate. The regression line of fluorescence ratio is also presented.

The scatterplot results demonstrate that there is some co-localisation between the fluorescent intensities of the Flu-RI-OR2-TAT peptide and the astrocytes in the cortex as the coordinates of the two channels demonstrate a tendency to align on a straight line.

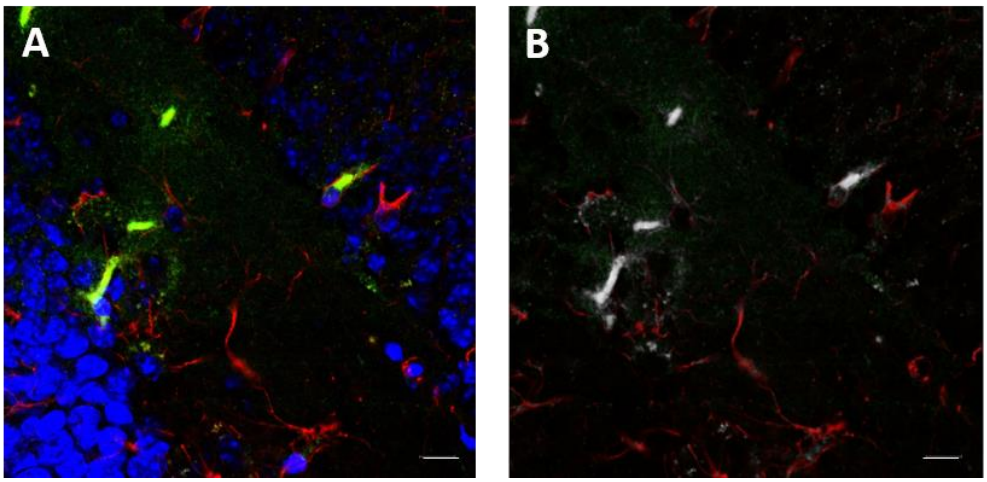

Figure 7.4. Co-localisation of Flu-RI-OR2-TAT with astrocytes in dentate gyrus.

The figure illustrates the (A) confocal image analysed, (B) pixel map where colocalised pixels are shown as white. SB = 10 µm.

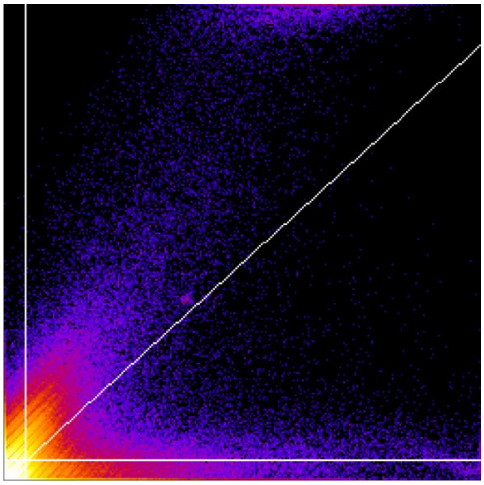

Figure 7.5. Scatterplot of colocalised pixel map of Flu-RI-OR2-TAT with astrocytes in dentate gyrus.

The scatterplot illustrates the threshold of the red channel on x-axis and the threshold of the green channel on y-axis. The intensity of a given pixel in channel 1 is used as an x-coordinate whereas the corresponding pixel's intensity in channel 2 is represented as the y-coordinate. The regression line of fluorescence ratio is also presented.

Similar to the cortex of the brain, the scatterplot shows that the Flu-RI-OR2-TAT peptide co-localises with astrocytes in the DG of the hippocampal formation.

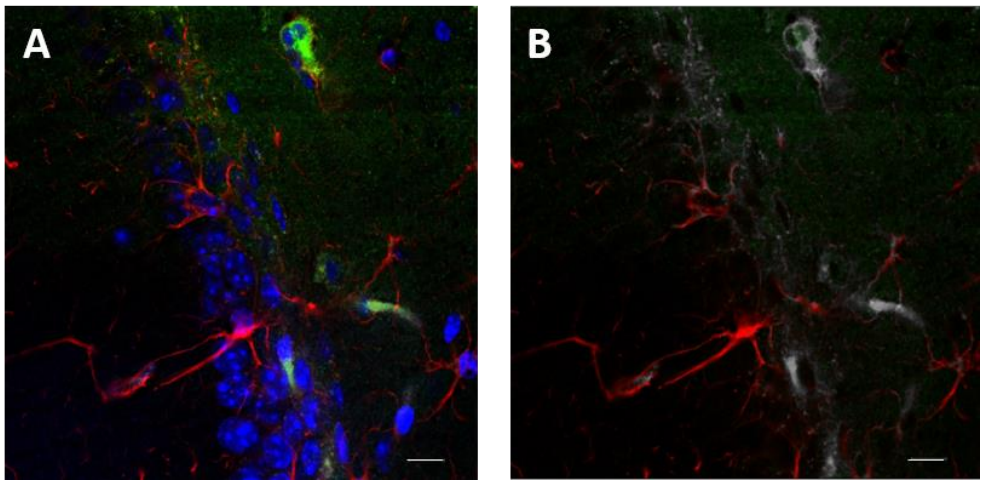

Figure 7.6. Co-localisation of Flu-RI-OR2-TAT with astrocytes in hippocampus.

The figure illustrates the (A) confocal image analysed, (B) pixel map where colocalised pixels are shown as white. SB = 10 µm.

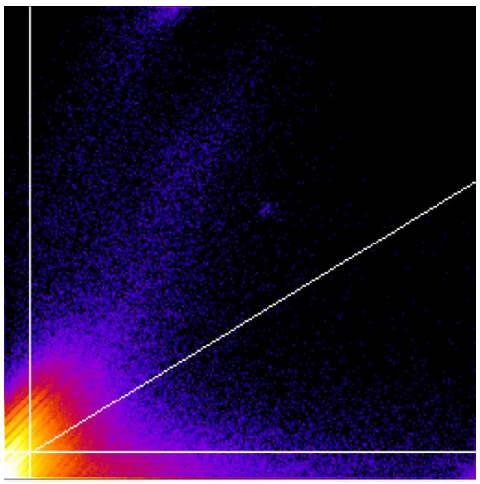

Figure 7.7. Scatterplot of colocalised pixel map of Flu-RI-OR2-TAT with astrocytes in hippocampus.

The scatterplot illustrates the threshold of the red channel on x-axis and the threshold of the green channel on y-axis. The intensity of a given pixel in channel 1 is used as an x-coordinate whereas the corresponding pixel's intensity in channel 2 is represented as the y-coordinate. The regression line of fluorescence ratio is also presented.

Even though there is some association between the peptide and astrocytes in the hippocampus of the brain, the degree of co-localisation is not as high as in the cortex

and DG, as the coordinates of the fluorescent intensities locate further away from the regression line compared to the previous regions examined.

Quantitative coefficients	Cortex	Dentate Gyrus	Hippocampus
Costes' p-value	1	1	1
Pearson's Rr value	0.505	0.535	0.357
Manders' R value	0.599	0.586	0.347
Manders' M1 coefficient	0.785	0.874	0.908
Manders' M2 coefficient	0.978	0.901	0.896
Manders' tM1 coefficient	0.413	0.544	0.548
Manders' tM2 coefficient	0.624	0.603	0.510

Table 7.1. Co-localisation coefficients of Flu-RI-OR2-TAT with astrocytes.

The table demonstrates the Costes' p-value obtained from "Colocalization Test", and the Pearson's correlation coefficient, Manders' overlap coefficient, Manders' colocalization coefficients M1 and M2, and Manders' thresholded coefficients tM1 and tM2 obtained from "Coloc2".

As all of the conditions examined demonstrate a Costes' p-value of 1 I conclude that there is co-localisation between the Flu-RI-OR2-TAT peptide and astrocytes in the cortex, DG and hippocampus of the brain. Examination of the thresholded Manders' coefficients suggest that there is 41% overlap of astrocyte intensity with the peptide, whilst 62% pixels of the peptide intensity overlap with the astrocyte intensity in the cortex. In the DG, 54% of the red pixels (astroglia) overlap with the green pixels (Flu-RI-OR2-TAT), whereas 60% of the peptide's pixels overlap with the astroglial pixels. Finally, in the hippocampus, about 55% of the astroglial pixels co-localise with the peptide's pixels, whereas 51% of the peptide's pixels co-localise with the red pixels (astroglia).

7.3.1.2. Evaluation of co-localisation with activated microglia (anti-Iba-1)

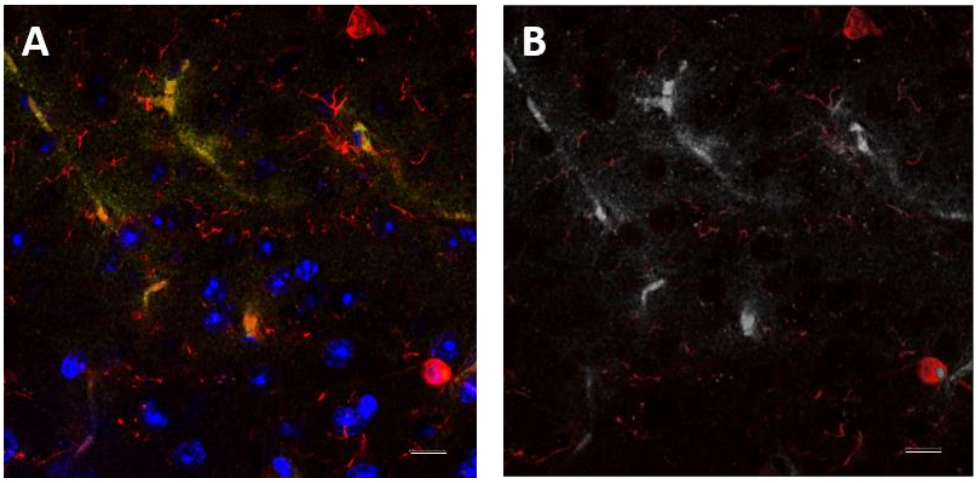

Figure 7.8. Co-localisation of Flu-RI-OR2-TAT with activated microglia in cortex.

The figure illustrates the (A) confocal image analysed, (B) pixel map where colocalised pixels are shown as white. SB = 10 µm.

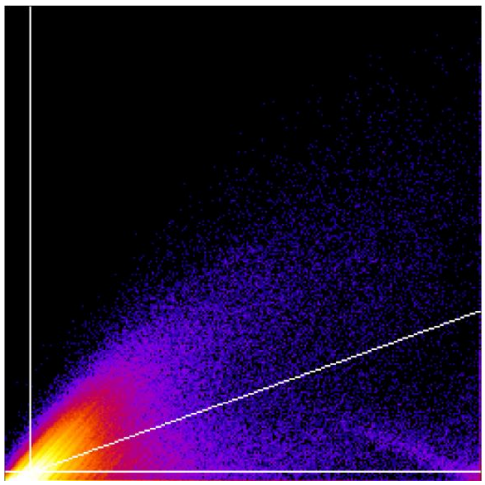

Figure 7.9. Scatterplot of colocalised pixel map of Flu-RI-OR2-TAT with activated microglia in cortex.

The scatterplot illustrates the threshold of the red channel on x-axis and the threshold of the green channel on y-axis. The intensity of a given pixel in channel 1 is used as an x-coordinate whereas the corresponding pixel's intensity in channel 2 is represented as the y-coordinate. The regression line of fluorescence ratio is also presented.

Examination of the scatterplot of colocalised pixels between the activated microglia and Flu-RI-OR2-TAT peptide in the cortex, indicates that there is co-localisation between the two channels as the coordinates align close to the regression line.

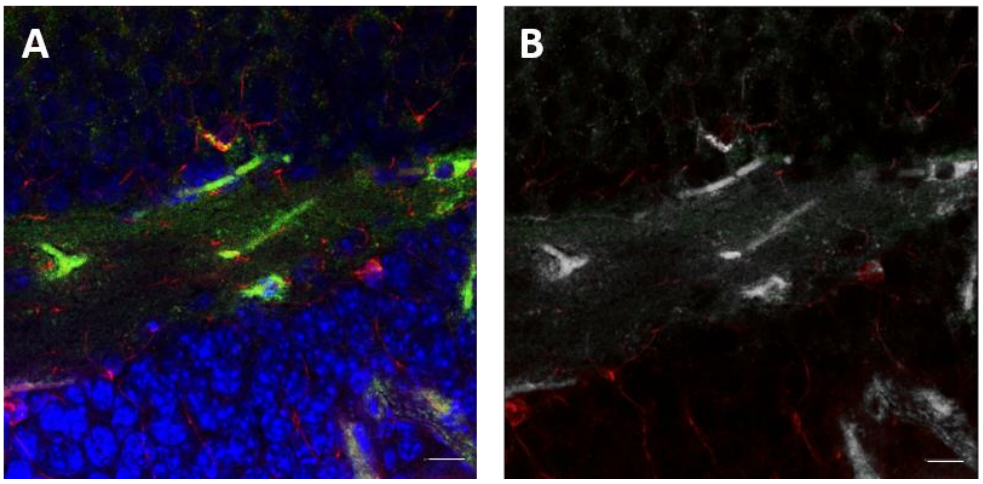

Figure 7.10. Co-localisation of Flu-RI-OR2-TAT with activated microglia in dentate gyrus.

The figure illustrates the (A) confocal image analysed, (B) pixel map where colocalised pixels are shown as white. SB = 10 µm.

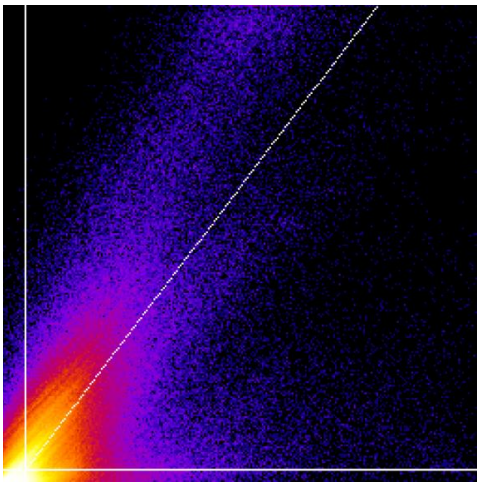

Figure 7.11. Scatterplot of colocalised pixel map of Flu-RI-OR2-TAT with activated microglia in dentate gyrus.

The scatterplot illustrates the threshold of the red channel on x-axis and the threshold of the green channel on y-axis. The intensity of a given pixel in channel 1 is used as an x-coordinate whereas the corresponding pixel's intensity in channel 2 is represented as the y-coordinate. The regression line of fluorescence ratio is also presented.

The scatterplot of colocalised pixels between the Flu-RI-OR2-TAT peptide and activated microglia in the DG, demonstrates a strong co-localisation between the two channels.

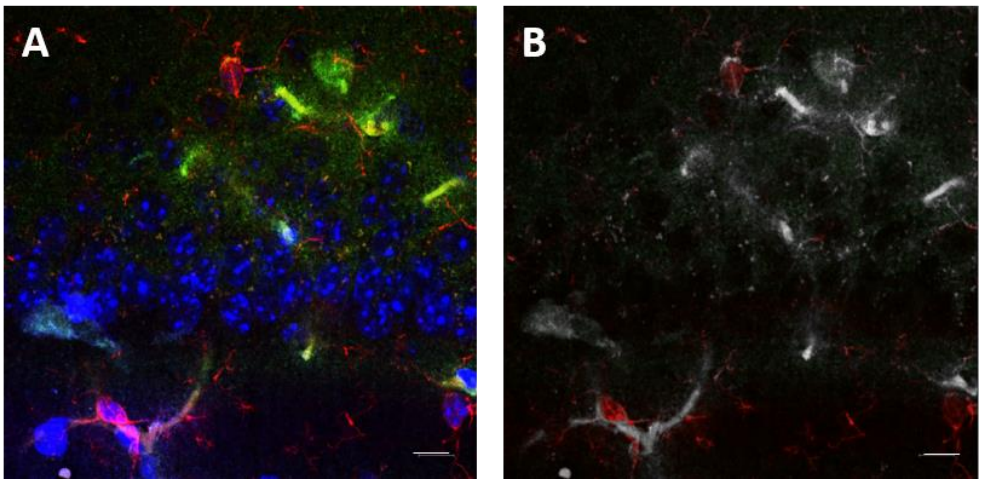

Figure 7.12. Co-localisation of Flu-RI-OR2-TAT with activated microglia in hippocampus.

The figure illustrates the (A) confocal image analysed, (B) pixel map where colocalised pixels are shown as white. SB = 10 µm.

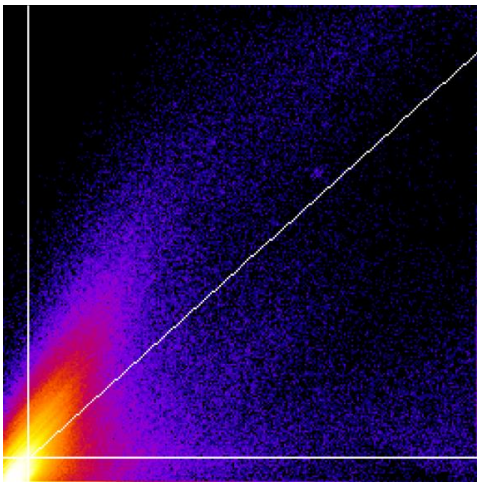

Figure 7.13. Scatterplot of colocalised pixel map of Flu-RI-OR2-TAT with activated microglia in hippocampus.

The scatterplot illustrates the threshold of the red channel on x-axis and the threshold of the green channel on y-axis. The intensity of a given pixel in channel 1 is used as an x-coordinate whereas the corresponding pixel's intensity in channel 2 is represented as the y-coordinate. The regression line of fluorescence ratio is also presented.

Comparison of the scatterplot showing the co-localisation between the Flu-RI-OR2-TAT and activated microglia in the hippocampus indicates that the peptide does co-localise with the cell marker but not as strongly as in the DG and cortex.

Quantitative coefficients	Cortex	Dentate Gyrus	Hippocampus
Costes' p-value	1	1	1
Pearson's Rr value	0.616	0.687	0.599
Manders' R value	0.605	0.635	0.539
Manders' M1 coefficient	0.848	0.896	0.948
Manders' M2 coefficient	1	0.991	0.988
Manders' tM1 coefficient	0.660	0.711	0.681
Manders' tM2 coefficient	0.877	0.868	0.775

Table 7.2. Co-localisation coefficients of Flu-RI-OR2-TAT with activated microglia.

The table demonstrates the Costes' p-value obtained from "Colocalization Test", and the Pearson's correlation coefficient, Manders' overlap coefficient, Manders' colocalization coefficients M1 and M2, and Manders' thresholded coefficients tM1 and tM2 obtained from "Coloc2".

The Costes' coefficient demonstrates 100% co-localisation of the Flu-RI-OR2-TAT peptide with activated microglia in the cortex, DG and hippocampus of the brain. Examination of the thresholded Manders' coefficients demonstrate that 88% of the peptide co-localises with activated microglia in the cortex, 87% in the DG, and about 78% in the hippocampus. On the other hand, in the cortex, 66% of the activated microglia pixels co-localise with the pixels of the peptide, 71% of red pixels (activated microglia) co-localise with green pixels (Flu-RI-OR2-TAT) in the DG, whereas in the hippocampus, 68% of activated microglia co-localise with the Flu-RI-OR2-TAT peptide.

7.3.1.3. Evaluation of co-localisation with neurons (anti-NeuN)

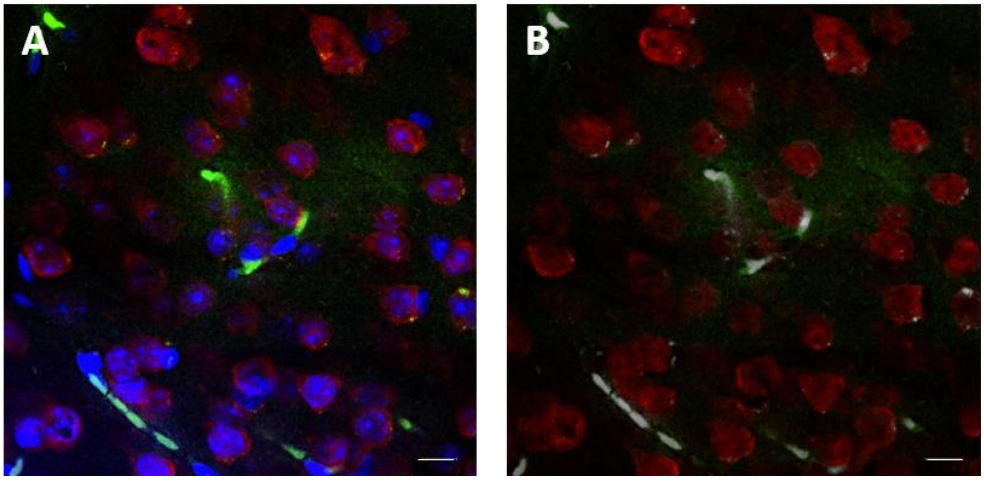

Figure 7.14. Co-localisation of Flu-RI-OR2-TAT with neurons in cortex.

The figure illustrates the (A) confocal image analysed, (B) pixel map where colocalised pixels are shown as white. SB = 10 µm.

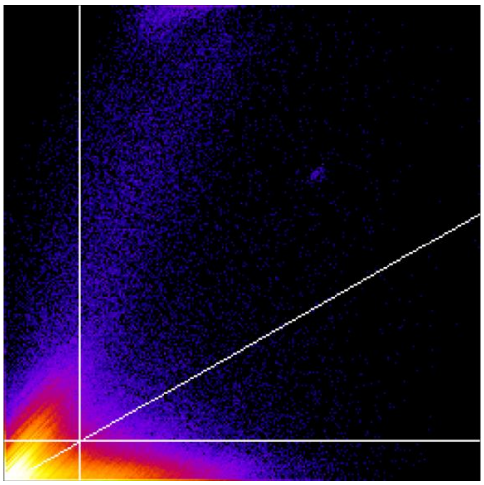

Figure 7.15. Scatterplot of colocalised pixel map of Flu-RI-OR2-TAT with neurons in cortex.

The scatterplot illustrates the threshold of the red channel on x-axis and the threshold of the green channel on y-axis. The intensity of a given pixel in channel 1 is used as an x-coordinate whereas the corresponding pixel's intensity in channel 2 is represented as the y-coordinate. The regression line of fluorescence ratio is also presented.

The scatterplot of colocalised pixels of Flu-RI-OR2-TAT and neurons in the cortex of the brain indicates that, even though there is co-localisation between the two channels, there is no strong connection between them.

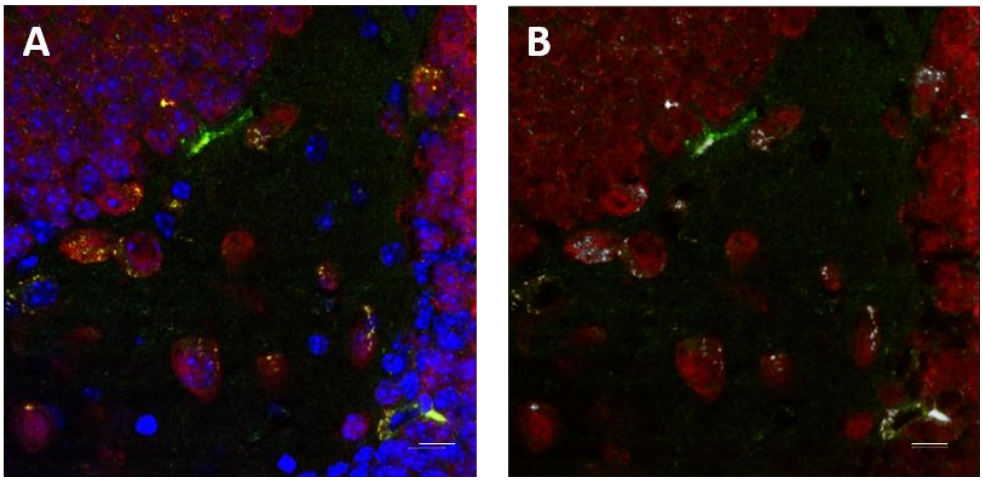

Figure 7.16. Co-localisation of Flu-RI-OR2-TAT with neurons in dentate gyrus.

The figure illustrates the (A) confocal image analysed, (B) pixel map where colocalised pixels are shown as white. SB = 10 µm.

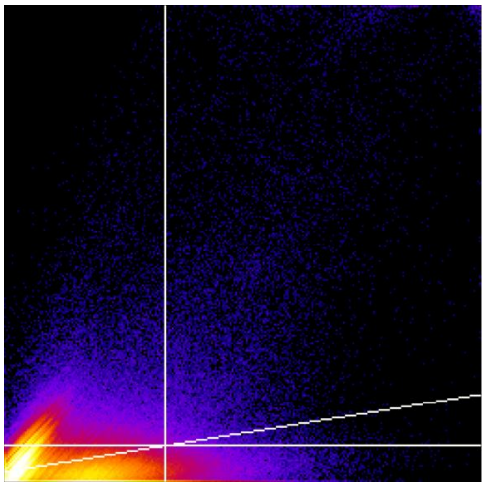

Figure 7.17. Scatterplot of colocalised pixel map of Flu-RI-OR2-TAT with neurons in dentate gyrus.

The scatterplot illustrates the threshold of the red channel on x-axis and the threshold of the green channel on y-axis. The intensity of a given pixel in channel 1 is used as an x-coordinate whereas the corresponding pixel's intensity in channel 2 is represented as the y-coordinate. The regression line of fluorescence ratio is also presented.

The scatterplot of colocalised pixels between the Flu-RI-OR2-TAT and neurons in the DG indicates that there is low correlation between the two channels.

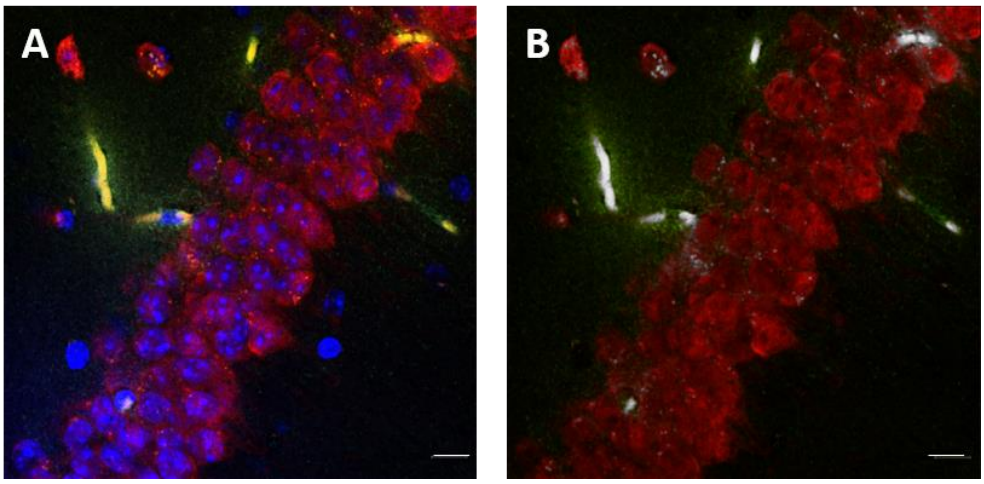

Figure 7.18. Co-localisation of Flu-RI-OR2-TAT with neurons in hippocampus.

The figure illustrates the (A) confocal image analysed, (B) pixel map where colocalised pixels are shown as white. SB = 10 µm.

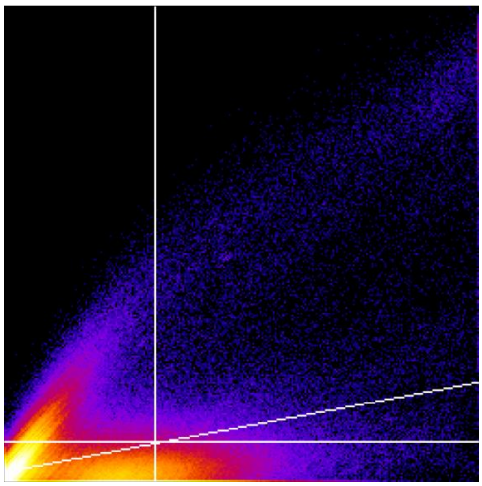

Figure 7.19. Scatterplot of colocalised pixel map of Flu-RI-OR2-TAT with neurons in hippocampus.

The scatterplot illustrates the threshold of the red channel on x-axis and the threshold of the green channel on y-axis. The intensity of a given pixel in channel 1 is used as an x-coordinate whereas the corresponding pixel's intensity in channel 2 is represented as the y-coordinate. The regression line of fluorescence ratio is also presented.

The scatterplot of colocalised pixels demonstrates that even though there is some co-localisation between the Flu-RI-OR2-TAT peptide and neurons in the hippocampus, there are also a lot of neurons that do not correlate with the peptide's green pixels, shifting the slope of the regression line towards the x-axis.

Quantitative coefficients	Cortex	Dentate Gyrus	Hippocampus
Costes' p-value	1	1	1
Pearson's Rr value	0.262	0.247	0.325
Manders' R value	0.374	0.595	0.595
Manders' M1 coefficient	0.811	0.838	0.788
Manders' M2 coefficient	0.975	0.992	0.985
Manders' tM1 coefficient	0.171	0.166	0.222
Manders' tM2 coefficient	0.239	0.130	0.236

Table 7.3. Co-localisation coefficients of Flu-RI-OR2-TAT with neurons.

The table demonstrates the Costes' p-value obtained from "Colocalization Test", and the Pearson's correlation coefficient, Manders' overlap coefficient, Manders' colocalization coefficients M1 and M2, and Manders' thresholded coefficients tM1 and tM2 obtained from "Coloc2".

Even though the Costes' p-value indicates that the Flu-RI-OR2-TAT peptide co-localises with some neurons in the cortex, DG, and hippocampus of the brain, examination of the thresholded Manders' coefficients indicate that the correlation of the two channels is low. In the cortex and hippocampus, 24 % of the peptide overlaps with neurons, whereas in the DG, only 13% of the peptide overlaps with the red pixels. Comparing the percentages of overlap between the red pixels (neurons) and green pixels (Flu-RI-OR2-TAT peptide), there is 17% overlap in the cortex and DG, and 22% percent overlap in the hippocampus of the brain.

7.3.2. Co-localisation of Flu-RI-OR2-NAG with cell markers in cortex, DG and hippocampus

7.3.2.1. Evaluation of co-localisation with astrocytes (anti-GFAP)

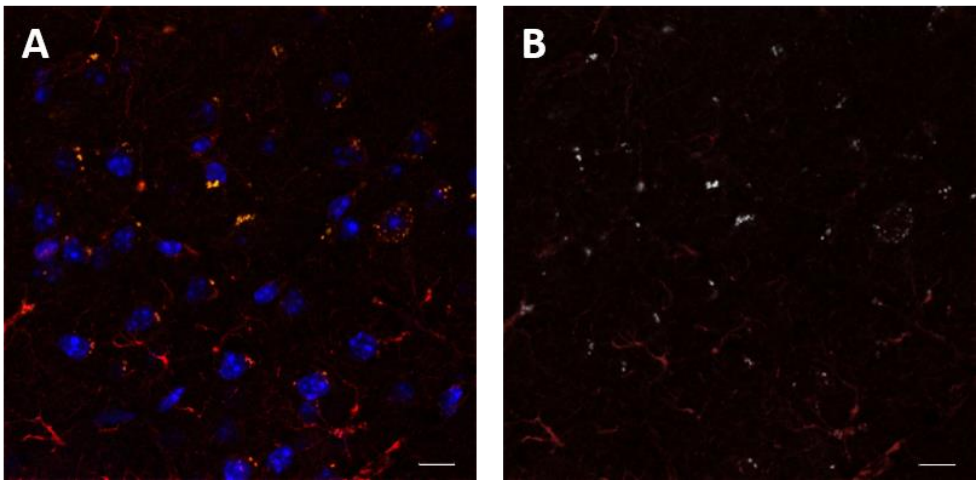

Figure 7.20. Co-localisation of Flu-RI-OR2-NAG with astrocytes in cortex.

The figure illustrates the (A) confocal image analysed, (B) pixel map where colocalised pixels are shown as white. SB = 10 µm.

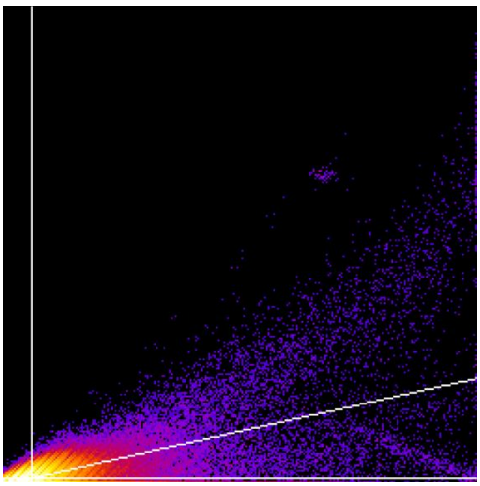

Figure 7.21. Scatterplot of colocalised pixel map of Flu-RI-OR2-NAG with astrocytes in cortex.

The scatterplot illustrates the threshold of the red channel on x-axis and the threshold of the green channel on y-axis. The intensity of a given pixel in channel 1 is used as an x-coordinate whereas the corresponding pixel's intensity in channel 2 is represented as the y-coordinate. The regression line of fluorescence ratio is also presented.

The scatterplot comparing the Flu-RI-OR2-NAG peptide and astrocytes co-localisation in cortex demonstrates weak co-localisation of the peptide with the cell marker as the slope of the regression line shifts towards the red pixels of the astrocytes.

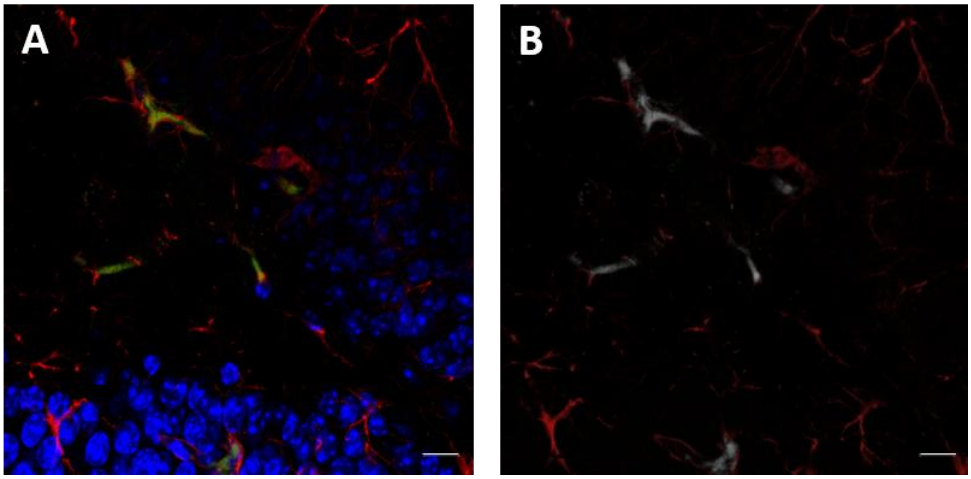

Figure 7.22. Co-localisation of Flu-RI-OR2-NAG with astrocytes in dentate gyrus.

The figure illustrates the (A) confocal image analysed, (B) pixel map where colocalised pixels are shown as white. SB = 10 µm.

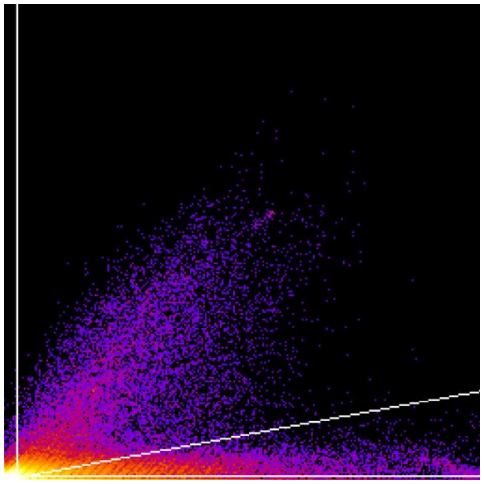

Figure 7.23. Scatterplot of colocalised pixel map of Flu-RI-OR2-NAG with astrocytes in dentate gyrus.

The scatterplot illustrates the threshold of the red channel on x-axis and the threshold of the green channel on y-axis. The intensity of a given pixel in channel 1 is used as an x-coordinate whereas the corresponding pixel's intensity in channel 2 is represented as the y-coordinate. The regression line of fluorescence ratio is also presented.

Similar to the previous scatterplot, weak correlation is observed between the Flu-RI-OR2-NAG peptide and astrocytes in the DG of the hippocampal formation.

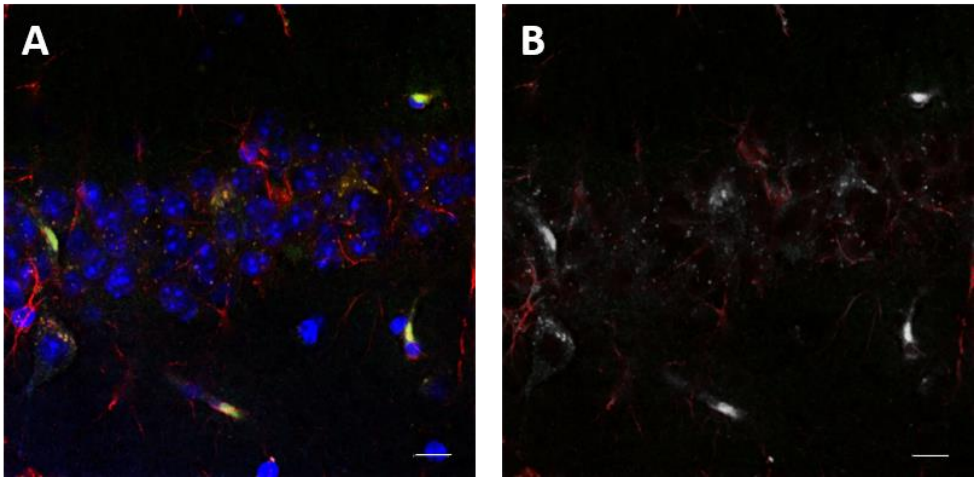

Figure 7.24. Co-localisation of Flu-RI-OR2-NAG with astrocytes in hippocampus.

The figure illustrates the (A) confocal image analysed, (B) pixel map where colocalised pixels are shown as white. SB = 10 µm.

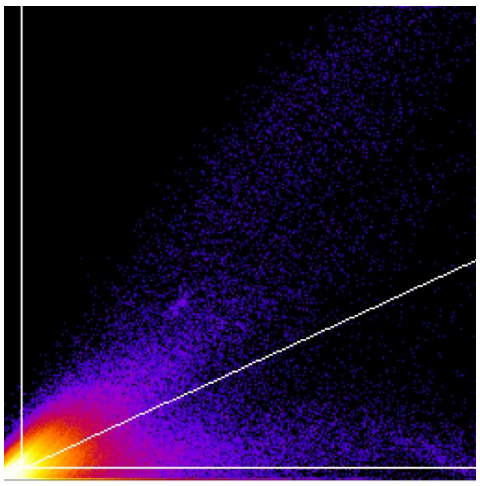

Figure 7.25. Scatterplot of colocalised pixel map of Flu-RI-OR2-NAG with astrocytes in hippocampus.

The scatterplot illustrates the threshold of the red channel on x-axis and the threshold of the green channel on y-axis. The intensity of a given pixel in channel 1 is used as an x-coordinate whereas the corresponding pixel's intensity in channel 2 is represented as the y-coordinate. The regression line of fluorescence ratio is also presented.

Even though the slope of the regression line comparing the fluorescent intensities of Flu-RI-OR2-NAG peptide and astrocytes in the hippocampus is higher than the grade

of correlation in cortex and DG, there is no strong co-localisation observed between the two channels.

Quantitative coefficients	Cortex	Dentate Gyrus	Hippocampus
Costes' p-value	1	1	1
Pearson's Rr value	0.644	0.426	0.630
Manders' R value	0.700	0.327	0.623
Manders' M1 coefficient	0.584	0.626	0.901
Manders' M2 coefficient	0.999	0.939	0.976
Manders' tM1 coefficient	0.031	0.537	0.727
Manders' tM2 coefficient	0.073	0.725	0.728

Table 7.4. Co-localisation coefficients of Flu-RI-OR2-NAG with astrocytes.

The table demonstrates the Costes' p-value obtained from "Colocalization Test", and the Pearson's correlation coefficient, Manders' overlap coefficient, Manders' colocalization coefficients M1 and M2, and Manders' thresholded coefficients tM1 and tM2 obtained from "Coloc2".

The Costes' p-value demonstrates that all of the peptides co-localise with astrocytes in the cortex, DG and hippocampus of the brain. The thresholded Manders' coefficients demonstrate that 7% of the Flu-RI-OR2-NAG peptide co-localises with astrocytes in the cortex and 73% in the DG and hippocampus. On the other hand, 3% of astrocytes co-localise with the Flu-RI-OR2-NAG peptide in the DG, 54% in the DG and 73% in the hippocampus.

7.3.2.2. Evaluation of co-localisation with activated microglia (anti-Iba-1)

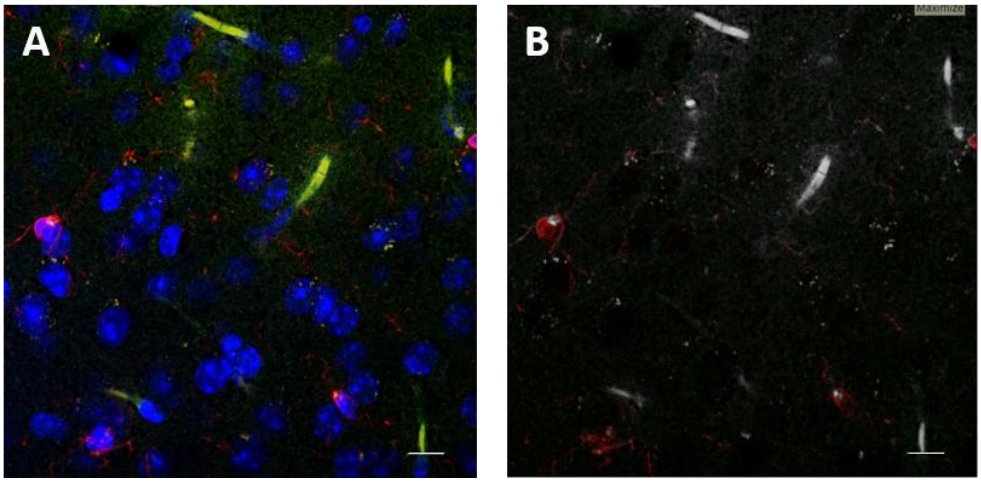

Figure 7.26. Co-localisation of Flu-RI-OR2-NAG with activated microglia in cortex.

The figure illustrates the (A) confocal image analysed, (B) pixel map where colocalised pixels are shown as white. SB = 10 µm.

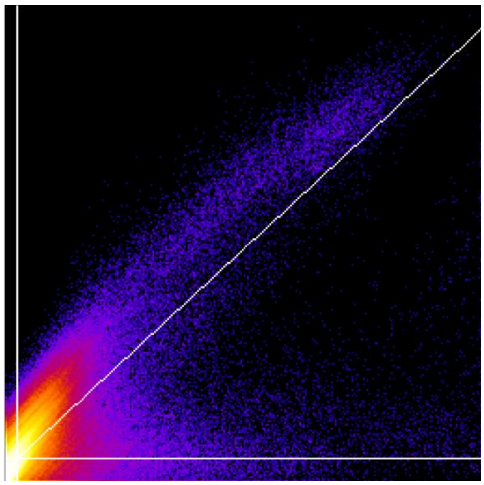

Figure 7.27. Scatterplot of colocalised pixel map of Flu-RI-OR2-NAG with activated microglia in cortex.

The scatterplot illustrates the threshold of the red channel on x-axis and the threshold of the green channel on y-axis. The intensity of a given pixel in channel 1 is used as an x-coordinate whereas the corresponding pixel's intensity in channel 2 is represented as the y-coordinate. The regression line of fluorescence ratio is also presented.

The scatterplot showing the correlation of Flu-RI-OR2-NAG peptide and activated microglia in the cortex of the brain, demonstrates strong overlap between the two examined channels.

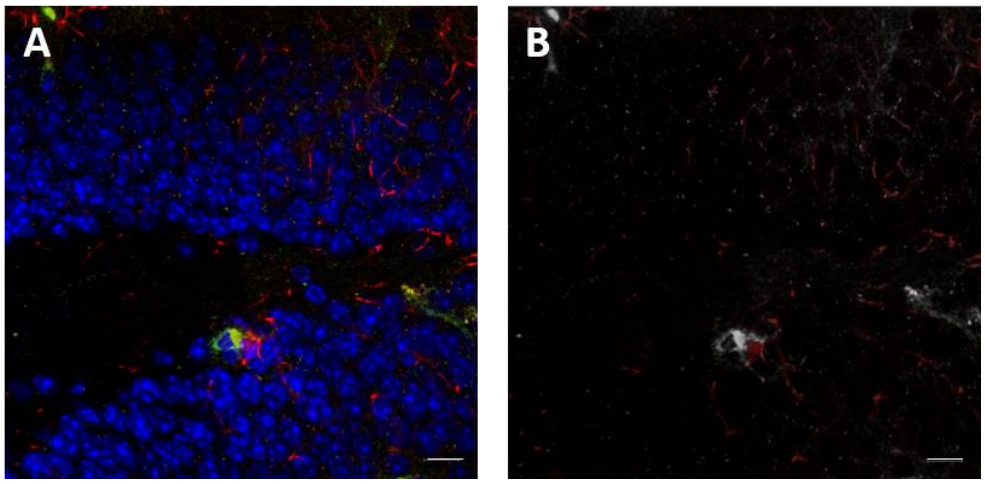

Figure 7.28. Co-localisation of Flu-RI-OR2-NAG with activated microglia in dentate gyrus.

The figure illustrates the (A) confocal image analysed, (B) pixel map where colocalised pixels are shown as white. SB = 10 µm.

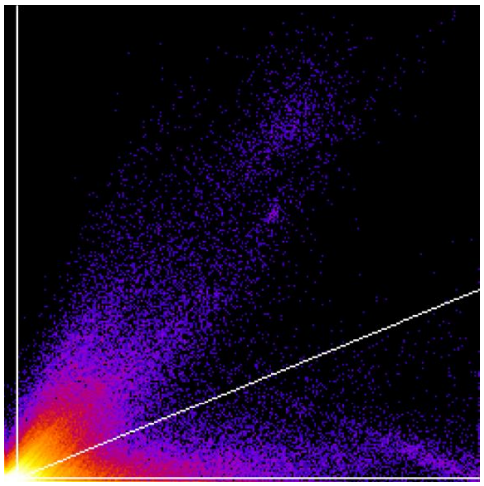

Figure 7.29. Scatterplot of colocalised pixel map of Flu-RI-OR2-NAG with activated microglia in dentate gyrus.

The scatterplot illustrates the threshold of the red channel on x-axis and the threshold of the green channel on y-axis. The intensity of a given pixel in channel 1 is used as an x-coordinate whereas the corresponding pixel's intensity in channel 2 is represented as the y-coordinate. The regression line of fluorescence ratio is also presented.

Investigation of co-localisation of the Flu-RI-OR2-NAG peptide and activated microglia in the DG demonstrates some overlap of intensities between the two channels.

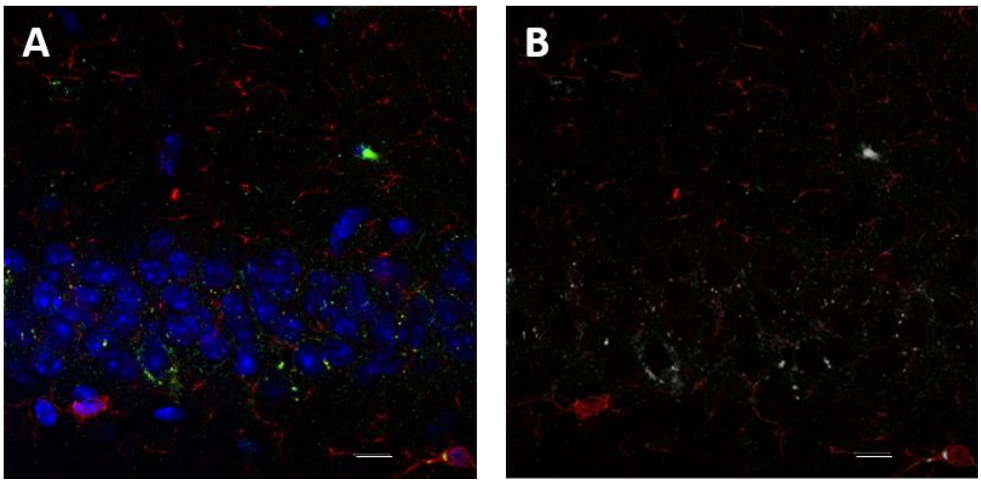

Figure 7.30. Co-localisation of Flu-RI-OR2-NAG with activated microglia in hippocampus.

The figure illustrates the (A) confocal image analysed, (B) pixel map where colocalised pixels are shown as white. SB = 10 µm.

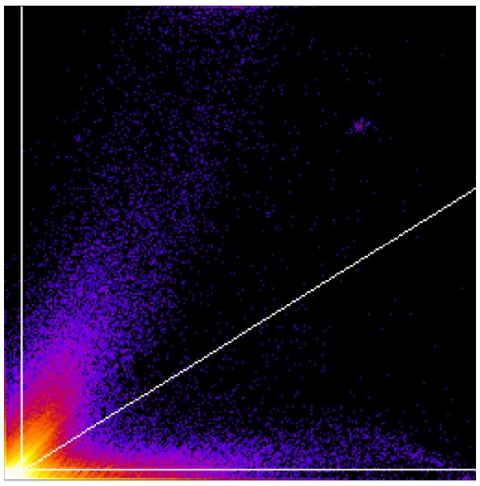

Figure 7.31. Scatterplot of colocalised pixel map of Flu-RI-OR2-NAG with activated microglia in hippocampus.

The scatterplot illustrates the threshold of the red channel on x-axis and the threshold of the green channel on y-axis. The intensity of a given pixel in channel 1 is used as an x-coordinate whereas the corresponding pixel's intensity in channel 2 is represented as the y-coordinate. The regression line of fluorescence ratio is also presented.

Examination of the scatterplot demonstrates that the Flu-RI-OR2-NAG peptide co-localises weakly with activated microglia in the hippocampus of the brain.

Quantitative coefficients	Cortex	Dentate Gyrus	Hippocampus
Costes' p-value	1	1	1
Pearson's Rr value	0.691	0.530	0.419
Manders' R value	0.714	0.453	0.373
Manders' M1 coefficient	0.975	0.758	0.724
Manders' M2 coefficient	0.915	0.966	0.932
Manders' tM1 coefficient	0.788	0.681	0.496
Manders' tM2 coefficient	0.755	0.841	0.688

Table 7.5. Co-localisation coefficients of Flu-RI-OR2-NAG with activated microglia.

The table demonstrates the Costes' p-value obtained from "Colocalization Test", and the Pearson's correlation coefficient, Manders' overlap coefficient, Manders' colocalization coefficients M1 and M2, and Manders' thresholded coefficients tM1 and tM2 obtained from "Coloc2".

The Costes' p-values demonstrates true co-localisation between the Flu-RI-OR2-NAG peptide and activated microglia in the cortex, DG and hippocampus of the brain. Evaluation of the thresholded Manders' values indicate the 76% of the peptide co-localises with activated microglia in the cortex, 84% in the DG and 69% in the hippocampus of the brain. With respect to the fluorescence of the red channel, 79% of activated microglia co-locate with the peptide in the cortex, 68% in the DG, and 50% in the hippocampus.

7.3.2.3. Evaluation of co-localisation with neuronal nuclei (anti-NeuN)

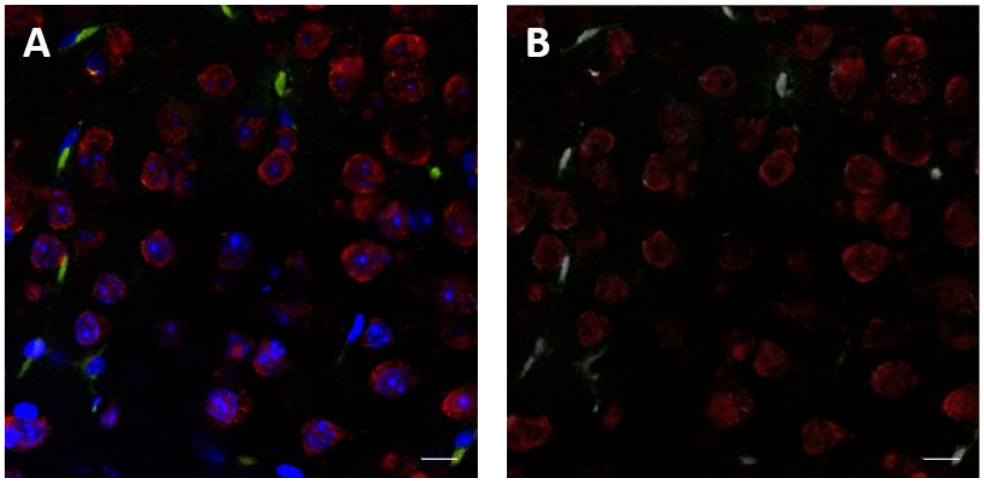

Figure 7.32. Co-localisation of Flu-RI-OR2-NAG with neurons in cortex.

The figure illustrates the (A) confocal image analysed, (B) pixel map where colocalised pixels are shown as white. SB = 10 µm.

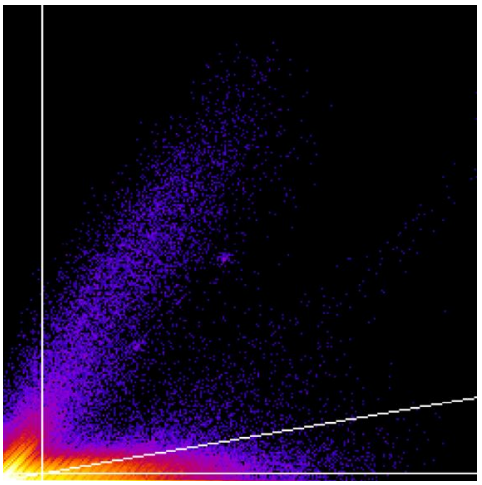

Figure 7.33. Scatterplot of colocalised pixel map of Flu-RI-OR2-NAG with neurons in cortex.

The scatterplot illustrates the threshold of the red channel on x-axis and the threshold of the green channel on y-axis. The intensity of a given pixel in channel 1 is used as an x-coordinate whereas the corresponding pixel's intensity in channel 2 is represented as the y-coordinate. The regression line of fluorescence ratio is also presented.

The scatterplot demonstrates that the fluorescent pixels of the Flu-RI-OR2-NAG peptide weakly overlap with the fluorescent pixels of the neurons in the cortex, however the slope of the regression line is low due to the abundance of neurons in the cortex of the brain.

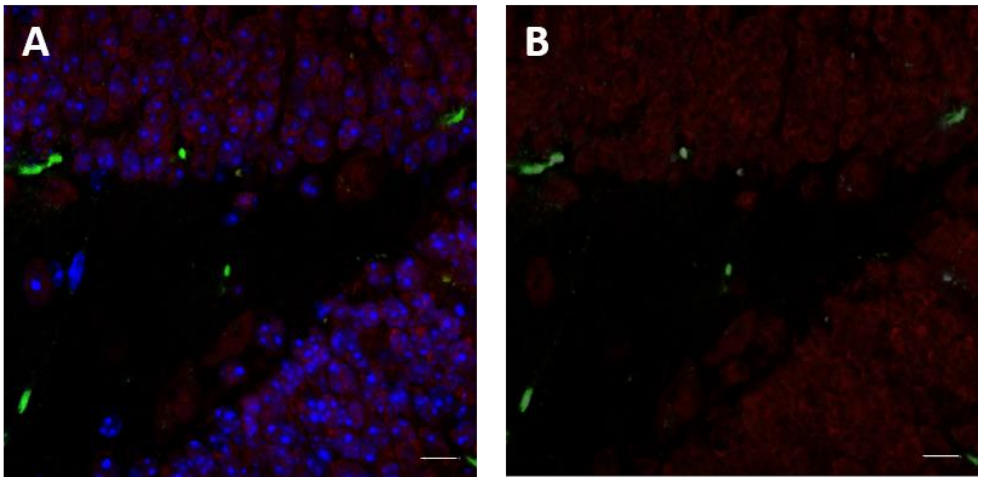

Figure 7.34. Co-localisation of Flu-RI-OR2-NAG with neurons in dentate gyrus.

The figure illustrates the (A) confocal image analysed, (B) pixel map where colocalised pixels are shown as white. SB = 10 µm.

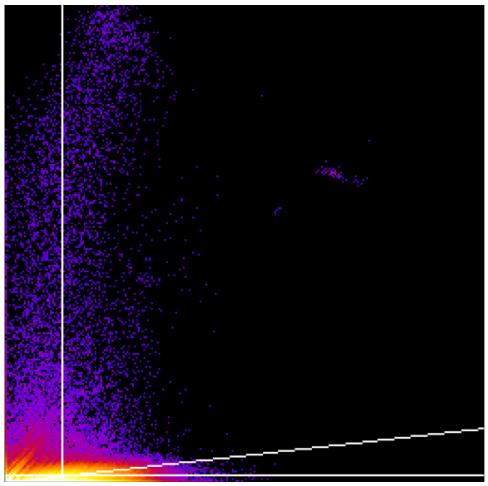

Figure 7.35. Scatterplot of colocalised pixel map of Flu-RI-OR2-NAG with neurons in dentate gyrus.

The scatterplot illustrates the threshold of the red channel on x-axis and the threshold of the green channel on y-axis. The intensity of a given pixel in channel 1 is used as an x-coordinate whereas the corresponding pixel's intensity in channel 2 is represented as the y-coordinate. The regression line of fluorescence ratio is also presented.

Examination of the scatterplot between the Flu-RI-OR2-NAG peptide and neurons in the DG of the brain shows weak overlap of the two channels' images.

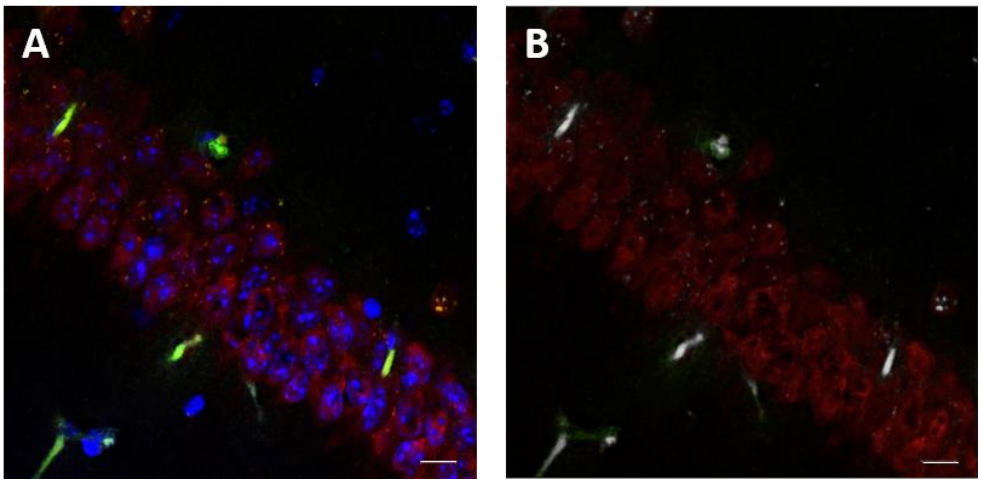

Figure 7.36. Co-localisation of Flu-RI-OR2-NAG with neurons in hippocampus.

The figure illustrates the (A) confocal image analysed, (B) pixel map where colocalised pixels are shown as white. SB = 10 µm.

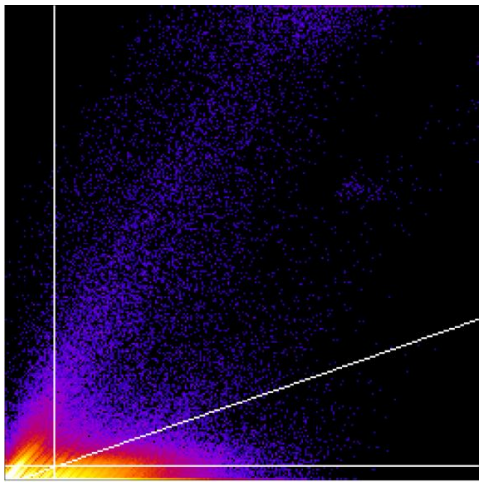

Figure 7.37. Scatterplot of colocalised pixel map of Flu-RI-OR2-NAG with neurons in hippocampus.

The scatterplot illustrates the threshold of the red channel on x-axis and the threshold of the green channel on y-axis. The intensity of a given pixel in channel 1 is used as an x-coordinate whereas the corresponding pixel's intensity in channel 2 is represented as the y-coordinate. The regression line of fluorescence ratio is also presented.

The regression line of the scatterplot comparing the Flu-RI-OR2-NAG peptide and neurons in the hippocampus demonstrates that the peptide overlaps with the cell marker to a higher degree than the rest of the brain regions examined.

Quantitative coefficients	Cortex	Dentate Gyrus	Hippocampus
Costes' p-value	1	1	1
Pearson's Rr value	0.295	0.100	0.367
Manders' R value	0.245	0.146	0.562
Manders' M1 coefficient	0.627	0.491	0.644
Manders' M2 coefficient	0.939	0.964	0.991
Manders' tM1 coefficient	0.416	0.247	0.253
Manders' tM2 coefficient	0.480	0.498	0.539

Table 7.6. Co-localisation coefficients of Flu-RI-OR2-NAG with neurons.

The table demonstrates the Costes' p-value obtained from "Colocalization Test", and the Pearson's correlation coefficient, Manders' overlap coefficient, Manders' colocalization coefficients M1 and M2, and Manders' thresholded coefficients tM1 and tM2 obtained from "Coloc2".

The p-values resulted from the Costes' randomization test demonstrate that the Flu-RI-OR2-NAG peptide co-localises with neurons in the cortex, DG and hippocampus. The results observed from the thresholded Manders' coefficients indicate that 48% of the peptide co-localises with neurons in the cortex, 50% in the DG, and 54% in the hippocampus. On the other hand, 42% of neurons co-localise with the Flu-RI-OR2-NAG peptide in the cortex and 25% in the DG and hippocampus of the brain.

7.3.3. Co-localisation of BODIPY-PINPs with cell markers in cortex, DG and hippocampus

7.3.3.1. Evaluation of co-localisation with astrocytes (anti-GFAP)

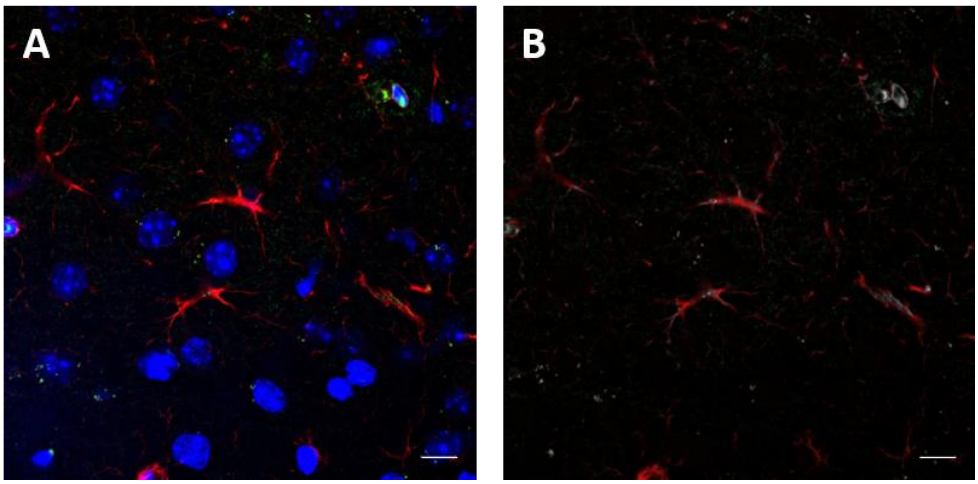

Figure 7.38. Co-localisation of BODIPY-PINPs with astrocytes in cortex.

The figure illustrates the (A) confocal image analysed, (B) pixel map where colocalised pixels are shown as white. SB = 10 µm.

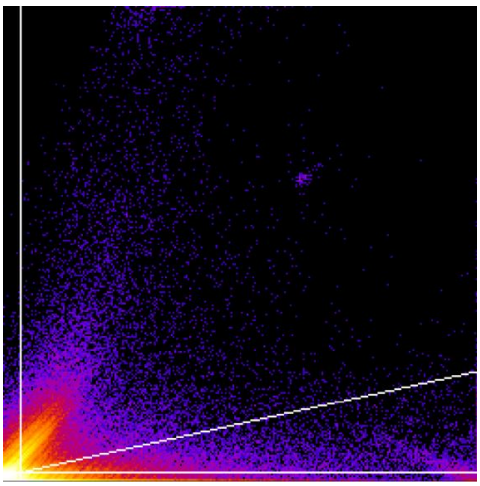

Figure 7.39. Scatterplot of colocalised pixel map of BODIPY-PINPs with astrocytes in cortex.

The scatterplot illustrates the threshold of the red channel on x-axis and the threshold of the green channel on y-axis. The intensity of a given pixel in channel 1 is used as an x-coordinate whereas the corresponding pixel's intensity in channel 2 is represented as the y-coordinate. The regression line of fluorescence ratio is also presented.

Investigation of the scatterplot demonstrates weak overlap of the pixel intensities between the BODIPY-PINPs and astrocytes in the cortex of the brain.

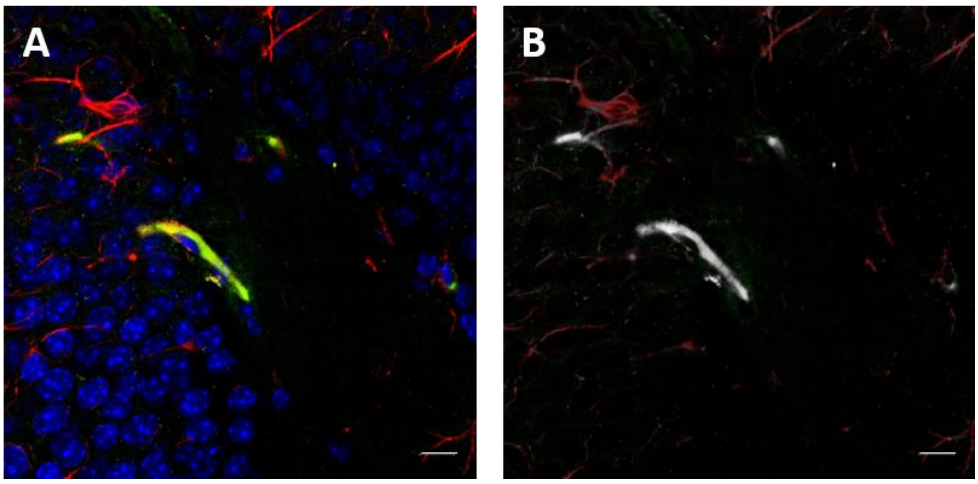

Figure 7.40. Co-localisation of BODIPY-PINPs with astrocytes in dentate gyrus.

The figure illustrates the (A) confocal image analysed, (B) pixel map where colocalised pixels are shown as white. SB = 10 µm.

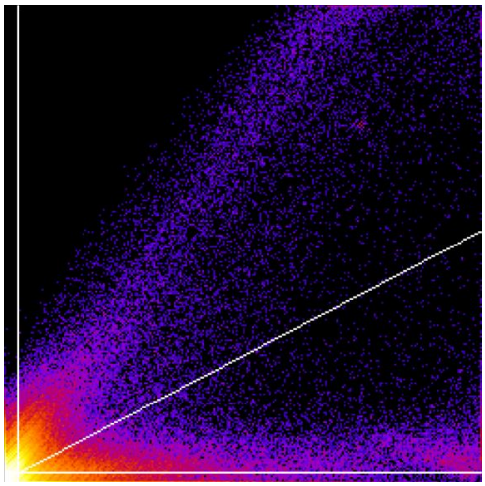

Figure 7.41. Scatterplot of colocalised pixel map of BODIPY-PINPs with astrocytes in dentate gyrus.

The scatterplot illustrates the threshold of the red channel on x-axis and the threshold of the green channel on y-axis. The intensity of a given pixel in channel 1 is used as an x-coordinate whereas the corresponding pixel's intensity in channel 2 is represented as the y-coordinate. The regression line of fluorescence ratio is also presented.

Comparing the regression line from the scatterplot of colocalised pixels of BODIPY-PINPs and astrocytes demonstrates that the two channels co-localise better in the dentate gyrus rather than the cortex of the brain.

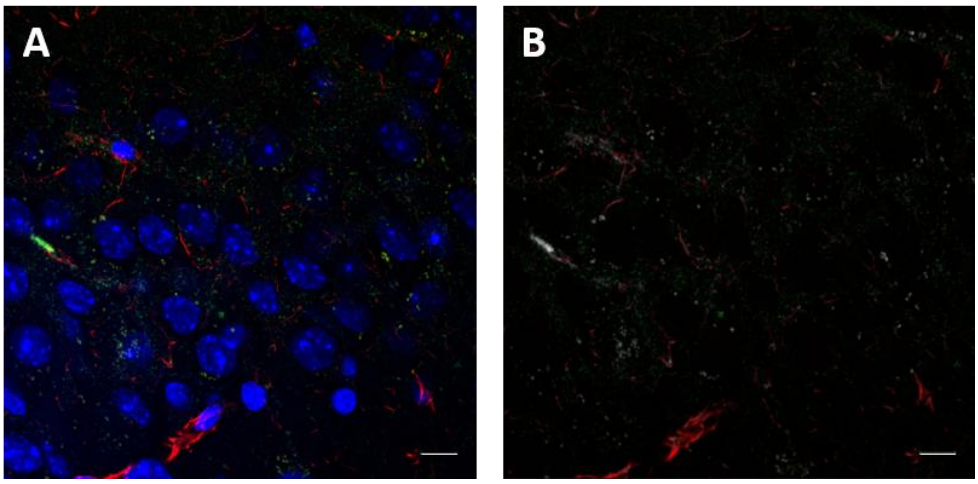

Figure 7.42. Co-localisation of BODIPY-PINPs with astrocytes in hippocampus.

The figure illustrates the (A) confocal image analysed, (B) pixel map where colocalised pixels are shown as white. SB = 10 µm.

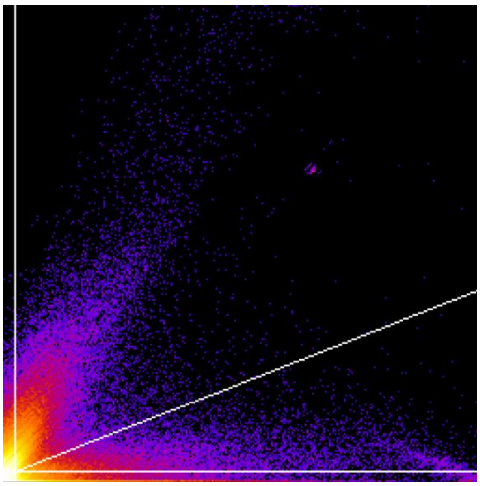

Figure 7.43. Scatterplot of colocalised pixel map of BODIPY-PINPs with astrocytes in hippocampus.

The scatterplot illustrates the threshold of the red channel on x-axis and the threshold of the green channel on y-axis. The intensity of a given pixel in channel 1 is used as an x-coordinate whereas the corresponding pixel's intensity in channel 2 is represented as the y-coordinate. The regression line of fluorescence ratio is also presented.

The scatterplot of colocalised pixels between the BODIPY-PINPs peptide and astrocytes in the hippocampus of the brain indicates weak overlap between the two channels.

Quantitative coefficients	Cortex	Dentate Gyrus	Hippocampus
Costes' p-value	1	1	1
Pearson's Rr value	0.319	0.558	0.341
Manders' R value	0.150	0.492	0.194
Manders' M1 coefficient	0.731	0.875	0.795
Manders' M2 coefficient	0.881	0.865	0.797
Manders' tM1 coefficient	0.578	0.747	0.577
Manders' tM2 coefficient	0.641	0.651	0.512

Table 7.7. Co-localisation coefficients of BODIPY-PINPs with astrocytes.

The table demonstrates the Costes' p-value obtained from "Colocalization Test", and the Pearson's correlation coefficient, Manders' overlap coefficient, Manders' colocalization coefficients M1 and M2, and Manders' thresholded coefficients tM1 and tM2 obtained from "Coloc2".

The p-values observed from the Costes' randomisation test indicate that the BODIPY-PINPs co-localise with astrocytes in the cortex, DG and hippocampus of the brain. Evaluation of the Manders' thresholded coefficients indicates that 64% of the peptide co-locates with astrocytes in the cortex, 65% in the DG and 51% in the hippocampus. Relative to the red fluorescent pixels, 58% of the astrocytes co-localise with the BODIPY-PINPs in the cortex and hippocampus and 75% in the DG of the brain.

7.3.3.2. Evaluation of co-localisation with activated microglia (anti-Iba-1)

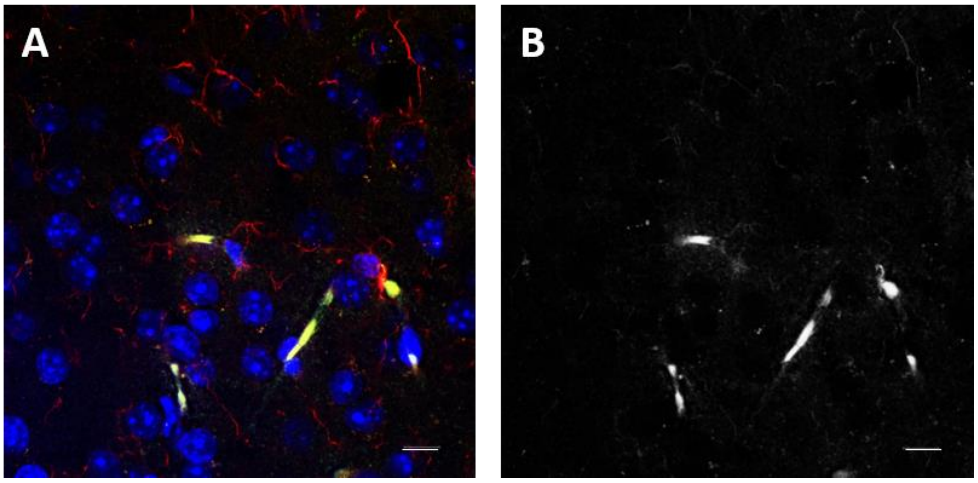

Figure 7.44. Co-localisation of BODIPY-PINPs with activated microglia in cortex.

The figure illustrates the (A) confocal image analysed, (B) pixel map where colocalised pixels are shown as white. SB = 10 µm.

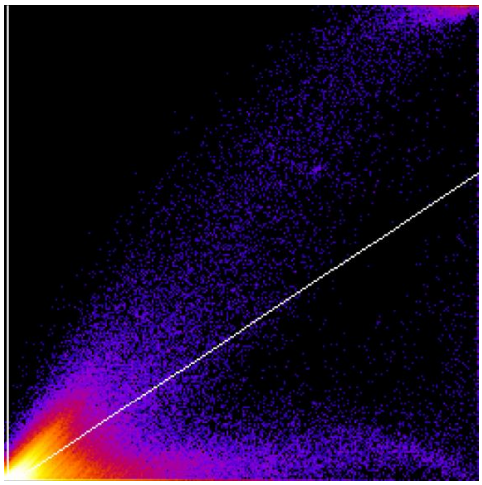

Figure 7.45. Scatterplot of colocalised pixel map of BODIPY-PINPs with activated microglia in cortex.

The scatterplot illustrates the threshold of the red channel on x-axis and the threshold of the green channel on y-axis. The intensity of a given pixel in channel 1 is used as an x-coordinate whereas the corresponding pixel's intensity in channel 2 is represented as the y-coordinate. The regression line of fluorescence ratio is also presented.

The scatterplot indicates strong overlap between the BODIPY-PINPs and activated microglia in the cortex of the brain.

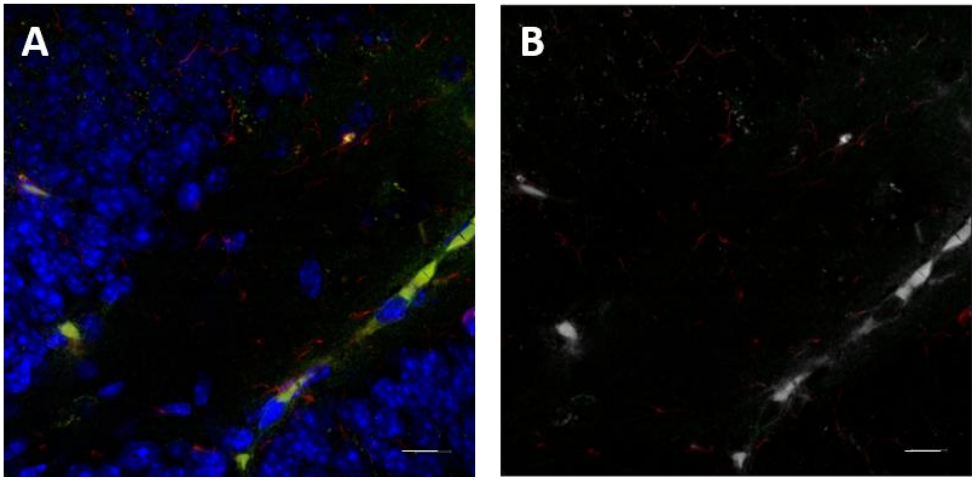

Figure 7.46. Co-localisation of BODIPY-PINPs with activated microglia in dentate gyrus.

The figure illustrates the (A) confocal image analysed, (B) pixel map where colocalised pixels are shown as white. SB = 10 µm.

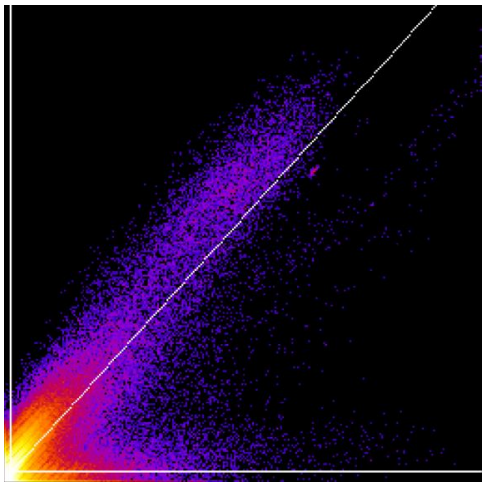

Figure 7.47. Scatterplot of colocalised pixel map of BODIPY-PINPs with activated microglia in dentate gyrus.

The scatterplot illustrates the threshold of the red channel on x-axis and the threshold of the green channel on y-axis. The intensity of a given pixel in channel 1 is used as an x-coordinate whereas the corresponding pixel's intensity in channel 2 is represented as the y-coordinate. The regression line of fluorescence ratio is also presented.

Evaluation of the scatterplot of colocalised pixels demonstrates really strong correlation between BODIPY-PINPs and activated microglia in the DG of the hippocampal formation complex.

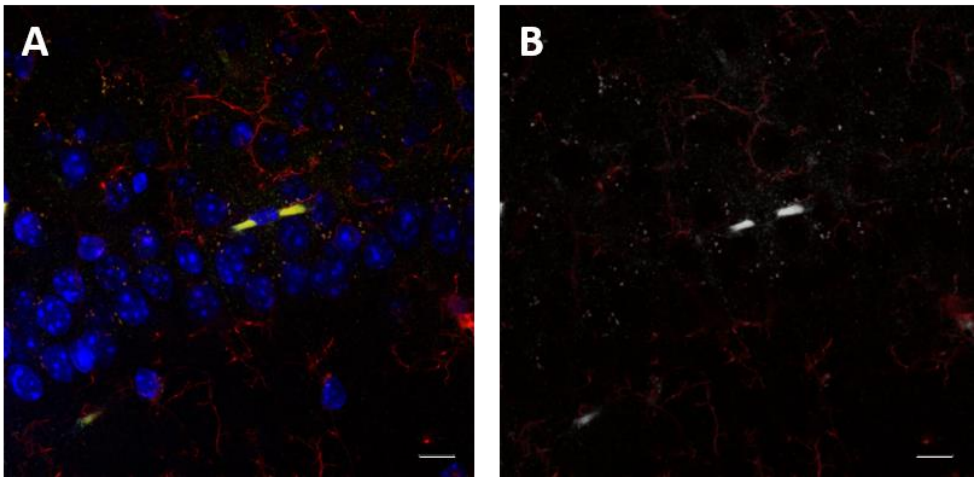

Figure 7.48. Co-localisation of BODIPY-PINPs with activated microglia in hippocampus.

The figure illustrates the (A) confocal image analysed, (B) pixel map where colocalised pixels are shown as white. SB = 10 µm.

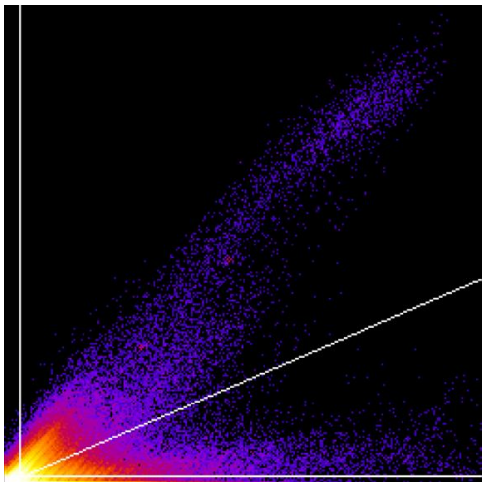

Figure 7.49. Scatterplot of colocalised pixel map of BODIPY-PINPs with activated microglia in hippocampus.

The scatterplot illustrates the threshold of the red channel on x-axis and the threshold of the green channel on y-axis. The intensity of a given pixel in channel 1 is used as an x-coordinate whereas the corresponding pixel's intensity in channel 2 is represented as the y-coordinate. The regression line of fluorescence ratio is also presented.

The scatterplot indicates strong overlap between the BODIPY-PINPs peptide and activated microglia in the hippocampus of the brain.

Quantitative coefficients	Cortex	Dentate Gyrus	Hippocampus
Costes' p-value	1	1	1
Pearson's Rr value	0.701	0.824	0.605
Manders' R value	0.698	0.842	0.620
Manders' M1 coefficient	0.806	0.923	0.740
Manders' M2 coefficient	0.993	0.886	0.988
Manders' tM1 coefficient	0.677	0.800	0.642
Manders' tM2 coefficient	0.806	0.774	0.758

Table 7.8. Co-localisation coefficients of BODIPY-PINPs with activated microglia.

The table demonstrates the Costes' p-value obtained from "Colocalization Test", and the Pearson's correlation coefficient, Manders' overlap coefficient, Manders' colocalization coefficients M1 and M2, and Manders' thresholded coefficients tM1 and tM2 obtained from "Coloc2".

Evaluation of the p-values from the Costes' randomization test indicates that there is true co-localisation between the BODIPY-PINPs and activated microglia in all of the examined regions of the brain. The values resulting from the Manders' thresholded test indicate that 81% of the peptide co-localises with activated microglia in the cortex, 75% in the DG and 76% in the hippocampus. On the other hand, 68% of activated microglia co-locate with BODIPY-PINPs in the cortex of the brain, 80% in the DG and 64% in the hippocampus.

7.3.3.3. Evaluation of co-localisation with neurons (anti-NeuN)

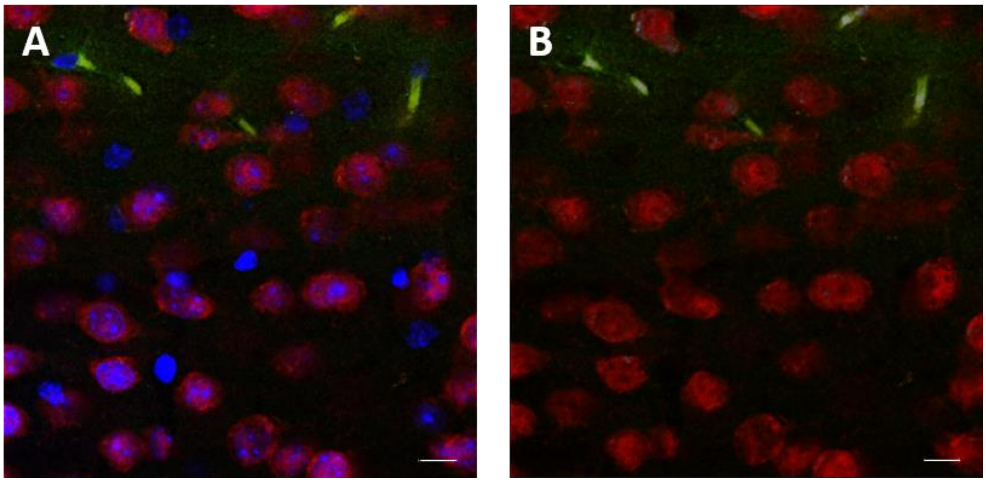

Figure 7.50. Co-localisation of BODIPY-PINPs with neurons in cortex.

The figure illustrates the (A) confocal image analysed, (B) pixel map where colocalised pixels are shown as white. SB = 10 µm.

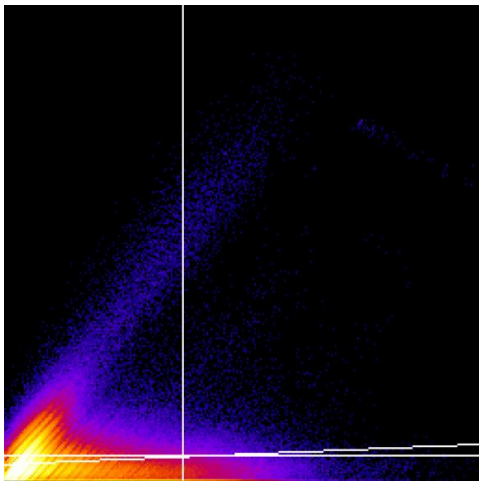

Figure 7.51. Scatterplot of colocalised pixel map of BODIPY-PINPs with neurons in cortex.

The scatterplot illustrates the threshold of the red channel on x-axis and the threshold of the green channel on y-axis. The intensity of a given pixel in channel 1 is used as an x-coordinate whereas the corresponding pixel's intensity in channel 2 is represented as the y-coordinate. The regression line of fluorescence ratio is also presented.

The scatterplot resulting from the colocalised pixels of the BODIPY-PINPs and neurons in the cortex of the brain demonstrates very weak overlap between the two channels.

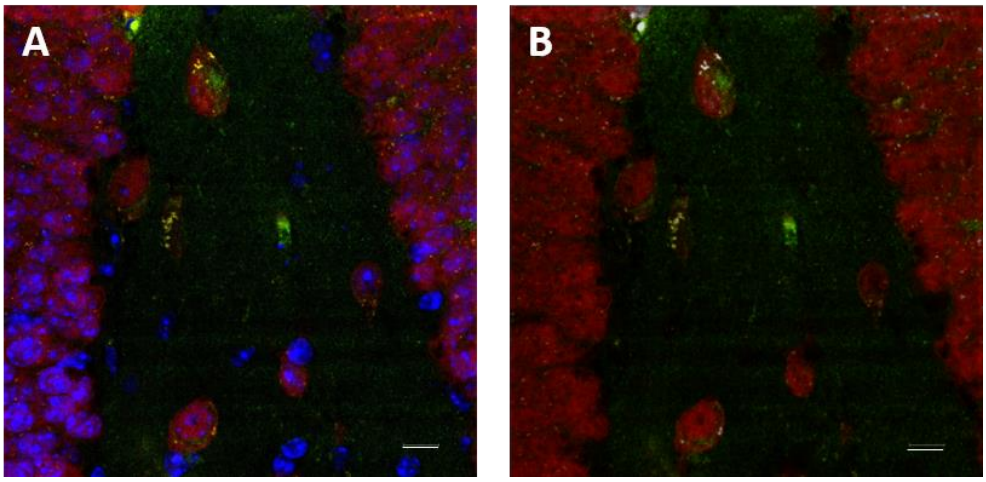

Figure 7.52. Co-localisation of BODIPY-PINPs with neurons in dentate gyrus.

The figure illustrates the (A) confocal image analysed, (B) pixel map where colocalised pixels are shown as white. SB = 10 µm.

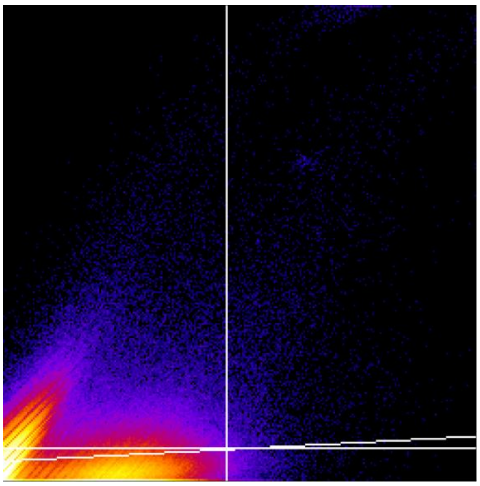

Figure 7.53. Scatterplot of colocalised pixel map of BODIPY-PINPs with neurons in dentate gyrus.

The scatterplot illustrates the threshold of the red channel on x-axis and the threshold of the green channel on y-axis. The intensity of a given pixel in channel 1 is used as an x-coordinate whereas the corresponding pixel's intensity in channel 2 is represented as the y-coordinate. The regression line of fluorescence ratio is also presented.

Similarly to the cortex, comparison of the pixels intensity between the BODIPY-PINPs and neurons in the DG of the brain show only weak overlap.

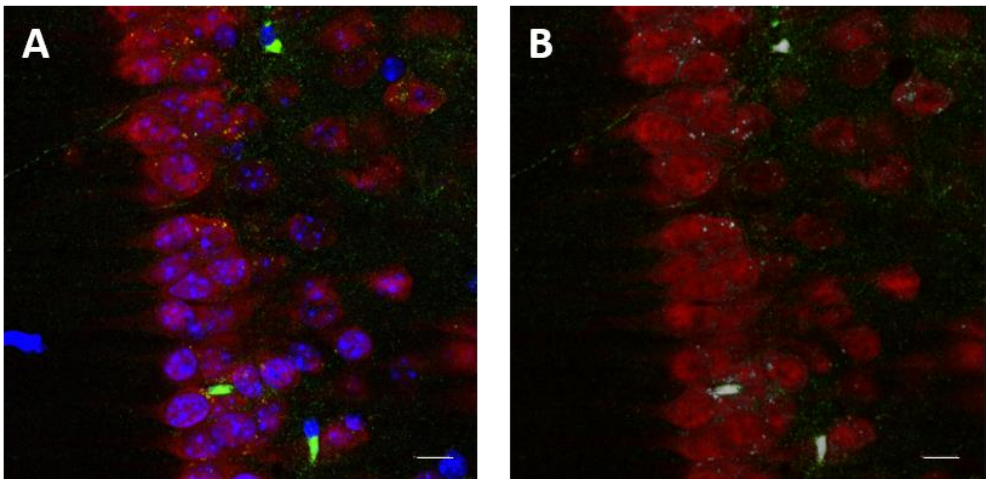

Figure 7.54. Co-localisation of BODIPY-PINPs with neurons in hippocampus.

The figure illustrates the (A) confocal image analysed, (B) pixel map where colocalised pixels are shown as white. SB = 10 µm.

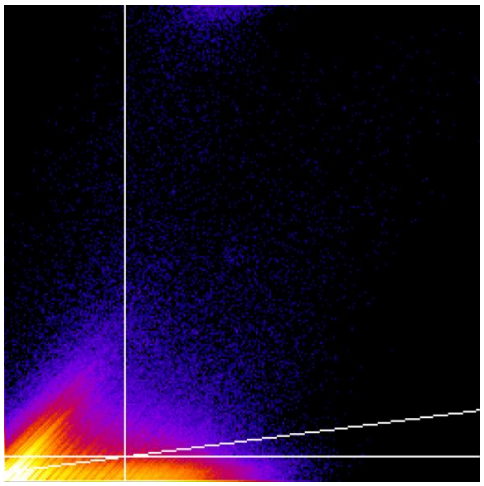

Figure 7.55. Scatterplot of colocalised pixel map of BODIPY-PINPs with neurons in hippocampus.

The scatterplot illustrates the threshold of the red channel on x-axis and the threshold of the green channel on y-axis. The intensity of a given pixel in channel 1 is used as an x-coordinate whereas the corresponding pixel's intensity in channel 2 is represented as the y-coordinate. The regression line of fluorescence ratio is also presented.

Data from the scatterplot comparing the colocalised pixels of BODIPY-PINPs and neurons in the hippocampus indicate weak and random overlap between the two channels.

Quantitative coefficients	Cortex	Dentate Gyrus	Hippocampus
Costes' p-value	1	1	1
Pearson's Rr value	0.085	0.095	0.184
Manders' R value	0.102	0.535	0.291
Manders' M1 coefficient	0.889	0.826	0.794
Manders' M2 coefficient	0.995	0.868	0.972
Manders' tM1 coefficient	0.271	0.251	0.263
Manders' tM2 coefficient	0.057	0.043	0.240

Table 7.9. Co-localisation coefficients of BODIPY-PINPs with neurons.

The table demonstrates the Costes' p-value obtained from "Colocalization Test", and the Pearson's correlation coefficient, Manders' overlap coefficient, Manders' colocalization coefficients M1 and M2, and Manders' thresholded coefficients tM1 and tM2 obtained from "Coloc2".

The results of the Costes' randomization test indicates that the BODIPY-PINPs do co-localise with neurons in the brain. However, evaluation of the Manders' thresholded coefficients demonstrate that 6% of the peptide co-localises with neurons in the cortex, 4% in the DG and 24% in the hippocampus. Relative to the channel 1 pixels, 27% of neurons co-localise with the BODIPY-PINPs in the cortex, 25% in the DG and 26% in the hippocampus of the brain.

7.4. Discussion

This Chapter presents a co-localisation study of Flu-RI-OR2-TAT, Flu-RI-OR2-NAG and BODIPY-PINPs with neuronal and glial cells in the cortex, DG and hippocampus of the brain. Previously published data by Parthsarathy and colleagues demonstrated that the Flu-RI-OR2-TAT peptide co-localises with activated microglial cells in the brains of APP/PS1 transgenic mice (Parthsarathy et al., 2013).

Peripheral administration of 100 nmol/kg of Flu-RI-OR2-TAT and Flu-RI-OR2-NAG peptides and 4 µmol/kg of BODIPY-PINPs results in BBB penetration after 1 h, as

demonstrated in the previous Chapter (Chapter 6). Here, these peptides and peptide-nanoparticles showed some co-localisation with astrocytes, activated microglia and neurons in the cortex, DG and hippocampus of the brain, in WT mice with C57/BL6 background. The table below (Table 7.10.) represents a summary of the colocalization study.

Brain Region	***Cell type***	***Flu-RI-OR2-TAT***	***Flu-RI-OR2-NAG***	***BODIPY-PINPs***
Cortex	*Astrocytes*	High	Low	Low
	Activated microglia	Moderate	High	High
	Neurons	Moderate	Low	Low
DG	*Astrocytes*	High	Low	Moderate
	Activated microglia	High	Moderate	High
	Neurons	Low	Low	Low
Hippocampus (CA1)	*Astrocytes*	Moderate	Moderate	Moderate
	Activated microglia	High	Moderate	Moderate
	Neurons	Low	Low	Low

Table 7.10. Summary table of colocalisation between peptides and cells.

The table represents a summary of the colocalization between the three peptides (Flu-RI-OR2-TAT, Flu-RI-OR2-NAG and BODPY-PINPs) and the cell types (astrocytes, activated microglia, neurons) examined in the cortex, hippocampus, and DG of WT mouse brains.

The Flu-RI-OR2-TAT peptide demonstrated some tendency to co-localise with activated microglial cells, as indicated in the previous study by Parthsarathy and colleagues (Parthsarathy et al., 2013), in all regions of the brain that were investigated in this study. The same property was observed with BODIPY-PINPs and Flu-RI-OR2-NAG peptides, where they were mainly found inside activated microglia, rather than astrocytes and neurons. Activated microglial cells function as immune macrophages in the presence of cytotoxic compounds in the brain. This ability is also evident when increased concentrations of Aβ are present in the brains of AD

patients. More specifically, activated microglial cells tend to cluster around the senile plaques in the brain and mediate inflammation pathways by the secretion of cytokines and activation of macrophages to aid the clearance of Aβ (Mandrekar and Landreth, 2013; Lai and McLaurin, 2012; Solito and Sastre, 2012;).

Previously published work on APP/PS1 mice by Parthsarathy and colleagues supported that the presence of the Flu-RI-OR2-TAT peptide inside activated microglia is due to the attachment of the peptide to Aβ fibrils, as the activated microglial cells are responsible for the active take up of amyloid by phagocytosis resulting in the clearance of Aβ from the brain (Paresce et al., 1997). As the Flu-RI-OR2-NAG and BODIPY-PINPs were found colocalised with activated microglial cells, there is the likelihood that these peptides can retain this property. However, further ultrastructural studies and colocalisation examination with an Aβ marker are required to confirm this. Additionally, as the peptides co-localise with astrocytes, this further supports the fact that the peptides can penetrate across the BBB, since astroglial cells are located close to the BBB (Abbott, 2002) and structurally support the tight junctions formed by the endothelial cells, controlling the access of substances crossing from blood to the CNS.

The mechanism by which the peptides are inserted inside the cells was not investigated in this project. With reference to the Flu-RI-OR2-NAG, the peptide was formulated with the NAG transit sequence so as the inhibitor can utilise the glucose transporters that are located at the BBB (GLUT1) (Bell et al., 1990) to penetrate inside the brain, and the GLUT3 transporters on the membrane of neurons (Bell et al., 1990) and NAG transporters expressed at the Golgi complex of the cells (Abeijon et al., 1996) to penetrate inside cells. On the other hand, the TAT sequence of the RI-OR2-TAT inhibitor has been widely used as a transit sequence enabling a diversity of molcules across the BBB (Dietz and Bahr, 2004; Ramanathan et al., 2001); and this activity was also proven to be retained in the retro-inverso version of the TAT sequence (Repici et al., 2007; Zhang et al., 2009). However, the exact mechanism by which the TAT sequence enables the penetration of compounds inside cells remains unclear (Zhang et al., 2009).

7.5. Conclusions

The results from this study have demonstrated that Flu-RI-OR2-TAT, Flu-RI-OR2-NAG and BODIPY-PINPs are found mainly inside or in association with microglial cells, rather than astrocytes and neurons in the cerebral cortex, DG and hippocampus of the brains of WT mice acutely injected i.p. with 100 nmol/kg of the free peptides and 4 μmol/kg of the peptide-decorated liposomes, after 1 h.

One of the limitations related to this study is the absence of a vascular marker in the brain. Endothelial cells in the brain comprise the microvasculature, which along with the astroglial cells, form the BBB in the CNS (Abbott, 2002; Tanapat, 2013). Co-localisation of the peptides with vascular endothelial cells would further confirm that they are able to cross the BBB and deposit in the brain. Additionally, as the acquisition of the images (63X objective) for this study was performed at the same time as the images acquired for the BBB penetration study (40X objective), the sections exhibited partial photobleaching that might have interfered with the statistical analysis of the study, even though the majority of the colocalization tools employed in this Chapter are independent of the channels' and background intensities.

With a therapeutic focus, the study further supports findings that the peptides can cross an intact and functional BBB, as demonstrated previously in Chapter 6. Additionally, the ability of the peptides to co-locate with activated microglia indicates that they may be involved in the clearance mechanisms responsible for removal of Aβ from the brains of diseased individuals.

Chapter 8: Final discussion and further work

8.1. Background

AD is the most common neurodegenerative disease, affecting mainly elderly individuals, and is characterised by the accumulation of extracellular senile plaques containing the Aβ peptide, and intracellular neurofibrillary tangles composed of hyperphosphorylated tau protein (Bird, 2008). Currently, AD is considered as an epidemic since 46.8 million people worldwide are believed to be affected by the disease, or by a related dementia, a number that is expected to increase to 74.7 million by 2030 and 131.5 million by 2050. It is estimated that a new case of dementia occurs every 3.2 sec (WWW, BrightFocus Foundation).

8.1.1. Drugs targeting the Aβ aggregation pathway

Aβ pathology is a central component in AD. Accumulating research evidence has supported the hypothesis that Aβ oligomerisation and fibrillogenesis are crucial and primary pathogenic events in AD (Lansbury and Lashuel, 2006; Haass and Selkoe, 2007; Walsh and Selkoe; 2007). It was originally proposed that the mature end-products of the Aβ aggregation process, the amyloid fibrils which are present in the senile plaques of the brain, are the primary neurotoxic factors that are associated with the progression of the disease (Hardy and Allsop, 1991). However, later studies on AD have supported the idea that the early nonfibrillar aggregates, known as the soluble oligomers, are the main pathogenic components that are partly responsible for neurodegeneration and neuronal cell death in the brains of diseased individuals (Hardy and Selkoe, 2002). Oligomeric forms of Aβ are now thought to be more toxic than the mature fibrils (Klein et al., 2001; Hardy and Selkoe, 2002; Varvel et al., 2008), consequently resulting in the potent memory and learning deficits (Chromy et al., 2003; Bitan et al., 2003) as well as cognitive impairment (Tomic et al., 2009), that are the main symptoms of the disease.

Therefore, the invention and development of drugs that directly inhibit the very early stages of the aggregation process, rather than the late stages of amyloid fibril

formation, is considered to be a viable therapeutic strategy for slowing or even halting the progression of AD. Many studies have been performed in recent years in order to develop new drugs that target the formation, clearance or aggregation of Aβ, with all of them proven to be ineffective (Mangialasche et al., 2010). Several of these inhibitor drugs target the β-secretase (Klaver et al., 2010) and γ-secretase (Wolfe, 2008) proteolytic enzymes that are both involved in the production of Aβ from the APP protein (LaFerla et al., 2007). Both approaches have resulted in various side effects in patients, as both enzymes have substrates other than APP (Gandy, 2005).

8.1.2. Other approaches used in drug development

Various other approaches to drug development, such as direct immunisation with Aβ, or passive immunisation with anti-Aβ antibodies, have also failed to progress in clinical trials, often due to adverse side effects, including activation of brain inflammatory responses that result in microhaemorrhages (Sperling et al., 2012) and the development of meningoencephalitis (Gilman et al., 2005). In particular, studies based on passive immunisation with anti-Aβ antibodies have resulted in the development of Bapineuzumab (Johnson and Johnson) and Solanezumab (Elli Lilly), both of which failed in late-clinical trials, as they did not demonstrate any improved cognition in mild-to-moderate AD (Sperling et al., 2012; WWW, ClinicalTrials.gov). One more promising discovery, Curcumin, has demonstrated inhibition of Aβ aggregation (Yang et al., 2005), but is unsuitable as a drug candidate because it exhibits poor bioavailability and biodistribution.

Currently, four drugs are approved for use in patients with AD. However, the three acetylcholinesterase inhibitor drugs Galantamine, Donepezil and Rivastigmine, and the NMDA receptor antagonist drug Memantine, temporarily alleviate the symptoms of AD but do not have a major impact on disease progression (Inglis, 2002; Areosa et al., 2006; Schneider et al. 2011). Consequently, there is an urgent need to develop more effective drugs that prevent, delay the onset, slow the progression, or more effectively improve the symptoms of AD.

8.1.3. The RI-OR2 peptide-based aggregation inhibitors

Published data by Parthsarathy and colleagues (Parthsarathy et al., 2013) demonstrated that the RI-OR2-TAT peptide inhibits Aβ oligomer and fibril formation, as well as blocking their toxic effects *in vitro* using cultured SH-SY5Y human neuroblastoma cells. This peptide inhibitor was also found to cross the BBB and bind to amyloid plaques and activated microglial cells in the cerebral cortex of APP/PS1 Alzheimer's transgenic mice, following its peripheral administration (100 nmol/kg) once per day for 21 days. Data from the same research also showed that the RI-OR2-TAT peptide inhibitor was able to reduce amyloid deposition, oxidation and inflammation, yet also stimulate neurogenesis in the DG of the same mouse model of AD (Parthsarathy et al., 2013).

The incorporation of the retro-inverted version of the HIV-1 'TAT' sequence on the former developed peptide, RI-OR2 (Taylor et al., 2010), was aimed at targeting the peptide into the brain. The TAT sequence has previously been shown to enable a variety of different molecules to cross the BBB (Dietz and Bahr, 2004; Ramanathan et al., 2001); an activity that was proven to be retained in the retro-inverso version of the TAT sequence (Repici et al., 2007; Zhang et al., 2009). In RI-OR2-TAT, the retro-inverso TAT sequence was integrated so that the protease resistance of the whole molecule was maintained (Parthsarathy et al., 2013).

However, one problem associated with the use of the TAT sequence is that the peptide is not targeted selectively to the brain, possibly resulting in various adverse peripheral side effects. This limitation of the RI-OR2-TAT peptide as well its effect on the level of Aβ aggregation could be improved by using a more brain-selective delivery mechanism, ideally in a combination with a more potent inhibitor. An approach that was suggested by Parthsarathy and colleagues to increase the potency of RI-OR2-TAT against Aβ aggregation, was to attach the peptide onto the surface of lipid nanoparticles, to produce a multivalent inhibitor (Parthsarathy et al., 2013). The resulting PINPs have been studied as part of this project. Another approach taken here is to use NAG as an alternative targeting mechanism to TAT, in an attempt to develop a new more brain-selective version of the RI-OR2 aggregation inhibitor.

8.2. Findings of the study

The scope of this PhD thesis project was to develop a new peptide inhibitor, RI-OR2-NAG, as an alternative anti-aggregation peptide to RI-OR2-TAT. Additionally, this project was aiming at determining whether RI-OR2-TAT, RI-OR2-NAG and PINPs, are able to penetrate across an intact and functional BBB, and investigate the accumulation of the peptides in the brain and distribution in other body tissues of WT mice with C57/BL6 background following their peripheral administration.

8.2.1. Penetration across an intact BBB

The ability of RI-OR2-TAT and PINPs to cross the BBB have been assessed previously. Parthsarathy and colleagues have demonstrated that the RI-OR2-TAT peptide was able to cross the BBB of APP/PS1 transgenic mice (Parthsarathy et al., 2013). On the other hand, PINPs can penetrate an artificial BBB composed of a hCMEC/D3 human brain endothelial cells monolayer (Gregori et al., 2017). In this project, RI-OR2-TAT, RI-OR2-NAG and PINPs have been shown to penetrate a dynamic and functional BBB, 1 h after peripheral administration of 100 nmol/kg of the free peptides and 4 μmol/kg of the PINPs.

The PINPs demonstrated significantly improved results compared to the two free peptides, RI-OR2-TAT and RI-OR2-NAG, indicating that the attachment of the RI-OR2-TAT peptide onto the surface of nanoliposomes favours the penetration of the peptide into the brain. This property of the PINPs can be partly attributed to the "stealth" characteristics of PEGylated liposomes, and also to the naturally occurring outer lipid membrane layer of this type of nanoliposome device that facilitates penetration across cell membranes and biological barriers (Szoka and Papahadjopoulos, 1980).

In the case of the RI-OR2-NAG peptide, it was believed that incorporation of the NAG transit moiety onto the RI-OR2 could possibly target the peptide to the brain more effectively and selectively than the TAT transit sequence of the RI-OR2-TAT peptide. By utilising the glucose transporters located at the BBB (GLUT1) and on the membranes of neurons (GLUT3) (Bell et al., 1990), as well as the NAG transporter

(SLC35A3) expressed at the Golgi complex of cells (Abeijon et al., 1996), the RI-OR2-NAG peptide should penetrate the BBB of the CNS and accumulate inside the brain. Even though this study has demonstrated that the RI-OR2-NAG peptide is found inside the brain, it was present at lower concentrations than RI-OR2-TAT and PINPs, suggesting that NAG-facilitated transport across the BBB is less effective than the TAT transit system.

8.2.2. Distribution and excretion of the peptides

Luminex technology was used to identify the distribution of the peptides in the body of WT mice, 1 h following their peripheral administration by i.p. injection. RI-OR2-TAT showed a a relatively high concentration in the stomach compared to other tissues of the mice, which is possibly due to the primary absorption metabolism by the liver and distribution through the general blood circulation. The peptide was also detected at significantly higher concentrations in the small intestine, indicating a possible mechanism of elimination through bile secretion. The peptide could either then be excreted through the faeces or reabsorbed back into the systemic circulation by the intestinal mucosa of the small intestine (Roberts et al., 2002). These findings are also supported by the detection of the peptide in the liver, and its absence from the kidneys.

With respect to RI-OR2-NAG, this peptide was primarily detected in the small intestines of the mice, and also in the kidneys. This suggests that the peptide was already subjected to bile secretion and possibly reabsorbed by the intestinal mucosa into the blood circulation for distribution and elimination through the kidneys by urine (Roberts et al., 2002). A similar distribution was observed by the PINPs. However, these results should be interpreted with great caution due to the limitations in effectively developing sensitive assays for detection of these peptides.

One of the most important findings of this study is, however, that the peptides were detected at low levels in the brains of the mice, supporting the idea that they can penetrate across the BBB from the blood circulation and enter the brain.

8.2.3. The anti-aggregational properties of the peptides

Previously published data on RI-OR2-TAT showed that the peptide was able to inhibit Aβ aggregation up to a molar ratio of 1:5 (inhibitor to Aβ) as demonstrated by the ThT assay (Parthsarathy et al., 2013). On the other hand, Gregori, Taylor and colleagues have demonstrated that the attachment of the peptide onto the surface of the liposome induced a dramatic improvement in the ability of the peptide to inhibit the aggregation process. As demonstrated by ThT data, the peptide inhibited 50% of the aggregation at a molar ratio of 1:50 of lipid to Aβ, or more specifically at a molar ratio of 1:2,000 of RI-OR2-TAT to Aβ, as the surface peptide comprises 2.5% of the total lipid (Gregori et al., 2017). More importantly, the peptide demonstrates about 25% inhibition even at a molar ratio of 1:5,000 lipid to Aβ or 1:200,000 RI-OR2-TAT to Aβ (Gregori et al., 2017).

The explanation for this increase in potency of the PINPs peptide relative to the free RI-OR2-TAT peptide can be partly attributed to the presence of multiple copies of the RI-OR2-TAT peptide on the surface of the nanoliposomes, allowing the simultaneous interaction of the peptide with many sites on aggregated Aβ (Figure 8.1.) (Gregori et al., 2017). This idea is supported by previous work with tetrameric dendrimers of the KLVFF peptide, which are much more potent and effective than the monomer at inhibiting Aβ aggregation (Chafekar et al., 2007). Thus, in the case of PINPs, multiple copies of the KLVFF sequences should also result in a more potent inhibitor. Another possible explanation for the high potency of PINPs could be associated with the highly positive electric charge of the TAT region of the peptide. The RI-OR2-TAT peptide contains several positively-charged amino acids, and multiple copies of this peptide on the surface of the liposomes could help to attract and bind the Aβ peptide by electrostatic interactions (Figue 8.1.) (Gregori et al., 2017).

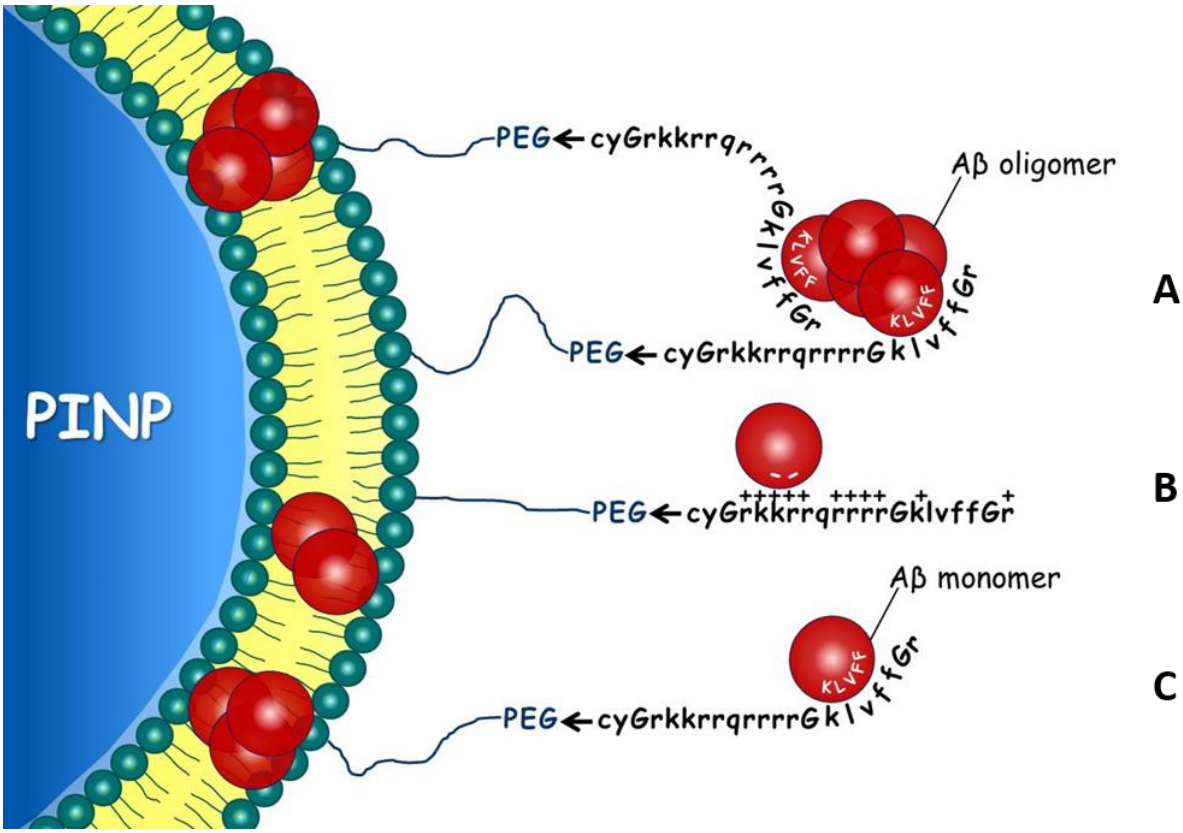

Figure 8.1. Possible mechanisms of action of PINPs.

The figure illustrates the possible mechanisms by which the PINPs peptide inhibits the aggregation of Aβ. The retro-inverted "ffvlk" peptide of the free RI-OR2-TAT peptide is designed to interact with the "KLVFF" sequence(s) of the (A) oligomeric and (C) monomeric Aβ. It is also possible that the Aβ interacts with the positively charged TAT sequence of the peptide (B), and once captured, the Aβ molecules are inserted into the lipid bilayer of the liposomes.

With respect to RI-OR2-NAG, this peptide proved to be a more potent inhibitor of Aβ aggregation than RI-OR2-TAT peptide, in the ThT experiments reported here. Even though the main binding region (retro-inverted ffvlk) is identical between the two free peptides, there is a possibility the the attachment of the NAG sequence to the main RI-OR2 peptide enhances the binding affinity of the peptide to the native Aβ by altering the conformation of the three-dimentional peptide structure. Consequently, the attachment of the RI-OR2-NAG peptide onto the surface of lipid scaffolds would possibly result in a better peptide inhibitor than the PINPs, and also exhibit the advanced brain and cell penetration properties of the nanoliposomes (Szoka and Papahadjopoulos, 1980). However, these hypotheses need to be further examined.

8.3. Limitations of the study

The main limitation of the study is related to the administration of the peptides which was performed intraperitoneally. Ideally, the study of drug distribution should be conducted by administering the compounds intravenously. In that case, the peptides would avoid the first pass metabolism effect and enter the circulation as unchanged compounds where they exhibit 100% bioavailability (Shargel and Yu, 1999) allowing the accurate qualification of distribution and metabolism of the peptides.

Another significant limitation of the project is the limited number of animals used in the BBB penetration study (Chapter 6). The small number of animals treated with each peptide inhibitor has resulted in large error bars during the statistical analysis of the experiments, that do not allow the effective comparison on the deposition of the peptides within the cortex, hippocampus and DG of the normal brain.

Additionally, another restriction of this study is the likelihood of inaccurate quantification of the distribution of some of the peptides in the tissues by the immunoassays employed for this purpose (Chapters 4 and 5). The lack of sensitivity of the developed assays for the Flu-RI-OR2-NAG and PINPs peptides in particular, has probably resulted in fallacious determination of the concentrations of the peptides in different tissues. However, the observed pattern of tissue distribution is probably accurate for the Flu-RI-OR2-TAT, although comparison between peptides is problematic. In general, the Luminex technology is more sensitive compared to other assay-based techniques, particularly to the ELISA assay that was used for detection of the PINPs peptide. However, there are various potential problems with optimisation of an assay for detection of the PINPs peptide, including the adhesion of this lipid-bound peptide to the Luminex plate filter, poor biotinylation of the detection antibody, and the use of non-matched antibody pairs.

8.4. Future work

With reference to the limitations of this study, future research should include the administration of the peptides intravenously to study the biodistribution of the drugs (Shargel and Yu, 1999), as well as other possible routes of administration. Of particular interest, is the possibility of intranasal administration of the peptides or peptide-liposomes to facilitate immediate absorption into the brain, avoiding also the metabolism of the peptides upon absorption by barriers other than the BBB. Additionally, examination of variable durations of treatment would provide information on the half-life of the peptides, as well as elimination rate and other important pharmacokinetic factors.

With respect to the detection of the peptides, alternative antibodies could be tested for the Flu-RI-OR2-NAG and BODIPY-PINPs assays, in order to develop more sensitive methods that would more accurately quantify the tissue-specific distribution of these peptides.

8.5. Final conclusion

Reflecting on the hypotheses and aims of this thesis project, the RI-OR2-TAT, RI-OR2-NAG and PINPs peptides proved that are able to cross a dynamic and intact BBB (Chapter 6) and were found colocalised with major neuronal and glial cells in the cortex, hippocampus and DG of the mouse brains (Chapter 7). Regarding the properties of the two free peptides, the RI-OR2-NAG demonstrated more potent inhibition of Aβ fibrillogenesis compared to RI-OR2-TAT, showed no toxic effects on cultured neuroblastoma cells, yet displayed slower penetration inside cells (Chapter 3) in contrast to RI-OR2-TAT that has previously shown deposition in cells within 10 min of incubation (Parthsarathy et al., 2013).

On the other hand, the attempt to study the bio-distribution and possible elimination routes of the Flu-RI-OR2-TAT, Flu-RI-OR2-NAG and BODIPY-PINPs peptides was not achieved (Chapter 5). The main reason of failing to demonstrate these properties of

the peptides was the inaccurate development of detection assays for Flu-RI-OR2-NAG and BODIPY-PINPs (Chapter 4), as well as my incabability of applying an intravenous administration of the peptides. The i.p. administration of the inhibitor peptides resulted in their decreased bio-availability due to the "first-pass" effect occurring prior their absorption in circulation and tissue distribution.

In conclusion, the attachment of the RI-OR2-TAT peptide onto the surface of lipid nanoparticle scaffolds has resulted in the generation of a potent and multivalent inhibitor of the Aβ aggregation process which also exhibits improved BBB penetration properties. Since the RI-OR2-NAG peptide appears to be a better aggregation inhibitor than RI-OR2-TAT, the attachment of RI-OR2-NAG onto liposomes could be particularly beneficial. This would confer on the liposome-attached RI-OR2-NAG peptide the unique features possessed by the nanoliposomes, including targeted delivery into the brain, stealth properties to avoid the immune system, and increased bioavailability and circulation times.

Finally, we are currently working on a collaborative project with the University of Eastern Finland and the University of Rome "La Sapienza". It has been demonstrated that young APP/PS1 mice exhibit epileptic spiking due to the presence and accumulation of Aβ in the brain; an effect that is not observed in WT mice (Minkeviciene et al., 2009). This project involves the investigation of brain biomarkers following i.p. administration of 100 nmol/kg of RI-OR2-TAT peptide once per day for 21 days in 3 months old APP/PS1 transgenic mice. More importantly though, epileptic electroencephalogram (EEG) recordings of the cortex and hippocampus of the mice will be performed to investigate the effects of RI-OR2-TAT on normalisation of epileptic EEG. The recordings will be performed once per week and compared with a baseline EEG recording in treated and untreated APP/PS1 transgenic mice.

Of particular interest here, no peptide-based inhibitor targeting the Aβ aggregation process has been tested yet in any advanced clinical trial (Taylor et al., 2010; Parthsarathy et al., 2013). I believe that our peptide inhibitors, PINPs, RI-OR2-TAT

and RI-OR2-NAG, show encouraging results; and further studies and development of the peptides will hopefully enable them firstly to enter human clinical trials and ultimately to be used as an early-intervention disease-modifying therapy to slow or event prevent the clinical symptoms of AD.

Bibliography

Abbott, N. J. (2002) Astrocyte-endothelial interactions and blood-brain permeability. *J. Anat.*, **200**: 629 – 638.

Abbott, N. J., Patabendige, A. A., Dolman, D. E., Yusof, S. R., and Begley, D. J. (2010) Structure and function of the blood-brain barrier. *Neurobiol. Dis*., **37**: 13 – 25.

Abbott, N. J., Ronnback, L., and Hansson, E. (2006) Astrocyte-endothelial interactions at the blood-brain barrier. *Nat. Rev. Neurosci*., **7**: 41 – 53.

Abeijon, C., Robbins, P. W., and Hirschberg, C. B. (1996) Molecular cloning of the Golgi apparatus uridine diphosphate-*N*-acetylglucosamine transporter from *Kluyveromyces lactose*. *Proc. Natl. Acad. Sci. USA*, **93**: 5963 – 5968.

Adolfsson, O., Pihlgren, M., Toni, N., Varisco, Y., Buccarello, A. L., Antoniello, K., Lohmann, S., Piorkowska, K., Gafner, V., Atwal, J. K., Maloney, J., Chen, M., Gogineni, A., Weimer, R. M., Mortensen, D. L., Friesenhahn, M., Ho, C., Paul, R., Pfeife, A., Muhs, A., and Watts, R. J. (2012) An effector-reduced anti-β-amyloid (Aβ) antibody with unique aβ binding properties promotes neuroprotection and glial engulfment of Aβ. *J. Neurosci*., **32**: 9677 – 9689.

Aimone, J. B., Deng, W., and Gage, F. H. (2010) Adult neurogenesis: integrating theories and separating functions. *Tends Cogn. Sci.,* **14**: 325 – 337.

Akter, K., Lanza, E. A., Martin, S. A., Myronyuk, N., Rua, M., and Raffa, R. B. (2011) Diabetes mellitus and Alzheimer's disease: shared pathology and treatment? *Br. J. Clin. Pharmacol.*, **71**: 365 – 376.

Allsop, D., and Mayes, J. (2014) Amyloid β-peptide and Alzheimer's disease. *Essays Biochem.*, **56**: 99 – 110.

Allsop, D., Mayes, J., Moore, S., Masad, A., and Tabner, B. J. (2008) Meta-dependent generation of reactive oxygen species from amyloid proteins implicated in neurodegenerative disease. *Biochem. Soc. Trans*., **36**: 1239 – 1298.

Alzheimer, A. (1907) Über eine eigenartige Erkrankung der Hirnirinde. *Allgemeine Zeitschrift für Psychiatrie und Psychisch-Gerichtliche Medizine*, **64**: 146 – 148.

Amaral, D. G., and Lavenex, P. (2007) The hippocampus book: Hippocampal neuroanatomy. Oxford University Press, New York.

Amaral, D. G., and Witter, M. P. (1989) The three-dimensional organization of the hippocampal formation: a review of anatomical data. *Neuroscience*, **31**: 571 – 591.

Anand, R., Gill, K. D., and Mahdi, A. A. (2014) Therapeutics of Alzheimer's disease: past, present and future. *Neuropharmacology*, **76**: 27 – 50.

Anderson, J. J., Holtz, G., Baskin, P. P., Turner, M., Rowe B., Wang, B., Kounnas, M. Z., Lamb, B. T., Barten, D., Felsestein, K., McDonald, I., Srinivasan, K., Munoz, B., and Wanger, S. L. (2005) Reductions in β-amyloid concentration in vivo by γ-secretase inhibitors. *Biochem. Pharmacol*., **69**: 689 – 698.

Areosa, S. A., Sherriff, F., and McShane, R. (2006) Memantine for dementia. *Cochrane Database Syst. Rev*., **20**.

Armulik, A., Genové, G., Mäe, M., Nisancioglu, M. H., Wallgard, E., Niaudet, C., He, L., Norlin, J., Lindblom, P., Strittmatter, K., Johansson, B. R., and Betsholtz, C. (2010) Pericytes regulate the blood-brain barrier. *Nature*, **468**: 557 – 561.

Arosio, P., Knowles, T. P., and Linse, S. (2015) On the lag phase in amyloid fibril formation. *Phys. Chem. Chem. Phys*., **17**: 7608 – 7618.

Austen, B. M., Paleologou, K. E., Ali, S. A. E., Qureshi, M. M., Allsop, D., and El-Agnaf, O. (2008) Designing peptide inhibitors for oligomerization and toxicity of Alzheimer's β-amyloid peptide. *Biochemistry*, **47**: 1984 – 1992.

Baker, H. N., Murphy, R., Lopez, E., and Garcia, C. (2012) Conversion of a capture ELISA to a Luminex xMAP assay using a multiplex antibody screening method. *J. Vis. Exp.*, **65**.

Balabanov, R., and Dore-Duffy, P. (1998) Role of the CNS microvascular pericyte in the blood-brain barrier. *J. Neurosci. Res*., **53**: 637 – 644.

Banks, W. A. (2012) Drug delivery to the brain in Alzheimer's disease: consideration of the Blood-brain barrier. *Adv. Drug Deliv. Rev*., **64**: 629 – 639.

Bannerman, D. M., Rawlins, J. N., McHugh, S. B., Deacon, R. M., Yee, B. K., Bast, T., Zhang, W. N., Pothuizen, H. H., and Feldon, J. (2004) Regional dissociations within the hippocampus – memory and anxiety. *Neursci. Biobehav. Rev*., **28**: 273 – 283.

Bard, F., Cannon, C., Barbour, R., Burke, R. L., Games, D., Grajeda, H., Guido, T., Hu, K., Huang, J., Johnson-Wood, K., Khan, K., Kholodenko, D., Lee, M., Lieberburg, I., Motter, R., Nguyen, M., Soriano, F., Vasquez, N., Weiss, K., Welch, B., Seubert, P., Schenk, D., and Yednock, T. (2000) Peripherally administered antibodies against amyloid-β peptide enter the central nervous system and reduce pathology in a mouse model of Alzheimer's disease. *Nat. Med*., **6**: 916 – 919.

Barltrop, J. A., Owen, T. C., Cory, A. H., and Cory, J. C. (1991) 5-(3-carboxymethoxyphenyl)-2-(4,5-dimethylthiazoly)-3-(4-sulfophenyl)tetrazolium, inner salt (MTS) and related analogs of 3-(4,5-dimethylthiazolyl)-2,5-dimethyltetrazolium bromide (MTT) reducing to purple water-soluble formazans as cell-viability indicators. *Bioorg. Med. Chem, Lett*., **1**: 611 – 614.

Barnham, K. J., McKinstry, W. J., Multhaup, G., Galatis, D., Morton, C. J., Curtain, C. C., Williamson, N. A., White, A. R., Hinds, M. G., Norton, R. S., Beyreuther, K., Master, C. L., Parker, M. W., and Cappai, R. (2003) Structure of the Alzheimer's disease amyloid precursor protein copper binding domain. A regulator of neuronal copper homeostasis. *J. Biol. Chem*., **278**: 17401 – 17407.

Bazzoni, G. (2011) Pathology of junctional adhesion molecules. *Antioxid. Redox Signal*, **15**: 1221 – 1234.

Begley, D. J. (2004) Delivery of therapeutic agents to the central nervous system: the problems and the possibilities. *Pharmacol. Ther*., **104**: 29 – 45.

Bekris, L. M., Yu, C. E., Bird, T. D., and Tsuang, D. W. (2010) Genetics of Alzheimer Disease. *J. Geriatr. Psychiatry Neurol.*, **23**: 213 – 227.

Bell, G., Kayano, T., Buse, J., Burant, C., Takeda, J., Lin, D., Fukumoto, H., and Seino, S. (1990) Molecular biology of mammalian glucose transporters. *Diabetes Care*, **13** (3): 198 – 208.

Berridge, M. V., and Tan, A. S. (1993) Characterization of the cellular reduction of 3-(4,5-dimethylthiazol-2-yl)-2,5-dimethyltetrazolium bromide (MTT): Subcellular localization, substrate dependence, and involvement of mitochondrial electron transport in MTT reduction. *Arch. Biochem. Biophys*., **303**: 474 – 482.

Bertram, L., Lill, C. M., and Tanzi, R.E. (2010) The genetics of Alzheimer disease: back to the future. *Neuron*, **68**: 270 – 281.

Biedler, J. L., Helson, L., and Spengler, B. A. (1973) Morphology and growth, tumorigenicity, and cytogenetics of human neuroblastoma cells in continuous culture. *Cancer Res.,* **33**: 2643 – 2652.

Biedler, J. L., Roffler-Tarlov, S., Schachner, M., and Freedman, L. S. (1978) Multiple neurotransmitter synthesis by human neuroblastoma cell lines and clones. *Cancer Res*., **38**: 3751 – 3757.

Biessels, G. J., De Leeuw, F. E., Lindeboom, J., Barkhof, F., and Scheltens, P. (2006) Increased cortical atrophy in patients with Alzheimer's disease and type 2 diabetes mellitus. *J. Neurol. Neurosurg. Psychiatry*, **77**: 304 – 307.

Bird, T. D. (2008) Genetic aspects of Alzheimer disease. *Genet. Med*., **10**: 231 – 239.

Bitan, G., Kirkitadze, M. D., Lomakin, A., Vollers, S. S., Benedek, G. B., and Teplow, D. B. (2003) Amyloid β-protein (Aβ) assembly: Aβ40 and Aβ42 oligomerize through distinct pathways. *Proc. Natl. Acad. Sci. USA*, **100**: 330 – 335.

Blasig, I. E., Bellmann, C., Cording, J., Del Vecchio, G., Zwanziger, D., Huber, O., and Haseloff, R. F. (2011) Occludin protein family: oxidative stress and reducing conditions. *Antioxid. Redox Signal*, **15**: 1195 – 1219.

Blennow, K., de Leon, M. J., and Zetterberg, H. (2006) Alzheimer's disease. *Lancet*, **368**: 387 – 403.

Blessed, G., Tomlinso, B. E., and Roth, M. (1968) Association between quantitative measures of dementia and of senile change in cerebral grey matter of elderly subjects. *Br. J. Psychiatry*, **114**: 797 – 811.

Bohrmann, B., Baumann, K., Benz, J., Gerber, F., Huber, W., Knoflach, F., Messer, J., Oroszlan, K., Rauchenberger, R., Ritchter, W. F., Rothe, C., Urban, M., Bardroff, M., Winter, M., Nordstedt, C., and Loetscher, H. (2012) Gantenerumab: a novel human anti-Aβ antibody demonstrates sustained cerebral amyloid-β binding and elicits cell-mediated removal of human amyloid-β. *J. Alzheimers Dis*., **28**: 49 – 69.

Bouchon, A., Dietrich,J., and Colonna, M. (2000) Cutting edge: inflammatory responses can be triggered by TREM-1, a novel receptor expressed on neutrophils and monocytes. *J. Immunol.*, **164**: 4991 – 4995.

Bryant, B., and Knights, K. (2014) Pharmacology for Health Professionals (4th Ed.). Elsevier, Mosby, Australia.

Bucciantini, M., Giannoni, E., Chiti, F., Baroni, F., Formigli, L., Zurdo, J., Taddei, N., Ramponi, G., Dobson, C. M., and Allsop, D. (2006) Inherent toxicity of aggregates implies a common mechanism for protein misfolding diseases. *Nature*, **416**: 507 – 511.

Cai, J., Qi, X., Kociok, N., Skosyrski, S., Emilio, A., Ruan, Q., Han, S., Liu, L., Chen, Z., Rickman, C. B., Golde, T., Grant, M. B., Saftig, P., Serneels, L., De Strooper, B., Joussen, A. M., and Boulton, M. E. (2012) β-Secretase (BACE1) inhibition causes retinal pathology by vascular dysregulation and accumulation of age pigment. *EMBO Mol. Med.*, **4**: 980 – 991.

Campbell, K., and Steindler, D. (2002) Radial glia: multi-purpose cells for vertebrate brain development. *Trends Neurosci*., **25**: 235 – 238.

Carson, J. A., and Turner, A. J. (2002) Beta-amyloid catabolism: roles for neprilysin (NEP) and other metallopeptidases? *J. Neurochem*., **81**: 1 – 8.

Castani, E. M., Prelli, F., Wisniewski, T., Golabek, A., Kumar, R. A., Soto, S., and Frangine, B. (1995) Fibrillogenesis in Alzheimer's disease of amyloid beta peptides and apolipoprotein E. *Biochem. J.*, **306**: 599 – 604.

Chafekar, S. M., Malda, H., Merkx, M., Meijer, E. W., Viertl, D., Lashuel, H. A., Baas, F., and Scheper, W. (2007) Branched KLVFF tetramers strongly potentiate inhibition of β-amyloid aggregation. *ChemBioChem*., 8**:** 1857 – 1864.

Chen, C., Han, D., Cai, C., and Tang, X. (2010) An overview of liposome lyophilisation and its future potential. *J. Control. Release*, **142**: 299 – 311.

Chen, Y., and Liu, L. (2012) Modern methods for delivery of drugs across the blood-brain barrier. *Adv. Drug Deliv. Rev*., **64**: 640 – 665.

Cheret, C., Willem, M., Fricker, F. R., Wende, H., Wulf-Goldenberg, A., Tahirovic, S., Nave, K. A., Saftig, P., Haass, C., Garratt, A. N., Bennett, D. L., and Birchmeier, C. (2013) Bace1 and Neuregulin-1 cooperate to control formation and maintenance of muscle spindles. *EMBO J.*, **32**: 2015 – 2028.

Chorev, M., and Goodman, M. (1993) A dozen years of retro-inverso peptidomimetics. *Acc. Chem. Res*., **26**: 266 – 273.

Chorev, M., and Goodman, M. (1995) Recent developments in retro peptides and proteins: An ongoing topochemical exploration. *Trends Biotechnol*., **13**: 438 – 445.

Chromy, B. A., Nowak, R. J., Lambert, M. P., Viola, K. L., Chang, L., Velasco, P. T., Jones, B. W., Fernandez, S. J., Lacor, P. N., Horowitz, P., Finch, C. E., Krafft, G. A., and Klein, W. L. (2003) Self-assembly of Aβ(1-42) into globular neurotoxins. *Biochemistry*, **42**: 12749 – 12760.

Clearly, J. P., Walsh, D. M., Hofmeister, J. J., Shankar, G. M., Kuskowski, M. A., Selkoe, D. J., and Ashe K. H. (2005) Natural oligomers of the amyloid-β protein specifically disrupt cognitive function. *Nat. Neurosci*., **8**: 79 – 84.

Cloherty, E., Sultzman, L., Zottola, R., and Carruthers, A. (1995) Net sugar transport is a multistep process. Evidence of cytosolic sugar binding sites in erythrocytes. *Biochemistry*, **34**: 15395 – 15406.

Cohen, S. I., Vendruscolo, M., Dobson, C. M., and Knowles, T. P. (2012) From macroscopic measurements to microscopic mechanisms of protein aggregation. *J. Mol. Biol*., **421**: 160 – 171.

Colonna, M. (2003) TREMs in the immune system and beyond. *Nat. Rev. Immunol*., **3**: 445 – 453.

Colovic, M. B., Krstic, D. Z., Lazarevic-Pasti, T. D., Bondzic, A. M., and Vasic, V. M. (2013) Acetylcholinesterase Inhibitors: Pharmacology and Toxicology. *Curr. Neuropharmacol*., **11**: 315 – 335.

Corder, E. H., Saunders, A. M., Strittmatter, W. J., Schmechel, D. E., Gaskell, P. C., Small, G. W., Roses, A. D., Haines, J. L., and Pericak-Vance, M. A. (1993) Gene dose of apolipoprotein E type 4 allele and the risk of Alzheimer's disease in late onset families. *Science*, **261**: 921 – 923.

Costes, S. V., Daelemans, D., Cho, E. H., Dobbin, Z., and Pavlakis G. (2004) Automatic and quantitative measurement of protein-protein colocalization in live cells. *Biophys. J.*, **86**: 3991 – 4003.

Cowan, C. M., Chee, F., Shepherd, D., and Mudher, A. (2010) Disruption of neuronal function by soluble hyperphosphorylated tau in a Drosophila model of tauopathy. *Biochem. Soc. Trans*., **38**: 564 – 570.

Csajka, C., and Verotta, D. (2006) Pharmacokinetic-Pharmacodynamic Modelling: History and Perspectives. J*. Pharmacokinet. Pharmacodyn*., **33**: 227 – 279.

Cummings, J. L., Morstorf, T., and Zhong, K. (2014) Alzheimer's disease drug-development pipeline: few candidates, frequent failures. *Alzheimers Res. Ther*., **6**: 37.

Curtain, C. C., Ali, F., Volitaki, I., Cherny, R. A., Norton, R. S., Beyreuther, K., Barrow, C. J., Masters, C. L., Bush, A. I., and Barnham, K. J. (2001) Alzheimer's disease amyoid-β binds copper and zinc to generate an allosterically ordered membrane-penetrating structure containing superoxide dismutase-like subunits. *J. Biol. Chem*., **23**: 20466 – 20473.

Danielson, P. B. (2002) The cytochrome P450 superfamily: biochemistry, evolution and drug metabolism in humans. *Curr. Drug Metab*., **3**: 561 – 597.

Davies, L., Wolska, B., Hilbich, C., Multhaup, G., Martins, R., Simms, G., Beyreuther, K., and Masters, C. L. (1988) A4 amyloid protein deposition and the diagnosis of Alzheimer's disease: prevalence in aged brains determined by immunocytochemistry compared with conventional neuropathologic techniques. *Neurol.*, **38**: 1688 – 1693.

De Felice, F. G., Vieira, M. N., Saraiva, L. M., Figueroa-Villar, J. D., Garcia-Abreu, J., Liu, R., Chang, L., Klein, W. L., and Ferreira, S. T. (2004) Targeting the neurotoxic species in Alzheimer's disease: Inhibitors of Aβ oligomerization. *FASEB J*., **18**: 1366 – 1372.

De Mattos, R. B., Bales, K. R., Cummins, D. J., Dodart, C. J., Paul, S. M., and Holtzman, D. M. (2001) Peripheral anti-a beta antibody alters CNS and plasma a beta

clearance and decreases brain a beta burden in a mouse model of Alzheimer's disease. *Proc. Natl. Acad. Sci. USA*, **98**: 8850 – 8855.

De Strooper, B., Annaert, W., Cupers, P., Saftig, P., Craessaerts, K., Mumm, J. S., Schroeter, E. H., Schrijvers, V., Wolfe, M. S., Ray, W. J., Goate, A., and Kopan, R. (1999) A presenilin-1-dependent γ-secretase-like protease mediates release of Notch intracellular domain. *Nature*, **398**: 518 – 522.

Debbage, P. L., Griebel, J, Ried, M., Gneiting, T., DeVries, A., and Hutzler, P. (1998) Lectin intravital perfusion studies in tumor-bearing mice: micrometer-resolution, wide-are mapping of microvascular labelling, distinguishing efficiently and inefficiently perfused microregions in the tumor. *J. Histochem. Cytochem*., **45**: 627 – 639.

Demandolx, D., and Davoust, J. (1997) Multicolour analysis in confocal immunofluorescence microscopy. *J. Trace Microprobe Tech*., **13**: 217 – 225.

Deng, W., Aimone, J. B., and Gage, F. H. (2010) New neurons and new memories: how does adult hippocampal neurogenesis affect learning and memory? *Nat. Rev. Neurosci*., **11**: 339 – 350.

Derrick, B. E. (2007) Plastic processes in the dentate gyrus: a computational perspective. *Prog. Brain Res*., **163**: 417 – 451.

Dietz, G. P., Bahr, M (2004) Delivery of bioactive molecules into the cell: the Trojan horse approach. *Mol. Cell Neurosci*., **27**: 85 – 131.

Drummond, D. C., and Kirpotin, D. (2007) Liposomes useful for drug delivery to the brain. US2007/0110798.

Dunn, K. W., Kamocka, M. M., and McDonald, J. H. (2011) A practical guide to evaluating colocalization in biological microscopy. *Am. J. Physiol. Cell Physiol*., **300**: C723 – C742.

Eckerström, C., Olsson, E., Bjerke, M., Malmgren, H., Edman, A., Wallin, A., and Nordlund, A. (2013) A combination of neuropsychological, neuroimaging, and cerebrospinal fluid markers predicts conversion from mild cognitive impairment to dementia. *J. Alzheimers Dis*., **36**: 421 – 431.

Eglitis, M., and Mezey, E. (1997) Hematopoietic cells differentiate into both microglia and macroglia in the brains of adult mice. *Proc. Natl. Acad. Sci. USA*, **94**: 4080 – 4085.

Eichenbaum, H. (2013) What H.M. taught us. *J. Cogn. Neurosci*., **25**: 14 – 21.

El-Agnaf, O. M. A., Mahil, D. S., Petel, B. P., and Austen, B. M. (2000) Oligomerization and toxicity of β-amyloid-42 implicated in Alzheimer's disease. *Biochem. Biophys. Res. Commun*., **273**: 1003 – 1007.

El-Agnaf, O. M. A., Nagala, S., Patel, B. P., and Austen, B. M. (2001) Non-fibrillar oligomeric species of amyloid ABri peptide, implicated in familial British dementia, are more potent at inducing apoptotic cell death than protofibrils or mature fibrils. *J. Mol. Biol*., **310**: 157 – 168.

El-Agnaf, O. M. A., Paleologou, K. E., Greer, B., Abogrein, A. M., King, J. E., Salem, S. A., Fullwood, N. J., Benson, F. E., Hewitt, R., Ford, K. J., Martin, F. L., Harriott, P., Cookson, M. R., and Allsop, D. (2004) A strategy for designing inhibitors of α-synuclein aggregation and toxicity as a novel treatment for Parkinson's disease and related disorders. *FASEB J*., **18**: 1315 – 1317.

El-Agnaf, O. M. A., Salem, S. A., Paleologou, K. E., Curran, M. D., Gibson, m. J., Court, J. A., Schlossmacher, M. G., and Allsop, D. (2006) Detection of oligomeric forms of α-synuclein protein in human plasma as a potential biomarker for Parkinson's disease. *FASEB J*., **20**: 419 – 425.

El-Agnaf, O. M. A., Walsh, D. M., and Allsop, D. (2003) Soluble oligomers for the diagnosis of neurodegenerative diseases. *Lancet Neurol*., **2**: 461 – 462.

Eng, L., Ghirnikar, R., and Lee, Y. (2000) Glial fibrillary acidic protein: GFAP-thirty-one years (1969 – 2000). *Neurochem. Res*., 25: 1439 – 1451.

Erickson, M. A., and Banks, W. A. (2013) Blood-brain barrier dysfunction as a cause and consequence of Alzheimer's disease. *J. Cereb. Blood Flow Metab*., **33**: 1500 – 1513.

Eyo, D., and Dailey, M. (2013) Microglia: key elements in neural development, plasticity and pathology. *J. Neuroimmune Pharmacol*., **8**: 494 – 509.

Fanselow, M. S., and Dong, H. W. (2010) Are the dorsal and ventral hippocampus functionally distinct structures? *Neuron*, **65**: 7 – 19.

Farlow, M., Arnold, S. E., Van Dyck, C. H., Aisen, P. S., Snider, B. J., Porsteinsson, A. P., Friedrich, S., Dean, R. A., Gonzales, C., Sethuraman, G., DeMattos, R. B., Mohs, R., Paul, S. M., and Siemers, E. R. (2012) Safety and biomarker effects of solanezumab in patients with Alzheimer's disease. *Alzheimer Dement*., **8**: 261 – 271.

Farrer, L. A., Cupples, L. A., Haines, J. L., Hyman, B., Kukull, W. A., Mayeux, R., Myers, R. H., Pericak-Vance, M. A., Risch, N., and van Duijin, C. M. (1997) Effects of age, sex, and ethnicity on the association between apolipoprotein E genotype and Alzheimer's disease: a meta-analysis. *JAMA*, **278**: 1349 – 1356.

Ferrone, F. (1999) Analysis of protein aggregation kinetics. *Methods Enzymol*., **309**: 256 – 274.

Ferrone, F. A., Hofrichter, J., and Eaton, W. A. (1985) Kinetics of sickle haemoglobin polymerisation I. Studies using temperature-jump and laser photolysis techniques. *J. Mol. Biol.*, **183**: 591 – 610.

Ferrone, F. A., Hofrichter, J., and Eaton, W. A. (1985) Kinetics of sickle haemoglobin polymerization II. A double nucleation mechanism. *J. Mol. Biol*., **183**: 611 – 631.

Ficner, R., and Huber, R. (1993) Refined crystal structure of phycoerythrin from *Porphyridium cruentum* at 0.23-nm resolution and localisation of the γ subunit. *Eur. J. Biochem*., **218**: 103 – 106.

Findeis, M. A., Musso, G. M., Arico-Muendel, C.C., Benjamin, H. W., Hundal, A.M., Lee, J. J., Chin, J., Kelly, M., Wakefield, J., Hayward, N. J., and Molineaux, S. M. (1999) Modified-peptide inhibitors of amyloid-β peptide polymerization. *Biochemistry*, **38**: 6791 – 6800.

Frank, S., Burbach, G. J., Bonin, M., Walter, M., Streit, W., Bechmann, I., and Deller, T. (2008) TREM2 is upregulated in amyloid-plaque-associated microglia in aged APP23 transgenic mice. *Glia*, **56**: 1438 – 1447.

Franklin, K. B. J., and Paxinos, G. (2008) The mouse brain in stereotaxic coordinates. (3rd edition). Elsevier: Academic Press, Cambridge, MA.

Friedrich, R. P., Tepper, K., Rönicke, R., Soom, M., Westermann, M., Reymann, K., Kaether, C., and Fändrich, M. (2010) Mechanism of amyloid plaque formation suggests an intracellular basis of Aβ pathogenicity. *PNAS*, **107**: 1942 – 1947.

Fuster-Matanzo, A., Llorens-Martín, M., Gómez de Barreda, E., Ávila, J., and Hernández, F. (2011) Different Susceptibility to neurodegeneration of dorsal and ventral hippocampal dentate gyrus: A study with transgenic mice overexpressing GSK3β. *PLOS ONE*, **6**: e27262.

Gabizon, A., Catane, R., Uziely, B., Kaufman, B., Safra, T., Cohen, R., Martin, F., Huang, A., and Barenholz, Y. (1994) Prolonged circulation time and enhanced accumulation in malignant exudates of doxorubicin encapsulated in polyethylene-glycol coated liposomes. *Cancer Res*., **54**: 987 – 992.

Gandy, S. (2005) The role of cerebral amyloid-β accumulation in common forms of Alzheimer's disease. *J. Clin. Invest*., **115**: 1121 – 1129.

Garber, K. (2012) Genentech's Alzheimer's antibody trial to study disease prevention. *Nat. Biotechnol*., **30**: 731 – 732.

Gelperina, S., Kisich, K., Iseman, M. D., and Heifets, L. (2005) The potential advantages of nanoparticle drug delivery systems in chemotherapy of Tuberculosis. *Am. J. Respir. Crit. Care Med.*, **172**: 1487 – 1490.

Ghanta, J., Shen, C. L., Kiessling, L. L., and Murphy, R. M. (1996) A strategy for designing inhibitors of β-amyloid toxicity. *J. Biol. Chem*., **271**: 29525 – 29528.

Ghiso, J., and Frangione, B. (2002) Amyloidosis and Alzheimer's disease. *Adv. Drug Deliv. Rev*., **54**: 1539 – 1551.

Gilman, S., Koller, M., Black, R. S., Jenkins, L., Griffith, S. G., Fox, N. C., Eisner, L., Kirby, L., Boada Rovira, M., Forette, F., and Orgogozo, J. M. (2005) Clinical effects of Aβ immunization (AN1792) in patients with AD in an interrupted trial. *Neurology*, **64**: 1553 – 1562.

Goldgaber, D., Lerman, M. I., McBride, O. W., Saffiotti, U., and Gajdusek, D. C. (1987) Characterisation and chromosomal localisation of a cDNA encoding brain amyloid of Alzheimer's disease. *Nature*, **349**: 704 – 706.

Gordon, D. J., Sciarretta, K. L., and Meredith, S. C. (2001) Inhibition of β-amyloid(40) fibrillogenesis and disassembly of β-amyloid(40) fibrils by short β-amyloid congeners containing *N*-methyl amino acids at alternative residues. *Biochemistry*, **40**: 8237 – 8245.

Gosal, W. S., Myers, S. L., Radford, S. E., and Thomson, N. H. (2006) Amyloid under the atomic force microscope. *Protein Pept. Lett*., **13**: 261 – 270.

Green, M., and Loewenstein, P. M. (1988) Autonomous functional domains of chemically synthesized human immunodeficiency virus tat trans-activator protein. *Cell*, **55**: 1179 – 1188.

Green, N. M. (1975) Avidin. *Adv. Protein Chem*., **29**: 85 – 133.

Green, R. C., Schneider, L. S., Amato, D. A., Beelen, A. P., Wilcock, G., Swabb, E. A., and Zavitz, K. H. (2009) Tarenflurbil Phase 3 Study Group. Effect of tarenflurbil on cognitive decline and activities of daily living patients with mild Alzheimer's disease: a randomized controlled trial. *JAMA*, **302**: 2557 – 2564.

Gregori, M., Taylor, M., Salvati, E., Re, F., Mancini, S., Balducci, C., Forloni, G., Zambelli, V., Sesana, S., Michael, M., Michail, C., Tinker-Mill, C., Kolosov, O., Scherer, M., Harries, S., Fullwood, N. J., Masserini, M., and Allsop, D. (2017) Retro-inverso inhibitor nanoparticles as potent inhibitors of aggregation of the Alzheimer's Aβ peptide. *Nanomedicine: Nanomed., Nanotech., Biol., Med.*, **13**: 723 – 732.

Griffin, J. P. (2009) The textbook of Pharmaceutical Medicine (6th Ed.). *Wiley-Blackwell: Chichester, West Sussex; Hoboken, New Jersey*.

Guerreiro, R., Wojtas, A., Bras, J., Carrasquillo, M., Rogaeva, E., Majounie, E., Cruchaga, C., Sassi, C., Kauwe, J. S. K., Younkin, S., Hazrati, L., Collinge, J., Pocock, J., Lashley, T., Williams, J., Lambert, J. C., Amouyel, P., Goate, A., Rademakers, R., Morgan, K., Powell, J., George-Hyslop, P. St., Singleton, A., Hardy, J., and The Alzheimer Genetic Analysis Group. (2013) TREM2 variants in Alzheimer's disease. *N. Engl. J. Med*., **368**: 117 – 127.

Haan, M. N. (2006) Therapy inside: type 2 diabetes mellitus and the risk on late-onset Alzheimer's disease. *Nat. Clin. Pract. Neurol*., **2**: 159 – 166.

Haass, C., and Selkoe, D. J. (2007) Soluble protein oligomers in neurodegeneration: lessons from the Alzheimer's amyloid β-peptide. *Nat. Rev. Mol. Cell Biol*., **8**: 101: 112.

Haass, C., Schlossmacher, M. G., Hung, A. Y., Vigo-Pelfrey, C., Mellon, A., Ostaszewski, B. L., Lieberburg, I., Koo, E. H., Schenk, D., Teplow, D. B., and Selkoe, D. J. (1992) Amyloid β-peptide is produced by cultured cells during normal metabolism. *Nature*, **359**: 322 – 325.

Hardy, J., and Allsop, D. (1991) Amyloid deposition as the central event in the aetiology of Alzheimer's disease. *Trends Pharmacol. Sci*., **12**: 383 – 388.

Hardy, J., and Selkoe, D. J. (2002) The amyloid hypothesis of Alzheimer's disease: progress and problems on the road to therapeutics. *Science*, **297**: 353 – 356.

Hebert, D., and Carruthers, A. (1992) Glucose transporter oligomeric structure determines transporter function. Reversible redox-dependent interconversions of tetrameric and dimeric GLUT1. *J. Biol. Chem*., **267**: 23829 – 23838.

Hendrickson, W. A., Pahler, A., Smith, J. L., Satow Y., Merritt, E. A., and Phizackerley, R. P. (1989) Crystal Structure of core streptavidin determined from multiwavelength anomalous diffraction of synchrotron radiation. *Proc. Natl. Acad. Sci. USA*, **86**: 2190 – 2194.

Hilbich, C., Kisters-Woike, B., Reed, J., Masters, C. L., and Beyreuther, K. (1992) Substitutions of hydrophobic amino acids reduce the amyloidogenicity of Alzheimer's disease beta A4 peptides. *J. Mol. Biol.*, **228**: 460 – 473.

Holzman, D. M., Bales, K R., Tenkova, T., Fagan, A. M., Parsadanian, M., Sartorius, L. J., Mackey, B., Onley, J., McKeel, D., Wozniak, D., and Paul, S. M. (2000) Apolipoprotein E isoform-dependent amyloid deposition and neuritic degeneration in a mouse model of Alzheimer's disease. *Proc. Natl. Acad. Sci. U.S.A*., **97**: 2892 – 2897.

Huang, X. D., Atwood, C. S., Hartshorn, M. A., Malthaup, G., Goldstein, L. E., Scarpa, R. C., Cuajungco, M. P., Gray, D. N., Lim, J., Moir, R. D., Tanzi, R. E., and Bush, A. I. (1999) The Aβ peptide of Alzheimer's disease directly produces hydrogen peroxide through metal ion reduction. *Biochemistry*, **38**: 7906 – 7916.

Huang, X. D., Atwood, C. S., Moir, R. D., Hartshorn, M. A., Tanzi, R. E., and Bush, A. I. (2004) Trace metal contamination initiates the apparent auto-aggregation, amyloidosis, and oligomerization of Alzheimer's Aβ peptides. *J. Biol. Inorg. Chem*., **9**: 954 – 960.

Huang, X. D., Cuajungco, M. P., Atwood, C. S., Hartshorn, M. A., Tyndall, J. D. A., Hanson, G. R., Stokes, K. C., Leopold, M., Multhaup, G., Goldstein, L. E., Scarpa, R.

C., Saunders, A. J., Lim, J., Moir, R. D., Glabe, C., Bowden, E. F., Master, C. L., Fairlie, D. P., Tanzi, R. E., and Bush, A. I. (1999) Cu(II) potentiation of Alzheimer's Aβ neurotoxicity – Correlation with cell-free hydrogen peroxide production and metal reduction. *J. Biol. Chem*., **274**: 37111 – 37116.

Imai, Y., Ibata, I., Ito, D., Ohsawa, K., and Kohsaka, S. (1996) A novel gene iba1 in the major histocompatibility complex class III region encoding an EF hand protein expressed in a monocytic lineage. *Biochem. Biophys. Res. Commun*., **224**: 855 – 862.

Inglis, F. (2002) The tolerability and safety of cholinesterase inhibitors in the treatment of dementia. *Int. J. Clin. Pract.*, **127**: 45 – 63.

Iqbal, K., Alonso Adel, C., Chen, S., Choham, M. O., El-Akkad, E., Gong, C. X., Khatoon, S., Li, B., Liu, F., Rahman, A., Tanimukai, H., and Grindle-Iqbal, I. (2005) Tay pathology in Alzheimer's disease and other taupathies. *Biochem. Biophys. Acta*., **1739**: 198 – 210.

Isausti, R., and Amaral, D. G. (2012) The human nervous system (3rd Ed.): Hippocampal Formation. Elsevier: Academic Press, Cambridge, MA.

Ishida, N., and Kawakita, M. (2004) Molecular physiology and pathology of the nucleotide sugar transporter family (SLC35). *Pflugers Arch. – Eur. J. Physiol*., **447**: 768.

Ito, D., Imai, Y., Ohsawa, K., Nakajima, K., Fukuuchi, Y., and Kohsaka, S. (1998) Microglia-specific localisation of a novel calscium binding protein, Iba1. *Brain Res. Mol. Brain Res*., **57**: 1 – 9.

Ito, K., Corrigan, B., Romero, K., Anziano, R., Neville, J., Stephenson, D., and Lalonde, R. (2013) Understanding placebo responses in Alzheimer's disease clinical trials from the literature meta-data and CAMD database. *J. Alzheimers Dis*., **37**: 173 – 183.

Iwatsubo, T., Odaka, A., Suzuki, N., Mizusawa, H., Nukina, N., and Ihara, Y. (1994) Visualisation of Aβ42(43) and Aβ40 in senile plaques with end-specific Aβ

monoclonals: Evidence that an initially deposited species is Aβ42(43). *Neuron*, **13**: 45 – 53.

Jarrett, J. T., Berger, E. P., and Lansbury, P. T. Jr. (1993) The carboxy terminus of the β-amyloid protein is critical for the seeding of amyloid formation: implications for the pathogenesis of Alzheimer's disease. *Biochemistry*, **32**: 4693 – 4697.

Jellinger, K. A. (2004) Head injury and dementia. *Curr. Opin. Neurol*., **17**: 719 – 723.

Jessen, K. R., and Mirsky, R. (1980) Glial cells in the enteric nervous system contain glial fibrillary acidic protein. *Nature*, **286**: 736 – 737.

Jiang, Q., Heneka, M., and Landreth, G. E. (2008) The role of peroxisome proliferator-activated receptor-gamma (PPARgamma) in Alzheimer's disease: therapeutic implication. *CNS Drugs*, **22**: 1 – 4.

Jones, B. (2012) Alzheimer disease: TREM2 linked to late-onset AD. *Nat. Rev. Neurol*., **9**: 5.

Jonsson, T., Atwal, J. K., Steinberg, S., Snaedal, J., Jonsson, P. V., Bjornsson, S., Stefansson, H., Sulem, P. Gudbjartsson, D., Maloney, J., Hoyte, K., Gustafson, A., Liu, Y., Lu, Y., Bhangale, T., Graham, P. R., Huttenlocher, J., Bjornsdottir, G., Andereassen, O. A., Jonsson, E. G., Palotie, A., Behrens, T. W., Magnusson, O. T., Kong, A., Thorsteinsdottir, U., Watts, R. J., and Stefansson, K. (2012) A mutation in APP protects against Alzheimer's disease and age-related cognitive decline. *Nature*, **488**: 96 – 99.

Jonsson, T., Stefansson, H., Steinberg, S., Jonsdottir, I., Jonsson, P.V., Snaedal, J., Bjornsson, S., Huttenlocher, J., Levey, A. I., Rulescu, D., Hampel, H., Giegling, I., Andereassen, O. A., Engedal, K., Ulstein, I., Djurovic, S., Ibrahim-Verbass, C., Hofman, A., Ikman, M. A., vanDuijin, C. M., Thorsteindottir, U., Kong, A., and Stefansson, K. (2013) Variant of TREM2 associated with the risk of Alzheimer's disease. *N. Engl. J. Med*., **368**: 107 – 116.

Kandel, E. R., Schwartz, J. H., and Jessel, T. M. (2000) Principles of Neural Science (4th Ed.). McGraw-Hill, New York.

Kang, J., Lemaire, H. G., Unterbeck, A., Salbaum, J. M., Masters, C. L., Grzeschik, K. H., Multhaup, G., Beyreuther, K., and Muller-Hill, B. (1987) The precursor of Alzheimer's disease amyloid A4 protein resembles a cell-surface receptor. *Nature*, **325**: 733 – 736.

Kayed, R., Head, E., Thompson, J. L., McIntire, R. M., Milton, S. C., Cotman, C. W., and Glabe, C. G. (2003) Common structure of soluble amyloid oligomers implies common mechanisms of pathogenesis. *Science*, **300**: 486 – 489.

Kayed, R., Sokolov, Y., Edmonds, B., McIntire, T. M., Milton, S. C., Hall, J. E., and Glabe, C. G. (2004) Permeabilization of lipid bilayers in common conformation-dependent activity of soluble amyloid oligomers in protein misfolding diseases. *J. Biol. Chem*., **279**: 46363 – 46366.

Kheirbek, M. A., and Hen, R. (2011) Dorsal vs ventral hippocampal neurogenesis: Implications for cognition and mood. *Neuropsychopharmacology*, **36**: 373 – 374.

Kidd, M. (1963) Paired helical filaments in electron microscopy of Alzheimer's disease. *Nature*, **197**: 192 – 193.

Kim, H. J., Chae, S. C., Lee, D. K., Chromy, B., Lee, S. C., Park, Y. C., Klein, W. L., Krafft, G. A., and Hong, S. T. (2003) Selective neuronal degeneration induced by soluble oligomeric amyloid β protein. *FASEB J*., **17**: 118 – 120.

Kim, K., Adelstein, R., and Kawamoto, S. (2009) Identification of neuronal nuclei (NeuN) as Fox-3, a new member of the Fox-1 gene family of splicing factors. *J. Biol. Chem*., **284**: 31052 – 31061.

King, C. D., Rios, G. R., Green, M. D., and Tephly, T. R. (2000) UDP-glucuronosyltransferases. *Curr. Drug Metab*., **1**: 143 – 161.

Klaver, D. W., Wilce, M. C., Cui, H., Hung, A. C., Gasperini, R., Foa, L., and Small, D. H. (2010) Is BACE1 a suitable therapeutic target for the treatment of Alzheimer's disease? Current strategies and future directions. *Biol. Chem*., **391**: 849 – 859.

Klein, W. L., Krafft, G. A., and Finch, C. E. (2001) Targeting small Aβ oligomers the solution to an Alzheimer's disease conundrum? *Trends Neurosci*., **24**: 219 – 224.

Klunk, W. E., Engler, H., Nordberg, A., Wang, Y., Blomqvist, G., Holt, D. P., Bergstrom, M., Savitcheva, I., Huang, G., Estrada, S., Ausen, B., Debnath, M. L., Barletta, J., Price, J. C., Sandell, J., Lopresti, B. J., Wall, A., Koivisto, P., Antoni, G., Mathis, C. A., and Langstrom, B. (2004) Imaging brain amyloid in Alzheimer's diseases with Pittsburgh Compound-B. *Am. Neurol. Assoc*., **55**: 306 – 319.

Knight, R. (1996) Contribution of human hippocampal region to novelty detection. *Nature*, **383**: 256 – 259.

Kokkoni, N., Scott, K., Amijee, H., Mason, J. M., and Doig, A. J. (2006) N-Methylated peptide inhibitors of β-amyloid aggregation and toxicity. Optimisation of the inhibitor structure. *Biochemistry*, **45**: 9906 – 9918.

Konopka, J B. (2012) N-Acetylglucosamine functions in cell signalling. *Hindawi Scientifica*, 1-15.

Kroner, Z. (2009) The relationship between Alzheimer's disease and diabetes: type 3 diabetes? *Altern. Med. Rev*., **14**: 373 – 379.

La Ferla, F. M., Green, K. N., and Oddo, S. (2007) Intracellular amyloid-β in Alzheimer's disease. *Nat. Rev. Neurosci*., **8**: 499 – 509.

Lai, A. Y., and McLaurin, J. (2012) Clearance of amyloid-β peptides by icroglia and macrophages: the issue of what, when and where. *Future Neurol*., **7**: 165 – 176.

Lambert, J. C., and Amouyel, P. (2007) Genetic heterogeneity of Alzheimer's disease: complexity and advances. *Psychoneuroendocrinology*, **32**: S62 – S70.

Lambert, M. P., Barlow, A. K., Chromy, B. A., Edwards, C. Freed, R., Liosatos, M., Morgan, T. E., Rozovsky, I., Trommer, B., Viola, K. L., Wals, P., Zhang, C., Finch, C. E., Krafft, G. A., and Klein, W. L. (1998) Diffusible, nonfibrillar ligands derived from Abeta1-42 are potent central nervous system neurotoxins. *Proc. Natl. Acad. Sci. USA*, **95**:6448 – 6453.

Lane, R. M., Potkin, S. G., and Enz, A. (2006) Targeting acetylcholinesterase and butyrylcholinesterase in dementia. *Int. J. Neuropsychoph*., **9**: 101 – 124.

Lansbury, P. T., and Lashuel, H. A. (2006) A century-old debate on protein aggregation and neurodegeneration enters the clinic. *Nature*, **443**: 774 – 779.

Lathe, R. (2001) Hormones and the hippocampus. *J. Endocrinol*., **169**: 205 – 231.

Le Vine, H., III (1993) Thioflavin T interaction with synthetic Alzheimer's disease β-amyloid peptides : Detection of amyloid aggregation in solution. *Protein Sci.,* **2**: 404 – 410.

Le Vine, H., III (1995) Thiovlavin T interaction with amyloid β-sheet structures. *Amyloid*, **2**: 1 – 6.

Le Vine, H., III (2004) Alzheimer's β-peptide oligomer formation at physiologic concentrations. *Anal. Biochem*., **335**: 81 – 90.

Leuner, B., and Gould, E. (2010) Stuctural plasticity and hippocampal function. *Annu. Rev. Psychol*., **61**: 111 – 145.

Lovell, M. A., Robertson, J. D., Teesdale, W. J., Campbell, J. L., and Markesbery, W. R. (1998) Coper, iron and zinc in Alzheimer's disease senile plaques. *J. Neurol. Sci*., **158**: 47 – 52.

Lowe, T. L., Strzelec,A., Kiessling, L. L., and Murphy, R.M. (2001) Structure-function relationships for inhibitors of β-amyloid toxicity containing the recognition sequence KLVFF. *Biochemistry*, **40**: 7882 – 7889.

Luchsinger, J. A., Tang, M. X., Shea, S., and Mayex, R. (2004) Hyperinsulinemia and risk of Alzheimer disease. *Neurol*., **63**: 1197 – 1192.

Luissint, A. C., Artus, C., Glacial, F., Ganeshamoorthy, K., and Couraud, P. O. (2012) Tight junctions at the blodd brain barrier: physiological architecture and disease – associated dysregulation. *Fluids Barriers CNS*, **9**: 23.

Lukas, G., Brindle, S. D., and Greengard, P. (1971) The route of absorption of intraperitoneally administered compounds. *J. Pharmacol. Exp. Ther*., **178**: 562 – 564.

Manders, E. M. M., Stap, J., Brakenhoff, G., van Driel, R., and Aten, J. (1992) Dynamics of three-dimensional replication patterns during the S-phase, analysed by double labelling of DNA and confocal microscopy. *J. Cell Sci*., **103**: 857 – 862.

Manders, E. M. M., Verbeek, F. J., and Aten, J. A. (1993) Measurement of co-localization of objects in dual-colour confocal images. *J. Microsc.,* **169**: 375 – 382.

Mandrekar, S., and Landreth, G. E. (2010) Microglia and inflammation in Alzheimer's disease. *CNS Neurol. Disord. Drug Targets*, **9**: 156 – 167.

Mangialasche, F., Solomon, A., Winblad, B., Merocci, P., and Kivipelto, M. (2010) Alzheimer's disease: clinical trials and drug development. *Lancet Neurol*., **9**: 702 – 716.

Markesbery, W. R. (1997) Oxidative stress hypothesis in Alzheimer's disease. *Free Radic. Biol. Med*., **23**: 134 – 147.

Markesbery, W. R., Kryscio, R. J., Lovell, M. A., and Morrow, J. D. (2005) Lipid peroxidation is an early event in the brain in amnestic mild cognitive impairment. *Ann. Neurol*., **58**: 730 – 735.

Martins, I. J., Hone, E., Foster, J. K., Sünram-Lea, S. I., Gnjec, A., Fuller, S. J., Nolan, D., Gandy, S. E., and Martins, R. N. (2006) Apolipoprotein E, cholesterol

metabolisms, diabetes, and the convergence of risk factors for Alzheimer's disease and cardiovascular disease. *Mol. Psychiatry*, **11**: 721 – 736.

Mayeux, R. (2003) Epidemiology of neurodegeneration. *Annu. Rev. Neurosci*., **26**: 81 – 104.

Mc Geer, P. L., Rogers, J., and McGeer, E. G. (2006) Inflammation, anti-inflammatory agents and Alzheimer disease: the last 12 years. *J. Alzheimers Dis*., **9**: 271 – 276.

Medina, R., Rahner, C., Mitic, L. L., Anderson, J. M., and Van Itallie, C. M. (2000) Occludin localization at the tight junction requires the second extracellular loop. *J. Membr. Biol*., **178**: 235 – 247.

Meibohm, B., and Derendorf, H. (1997) Basic concepts of pharmacokinetic/ pharmacodynamic (PK/PD) modelling. *Int. J. Clin. Pharmacol. Ther*., **35**: 401 – 13.

Meyer, M. R., Tschanz, J. T., Norton, M. C., Welsh-Bohmer, K. A., Steffens, D. C., Wyse, B. W., and Breitner, J. C. (1998) ApoE genotype predicts when –not whether- one is predisposed to develop Alzheimer's disease. *Nature Genet*., **19**: 321 – 322.

Minkeviciene, R., Rheims, S., Dobszay, M. B., Zilberter, M., Hartikainen, J., Fülöp, L., Penke, B., Zilberter, Y., Harkany, T., Pitkänen, A., and Tanila, H. (2009) Amyloid-β induced neuronal hyperexcitability triggers progressive epilepsy. *J. Neurosci*., **29**: 3453 – 3462.

Morgan, D. (2011) Immunotherapy for Alzheimer's disease. *J. Intern. Med*., **269**: 54 – 63.

Mortimer, J. A., Snowdon, D. A., and Markesbery, W. R. (2003) Head circumference, education and risk of dementia: findings from the Nun Study. *J. Clin. Exp. Neuropsychol*., **25**: 671 – 679.

Moser, M. B., and Moser, E. I. (1998) Functional differentiation in the hippocampus. *Hippocampus*, **8**: 608 – 619.

Mullan, M., Crawford, F., Axelman, K., Houlden, H., Lilius, L., Winbland, M., and Lannfelt, L. (1992) A pathogenic mutation for probable Alzheimer's disease in the APP gene at the N-terminus of beta-amyloid. *Nat. Genet*., **1**: 345 – 347.

Mullen, R., Buck, C., and Smith, A. (1992) NeuN, a neuronal specific nuclear protein in vertebrates. *Development*, **116**: 201 – 211.

Naiki, H., Higuchi, K., Hosokawa, M., and Takeda, T. (1989) Fluorometric determination of amyloid fibrils in vitro using the fluorescent dye, thioflavin T1. *Anal. Biochem*., **177**: 244 – 249.

Neumann, H., and Daly, M. J. (2013) Variant TREM2 as a risk factor for Alzheimer's disease. *N. Engl. J. Med*., **368**: 182 – 184.

Nickla, C. K., Raidasa, S. K., Zhaob, H., Sausbierb, M., Ruthb, P., Teggec, W., Braydena, J. E., and Dostmanna, W. R. (2010) D-Amino acid analogues of DT-2 as highly selective and superior inhibitors of cGMP-dependent protein kinase Iα. *Biochim. Biophys. Acta*, **1804**: 524 – 532.

Niemitz, E. (2012) TREM2 and Alzheimer's disease. *Nat. Genet*., **45**: 11.

Nunomura, A., Perry, G., Aliev, G., Hirai, K., Takeda, A., Balraj, E. K., Jones, P. K., Ghanbari, H., Wataya, T., Shimohama, S., Chiba, S., Atwood, C.S., Petersen, R. B., and Smith, M. A. (2001) Oxidative damage is the earliest event in Alzheimer's disease. *J. Neuropathol. Exp. Neurol.*, **60**: 759 – 767.

OECD (2010) Dementia Prevalence. *OECD, Health at a Glance: Europe*., **2010**: 54 – 55.

Ohsawa, K., Imai, Y., Sasaki, Y., and Kohsaka, S. (2004) Microglia/macrophage-specific protein Iba1 binds to fibrin and enhances its actin-bundling activity. *J. Neurochem*., **88**: 844 – 856.

Oka, Y., Asano, T., Shibasaki, Y., Lin, J., Tsukuda, K., Katagiri, H., Akanuma, Y., and Takaku, F. (1990) C-terminal truncated glucose transporter is locked into an inward-facing form without transport activity. *Nature*, **345**: 550 – 553.

Opazo, C., Barría, M. I., Ruiz, F. H., and Inestrosa, N. C. (2003) Copper reduction by copper binding proteins and its relation to neurodegenerative diseases. *Biometals*, **16**: 91 – 98.

Ostrowitzki, S., Deptula, D., Thurfjell, L., Barkhof, F., Bohrmann, B., Brooks, D. J., Klunk, W. E., Ashford, E., Yoo, K., Xu, Z. X., Loetscher, H., and Santarelli, L. (2012) Mechanism of amyloid removal in patients with Alzheimer disease treated with gantenerumab. *Arch. Neurol*., **69**: 198 – 207.

Ott, A., Stolk, R. P., van Harskamp, F., Pols, H. A., Hofman, A., and Breteler, M. M. (1999) Diabetes mellitus and the risk of dementia: the Rotterdam Study. *Neurology*, **53**: 1937 – 1942.

Padurariu, M., Ciobica, A., Mavroudis, I., Fotiou, D., and Boloyannis, S. (2012) Hippocampal neuronal loss in the CA1 and CA3 of Alzheimer's disease patients. *Psyciatr. Danub*., **24**: 152 – 158.

Paloneva, J., Manninen, T, Christman, G., Hovanes, K., Mandelin, J., Adolfsson, R., Bianchin, M., Bird, T., Miranda, R., Salmaggi, A., Tranebjaerg, L.,Konttinen, Y., and Peltonen, L. (2002) Mutations in two genes encoding different subunits of a receptor signalling complex result in an identical disease phenotype. *Am. J. Hum. Genet*., **71**: 656 – 662.

Pardridge, W. A. (2005) The blood-brain barrier: Bottleneck in brain development. *NEuroRx*., **2**: 3 – 14.

Paresce, D., Chung, H., and Maxfield, F. (1997) Slow degradation of aggregates of the Alzheimer's disease amyloid β-protein by microglial cells. *J. Biol. Chem*., **114**: 29390 – 29397.

Parthsarathy, V., McClean, P. L., Holscher, C., Taylor, M., Tinker, C., Jones, G., Kolosov, O., Salvati, E., Gregori, M., Masserini, M., and Allsop, D. (2013) A novel retro-inverso peptide inhibitor reduces amyloid deposition, oxidation and

inflammation and stimulates neurogenesis in the APPswe/PS1ΔE9 mouse model of Alzheimer's disease. *PLOS ONE*, **8**: 1 – 11.

Petersen, R. C. (2004) Mild cognitive impairment as a diagnostic entity. *J. Intern. Med*., **256**: 183 – 194.

Piccio, L., Buonsanti, C., Mariani, M. Cella, M., Gilfillan, S., Cross, A. H., Colonna, M., and Panina-Bordignon, P. (2007) Blockade of TREM-2 exacerbates experimental autoimmune encephalomyelitis. *Eur. J. Immunol*., **37**: 1290 – 1301.

Poduslo, J. F., Curran, G. L., Kumar, A., Fragione, B., and Soto, C. (1999) β-sheet breaker peptide inhibitor for Alzheimer's amyloidogenesis with increased blood-brain barrier permeability and resistance to proteolytic degradation in plasma. *J. Neurobiol*., **39**: 371 – 382.

Poirier, J., Davingnon, J., Bouthillier, D., Kogan, S., Bertrand, P., and Gauthier, S. (1993) Apolipoprotein E polymorphism and Alzheimer's disease. *Lancet*, **342**: 697 – 699.

Pond, S. M., and Tozer, T. N. (1984) First-pass elimination. Basic concepts and clinical concequences. *Clin. Pharmacokinet*., **9**: 1 – 25.

Puglielli, L. (2008) Aging of the brain, neurotrophin signalling, and Alzheimer's disease: Is IGF1-R the common culprit? *Neurobiol. Aging*, **29**: 795 – 811.

Raber, J., Huang, Y., and Ashford, J. W. (2004) ApoE genotype accounts for the vast majority of AD risk and AD pathology. *Neurobiol. Aging*, **25**: 641 – 650.

Ramanathan, S., Pooyan, S., Stein, S., Prasad, P. D., Wang, J., Leibowitz, M. J., Ganapathy, V., and Sinko, P. J. (2001) Targeting the sodium-dependent multivitamin transporter (SMVT) for improving the oral absorption properties of a retro-inverso Tat nanopeptide. *Pharm. Res*., **18**: 950 – 956.

Reisberg, B., Doody, R., Stoffler, A., Schmitt, F., Ferris, S., Mobius, H. J., and Memantine Study Group (2003) Memantine in moderate-to-severe Alzheimer's disease. *New Engl. J. Med.*, **348**: 1333 – 1341.

Repici, M., Centeno, C., Tomasi, S., Forloni, G., Bonny, C., Vercelli, A., and Borsello, T. (2007) Time-course of c-Jun N-terminal kinase activation after cerebral ischemia and effect of D-JNKI1 on C-Jun and caspase-3 activation. *Neuroscience*, **150**: 40 – 49.

Riederer, B. M., Leuba, G., and Elhajj, Z. (2013) Oxidation and ubiquitination in neurodegeneration. *Exp. Biol. Med. (Maywood)*, **238**: 519 – 524.

Rinne, J. O., Brooks, D. J., Rossor, M. N., Fox, N. C., Bullock, R., Klunk, W. E., Mathis, C. A., Blennow, K., Barakos, J., Okello, K. A., Rodriquez Martinez de Llano, S., Liu, E., Koller, M., Gregg, K. M., Schenk, D., Black, R., and Grundman, M. (2010) ^{11}C-PiB PET assessment of change in fibrillar amyloid-β load in patients with Alzheimer's disease treated with bapineuzumab: a phase 2, double-blind, placebo-controlled, ascending-dose study. *Lancet Neurol*., **9**: 363 -372.

Ristow, M. (2004) Neurodegenerative disorders associated with diabetes mellitus. *J. Mol. Med*., **82**: 510 – 529.

Robakis, N. K., Ramakrishna, N., Wolfe, G., and Wisniewski, H. M. (1987) Molecular cloning and characterisation of a cDNA encoding the neuritic plaque amyloid peptides. *Proc. Natl. Acad. Sci.* USA, **84**: 4190 – 4194.

Roberts, G. W., Allsop, D., and Bruton, C. (1990) The occult aftermath of boxing. *J. Neurol. Neurosurg. Psychiatry,* **53**: 373 – 378.

Roberts, M. S., Magnusson, B. M., Burczynski, F. J., and Weiss, M. (2002) Enterohepatic circulation: physiological, pharmacokinetic and clinical implimentations. *Clin. Pharmacokinet*., **41**: 751 – 790.

Rogaev, E. I., Sherrington, R., Rogaeva, E. A., Levesque, G., Ikeda, M., Liang, Y., Chi, H., Lin, C., Holman, K., Tsuda, T., Mar, L., Sorbi, S., Naemias, B., Piacentini, S.,

Amaducci, L., Chumakov, I., Cohen, D., Lannfelt, L., Fraser, P. E., Rommers, J. M., and George-Hyslop, P. St. (1995) Familial Alzheimer's disease in kindreds with missense mutations in a gene on chromosome 1 related to the Alzheimer's disease type 3 gene. *Nature*, **376**: 775 – 778.

Ross, R. A., Spengler, B. A., and Biedler, J. L. (1983) Coordinate morphological and biochemical interconversion of human neuroblastoma cells. *J. Natl. Cancer Inst*., **71**: 741 – 747.

Rowland, M. (1972) Influences of route of administration on drug availability. *J. Pharm. Sci.*, **61**: 70 – 74.

Rozemuller, J. M., Eikelenboom, P., and Stam, F. C. (1986) Role of microglia in plaque formation in senile dementia of the Alzheimer type. An immunohistochemical study. *Virchows Arch. B Cell Pathol.*, **51**: 247 – 254.

Saab, B. J., Georgiou, J., Nath, A., Lee, F. J., Wang, M., Michalon, A., Liu, F., Mansuy, I. M., and Roder, J. C. (2009) NCS-1 in the dentate gyrus promotes exploration, synaptic plasticity, and rapid acquisition of spatial memory. *Neuron*, **63**: 643 -656.

Saifer, M. G. P., Williams, L. D., Sobczyk, M. A., Michaels, S. J., and Sherman, M. R. (2014) Selectivity of binding of PEGs and PEG-like oligomers to anti-PEG antibodies induced by methoxyPEG-proteins. *Mol. Immunol*., **57**: 236 – 246.

Savonnière, S., Zeghari, N., Miccoli, L., Muller, S., Maugras, M., and Donner, M. (1996) Effects of lipid supplementation of culture media on cell growth, antibody production, membrane structure and dynamics in two hybridomas. *J. Biotechnol*., **48**: 161 – 173.

Schellenberg, G. D., and Montine, T. J. (2012) The genetics and neuropathology of Alzheimer's disease. *Acta Neuropath*., **124**: 305 – 323.

Schneider, L. S., Dagerman, K. S., Higgins, J. P., and McShane, R. (2011) Lack of evidence for the efficacy of memantine in mild Alzheimer disease. *Arch. Neurol*., **68**: 991 – 998.

Schenk, D., Barbour, R., Dunn, W., Gordon, G., Grajeda, H., Guido, T., Hu, K., Huang, J., Johnson-Wood, K., Khan, K., Kholodenko, D., Lee, M., Liao, Z., Lieberburg, I., Motter, R., Mutter, L., Soriano, F., Shopp, G., Vasquez, N., Vandevert, C., Walker, S., Wogulis, M., Yednock, T., Games, D., and Seubert P. (1999) Immunization with amyloid-β attenuates Alzheimer-disease-like pathology in PDAPP mouse. *Nature*, **400**: 173 – 177.

Schmidt, C., and Bodmeier, R. (1999) Incorporation of polymeric nanoparticles into solid dosage forms. *J. Control. Release*, **57**: 115 – 125.

Sciarretta, K. L., Gordon, D. J., and Meredith, S. C. (2006) Peptide-based inhibitors of amyloid assembly. *Methods Enzymol*., **413**: 273 – 312.

Selkoe, D. J. (2001) Alzheimer's disease: genes, proteins, therapy. *Physiol. Rev*., **81**: 741 – 766.

Selkoe, D. J. (2004) Cell biology of protein misfolding: The examples of Alzheimer's and Parkinson's diseases. *Nat. Cell Biol*., **11**: 1054 – 1061.

Sham, J. O., Zhang, Y., Finlay, W. H., Roa, W. H., and Lobenberg, R. (2004) Formulation and characterization of spray-dried powders containing nanoparticles for aerosol delivery to the lung. *Int. J. Pharm*., **269**: 457 – 467.

Shargel, L., and Yu, A. B. C. (1999) Applied Biopharmaceutics and Pharmacokinetics. *McGraw-Hill/Appleton & Lange: New York*.

Sherrington, E., Rogaev, E. I., Liang, Y., Rogaeva, E. A., Levesque, G., Ikeda, M., Chi, H., Lin, C., Holman, K., Tsuda, T., Mar, L., Foncin, J. F., Bruni, A. C., Montesi, M. P., Sorbi, S., Rainero, I., Pinessi, L., Nee, L., Chumakov, I., Pollen, D., Brookes, A., Sanseau, P., Rolinsky, R. J., Wasco, W., Da Silva, H. A., Haines, J. L., Pericak-Vance,

M. A., and George-Hyslop, P. St. (1995) Cloning of a novel gene bearing missense mutations in early familial Alzheimer's disease. *Nature*, **375**: 754 – 760.

Smith, M. A., Harris, P. L., Sayre, L. M., and Perry, G. (1997) Iron accumulation in Alzheimer's disease is a source of redox-generated free radicals. *Proc. Natl., Acad. Sci. USA.*, **94**: 9866 – 9868.

Smith, P. K., Krohn, R. I., Hermanson, G. T., Mallia, A. K., Gartner, F. H., Provenzano, M. D., Fujimoto, E. K., Goeke, N. M., Olson, B. J., and Klenk, D. C. (1985) Measurement of protein using bicinchoninic acid. *Anal. Biochem*., **150**: 76 – 58.

Solito, E., and Sastre, M. (2012) Microglia Function in Alzheimer's disease. *Front. Pharmacol.*, **3**: 14.

Solomon, B., Koppel, R., Frenkel, D., Hanan-Aharon, E. (1997) Disaggregation of Alzheimer's β-amyloid by site-directed mAb. *Proc. Natl. Acad. Sci. USA*, **94**: 4109 – 4112.

Solomon, B., Koppel, R., Hanan, E., Katzav, T. (1996) Monoclonal antibodies inhibit *in vitro* fibrillar aggregation of the Alzheimer's β-amyloid peptide. *Proc. Natl. Acad. Sci. USA*, **93**: 452 – 455.

Sorbi, S., Naemias, B., Forleo, P., Piacentini, S., Sherrington, R., Rogaev, E., George-Hyslop, P. St., and Amaducci, L. (1995) Missense mutation of S182 gene in Italian families with early-onset Alzheimer's disease. *Lancet*, **346**: 439 – 440.

Soto, D. J. (2003) Unfolding the role of protein misfolding in neurodegenerative diseases. *Nat*. *Rev. Neurosci*., **4**: 4 9 – 60.

Soto, D. J., Kndy, M. S., Baumann, M., and Frangione, B. (1996) Inhibition of Alzheimer's amyloidosis by peptides that prevent β-sheet conformation. *Biochem. Biophys. Res. Commun.*, **226**: 672 – 680.

Sperling, R., Salloway, S., Brooks, D. J., Tampieri, D., Barakos, J., Fox, N. C., Raskind, M., Sabbagh, M., Honig, L. S., Porsteinsson, A. P., Lieberburg, I., Arrighi, H. M.,

Morris, K. A., Lu, Y., Liu, E., Gregg, K. M., Brashear, H.R., Kinney, G. G., and Grundman, M. (2012) Amyloid-related imaging abnormalities in patients with Alzheimer's disease treated with bapineuzumab: a retrospective analysis. *Lancet Neurol*., **11**: 241 – 249.

Spuch, C., and Navarro, C. (2011) Liposomes for targeted delivery of active agents against neurodegenerative diseases (Alzheimer's disease and Parkinson's disease). *J. Drug. Deliv*., **2011**.

Steindler, D. (2012) Neurogenic astrocytes and their glycoconjugates: not just "glue" anymore. *Methods Mol. Biol*., **814**: 9 – 22.

Stratchan, M. W. (2005) Insulin and cognitive function in humans: experimental data and therapeutic considerations. *Biochem. Soc. Trans*., **33**: 1037 – 1040.

Stukel, J. M., Li, R. C., Maynard, H. D., and Caplan, M. R. (2010) Two-step synthesis of multivalent cancer-targeting constructs. *Biomacromolecules*, **11**: 160 – 167.

Szoka, F., and Papahadjopoulos, D. (1980) Comparative properties and methods of preparation of lipid vesicles (liposomes). *Annu. Rev. Biophys. Bioeng*., **9**: 467 – 508.

Tabner, B. J., El-Agnaf, O. M. A., Turnbukk, S., German, M. J., Paleologou, K. E., Hayashi, Y., Cooper, L. J., Fullwood, N. J., and Allsop, D. (2005) Hydrogen peroxide is generated during the very early stages of aggregation of the amyloid peptides implicated in Alzheimer Disease and Familial British Dementia. *J. Biol. Chem*., **280**: 35789 – 35792.

Takahashi, K., Prinz, M., Stagi, M., Chechneva, O., and Neumann, H. (2007) TREM2-transduced myeloid precursor mediate nervous tissue debris clearance and facilitate recovery in an animal model of multiple sclerosis. *PLoS Med*., **4**: 124.

Takayama, M., Itoh, S., Nagasaki, T., and Tanimizu, I. (1977) A new enzymatic method for determination of serum choline-containing phospholipids. *Clin. Chim. Acta*., **79**: 93 – 98.

Tanapat, P. (2013) Neuronal cell markers. *Mater. Methods*, **3**: 196.

Tanzi, R. E., Moir, R. D., and Wagner, S. L. (2004) Clearance of Alzheimer's Aβ peptide: the many roads to perdition. *Neuron*, **43**: 605 – 608.

Tassa, C., Duffner, J. L, Lewis, T. A., Weissleder, R., Schreiber, S. L., Koehler, A. N., and Shaw, S. Y. (2010) Binding affinity and kinetic analysis of targeted small molecule-modified nanoparticles. *Bioconjug. Chem*., **21**: 14 – 19.

Taylor, E. M., Otero, D. A., Banks, W. A., and O'Brien, J. S. (2000) Retro-inverso prosaptide peptides retain bioactivity, are stable *in vivo*, and are blood-brain barrier permeable. *J. Pharmacol. Exp. Ther.*, **295**: 190 – 194.

Taylor, M., Moore, S., Mayes, J., Parkin, E., Beeg, M., Canovi, M., Gobbi, M., Mann, D. M. A., and Allsop, D. (2010) Development of a proteolytically stable retro-inverso peptide inhibitor of β-amyloid oligomerization as a potential novel treatment for Alzheimer's disease. *Biochemistry*, **49**: 3261 – 3272.

Terasaki, M., Loew, L., Lippincott-Schwartz, J., and Zaal, K. (2001) Fluorescent staining of subcellular organelles: ER, Golgi complex, and mitochondria. *Curr. Protoc. Cell Biol*., **4**.

Terry, A. V., and Buccafusco, J. J. (2003) The cholinergic hypothesis of age and Alzheimer's disease-related cognitive deficits: Recent challenges and their implication for novel drug development. *J. Pharmacol. Exp. Ther*., **306**: 821 – 827.

Tietz, S., and Engelhardtm B. (2015) Brain Barriers: Crosstalk between complex tight junctions and adherens junctions. *J. Cell Biol*., **209**: 493.

Tjernberg, L. O., Naslund, J., Lindqvist, F., Johanson, J., Karlstrom, A. R., Thyberg, J., Terenius, L., and Nordstedt, C. (1996) Arrest of β-amyloid fibril formation by a pentapeptide ligand. *J. Biol. Chem*., **271**: 8545 – 8548.

Tomic, J. L., Pensalfini, A., Head, E., and Glave, C. G. (2009) Soluble fibrillar oligomer levels are elevated in Alzheimer's disease brain and correlate with cognitive dysfunction. *Neurobiol. Dis*., **35**: 352: 358.

Torchilin, V. P. (2005) Recent advances with liposomes as pharmaceutical carriers. *Nature Rev. Drug Discov.*, **4**: 145 – 160.

Tsapis, N., Bennett, D., Jackson, B., Weitz, D. A., and Edwards, D. A. (2002) Trojan particles: large porous carriers of nanoparticles for drug delivery. *Proc. Natl. Acad. Sci. USA*, **99**: 12001 – 12005.

Turner, P. V., Brabb, T., Pekow, C., and Vasbinder, M. A. (2011) Administration of substances to laboratory animals: Routes of administration and factors to consider. *J. Am. Assoc. Lab. Anim. Sci.*, **50**: 600 – 613.

Varvel, N. H., Bhaskar, K., Patil, A. R., Pimplikar, S. W., Herrup, K., and Lamb, B. T. (2008) Aβ oligomers induce neuronal cell cycle events in Alzheimer's disease. *J. Neurosci*., **28**: 10786 – 10793.

Verghese, P. B., Castellano, J. M., and Holtzman, D. M. (2011) Apolipoprotein E in Alzheimer's disease and other neurological disorders. *Lancet Neurol*., **10**: 241 – 252.

Vojnovic, B., and Barber, P. (2005) Spectra imaging applied to histology: (almost) all you wanted to know but were too afraid to ask. *Gray Cancer Institute, UK*: 1 – 13.

Wagner, S. L., Tanzi, R. E., Mobley, W. C., and Galasko, D. (2012) Potentil use of γ-secretase modulators in the treatment of Alzheimer's disease. *Arch. Neurol*., **69**: 1255 – 1258.

Wake, H., Moorhouse, A., Miyamoto, A., and Nabekura, J. (2013) Microglia: Actively surveying and shaping neuronal circuit structure and function. *Trends Neurosci*., **36**: 209 – 217.

Walsh, D. M., and Selkoe, D. J. (2007) Aβ oligomers: a decade of discovery. *J. Neurochem*., **101**: 1172 – 1184.

Ward, R. V., Jennings, K. H., Jerpas,, R., Neville, W., Owen, D. E., Hawkins, J., Christie, G., Davis, J. B., George, A., Karran, E. H., and Howlett, D. R. (2000) Fractionation and characterisation of oligomeric protofibrilar and fibrillar forms of β-amyloid peptide. *Biochem. J.,* **348**: 137 – 144.

Watanabe, K., Nakamura, K., Akikusa, S., Okada, T., Kodaka, M., Konakahara, T., and Okuno, H. (2002) Inhibitors of fibril formation and cytotoxicity of β-amyloid peptide composed of KLVFF recognition element and flexible hydrophilic disrupting element. *Biochem. Biophys. Res. Commun*., **290**: 121 – 124.

Webb, M. S., Harasym, T. O., Masin, D., Bally, M. B., and Mayer, L. D. (1995) Sphingomyelin-cholesterol liposomes significantly enhance the pharmacokinetic and therapeutic properties of vincristine in murine and human tumour models. *Br. J. Cancer*, **72**: 896 – 904.

Weber, P. C., Ohlendorf, D. H., Wendoloski, J. J., and Salemme, F. R. (1989) Structural origins of high-affinity biotin binding to streptavidin. *Science*, **243**: 85 – 88.

Weggen, S., Erisken, J. L., Das, P., Sagi, S. A., Wang, R., Pietrzik, C. U., Findlay, K. A., Smith, T. E., Murphy, M. P., Bulter, T., Kang, D. E., Marquez-Sterling, N., Golde, T. E., and Koo, E. H. (2001) A subset of NSAIDs lower amyloidogenic Abeta42 independently of cyclooxygenase activity. *Nature*, **414**: 212 -216.

Wisniewski, T., Ghiso, J., and Frangione, B. (1997) Biology of Aβ amyloid in Alzheimer's disease. *Neurobiol. Dis.*, **4**: 313 – 328.

Wolburg, H., Wolburg-Buckholtz, K., Liebner, S., and Engelhardt, B. (2001) Claudin1, claudin 2, and claudin 11 are present in tight junctions of choroid plexus epithelium of mouse. *Neurosci. Lett*., **307**: 77 – 80.

Wolf, M. S. (2008) Inhibition and modulation of γ-secretase for Alzheimer's disease. *Neurotherapeutics*, **5**: 391 – 398.

Wyss-Coray, T. (2006) Inflammation in Alzheimer disease: driving force, bystander or beneficial response? *Nature Med*., **12**: 1005 – 1015.

Xia, W., Yang, T., Shankar, G., Smith, I. M., Shen, Y., Walsh, D. M., and Selkoe, D. J. (2009) A specific enzyme-linked immunosorbent assay for measuring β-amyloid protein oligomers in human plasma and brain tissue of patients with Alzheimer disease. *Arch. Neurol*., **66**: 190 – 199.

Yang, F., Lim, G. P., Begum, A. N., Ubeda, O. J., Simmons, M. R., Ambegaokar, S. S., Chen, P. P., Kayed, R., Glabe, C. G., Frautschy, S. A., and Cole, G. M. (2005) Curcumin inhibits formation of amyloid β oligomers and fibrils, binds plaques, and reduces amyloid *in vivo*. *J Biol. Chem*., **18**: 5892 – 5901.

Zatta, P., Drago, D., Bolognin, S., and Sensi, S. L. (2009) Alzheimer's disease, metal ions and metal homeostatic therapy. *Trends Pharmacol. Sci*., **30**: 346 – 355.

Zhang, G., Leibowitz, M. J., Sinko, P.J., and Stein, S. (2003) Multiple-peptide conjugates for binding β-amyloid plaques of Alzheimer's disease. *Bioconjug. Chem*., **14**: 86 – 92.

Zhang, X., Jin, Y., Plummer, M. R., Pooyan, S., Gunaseelan, S., and Sinko, P. J. (2009) Endocytosis and membrane potential are required for HeLa cell uptake of R.I.-CKTat9, a retro-inverso Tat cell penetrating peptide. *Mol. Pharm*., **6**: 836 – 848.

Zinchuk, V., Zinchuk, O., and Okada, T. (2007) Quantitative colocalization analysis of multicolour confocal immunofluorescence microscopy images: Pushing pixels to explore biological phenomena. *Acta Histochem. Cytochem*., **40**: 101 – 111.

Websites:

- Alzheimer's Research UK, http://www.alzheimersresearchuk.org/ (Accessed January, 2017)
- Alzheimer's Society, http://www.alzheimers.org.uk/ (Accessed January, 2017)

- BrightFocus Foundation, http://www.brightfocus.org/alzheimers/ (Accessed May, 2017)
- ClinicalTrials.gov, http://clinicaltrials.com (Accessed April, 2017)
- Image J: Colocalization analysis, https://imagej.net/Colocalization_Analysis (Accessed May, 2017)
- Lilly, http://www.lilly.com (Accessed April, 2017)
- MSD Manual: Professional, http://www.msdmanuals.com/professional (Accessed May, 2017)
- MSD Manual: Veterinary, http://www.msdvetmanual.com/ (Accessed May, 2017)
- Organisation for Economic Co-operation and Development (OECD), Publishing "Dementia prevalence", http://www.oecd-ilibrary.org/ (Accessed January, 2017)
- Promega, https://www.promega.co.uk/ (Accessed April, 2017)
- United Nations Population Division, http://www.un.org/en/development/desa/population/ (Accessed January, 2017)

Appendix

Journal Article Publication

Gregori, M., Taylor, M., Salvati, E., Re, F., Mancini, S., Balducci, C., Forloni, G., Zambelli, V., Sesana, S., Michael, M., Michail, C., Tinker-Mill, C., Kolosov, O., Sherer, M., Harris, S., Fullwood, N. J., Masserini, M., and Allsop, D. (2017) Retro-inverso peptide inhibitor nanoparticles as potent inhibitors of aggregation of the Alzheimer's Aβ peptide. Nanomedicine: *Nanotechnology, Biology and Medicine*, **13**: 723 – 732.

BASIC SCIENCE

Nanomedicine: Nanotechnology, Biology, and Medicine
13 (2017) 723–732

Original Article

nanomedjournal.com

Retro-inverso peptide inhibitor nanoparticles as potent inhibitors of aggregation of the Alzheimer's Aβ peptide

Maria Gregori, PhD[a,1], Mark Taylor, PhD[b,1], Elisa Salvati, PhD[a], Francesca Re, PhD[a], Simona Mancini, PhD[a], Claudia Balducci, PhD[c], Gianluigi Forloni, PhD[c], Vanessa Zambelli, PhD[a], Silvia Sesana, MSc[a], Maria Michael, MSc[b], Christos Michail, MSc[b], Claire Tinker-Mill[d], Oleg Kolosov, PhD[d], Michael Sherer, MSc[b], Stephen Harris, BSc[e], Nigel J. Fullwood, PhD[b], Massimo Masserini, PhD[a], David Allsop, PhD[b,*]

[a]University of Milano-Bicocca, Nanomedicine Center NANOMIB and School of Medicine and Surgery, Monza, (MB), Italy
[b]University of Lancaster, Division of Biomedical and Life Sciences, Faculty of Health and Medicine, Lancaster, UK
[c]Department of Neuroscience, Istituto di Ricovero e Cura a Carattere Scientifico/Mario Negri Institute for Pharmacological Research, Milan, Italy
[d]University of Lancaster, Department of Physics, Faculty of Science and Technology, Lancaster, UK
[e]Quotient Bioresearch (Rushden) Ltd, Rushden, Northamptonshire, UK

Received 6 August 2016; accepted 10 October 2016

Abstract

Aggregation of amyloid-β peptide (Aβ) is a key event in the pathogenesis of Alzheimer's disease (AD). We investigated the effects of nanoliposomes decorated with the retro-inverso peptide RI-OR2-TAT (Ac-rGffvlkGrrrqrrkkrGy-NH_2) on the aggregation and toxicity of Aβ. Remarkably low concentrations of these peptide inhibitor nanoparticles (PINPs) were required to inhibit the formation of Aβ oligomers and fibrils in vitro, with 50% inhibition occurring at a molar ratio of ~1:2000 of liposome-bound RI-OR2-TAT to Aβ. PINPs also bound to Aβ with high affinity (K_d = 13.2-50 nM), rescued SHSY-5Y cells from the toxic effect of pre-aggregated Aβ, crossed an in vitro blood–brain barrier model (hCMEC/D3 cell monolayer), entered the brains of C57BL/6 mice, and protected against memory loss in APP_{SWE} transgenic mice in a novel object recognition test. As the most potent aggregation inhibitor that we have tested so far, we propose to develop PINPs as a potential disease-modifying treatment for AD.
© 2016 Elsevier Inc. All rights reserved.

Key words: Alzheimer's disease; Liposomes; Retro-inverso peptide; β-amyloid; Oligomer

There are currently ~36 million sufferers of Alzheimer's disease (AD) worldwide, costing the world economy US$604 billion in 2010, and these figures are set to rise dramatically in the future.[1] Current drug treatments only temporarily alleviate the symptoms of AD. Characteristic pathological changes of the disease are the presence of abundant senile plaques, containing amyloid-β peptide (Aβ) fibrils, and neurofibrillary tangles consisting of hyperphosphorylated Tau protein. However, Aβ oligomers are now thought to be the most toxic form of this peptide, with a potent ability to cause memory deficits, and inhibition of oligomer formation is a potential strategy for disease modification therapy.[2–8] It is also generally thought that Tau aggregation is a downstream consequence of Aβ aggregation.[9] The most advanced clinical trials aimed at disease modification in AD are based on drugs targeting the production or clearance of Aβ.[10]

The research leading to these results has received funding from the European Community's Seventh Framework Programme (FP7/2007-2013) under grant agreement no. 212043, and from The Alzheimer's Society UK (grant number 210 (AS-PG-2013-032)). There were also contributions from Lancaster University's Defying Dementia campaign.

Competing interests: The University of Lancaster has filed a patent (WO2013054110) on intellectual property related to this work, based on inventions of DA and MT. The patent has been licensed to MAC Clinical Research, UK.

The authors thank Pierre-Olivier Couraud from Institut National de la Santé et de la Recherche Médicale (INSERM, Paris, France) for providing the hCMEC/D3 cells.

*Corresponding author at: University of Lancaster, Division of Biomedical and Life Sciences, Lancaster, UK.
E-mail address: d.allsop@lancaster.ac.uk (D. Allsop).

[1] Maria Gregori and Mark Taylor contributed equally to this paper.

http://dx.doi.org/10.1016/j.nano.2016.10.006
1549-9634/© 2016 Elsevier Inc. All rights reserved.

Please cite this article as: Gregori M, et al, Retro-inverso peptide inhibitor nanoparticles as potent inhibitors of aggregation of the Alzheimer's Aβ peptide. *Nanomedicine: NBM* 2017;13:723-732, http://dx.doi.org/10.1016/j.nano.2016.10.006

We have published data on a small peptide (OR2 = H_2N-RGKLVFFGR-NH_2) that inhibits the formation of Aβ oligomers and fibrils.[11] RI-OR2 is a much more stable retro-inverted version of this peptide.[12] The addition of retro-inverted 'TAT' (HIV cell-penetrating peptide) to RI-OR2 allows it to enter cells and cross the blood–brain barrier (BBB).[13] Treatment of APPswe/PS1ΔE9 transgenic mice with RI-OR2-TAT caused reduction of brain Aβ burden (oligomers included), reduction of numbers of activated microglial cells, and an increase in the number of young neurons in the dentate gyrus.[13] However, RI-OR2-TAT only inhibits Aβ aggregation when present at relatively high concentrations (i.e. 1:5 molar ratio of inhibitor: Aβ at best).[13]

In recent years, there has been a growing interest in the use of liposomes as carriers for therapeutic agents, because of their attractive characteristics, such as biocompatibility, biodegradability, and chemical and physical stability.[14] Moreover, liposomes can be multi-functionalized on their surface, and it has been shown that multi-ligand-decorated nanosystems can be more efficient (compared to single ligand systems) at recognizing their molecular targets.[15] In the present study, we have covalently attached RI-OR2-TAT to nanoliposomes (NLs) using 'click' chemistry. We show that very low concentrations of these peptide inhibitor nanoparticles (PINPs) were required to inhibit the aggregation of Aβ and to protect cultured SHSY-5Y cells from the toxic effect of pre-aggregated Aβ. Moreover, they were efficient at crossing an in vitro BBB model, entered the brains of healthy mice, and protected against memory loss in APP_{SWE} transgenic mice.

Methods

Materials

Chemical reagents and Sepharose 4B-CL were from Sigma-Aldrich. Bovine brain sphingomyelin (Sm), cholesterol (Chol) and 1,2-distearoyl-sn-glycero-3-phosphoethanolamine-N-[maleimide (polyethylene glycol)-2000] (mal-PEG-PE) were from Avanti Polar Lipids Inc., USA. [^{3}H]-Sm, [^{3}H]-propranolol, [^{14}C]-sucrose, Ultima Gold scintillation cocktail and solvable tissue solubilizer were from PerkinElmer (Waltham, MA, USA). [^{14}C]-Chol was provided by Quotient Bioresearch Ltd. Polycarbonate filters for liposome extrusion were from Millipore Corp., Bedford, MA, USA and the extruder was from Lipex Biomembranes, Vancouver, Canada. Recombinant Aβ1-42, Ultrapure, was from rPeptide, Bogart, Georgia, USA. All other chemicals were reagent grade.

Production of NL decorated with RI-OR2-TAT (PINPs) by click chemistry

NL were composed of Sm/Chol (1:1 molar ratio) mixed with 5 molar % of mal-PEG-PE. Lipids were resuspended in chloroform/methanol (2:1, v:v) and dried under a gentle stream of nitrogen. The resulting film was resuspended in PBS, pH 7.4, vortexed and extruded 10 times through a 100 nm pore polycarbonate filter under 20 bar nitrogen pressure, at room temperature, to create UD (undecorated) liposomes. In order to covalently attach the peptide to these liposomes, an additional cysteine residue was incorporated at the C-terminus. NL were incubated with this peptide for 2 h at 37 °C and then overnight at 4 °C to obtain PINPs. To remove unbound peptide, the liposome suspension was passed through a Sepharose 4B-CL column (25 × 1 cm). The elution of PINPs was assessed by dynamic light scattering (DLS) and the amount of peptide bound to liposomes was quantified by Bradford assay.[16] Phospholipid recovery was determined by the method of Stewart.[17]

NL characterization

The size and polydispersity of NL were measured at 25 °C using a ZetaPlus particle sizer (Brookhaven Instruments Corporation, Holtsville, NY, USA). The particle size was assessed by DLS with a 6.52 mm laser, and polydispersity index was obtained from the intensity autocorrelation function of the light scattered at a fixed angle of 90°.

The NL were also analysed by use of a Nanosight machine (NanoSight Ltd., Minton Park, Amesbury, UK) with NL suspended in PBS, pH 7.4, and measured at 25 °C.

Aβ aggregation assays

These were performed using de-seeded $Aβ_{1-42}$.[12]

ThT assays were conducted in 384-well, clear-bottomed microtitre plates, with 25 μM $Aβ_{1-42}$, 15 μM ThT, and a range of concentrations of PINPs, in 10 mM PBS, pH 7.4, with a total reaction volume of 60 μL. Aggregation was monitored using a BioTek Synergy plate reader ($λ_{ex}$ = 442 nm, $λ_{em}$ = 483 nm) over 48 h at 30 °C, with the plate being shaken and read every 10 min. The results show average data from one of two experiments, each of which was performed in triplicate. Control assays involving incubation of pre-aggregated Aβ (incubated at 25 μM for 24 h) with ThT in the presence of each inhibitor ruled out the possibility that the inhibitors interfere with binding of ThT to fibrils.[12]

For the sandwich immunoassay, Aβ oligomers were captured by monoclonal antibody 6E10 and detected by a biotinylated form of the same antibody.[12] Briefly, 96-well plates (Maxisorb) were coated with 6E10, diluted 1:1000 in assay buffer (Tris-buffered saline (TBS) (pH 7.4), containing 0.05% γ-globulins and 0.005% Tween 20). The incubated samples of peptide, with or without liposome (12.5 μM Aβ and a series of dilutions of PINPs in PBS, pH 7.4, at 25 °C), were diluted to 1 μM Aβ and incubated, in triplicate, in the 96-well plates for 1 h at 37 °C. The plates were washed with 10 mM PBS, containing 0.5% Tween 20 (PBS-T). Following this, 100 μL of TBS containing 1:1000 biotinylated 6E10 was added and the plates were incubated for 1 h at 37 °C and washed. Europium-linked streptavidin was added at 1:500 dilution in StrepE buffer (TBS containing 20 μM DTPA, 0.5% bovine serum albumin, and 0.05% γ-globulins), incubated for 1 h, and washed. Enhancer solution was added, and the plates were read on a Wallac Victor 2 plate reader. The results shown are average data from one of two experiments, each performed in triplicate. Pre-aggregated peptide controls ruled out the possibility that the inhibitors block binding of 6E10 to Aβ.[12]

Atomic force microscopy (AFM)

$Aβ_{1-42}$ was incubated at 25 μM in the presence or absence of 1.25 μM PINPs (total lipids) in PBS, pH 7.4, for 24 h. Samples were diluted 1:10 in PBS and a 2 μL aliquot was deposited onto a mica surface coated with poly-L-lysine (PLL)[18] and allowed to

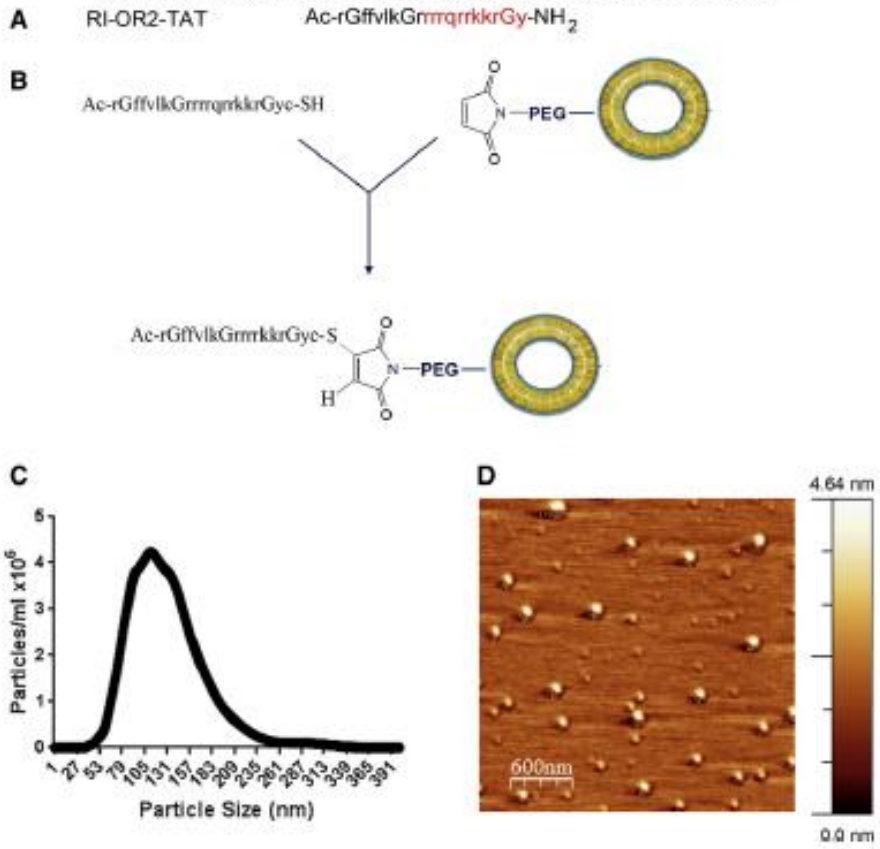

Figure 1. Preparation and characterization of PINPs. **(A)** Amino acid sequence of RI-OR2-TAT. Black letters indicate the RI-OR2 peptide and red letters the TAT sequence, with D-amino acids in lower case. **(B)** Construction of PINPs through 'click' chemistry involving a C-terminal cysteine residue. **(C)** Size distribution of PINPs measured on a Nanosight instrument. **(D)** AFM image of PINPs with no Aβ present.

dry. Images were obtained in tapping mode using a Multimode™ SPM NanoScope IIIa microscope (Digital Instruments, NY, USA). The silicon cantilever tips were 125 μm long, 30 μm wide and had a radius <10 nm (Budget Sensors, Bulgaria). The resonance frequency was 300 kHz and force constants 40 N/m. All images were first order flattened and edited using WSxM 5.0 Develop 4.3 software, (Nanotech, Madrid, Spain).[19]

Electron microscopy (EM) studies of PINPs incubated with Aβ

Negative stain EM was used to examine the structure of PINPs with and without incubation with Aβ. PINPS alone, or PINPs (2.5 μM total lipids) incubated with $A\beta_{1-42}$ (25 μM) at 37 °C for 48 h, were pipetted (4 μl) onto 300 mesh formvar and carbon coated copper grids (Agar Scientific, UK) and left for 1 min. The solvent was blotted away and the residue stained using 2% (w/v) phosphotungstic acid (PTA), pH 7.4. Immunogold labelling experiments were performed to identify any Aβ captured by PINPs. Here, the grids were blocked for 15 min in goat serum:PBS (1:10) and incubated at room temperature for 1 h with primary anti-Aβ antibody 6E10 (0.02 μl/ml). After washing, they were incubated with 10 nm colloidal gold-conjugated goat anti-mouse secondary antibody (G7777, Sigma-Aldrich) diluted 1/50 in PBS, for 2 h. After washing, any liquid remaining on the grids was blotted away, and the samples were stained with PTA. Grids were left to dry and examined by TEM.

Surface plasmon resonance (SPR) spectroscopy

SPR experiments were conducted using a Sensi Q semi-automatic SPR machine (ICx Nomadics). This apparatus has two parallel flow cells; one was used to immobilize $A\beta_{1-42}$ monomers, oligomers or fibrils, while the other was used as "reference" (empty surface). A COOH5 sensor chip (ICx Nomadics) was employed for this purpose and the peptide was immobilized by amine coupling chemistry. Briefly, after surface activation, the peptide was diluted to 10 μM in acetate buffer (pH 4.0) and injected for 5 min at a flow rate of 30 μL/min. Any remaining activated groups were blocked with ethanolamine (pH 8.0). The final immobilization level was ~5000 resonance units (1 RU = 1 pg of protein/mm^2). The empty

"reference" surface was prepared in parallel using the same immobilization procedure, but without addition of peptide. Sensorgrams were obtained via injection of four different concentrations of PINPs (0.3 μM, 0.6 μM, 0.9 μM, 1.2 μM of exposed peptide) in solution (PBS with 0.005% Tween 20), over the immobilized ligand or control surface, in parallel, at the same time. These SPR data can be interpreted to provide an estimate for affinity of binding of liposomes to Aβ.[12,13]

MTS/LDH assay

Cultured SHSY-5Y human neuroblastoma cells were maintained in Dulbecco's modified eagle medium (DMEM, Gibco) containing 10% fetal calf serum, 100 U/mL penicillin, 50 μg/mL streptomycin, at 37 °C and 5% CO_2 in a humidified incubator. Cells were transferred to sterile 96-well growth plates at 20,000 cells per well and four wells per condition. For the effect of PINPs alone on cells, the growth medium was DMEM. Cells were left to adhere for 24 h before the PINPs were added and cell viability was assessed using the CellTiter 96AqueousOne Solution Cell Proliferation (MTS) Assay kit (Promega) after further 24 h incubation. For the experiments looking at the protective effect of PINPS, the growth medium was changed to Optimem (Invitrogen) and $A\beta_{1-42}$ that had been pre-aggregated (for 24 h at 25 °C in PBS) was added to a concentration of 5 μM. The plates were returned to the incubator for 24 h and cell proliferation was assessed as above.

Uptake and transcytosis of NL by human brain endothelial cells

Immortalized hCMEC/D3 cells were cultured as described previously.[20] 5×10^4 cells/cm^2 were seeded on 12-well transwell inserts coated with type I collagen and cultured with 0.5 mL and 1 mL of culture medium in the upper and lower chamber, respectively. Cells were treated with UD liposomes and PINPs when the transendothelial electrical resistance (TEER) value (measured by EVOMX meter, STX2 electrode; World Precision Instruments, Sarasota, FL, USA) was found to be the highest. The functional properties of cell monolayers were assessed by measuring the endothelial permeability (EP) of [^{14}C]-sucrose and [^{3}H]-propranolol (between 0 and 120 min) as described previously.[21] Radiolabeled NL (0.5 mL; 400 nmol/mL of total lipids) were added to the upper chamber and incubated for 120 min. After these periods of incubation, the radioactivity in the upper and lower chambers was measured by liquid scintillation counting to calculate the EP of NL across the cell monolayers, taking account of their passage through the filter without cells.[21] After 2 h, hCMEC/D3 cells were washed with PBS and detached from the transwell inserts with trypsin/EDTA for 15 min at 37 °C. Cell-associated radioactivity was measured and the total lipid uptake calculated.

Assessment of LIP cytotoxicity on hCMEC/D3 cells

hCMEC/D3 cells were grown on 12-well plates until confluence. Medium was replaced and NL (400 nmol/mL of total lipids) suspended in cell culture medium were incubated at 37 °C with the cells for 24 h. After treatment, the cell viability was assessed by ([3-(4,5-dimethylthiazol-2-yl)-2,5-diphenyltetrazolium bromide]) (MTT) assay, as described previously.[22] Each sample was analyzed at least in triplicate. Moreover, TEER and permeability of [^{14}C]-sucrose were also determined in the presence of NL to assess the effect of NL on monolayer integrity.

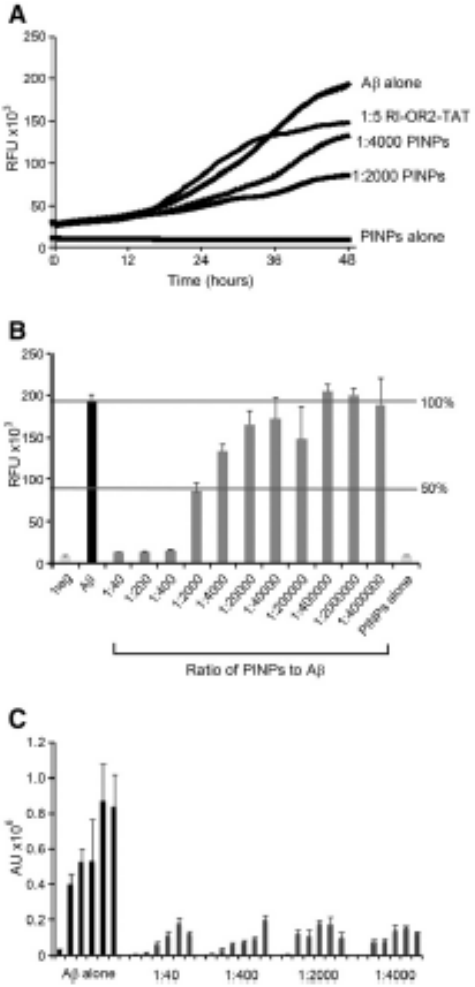

Figure 2. PINPs are potent inhibitors of $A\beta_{1-42}$ aggregation. All concentrations for PINPs refer to NL-linked inhibitory peptide, to allow comparison with free peptide. **(A)** Time-course of Aβ1-42 aggregation in the presence of non-linked RI-OR2-TAT (1:5 ratio of inhibitor to $A\beta_{1-42}$) or PINPs (1:400, 1:2000 ratio of NL-linked inhibitory peptide to $A\beta_{1-42}$), as determined by ThT assay. **(B)** Dilution series of PINPs against the ThT signal after 48 h incubation. Note that a molar ratio of 1:2000 of NL-linked inhibitory peptide to $A\beta_{1-42}$ (or 1:50 total lipids to $A\beta_{1-42}$) gives ~50% inhibition. **(C)** Data from an immunoassay for oligomeric Aβ. Samples were taken at 0, 2, 4, 8, 12 and 24 h (consecutive bars) from incubations of $A\beta_{1-42}$ alone, or $A\beta_{1-42}$ with 1:40, 1:400, 1:2000 and 1:4000 ratios of NL-linked inhibitory peptide to Aβ.

Biodistribution in healthy mice

Three C57 BL/6 male mice were administered with 0.4 mM (total lipid) of ^{14}C-labelled cholesterol PINPs, at ~2.22×10^8 dpm/kg,

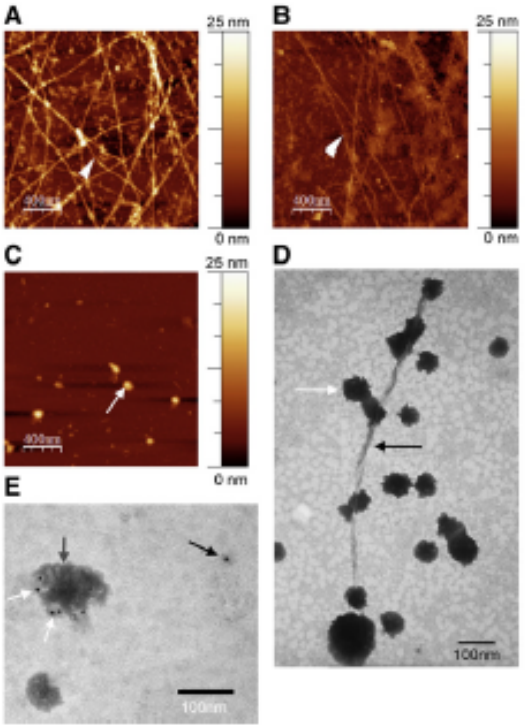

Figure 3. AFM and EM images confirm that PINPs interact with Aβ and inhibit its aggregation. **(A)** $A\beta_{1-42}$ at 25 μM was incubated alone for 144 h and examined by AFM. **(B)** Aβ with UD liposomes at a 1:20 ratio of lipids:Aβ. **(C)** Aβ with PINPs at a 1:20 ratio of lipids:Aβ. The presence of fibres (white arrowheads) in **(A)** and **(B)** indicates that UD liposomes do not interfere with Aβ aggregation, whereas **(C)** shows the clear absence of fibrils. PINPs are indicated by the white arrow. **(D)** $A\beta_{1-42}$ incubated with PINPs (4:1 ratio of lipids:Aβ) and stained with PTA. The PINPs (white arrow) are bound along the length of an amyloid fibril (black arrow) and to its termini. **(E)** 6E10 immunogold labelling of a PINP (grey arrow) following incubation with $A\beta_{1-42}$. White arrows show regions where Aβ was detected. The black arrow shows an Aβ monomer (or small oligomer) labelled with immunogold.

into a tail vein. The amount of radioactivity that reached the brain was assessed by quantitative whole body analysis (QWBA), while the concentration in blood was measured by liquid scintillation counter from samples taken prior to sacrifice. This work was performed by Quotient Bioresearch (Rushden) Ltd., using mice supplied by Charles Rivers UK Ltd., Margate, Kent.

Novel object recognition test in Tg mice

Drug and behavioral test naïve 22-month-old Tg2576 (APP_{SWE}) and WT age-matched littermates were used. All experiments were conducted during the light cycle. Animals (Tg or WT) were injected intraperitoneally with PINPs (100 μl, 100 nmol of peptide/kg) or with PBS (100 μl) once a day for 21 days. The weight of the animals was monitored during treatment. Two experimental groups were treated with PINPs (Tg2576 and WT mice, n = 10 for each), two control groups were treated with PBS (Tg2576 and WT, n = 10 for each). In the NOR test, mice are introduced into an arena containing two identical objects that they can explore freely. Twenty-four hours later, mice are reintroduced into the arena containing the familiar object and a novel object. Exploration was recorded in a 10 min trial by an investigator blinded to the genotype and treatment and the time that each object was explored recorded. Results are expressed as percentage time of investigation on objects per 10 min, or as discrimination index (DI), i.e., (seconds spent on novel − seconds spent on familiar)/(total time spent on objects). Animals with no memory impairment spend a longer time investigating the novel object, giving a higher DI.

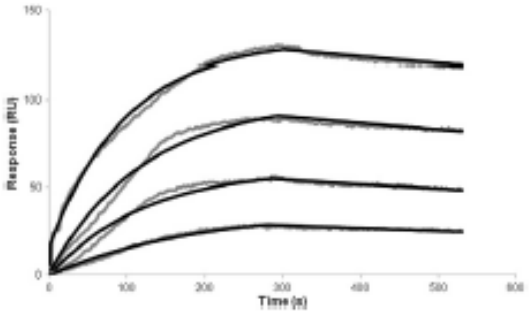

Figure 4. SPR data on binding of PINPs to Aβ fibrils. PINPs were injected at four different concentrations, for 5 min, at a flow rate of 30 μL/min (from bottom to top: 0.3 μM, 0.6 μM, 0.9 μM, 1.2 μM of exposed $A\beta_{1-42}$ peptide). The non-specific binding obtained from the reference surface has been subtracted from all data. Fitted curves are shown in black. The binding affinity (K_d) is calculated as 36-50 nM.

All procedures involving animals and their care were conducted according to EU laws and policies (EEC Council Directive 86/609, OJ L 358,1; 12 December 1987), the USDA Animal Welfare Act and NIH (Bethesda, MA, USA) policy on Humane Care and Use of Laboratory Animals. The procedures were reviewed and approved by the Mario Negri Institute Animal Care and Use Committee (1/04-D).

Results

Preparation and characterization of peptide inhibitor nanoparticles (PINPs)

To attach RI-OR2-TAT (Figure 1, *A*) covalently to the NL surface, we exploited a thiol-maleimide reaction employing an additional cysteine residue to provide the necessary thiol group.[23] This thiol function at the C-terminus of RI-OR2-TAT reacted with a maleimide-functionalized phospholipid present in the NL formulation (mal-PEG-PE) (Figure 1, *B*). The yield of coupling was 80%-90% and, consequently, PINPs contained 2%-2.5 mol% of peptide. The total lipid recovery of NL, after the reaction with the peptide and the purification step, was about 65%. Final preparations of PINPs were monodispersed, with a mean size of 143 ± 10 nm as determined by DLS. Their stability was verified by DLS which showed that the size and polydispersity index remained constant, in PBS, for up to 7 days. Analysis by a Nanosight instrument indicated an average size for PINPs of 131 ± 43 nm

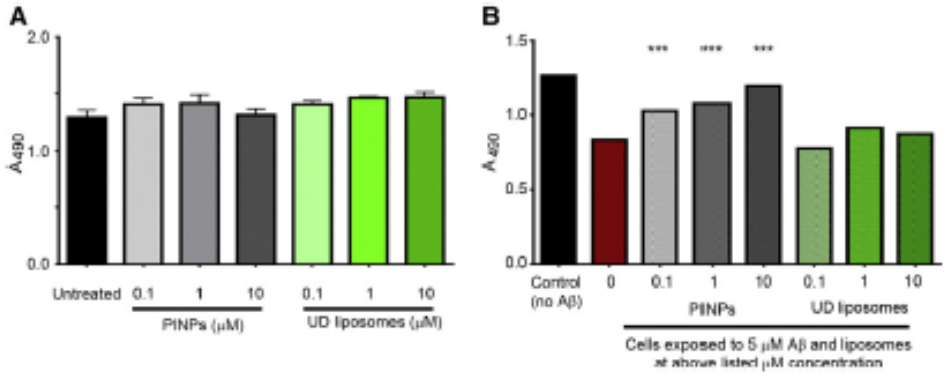

Figure 5. PINPs are not toxic and protect against the damaging effects of Aβ on cells. **(A)** MTS assay data for SHSY-5Y cells grown in the presence of various concentrations (total lipids) of PINPs or UD liposomes. **(B)** LDH assay data for cells exposed to pre-aggregated $Aβ_{1-42}$ (at 5 μM) in the presence or absence of varying concentrations (total lipids) of PINPS or UD liposomes. PINPs protected against the damaging effects of Aβ. (* = $P < 0.001$). Error bars are too small to be seen.

(Figure 1, *C*). AFM images showed NL particles with a mean diameter of ~100 nm (Figure 1, *D*), this slightly smaller size being most likely due to some dehydration of the sample.

Effects of PINPs on Aβ aggregation

RI-OR2-TAT alone was shown by ThT assay to inhibit $Aβ_{1-42}$ aggregation up to a molar ratio of 1:5 (inhibitor to $Aβ_{1-42}$), in agreement with previous data for RI-OR2 and RI-OR2-TAT.[12,13] When RI-OR2-TAT was attached to liposomes there was a dramatic improvement in ability to inhibit $Aβ_{1-42}$ fibril formation at low inhibitor concentrations (Figure 2, *A*). This finding is best illustrated in the dilution series shown in Figure 2, *B*. Here, it can be seen that 50% inhibition occurs at around 1:50 molar ratio of lipid to $Aβ_{1-42}$ or, as the inhibitory peptide is only ~2.5% of total lipids, ~1:2000 of RI-OR2-TAT to $Aβ_{1-42}$. In contrast, when UD liposomes (1:1) were tested for their ability to inhibit $Aβ_{1-42}$ aggregation, we found a slight stimulatory effect at higher ratios of 1:1 and 1:2 (lipid:$Aβ_{1-42}$) but no effect below 1:10 (data not shown).

A sensitive immunoassay was used to detect Aβ oligomers present at the earlier $Aβ_{1-42}$ incubation time points (at around 4 h under our experimental conditions).[12,13] PINPs inhibited the generation of an immunoassay signal at all time points examined, and at molar ratios down to as low as 1:100 lipid:$Aβ_{1-42}$ or 1:4000 inhibitory peptide:$Aβ_{1-42}$ (Figure 2, *C*). The slight differences between ThT assay and ELISA results could reflect the fact that the former detects mainly fibrils, whereas the latter detects oligomers.

AFM images showed fibrils of $Aβ_{1-42}$ following 6 days of incubation in PBS (Figure 3, *A*) and when incubated with UD liposomes (Figure 3, *B*). Few or no fibrils were detected when PINPs were present at a molar ratio of 1:10 of total lipids:Aβ (Figure 3, *C*), confirming that they inhibit aggregation. However, some structures possibly resembling small aggregates could be seen, suggesting that PINPs may not entirely inhibit aggregation. Negative stain EM revealed that the surface of the PINPs was smooth and their shape was generally spherical. However, when the PINPs were incubated with $Aβ_{1-42}$ they appeared to be covered with a 'furry' coat of what are possibly Aβ monomers or oligomers (Figure 3, *D*). Intriguingly, some PINPs were found attached along the length of Aβ fibrils, and at their free ends, suggesting that the interaction of the PINPs had resulted in termination of fibril growth (Figure 3, *D*). Further investigation with anti-Aβ immunogold labelling showed that the surface of the PINPs was decorated with gold particles, confirming capture of Aβ (Figure 3, *E*).

Binding affinity between PINPs and Aβ

PINPs were injected over immobilized Aβ fibrils at different concentrations of RI-OR2-TAT (0.3, 0.6, 0.9, 1.2 μM) and were shown to bind in a concentration-dependent manner (Figure 4). Curves were fitted separately using the simplest Langmuir 1:1 interaction model, and the calculated apparent affinity (K_d) was 36–50 nM. In addition, K_d values were 13.2 nM for Aβ oligomers and 22.5 nM for monomers (see Supplementary Information).

Effects of PINPs on the toxicity of Aβ

There was no loss in viability of SHSY-5Y cells, as measured by MTS assay, after 24 h incubation in the presence of PINPs at concentrations as high as 10 μM (total lipid) in normal (FCS supplemented DMEM) growth medium (Figure 5, *A*). A similar result was also found using the LDH cell viability assay (data not shown). Treatment of SHSY-5Y cells with 5 μM Aβ for 24 h gave a 39% reduction in cell viability, and the presence of PINPs rescued the cells from Aβ toxicity at all doses tested (Figure 5, *B*). UD liposomes were not toxic to neuroblastoma cells (Figure 5, *A*), and they did not rescue cells from the toxic effect of pre-aggregated Aβ (Figure 5, *B*).

Passage of PINPs across the blood–brain barrier

We measured the ability of PINPs to cross an artificial BBB model composed of a hCMEC/D3 cell monolayer.[24] hCMEC/D3 cells grown on transwell membrane inserts were incubated with UD liposomes or PINPs on day 12, when the maximal transendothelial electrical resistance (TEER) value was registered (123 ± 6 Ω · cm^2). Transport of [^{14}C]-sucrose and [^{3}H]-propranolol was measured, with paracellular EP values of 1.48×10^{-3} cm/min and

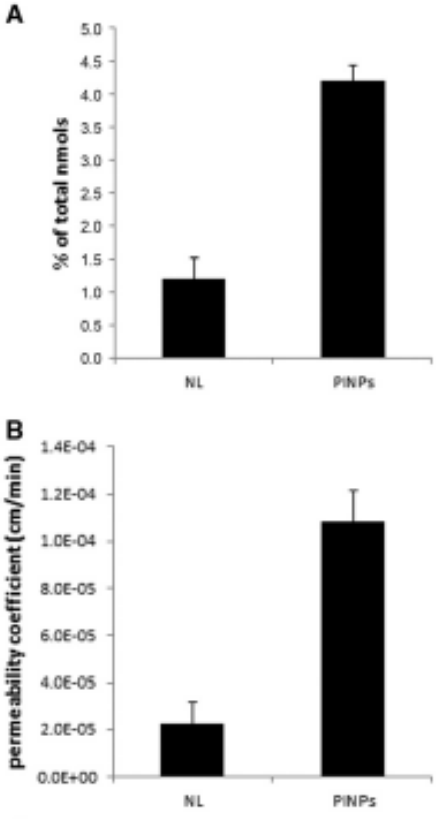

Figure 6. PINPs can flux across the hCMEC/D3 cell monolayer. 10^6 cells were incubated with UD liposomes (NL) or PINPs radiolabeled with ^{3}H-Sm, for 2 h at 37 °C, 5% CO_2. **(A)** Cellular uptake of nanoparticles (NP). After incubation, the amount of ^{3}H-Sm incorporated into the cells was measured and the nmol of total NP taken up by the cells calculated. **(B)** Transcytosis of NP through hCMEC/D3 cell monolayers. Radiolabeled UD liposomes (NLs) or PINPs were added to the upper chamber of the transwell monolayers and incubated for 2 h at 37 °C, 5% CO_2. The permeability across the cell monolayer was calculated. Each value is the mean (±SD) of at least three independent experiments. * = $P < 0.05$ by Student's *t* test.

3.51×10^{-3} cm/min, respectively, in agreement with values reported in the literature.[25] Radiolabelled UD liposomes or PINPs were added in the upper compartment and the cellular uptake and EP were measured up to 2 h of incubation. The radioactivity stably associated with cells was 1.19% ± 0.32% and 4.19% ± 0.24% of the administered dose ($P < 0.05$), respectively for UD liposomes and PINPs (Figure 6, *A*). Also the EP across the cell monolayers was higher for PINPs ($1.08 \pm 0.13 \times 10^{-4}$ cm/min), compared to UD liposomes ($2.25 \pm 0.89 \times 10^{-5}$ cm/min) ($P < 0.05$) (Figure 6, *B*). MTT assays showed that all of the preparations tested were non-toxic. Moreover, after hCMEC/D3 incubation with UD liposomes or PINPs, the TEER value and the permeability of [^{14}C]-sucrose ($119 \pm 8\ \Omega \cdot cm^2$ and 1.62×10^{-3} cm/min, respectively) did not change, within experimental error (<3%).

Table 1
Tissue distribution in C57 BL/6 mice using quantitative whole body analysis (QWBA).

	μg Equivalents of [^{14}C]-Cholesterol PEGylated nanoliposomes per gram of tissue (% of total dose/g)		
	Sample time after injection		
Tissue type	5 minutes	15 minutes	60 minutes
Brain	0.225 (0.415)	0.262 (0.490)	0.182 (0.362)
Liver	6.78 (12.5)	8.36 (15.6)	7.28 (14.5)
Kidney	1.52 (2.80)	1.19 (2.23)	0.889 (1.77)
Lung	32.1[A] (59.2)	49.4[A] (92.3)	22.8 (45.5)
Spleen	10.9 (20.0)	16 (29.8)	16 (31.8)
Blood	2.19 (4.04)	0.51 (0.952)	0.36 (0.718)

Three mice were injected via a tail vein, and a single mouse was sacrificed at 5, 15 and 60 min post injection. The amount of radioactivity was assessed using QWBA and converted to μg equivalents per gram of tissue (% of total dose/g in brackets).

[A] Above limit of accurate quantification (>23.5 μg equivalents/g) – extrapolated value reported.

Biodistribution of PINPs in healthy mice

QWBA measurements for biodistribution of PINPs are detailed in Table 1. Fifteen minutes after administration, 0.49%/g of the total dose was found in the brain and 0.952%/g in the blood, showing evidence for BBB penetration. However, the majority of the dose was found in lungs (~92%), and other tissues associated with phagocytosis by the mononuclear phagocyte system (i.e. adipose tissue, liver, bone marrow and spleen).

NOR (memory) test

Figure 7 shows that, although PBS-treated Tg2576 mice were unable to discriminate between the familiar and the novel object (percentage time of investigation per 10 min: familiar, 53.5 ± 1.5; novel, 46.5 ± 1.5; DI, −0.07 ± 0.03; n = 19), after treatment mice receiving PINPs significantly recovered their long-term recognition memory (percentage time of investigation per 10 min: familiar, 40.4 ± 1.6; novel, 59.6 ± 1.6; DI, 0.19 ± 0.03; n = 10), close to the values of PBS-treated WT mice (percentage time of investigation per 10 min: familiar, 39.6 ± 1.4; novel, 60.4 ± 1.4; DI, 0.23 ± 0.02; n = 10) (one-way ANOVA, Tukey's post hoc test. *$P < 0.05$). In addition, we demonstrated that treatment with PINPs had no negative effect on the memory of WT mice (percentage time of investigation per 10 min: familiar, 37.5 ± 4.7; novel, 62.5 ± 3.4; DI, 0.25 ± 0.09; n = 10) and did not affect mouse weight and motor activity (data not shown).

Discussion

Here, we linked RI-OR2-TAT covalently to the surface of NL composed of sphingomyelin and cholesterol. This lipid formulation has been widely utilized in vivo for therapeutic purposes and displays good blood circulation times, good biocompatibility, and high resistance to hydrolysis.[26] In addition, the 130-140 nm diameter is optimal for moving at an appreciable rate through the brain extracellular space.[27] We found that the presence of the carrier appears to increase the potency of RI-OR2-TAT as an aggregation inhibitor by 100-200 fold, where this is determined by the molar

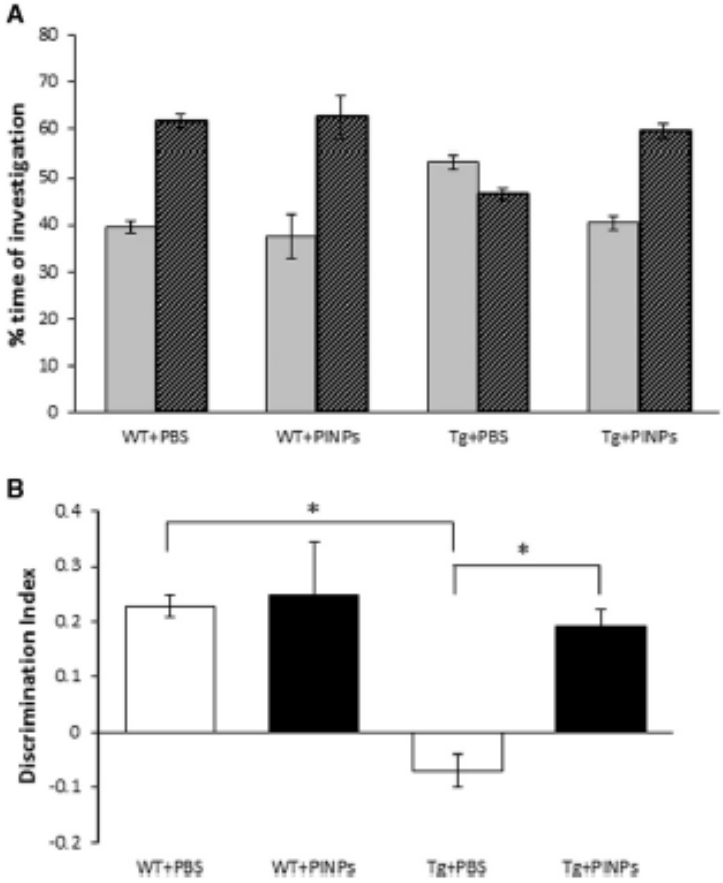

Figure 7. Treatment with PINPs significantly restores long-term recognition memory in Tg2576 mice. WT or Tg2576 mice were treated with PINPs or vehicle and, at the end of treatment, their memory was tested with the NOR test. **(A)** Histograms indicate the time percentage (mean ± SEM) of investigation of the familiar (grey) and novel (black) objects of the experimental groups tested. **(B)** Histograms report the corresponding DI (mean ± SEM). One-way ANOVA, Tukey's post hoc test. $^{*}P < 0.05$.

ratio of inhibitor:Aβ required to block the aggregation of Aβ1-42 under standard experimental conditions. We did not observe this phenomenon with curcumin-NL[28] and so it is not completely clear why there is this considerable jump in potency for PINPs compared to free peptide. However, creating multivalent peptide-dendrimers has been shown to increase the efficacy of a KLVFF peptide aggregation inhibitor[29] and this may be a factor in our study, due to several inhibitory peptides being able to interact simultaneously with oligomeric Aβ.

We reported previously a large increase in the affinity of RI-OR2-TAT for Aβ (K_d = 58-125 nM) compared to RI-OR2 alone (K_d = 9-12 μM), but this is not reflected in an equivalent jump in the ability of RI-OR2-TAT to inhibit Aβ aggregation at low concentrations of inhibitor.[12,13] We can conclude from this that an increase in binding affinity does not necessarily result in a more potent aggregation inhibitor. Here, we found that the affinity of PINPs for Aβ (K_d = 13.2-50 nM) is slightly higher than that obtained previously for RI-OR2-TAT, but the ability of PINPs to inhibit Aβ aggregation at low concentrations of the inhibitory peptide was greatly improved. In addition to multivalent interactions between RI-OR2-TAT and Aβ, another possible explanation for the potency of PINPs is based on the fact that RI-OR2-TAT contains many positively charged amino acid residues and the presence of multiple copies of this peptide on the NL surface (each PINP has around 1600 molecules of RI-OR2-TAT attached) would give a highly positively charged external layer that could attract and capture Aβ monomers, or oligomers as they form.[30] It is also feasible that Aβ is captured by the peptides exposed on the NL surface and is then incorporated into the lipid component of the NL, so effectively removing Aβ from solution. It is well known that Aβ oligomers insert into lipid membranes of cells and form pores or ion channels.[31–33]

The TAT portion of RI-OR-TAT, with its positively charged amino acid residues, also confers on the inhibitor an ability to

cross the BBB and reach the brain.[13] Here we show that this ability is maintained for PINPs. The PE of NL, using the in vitro BBB model, was much higher for PINPs than for UD liposomes, proving the effectiveness of the functionalized NL to flux across the cellular monolayer. Moreover, some PINPs are transported into the brain, through the BBB of healthy mice, and they show a protective effect on memory loss in Tg2576 mice. It is also possible that this is due to the 'sink' effect with the liposomes rapidly binding Aβ in blood before being removed, and this is driving export of Aβ from the brain.

Other NP-based treatments for AD are under investigation, including antibody-coated NP and secretase inhibitors as well as our previously published curcumin and lipid-ligand linked NL.[28,34–38] Despite promising preclinical data, no secretase inhibitor has succeeded in any advanced clinical trial[39] and, considering the serious side effects reported for immunisation with anti-Aβ antibodies,[40] anti-Aβ-coated NP could be problematic. In contrast, PINPs have 'stealth' properties and so should not elicit any immune response. Moreover, the aggregation of Aβ seems to be a purely pathological phenomenon, and so inhibition of this process should not result in problematic side-effects.

In addition to these therapeutic implications, PINPs also have potential as a molecular imaging agent.[41] The high affinity of RI-OR2-TAT for Aβ should allow specific labelling of amyloid plaques, and possibly Aβ oligomers, through addition of a relevant contrast agent (CT/MRI) or radiolabel (PET/SPECT) to form a multifunctional NP with 'theranostic' utility.

Appendix A. Supplementary data

Supplementary data to this article can be found online at doi:10.1016/j.nano.2016.10.006.

References

1. Wimo A, Prince M. *Alzheimer's Disease International World Alzheimer Report 2010 The Global Economic Impact of Dementia*. Alzheimer's Disease International (ADI); 2010.
2. Lambert MP, Barlow AK, Chromy BA, Edwards C, Freed R, Liosatos M, et al. Diffusible, nonfibrillar ligands derived from Aβ 1-42 are potent central nervous system neurotoxins. *S A* 1998;95:6448–53.
3. Wang HW, Pasternak JF, Kuo H, Ristic H, Lambert MP, Chromy B, et al. Soluble oligomers of β amyloid (1-42) inhibit long-term potentiation but not long-term depression in rat dentate gyrus. *Brain Res* 2002;924:133–40.
4. Walsh DM, Klyubin I, Fadeeva JV, Cullen WK, Anwyl R, Wolfe MS, et al. Naturally secreted oligomers of amyloid β protein potently inhibit hippocampal long-term potentiation in vivo. *Nature* 2002;416:535–9.
5. Kim HJ, Chae SC, Lee DK, Chromy B, Lee SC, Park YC, et al. Selective neuronal degeneration induced by soluble oligomeric amyloid β protein. *FASEB J* 2003;17:118–20.
6. Cleary JP, Walsh DM, Hofmeister JJ, Shankar GM, Kuskowski MA, Selkoe DJ, et al. Natural oligomers of the amyloid-β protein specifically disrupt cognitive function. *Nat Neurosci* 2005;8:79–84.
7. Walsh DM, Selkoe DJ. Aβ oligomers – a decade of discovery. *J Neurochem* 2007;101:1172–84.
8. Haass C, Selkoe DJ. Soluble protein oligomers in neurodegeneration: lessons from the Alzheimer's amyloid β-peptide. *Nat Rev Mol Cell Biol* 2007;8:101–12.
9. Ma Q-L, Yang F, Rosario ER, Ubeda OJ, Beech W, Gant DJ, et al. β-amyloid oligomers induce phosphorylation of tau and inactivation of insulin receptor substrate via c-Jun N-terminal kinase signaling: suppression by omega-3 fatty acids and curcumin. *J Neurosci* 2009;29:9078–89.
10. Howlett D. APP transgenic mice and their application to drug discovery. *Histol Histopathol* 2011;26:1611–32.
11. Austen BM, Paleologou KE, Ali SAE, Qureshi MM, Allsop D, El-Agnaf OMA. Designing peptide inhibitors for oligomerization and toxicity of Alzheimer's β-amyloid peptide. *Biochemistry* 2008;47:1984–92.
12. Taylor M, Moore S, Mayes J, Parkin E, Beeg M, Canovi M, et al. Development of a proteolytically stable retro-inverso peptide inhibitor of β amyloid oligomerization as a potential novel treatment for Alzheimer's disease. *Biochemistry* 2010;49:3261–72.
13. Parthasarathy V, McClean PL, Hölscher C, Taylor M, Tinker C, Jones G, et al. A novel retro-inverso peptide inhibitor reduces amyloid deposition, oxidation and inflammation and stimulates neurogenesis in the APPswe/PS1ΔE9 mouse model of Alzheimer's disease. *PLoS One* 2013;8:e54769, http://dx.doi.org/10.1371/journal.pone.0054769.
14. Torchilin VP. Recent advances with liposomes as pharmaceutical carriers. *Nat Rev Drug Discov* 2005;4:145–60.
15. Snakel JM, Li RC, Maynard HD, Caplan MR. Two-step synthesis of multivalent cancer-targeting constructs. *Biomacromolecules* 2010;11:160–7.
16. Bradford MM. A rapid and sensitive method for the quantitation of microgram quantities of protein utilizing the principle of protein-dye binding. *Anal Biochem* 1976;72:248–54.
17. Stewart JCM. Colorimetric determination of phospholipids with ammonium ferrothiocyanate. *Anal Biochem* 1980;104:10–4.
18. Tinker-Mill C, Mayes J, Allsop D, Kolosov OV. Ultrasonic force microscopy for nanomechanical characterization of early and late-stage amyloid-β peptide aggregation. *Sci Rep* 2014;4:4004.
19. Horcas I, Fernández R, Gómez-Rodríguez JM, Colchero J, Gómez-Herrero J, Baro AM. WSXM: a software for scanning probe microscopy and a tool for nanotechnology. *Rev Sci Instrum* 2007;78:013705.
20. Re F, Cambianica I, Sesana S, Salvati E, Cagnotto A, Salmona M, et al. Functionalization with ApoE-derived peptides enhances the interaction with brain capillary endothelial cells of liposomes binding amyloid-β peptide. *J Biotechnol* 2010;156:341–6.
21. Cecchelli R, Dehouck B, Descamps L, Fenart L, Buée-Scherrer VV, Duhem C, et al. In vitro model for evaluating drug transport across the blood–brain barrier. *Adv Drug Deliv Rev* 1999;36:165–78.
22. Re F, Cambianica I, Zona C, Sesana S, Gregori M, Rigolio R, et al. Functionalization of liposomes with ApoE-derived peptides at different density affects cellular uptake and drug transport across a blood–brain barrier model. *Nanomedicine* 2011;7:551–9.
23. Nobs L, Buchegger F, Gurny R, Allémann E. Current methods for attaching targeting ligands to liposomes and nanoparticles. *J Pharm Sci* 2004;93:1980–92.
24. Poller B, Gutmann H, Krähenbühl S, Weksler B, Romero I, Couraud PO, et al. The human brain endothelial cell line hCMEC/D3 as a human blood–brain barrier model for drug transport studies. *J Neurochem* 2008;107:1358–68.
25. Summerfield SG, Stevens AJ, Cutler L, del Carmen Osuna M, Hammond B, Tang SP, et al. Improving the in vitro prediction of in vivo central nervous system penetration: integrating permeability, P-glycoprotein efflux, and free fractions in blood and brain. *J Pharmacol Exp Ther* 2006;316:1282–90.
26. Webb MS, Harasym TO, Masin D, Bally MB, Mayer LD. Sphingomyelin-cholesterol liposomes significantly enhance the pharmacokinetic and therapeutic properties of vincristine in murine and human tumour models. *Cancer* 1995;72:896–904.
27. Nance EA, Woodworth GF, Sailor KA, Shih TY, Xu Q, Swaminathan G, et al. A dense poly(ethylene glycol) coating improves penetration of large polymeric nanoparticles within brain tissue. *Sci Transl Med* 2012;4(149):149ra119, http://dx.doi.org/10.1126/scitranslmed.3003594.

28. Taylor M, Moore S, Mourtas S, Niarakis A, Re F, Zona C, et al. Effect of curcumin-associated and lipid ligand functionalised nanoliposomes on aggregation of the Alzheimer's Aβ peptide. *Nanomedicine* 2011;7:541-50.
29. Chafekar SM, Malda H, Merkx M, Meijer EW, Viertl D, Lashuel HA, et al. Branched KLVFF tetramers strongly potentiate inhibition of β-amyloid aggregation. *Chembiochem* 2007;8:1857-64.
30. Wang Q, Shah N, Zhao J, Wang C, Zhao C, Liu L, et al. Structural, morphological, and kinetic studies of β-amyloid peptide aggregation on self-assembled monolayers. *Phys Chem Chem Phys* 2011;13:15200-10.
31. Arispe N, Rojas E, Pollard HB. Alzheimer disease amyloid β protein forms calcium channels in bilayer membranes: blockade by tromethamine and aluminum. *SA* 1993;90:567-71.
32. Arispe N, Pollard HB, Rojas E. Giant multilevel cation channels formed by Alzheimer disease amyloid β-protein [Aβ-(1–40)] in bilayer membranes. *SA* 1993;90:10573-7.
33. Fraser SP, Suh YH, Djamgoz MB. Ionic effects of the Alzheimer's disease β amyloid precursor protein and its metabolic fragments. *Trends Neurosci* 1997;20:67-72.
34. Richman M, Wilk S, Skirtenko N, Perelman A, Rahimipour S. Surface-modified protein microspheres capture amyloid-β and inhibit its aggregation and toxicity. *Chem Eur J* 2011;17:11171-7.
35. Gobbi M, Re F, Canovi M, Beeg M, Gregori M, Sesana S, et al. Lipid-based nanoparticles with high binding affinity for amyloid-β 1-42 peptide. *Biomaterials* 2010;31:6519-29.
36. Bana L, Minniti S, Salvati E, Sesana S, Zambelli V, Cagnotto A, et al. Liposomes bi-functionalized with phosphatidic acid and an ApoE-derived peptide affect Aβ aggregation features and cross the blood–brain-barrier: implications for therapy of Alzheimer disease. *Nanomedicine* 2014;10:1583-90.
37. Canovi M, Markoutsa E, Lazar AN, Pampalakis G, Clemente C, Re F, et al. The binding affinity of anti-Aβ1-42 MAb-decorated nanoliposomes to Aβ1 42 peptides in vitro and to amyloid deposits in post-mortem tissue. *Biomaterials* 2011;32:5689-97.
38. Yoo SI, Yang M, Brender JR, Subramanian V, Sun K, Joo NE, et al. Mechanism of fibrillation inhibition of amyloid peptides by inorganic nanoparticles reveals functional similarities with proteins. *Angew Chem Int Ed* 2011;50:5110-5.
39. Anand R, Gill KD, Mahdi AA. Therapeutics of Alzheimer's disease: past, present and future. *Neuropharmacology* 2014;76:27-50.
40. Delrieu J, Ousset PJ, Caillaud C, Vellas B. Clinical trials in Alzheimer's disease: immunotherapy approaches. *J Neurochem* 2012;120:S186-93.
41. Re F, Moresco R, Masserini M. Nanoparticles for neuroimaging. *Appl Phys* 2012;45:73001-12.